



HAL
open science

Modélisation Hamiltonienne à ports et commande distribuée de structures flexibles : application aux endoscopes biomédicaux à actionneurs à base de polymère électro-actif

Ning Liu

► **To cite this version:**

Ning Liu. Modélisation Hamiltonienne à ports et commande distribuée de structures flexibles : application aux endoscopes biomédicaux à actionneurs à base de polymère électro-actif. Automatique. Université Bourgogne Franche-Comté, 2020. Français. NNT : 2020UBFCD054 . tel-03261716

HAL Id: tel-03261716

<https://theses.hal.science/tel-03261716v1>

Submitted on 16 Jun 2021

HAL is a multi-disciplinary open access archive for the deposit and dissemination of scientific research documents, whether they are published or not. The documents may come from teaching and research institutions in France or abroad, or from public or private research centers.

L'archive ouverte pluridisciplinaire **HAL**, est destinée au dépôt et à la diffusion de documents scientifiques de niveau recherche, publiés ou non, émanant des établissements d'enseignement et de recherche français ou étrangers, des laboratoires publics ou privés.



THÈSE DE DOCTORAT DE L'ÉTABLISSEMENT UNIVERSITÉ
BOURGOGNE FRANCHE-COMTÉ
PRÉPARÉE À L'UNIVERSITÉ DE FRANCHE-COMTÉ

École doctorale n° 37
Sciences Pour l'Ingénieur et Microtechniques

Doctorat d'Automatique

par
Ning LIU

**Modélisation Hamiltonienne à ports et
commande distribuée de structures flexibles:
application aux endoscopes biomédicaux à
actionneurs à base de polymère électro-actif**

Thèse soutenue publiquement le 15 décembre 2020, à Besançon,
devant le jury composé de:

Laurent Lefèvre	Professeur des Universités, Grenoble INP- Esisar	Président
Thomas Meurer	Professeur, Université de Kiel Allemagne	Rapporteur
Edouard Laroche	Professeur des Universités, Université de Strasbourg	Rapporteur
Françoise Couenne	Chargée de Recherches CNRS, LAGEPP Lyon	Examinatrice
Yann Le Gorrec	Professeur des Universités, ENSMM Be- sançon	Directeur de thèse
Yongxin Wu	Maître de conférences, ENSMM Besançon	Codirecteur de thèse



PH.D. THESIS OF THE UNIVERSITY BOURGOGNE
FRANCHE-COMTÉ
PREPARED AT THE UNIVERSITY OF FRANCHE-COMTÉ

Doctoral school n° 37
Engineering Sciences and Microtechnologies

Ph.D. in Automatic

by
Ning LIU

**Port-Hamiltonian modeling and distributed
control of flexible structures:
application to bio-medical endoscopes with
electro-active polymer actuators**

Thesis defended publicly on December 15, 2020, in Besançon,
composition of jury:

Laurent Lefèvre	Professor of University, Grenoble INP-Esisar	President
Thomas Meurer	Professor, Kiel University, Germany	Reviewer
Edouard Laroche	Professor of University, University of Strasbourg	Reviewer
Françoise Couenne	Recherche Scientist CNRS, LAGEPP Lyon	Examiner
Yann Le Gorrec	Professor of University, ENSMM Besançon	Supervisor
Yongxin Wu	Associate Professor, ENSMM Besançon	Co-Supervisor

To my grandparents

Acknowledgment

During the three years of my Ph.D., I have received a lot of support from many people and I am very grateful to them.

First of all, I would express my deepest appreciation to my supervisors, Professor Yann Le Gorrec and Associate Professor Yongxin Wu. They have guided me in the field of port-Hamiltonian systems and have given me invaluable advises during the research. I also thank them for the time that they have spent reading my papers, giving me remarks, listening to my thoughts, and helping me to improve the research work. I will never forget the encouragement that Yann gave me after one of my presentations, which motivates me a lot to continue the work. I am also deeply indebted to Yongxin, for his enthusiasm, and for his help with the experimental setup, with the submission of papers, etc. I will keep these three years of working with them as a precious experience in my life.

Secondly, I would like to thank the jury members of my thesis defense committee, Professor Thomas Meurer, Professor Edouard Laroche, Doctor Françoise Couenne and Professor Laurent Lefèvre. I am grateful for their participation to my defense, and for their constructive remarks and advice. I wish to meet them in future conferences or seminars, and express my gratitude.

During the Ph.D., I have had the chances to discuss with professional people in my field, and I would like to thank them wholeheartedly. I owe a lot of thanks to Professor Bernard Maschke in University Lyon 1 and to Associate Professor Gou Nishida in Nihon University. Their work about the IPMC actuators has inspired my Ph.D. research. I am very appreciating for the discussion with them. I express again my gratitude to Professor Laurent Lefèvre, for his help with the controller design, and for the time he has spent revising our paper. I also thank Associate Professor Kanty Rabenorosoa in my laboratory, for involving me in the work of dielectric EAP actuators, which has broadened my research experiences, for helping me with the preparation of my thesis defense, and for improving my writing skills.

I express my grate appreciation to our PHS team. I would thank again Yann and Yongxin for organizing every convivial team meeting and afterwork meal. Special thank to Doctor Vincent Trenchant, for his patience and guidance with the structure preserving discretization work. To Mr. Andrea Mattioni. From the first day of my arrival in the lab, Andrea has helped me to get into the port-Hamiltonian system research, and have shared with me insightful knowledge about the system stability. To Associate Professor Hector Ramirez. I appreciate a lot to Hector for spending time revising the paper. To Mr. Jesús Toledo, for his encouragement and help during these three years. To Doctor Luis Mora for many scientific discussions we have had.

Furthermore, I would like to thank the director of our department, Professor Phillipe Lutz. I also thank every people in this lab, in particular Ms. Isabelle Gabet, Ms. Estelle Petite, Professor Jean-Marc Nicod, Associate Professor Emmanuel Piat, Associate Professor Zeina Al Masry, Associate Professor Abdenbi Mohand-Ousaid, Dr. Joël Abadie, Dr. Joël Bafumba Liseli, Mr. Jesús Toletto, Doctor Bhawnath Tiwari, Doctor Marwa Haddad, Doctor Abbas Homayouni Amlashi, Doctor Amine Benouhiba, Doctor Vladimir Gauthier, Doctor Omar Bougacha, Doctor Fawzia Amokrane, Doctor Benjamin Mauze, Ms. Chifaa Dahik, Mr. Yun-ling Lei, Mr. Kejun Hu, Mr. Luc Petiet, Mr. Pardeep Kumar, and Mr. Antoine André.

Last but not least, a huge thanks to my parents, my little brother, my grandparents, my aunt, and my uncles, for their unconditional support and encouragement. I would also like to thank my dear friends in France, Ms. Linhui Peng, Doctor Bingcong Jian, Mr. Shiyu Liu, Doctor Renzi Bai, Mr. Hang Guo, and Mr. Demeng Fan, for their accompanies in Lyon, and their help during these five years in France. Great thanks to my BFFs, Ms. Han Wang, Ms. Zhe Dong, and Mr. Chengzhi Jiang. Although in different continents with different time zones, their support and joy have helped me through the hardest periods and have lighten my life.

Ning LIU, February 9, 2021, in Besançon, France

Contents

	Acknowledgment	i
	Contents	iii
	List of Figures	vii
I	Introduction and state of the art	1
	I.1 Motivation and general context	2
	I.2 Literature review	4
	I.2.1 Endoscopes for surgery applications	4
	I.2.2 Toward miniaturized endoscopes	7
	I.2.3 Ionic polymer metal composite actuators	8
	I.3 Port-Hamiltonian Systems	11
	I.3.1 Finite dimensional PHSs	11
	I.3.2 Infinite dimensional PHSs	17
	I.3.3 Control for PHSs	23
	I.4 Contributions and outline	24
	I.4.1 Contributions	24
	I.4.2 Outline of the thesis	24
II	Port-Hamiltonian modeling of flexible bio-medical structures	27
	II.1 Model descriptions and simplifications	28
	II.1.1 1D beam model description	29
	II.1.2 Shell model description	29
	II.2 Port-Hamiltonian modeling of the IPMC actuator	30
	II.2.1 Electrical system	32
	II.2.2 Electro-stress diffusion system	35
	II.2.3 Mechanical system	39
	II.2.4 Multiscale coupling between subsystems	42
	II.2.5 Overall IPMC model	46

II.3	1D port-Hamiltonian model of the actuated endo- scope	51
II.4	2D port-Hamiltonian model of the actuated endo- scope	55
II.5	Summary	63
III	Numerical and experimental results	65
III.1	Structure preserving discretization methods	66
III.1.1	The mixed finite element approach	67
III.1.2	The finite difference method on staggered grids.....	77
III.1.3	Comparison of the mixed finite element method and the finite difference method on staggered grids	79
III.2	Application to the discretization of the IPMC actu- ator	81
III.2.1	Discretization of electric system	81
III.2.2	Discretization of electro-stress diffusion system	83
III.2.3	Discretization of the mechanical system	85
III.2.4	Descriptor form of the discretized global system	86
III.2.5	Elimination of the Lagrange multiplier	87
III.2.6	Simulation results and experimental validation	89
III.3	Summary	94
IV	In-domain distributed control	95
IV.1	Control problem formulation	98
IV.2	In-domain distributed CbI with early lumping ap- proach	99
IV.2.1	Fully-actuated case	104
IV.2.2	Under-actuated case	105
IV.2.3	Closed loop stability	108
IV.3	Numerical simulations	109
IV.3.1	Fully-actuated case	110
IV.3.2	Under-actuated case	113
IV.4	Summary	115
	Conclusions and perspectives	117
A	Bond Graph	121
A.1	Nodes with one port	122

A.2	Nodes with two ports	124
A.3	Nodes with multiple ports.....	124
B	Differential forms.....	127
C	Time integration	131
	Bibliography	135

List of Figures

I.1	Schematic diagram of an endoscope used in a MASTER system [Phee 10].....	2
I.2	Nasal surgery with endoscopes.	3
I.3	Different types of commercial endoscopes	4
I.4	Wire-driven push-pull manipulation of flexible endoscopes [Loeve 10]. 5	
I.5	Various actuation principles of endoscopes.....	6
I.6	Computer-aided design model of CTR with IPMC actuator [Chikhaoui 14a]. 8	
I.7	IPMC shape and structure.....	9
I.8	Applications of IPMC actuators.	9
I.10	Bond Graph of two separate mass-spring systems.	14
I.11	Bond Graph of two glued mass-spring systems.....	15
I.12	Schema bloc of CbI for PHS.	23
II.1	Model configuration of the micro-endoscope with the IPMC actuator.	28
II.2	Beam model configuration.	29
II.3	Shell model configuration.....	29
II.4	Diagram of the working principles of an IPMC actuator.	30
II.5	Coordinates representation of the IPMC actuator.	31
II.6	Local coordinates ξ and z with respect to the global coordinate x	31
II.7	Coordinate representation of the electrical system.....	32
II.8	Models of IPMC electrodes interface.....	32
II.9	Bond Graph of the electrical system dynamics.....	34
II.10	Coordinate representation of the electro-stress diffusion system.....	35
II.11	Solid and liquid phases of the gel.....	35
II.12	Bond Graph of the electro-stress diffusion system dynamics.....	38
II.13	Coordinate representation of the mechanical system.....	39

II.14	Force diagram of the Timoshenko beam.	40
II.15	Bond Graph of the mechanical system dynamics.	42
II.16	Diagram of the couplings between subsystems.	42
II.20	Schema of the overall IPMC actuator model.	48
II.21	Diagram of the inertial frame reference model, figure adapted from [Simo 86].	53
II.22	Deformation of the shell model.	57
II.23	Resultant forces and bending moments diagram.	58
III.1	Interconnection of adjacent elements.	70
III.2	Schema of the finite difference method on staggered grids.	78
III.4	Simulation results of the vibrating string, with the approximation method of mixed finite element.	79
III.5	Simulation results of the vibrating string, with the approximation method of finite difference on staggered grids.	80
III.6	Relative approximation error of the mixed finite element method and of the finite difference method on staggered grids with different discretized number $n = 10, 20, 50, 80, 100, 160, 320$	80
III.10	Experimental setup of the IPMC actuator.	89
III.12	Bode diagram of the impedance relevant to each discretized number N_ξ	91
III.13	Variation of the output current according to different discretization numbers N_z and N_b	91
III.15	Simulation results for M_{x1} , M_{x2} and M_{ext} along x-axis and the time ($N_\xi = 50$, $N_z = 10$ and $N_b = 100$).	93
IV.1	Simplified model for the control design.	96
IV.2	In-domain distributed CbI schema.	97
IV.3	Clamped-free vibrating string with fully-actuated case.	104
IV.4	Under-actuated case with $k = 2$	105
IV.5	Open loop simulation.	110
IV.6	Closed loop simulation in the fully-actuated case with pure damping injection and different damping coefficients α	110
IV.7	Closed loop simulation in the fully-actuated case with pure damping injection and with $\alpha = 4 \times 10^3$	111

IV.8	Close loop simulation in the fully-actuated case with energy shaping and damping injection and with different energy shaping parameters β	112
IV.9	Close loop simulation in the fully-actuated case with energy shaping and damping injection and with $\alpha = 4 \times 10^3$, $\beta = 5 \times 10^6$	112
IV.10	Evolution of the closed loop in the energy shaping and damping injection case with under actuation with 10 patches.	113
IV.11	Comparisons in the under-actuated case with 10 patches and 5 patches, respectively.	114
IV.12	Evolution of the closed loop in the energy shaping and damping injection case with under actuation with 5 patches.	114
IV.13	Closed loop evolution of the strain of the high order system, and comparison of the endpoint position of the low order and high order systems using the same controller.....	115
A.1	Bond Graph representations of Se and Sf.....	122
A.2	Bond Graph of linear R element.....	123
A.3	Bond Graph representations of ‘I’ and ‘C’ with integral causality. ...	123
A.4	Bond Graph representations of ‘TF’ and ‘Se’.....	124
A.5	Bond Graph representation of node types with multi-ports.....	125
A.6	Bond Graph representation of DTF	125

Chapter I

Introduction and state of the art

I.1	Motivation and general context	2
I.2	Literature review	4
I.2.1	Endoscopes for surgery applications	4
I.2.2	Toward miniaturized endoscopes	7
I.2.3	Ionic polymer metal composite actuators	8
I.3	Port-Hamiltonian Systems	11
I.3.1	Finite dimensional PHSs	11
I.3.2	Infinite dimensional PHSs	17
I.3.3	Control for PHSs	23
I.4	Contributions and outline	24
I.4.1	Contributions	24
I.4.2	Outline of the thesis	24

I.1 MOTIVATION AND GENERAL CONTEXT

This work is concerned with the mathematical modeling and control of smart micro-endoscopes actuated by biocompatible ionic polymer metal composite (IPMC) actuators.

This research arises naturally from the increasing need for minimally invasive surgeries, that led to the continuous evolvement of endoscopes. An endoscope is typically a slender or tubular instrument used to diagnose and to treat organs. They can access unattainable parts of the body without heavy surgical interventions. Conventional endoscopes are equipped with a control shaft at one side and a camera, a light, and other necessary instruments like laser or gripper at the other tip. As depicted in Fig. I.1, with the manipulation of the endoscopist, the endoscope can enter the treating area through natural orifices, like mouth, ears, nose and so on, in order to carry out medical diagnoses and treatments in the stomach, colon or other viscera of the patient. This kind of operation avoids creating external holes in the body of the patient, thus can reduce the trauma and recovery time [Ponsky 12]. It has been successfully applied in colorectal cancer diagnostic [Subramanian 05], cholecystectomy [Lehman 09], peroral cholangioscopy [Lee 20], etc.

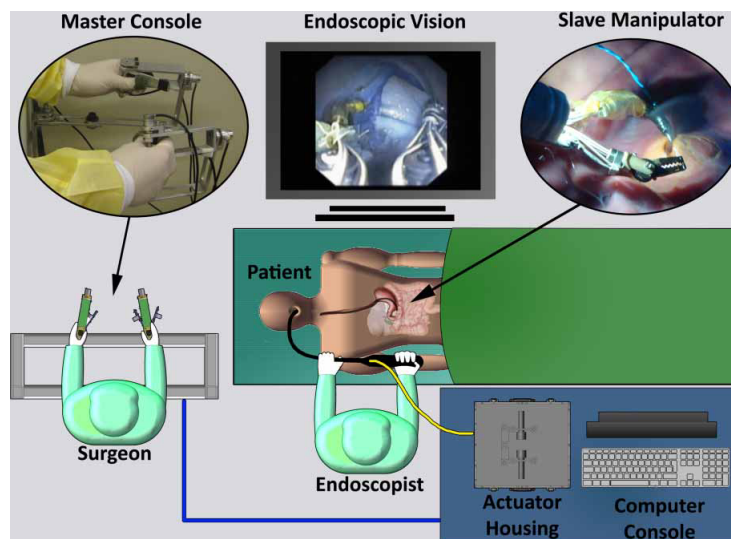


Figure I.1 – Schematic diagram of an endoscope used in a MASTER system [Phee 10].

The size of endoscopes varies according to the diagnostic areas, actuation, and operation functions [Chikhaoui 16]. A detailed introduction on the evolvement of conventional macro-endoscopes can be found in [Spaner 97, Abd-El-Barr 13]. Modern minimally invasive surgeries require that the endoscope can access to smaller regions, e.g. the nose, the brain, or the spine, to execute delicate surgeries. As depicted in Fig. I.2, the endoscope needs to go through quite thin cavities and be manipulated precisely in confined spaces, in order to reshape or remove

cartilage for the sake of fixing a deviated septum in the nose. As a consequence, the diameter of these specific endoscopes has to be reduced towards few millimeters and the structure has to be lighten in order to be flexible enough.

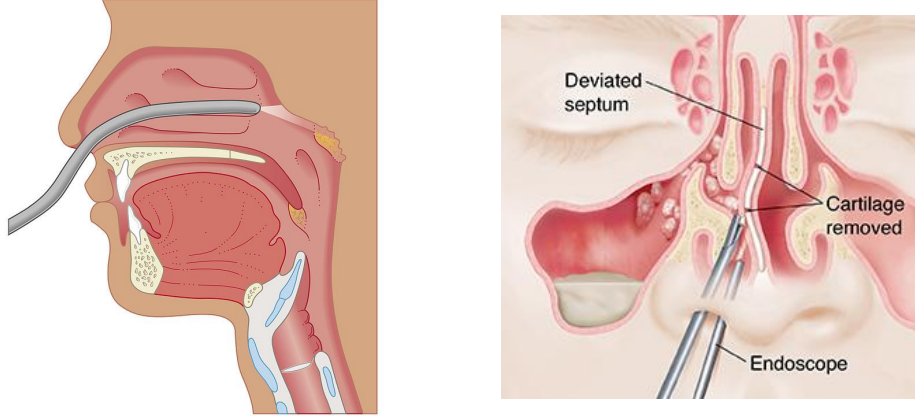


Figure I.2 – Nasal surgery with endoscopes.

To navigate and control the micro-endoscope, the embedded actuators must also be of very small size, and the structure of the actuator needs to be flexible enough to not lose the dexterity of the endoscope. Furthermore, the overall structure has to be biocompatible, meaning that the actuators should be non-toxic, and should be executed under a safe voltage range. To this end, recent works [Yoon 07, Chikhaoui 14b] propose to use electro-active polymer (EAP) actuators, especially the ionic polymer metal composite (IPMC) actuators, which match these aforementioned specifications and work well in humid environments.

The micro-endoscope embedded with IPMC actuators is expected to carry out the trajectory tracking, the shape control and the reduction of irrelevant vibrations. As a result, a precise multiphysical model for both the micro-endoscope and IPMC actuators as well as their coupling is of great necessity. The multiphysical aspect of this model lies in the electric circuit, the diffusion phenomenon inside the IPMC actuator and the mechanical deformation of the integrated structure. The relation between the input applied voltage and the output deformation is nonlinear. Moreover, both the micro-endoscope and IPMC actuators are flexible enough to be considered as a distributed parameter system formulated by partial differential equations (PDEs). To deal with this multiphysical, nonlinear and distributed parameter system, we shall use the infinite dimensional port-Hamiltonian framework as the energy, at the core of this framework, is the common factor to these multiphysical systems.

On the control aspect, the IPMC patches deliver distributed bending moments to the micro-endoscope. Therefore, an in-domain distributed control law under the infinite dimensional port-Hamiltonian framework is expected.

In what follows, we give a short literature review on endoscopes, IPMC actuators, and on the port-Hamiltonian framework. We also list the main contributions of this thesis and provide the outline of the manuscript.

I.2 LITERATURE REVIEW

I.2.1 Endoscopes for surgery applications

In the previous section, we have briefly introduced the definition and working principles of endoscopes, as well as the necessity towards miniaturized and smart micro-endoscopes for minimally invasive surgeries. In this subsection, we give an overview on existing endoscopes suitable for medical applications to help the reader to better understand the background of the thesis.

There are mainly three kinds of conventional endoscopes that can be used for medical applications. From the mechanical structural point of view, they can be sorted into rigid endoscopes, flexible endoscopes and capsule endoscopes [Li 16]. In what follows, we give a brief introduction on these endoscopes and their working principles and we provide several examples of existing commercial products of the three types of endoscopes.



(a) Rigid endoscope with working length of 175 mm, outer diameter of 4.3 mm, and rotatory angle of 10° to 100° .



(b) Flexible endoscope with working length of 1240 mm, outer diameter of 13.5 mm, and rotatory angle of -90° to 120° in the up-down direction and -90° to 110° in the left-right direction.



(c) Capsule endoscope PillCam SB3, with length of 26.2 mm, and diameter of 11.4 mm.

Figure I.3 – Different types of commercial endoscopes, with (a) ^a, (b) ^b, and (c) ^c.

a. <https://www.olympus.co.uk/medical/en/Products-and-solutions/Products/Product/ENDORIZON-SINUSCOPE.html>

b. <https://www.olympus.fr/medical/fr/Medical-FR-Landing-Page/Reprocessing-of-Olympus-Duodenoscopy-TJF-Q180V.html>

c. <https://www.medtronic.com/covidien/en-us/products/capsule-endoscopy/pillcam-sb-3-system.html>

The rigid endoscope is usually used for treating areas close to the insertion point. Embedded with multi mode fibers, it has a high image quality. As presented in Fig. I.3a, the endoscopist can rotate the tube and change the direction of the camera which is placed at the tip by rotating the two wheels at the other extremity. Yet its rigidity limits the access to distant fields for scans and manipulations, and may cause extra tissue damages to the patient. Flexible endoscopes, as depicted in Fig. I.3b, though do not have high image quality as the former one as a result of single mode optic fibers [Shahmoon 11], can access to smaller organs due to its larger flexibility in comparison with the rigid endoscope. The tube of flexible endoscopes is usually fabricated in Nitinol [Chikhaoui 16, Boushaki 14], and actuated by wires and levers inside the tube with the manipulation of the endoscopist. Different from the former two endoscopes, the capsule endoscope is a wireless device, which is shown in Fig. I.3c. It can be swallowed by the patient and move to small intestines with the help of gravity and peristaltic wave [Kim 05]. The locomotion can be improved by the use of electromagnetic forces [Lucarini 15]. However, the reachable zone of the capsule is very restricted because it can only be ingested or inoculated in blood vessels.

As mentioned before, conventional control of flexible endoscopes is realized via a wire-driven push-pull manipulation [Haga 04], where the wires inside the shaft pushes or pulls the endoscope to bend. This manipulation requires a high experience from the endoscopist. Furthermore, with the lack of dexterity, it is inevitable that the endoscope will push or even damage tissues nearby during the insertion process and cause discomfort for the patients. Therefore, the trajectory tracking, shape control and dynamic performance improvement of the endoscope are then necessary. To this end, one can add depth sensors [Loeve 10] on the tip of the tube and actuate the tube segment by segment with control wires, which is illustrated in Fig. I.4. By this way, the endoscopist can correct the shape of the endoscope and modify its trajectory. This control approach was adapted in the Neoguide Endoscopy System by [Eickhoff 07] and put into clinical use to traverse the natural shape of the colon. But, the use of wires is too expensive for micro-endoscopes with small diameters and it is not easy to miniaturize such an endoscope because of complex mechanical structures.

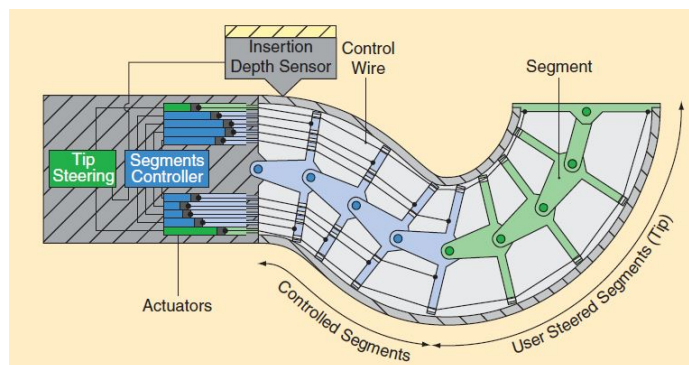


Figure I.4 – Wire-driven push-pull manipulation of flexible endoscopes [Loeve 10].

Alternative structures with different principles for the actuation have been proposed in the literature. Among them one can cite the motor driven [Chen 14], pneumatic [De Falco 17], and shape memory alloy (SMA) or shape memory polymer (SMP) actuation [Haga 04, Ikuta 88]. To the best of our knowledge, these actuated endoscopes have not been implemented in clinical use. In Fig. I.5a, the endoscope is composed of several segments, each of which is actuated by a motor and connected with each other through joints and springs. The idea of pneumatic actuated endoscopes comes from the octopus arm. As depicted in Fig. I.5b, the endoscope is divided into three modules, where pneumatic pipelines, stiffening channels and actuation chambers are placed. Pneumatic actuators are located in the actuation chambers. By controlling the pressure and flows of air coming into the chambers, one can control the deformation of the pneumatic actuators, thus that of the endoscope. The stiffening channel serves to tune the stiffness of the endoscope [De Falco 17]. The SMA actuated endoscope, as shown in Fig. I.5c is controlled by the temperature changes and can return to its initial configuration with the use of cooling water.

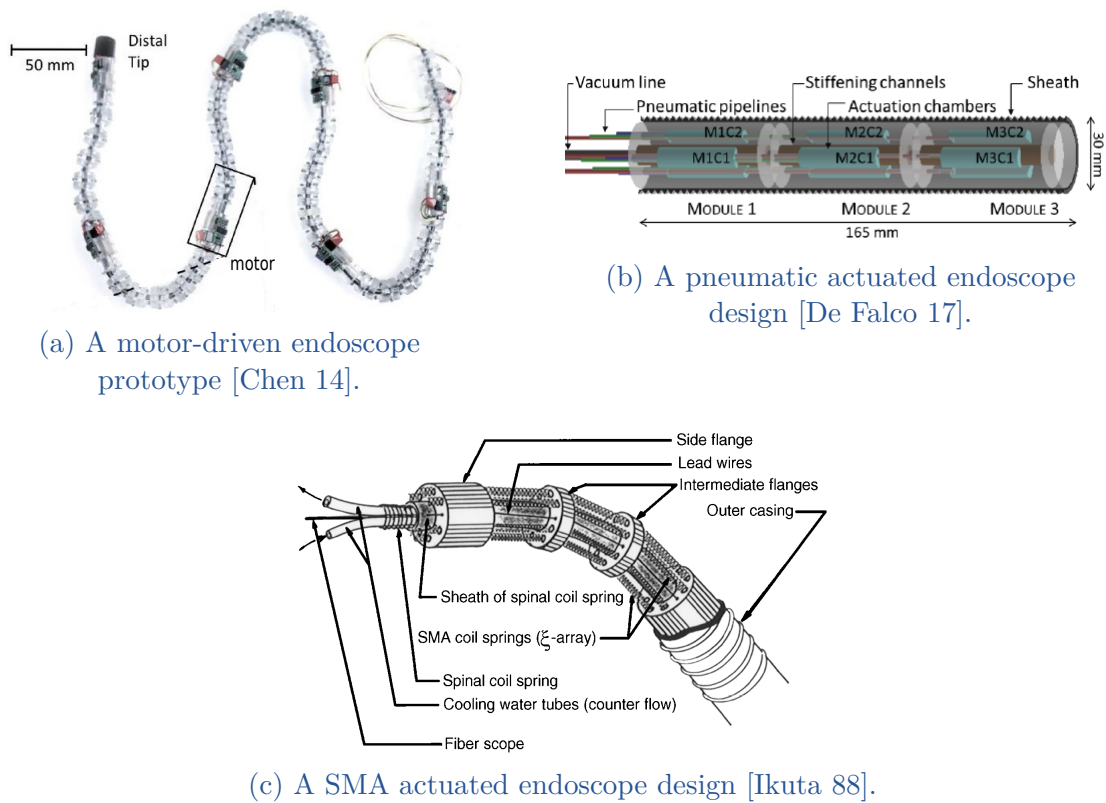


Figure I.5 – Various actuation principles of endoscopes.

We re-emphasize here the control objectives of the smart micro-endoscopes:

- to ideally conduct some end-tip trajectory tracking,
- to change the shape of the flexible structure,

- to reduce irrelevant vibrations due to some scanning probes at the end-tip of the apparatus.

Therefore, the control should allow to follow stable trajectories. Meanwhile, since the endoscope needs to bend to access smaller regions and to become rigid to carry out manipulations, its stiffness has to be tuned for necessary use [Gifari 19]. These control specifications require the actuators to be flexible enough, to generate distributed deformations, and to be small enough with adjustable stiffness for different uses (to be flexible when following the trajectory and to be stiff when grasping or scanning). For the safety of patients, the actuation voltage has to be as low as possible, especially for cardiac surgery where the heart is very sensible to the current [Shoa 09b]. From the fabrication aspect, the actuators are expected to be cheap and easy to fabricate.

These aforementioned requirements indicate that even if motors, pneumatic and SMA/SMP actuators give some interesting results in macroscopic configuration, their size or actuation principles are not suitable for the control of smart micro-endoscopes. Here we explain the main reasons. Motors are indeed expensive and usually have large dimensions that could limit the size of the endoscope. The pneumatic actuators need bulky air compressors, making the fabrication process complicated [Shoa 09a, Shoa 09b]. Besides, the actuation of pressure and air flow is more sophisticated than that of the electricity [De Greef 09]. In the case of SMA/SMP actuator, the actuation is usually slow because the cooling and heating processes take time.

As a result, to achieve the control requirements, electro-active polymer (EAP) actuators, and more precisely ionic polymer metal composite (IPMC) actuators are among the most promising choices that are currently investigated. The next subsection presents several models of micro-endoscopes, some of them being actuated using IPMC actuators.

I.2.2 Toward miniaturized endoscopes

Here we give a literature review on micro-endoscopes in terms of innovative design and control. According to the documentation, micro-endoscopes are designed using either active catheters [Masashi Ikeuchi 08, Shoa 09b, Shoa 09a, Yoon 07], or concentric tube robots (CTRs) [Webster 10, Girerd 17, Chikhaoui 14b].

Active catheters are small tubes used for fluid passage, and are usually implemented in vessels. The smallest catheter of diameter 200 μm , actuated by water pressure, has been fabricated in [Masashi Ikeuchi 08]. Active catheters actuated by IPMC actuators have been proposed in [Shoa 09b, Shoa 09a] and [Yoon 07].

CTRs are made up of a series of catheters (usually three tubes named the outer, middle and inner tubes) able to rotate, translate and bend. Usually the CTRs are actuated by translational and rotational motors, e.g. [Girerd 17]. To go further and get better dexterity, [Chikhaoui 14a] proposed a conceptual design of CTR coated with EAP actuators as its middle tube, which is presented in Fig. I.6. The diameter of outer, middle and inner tubes are of 4.5, 3.2, and

2.4 mm [Chikhaoui 14b], respectively. Our study is based on this preliminary design and aims at proposing both the mathematical model of the actuated flexible structure and its efficient control.

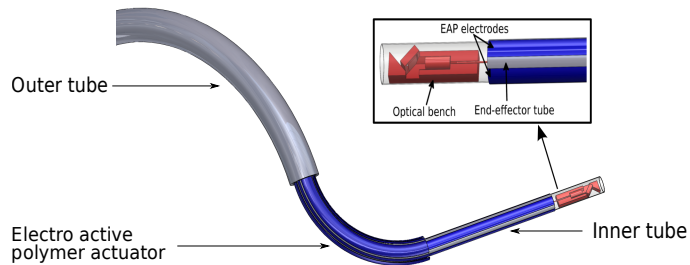


Figure I.6 – Computer-aided design model of CTR with IPMC actuator [Chikhaoui 14a].

The following subsection will present the features of IPMC actuators.

I.2.3 Ionic polymer metal composite actuators

As mentioned in Subsection I.2.1, the EAP actuators can be divided into two main categories, depending on their activation modes: electronic EAPs (e.g. piezoelectric polymers) and ionic EAPs (e.g. IPMCs) [Bar-Cohen 04, Bhandari 12]. The IPMC actuator is generally actuated with a small voltage (less than 5V) [Wang 15], and generates large deformations (up to 4 cm for an IPMC patch of 4 cm length applied with 2 V [Shahinpoor 01]). It has also a wide bandwidth from lower than 1 Hz up to few kHz compared to other piezoelectric or SMA actuators [Shahinpoor 16], making it suitable and safe in the applications of the endoscope actuation. However, its small blocking force (in the unit of gram-force [Shahinpoor 01]) may be seen as a drawback. A detailed comparison of IPMC actuators with other EAP actuators in terms of achievable performances is listed in Table I.1.

Table I.1 – Comparison of IPMC actuators with other kinds of EAP actuators [Bhandari 12].

EAP actuators	Strain(%)	Stress(MPa)	Efficiency(%)
IPMC	> 40	0.3	> 30
Piezoelectric	0.1	35	> 75
SMA	> 4	> 300	> 3.8

The shape and structure of an IPMC actuator patch are shown in Fig. I.7a and Fig. I.7b, respectively. The IPMC actuator consists of two electrode layers that are coated by platinum or gold [Takagi 14]. Between the two layers is a polyelectrolyte gel, typically perfluorosulfonic acid type called Nafion[®] [Takagi 14] or perfluorocarboxylic acid type named Flemion[®] [Asaka 14]. The applied voltage across the two electrodes causes the cations and solvent molecules inside the polyelectrolyte gel to move toward the cathode side of the electrodes. This transportation inside

the gel generates a swelling effect of the cathode as well as a shrinking effect of the anode side. As a result, the IPMC presents a quick bending effect to the anode side. A subsequent slow back relaxation is observed due to the pressure gradient of the solvent during the diffusion that will be detailed in Section II.2 and Subsection III.2.6.

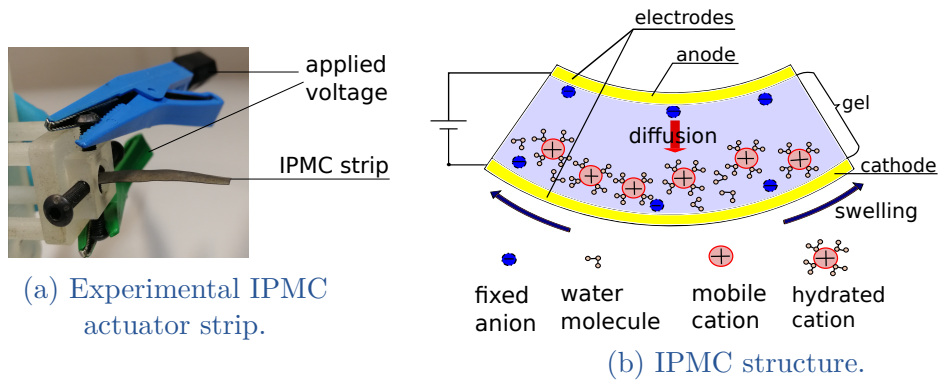


Figure I.7 – IPMC shape and structure.

The aforementioned properties of IPMC actuators make it very attractive in biomedical, and micro- or macro-electromechanical systems [Shahinpoor 05]. Two examples of such applications are given in Fig. I.8, where the IPMC patches are used as a gripper and as a pectoral fin of the manta-ray robot. On the other hand, even if it is not the focus of this thesis, IPMCs can also be used as sensors [Cha 13] and energy harvesters [Aureli 10].

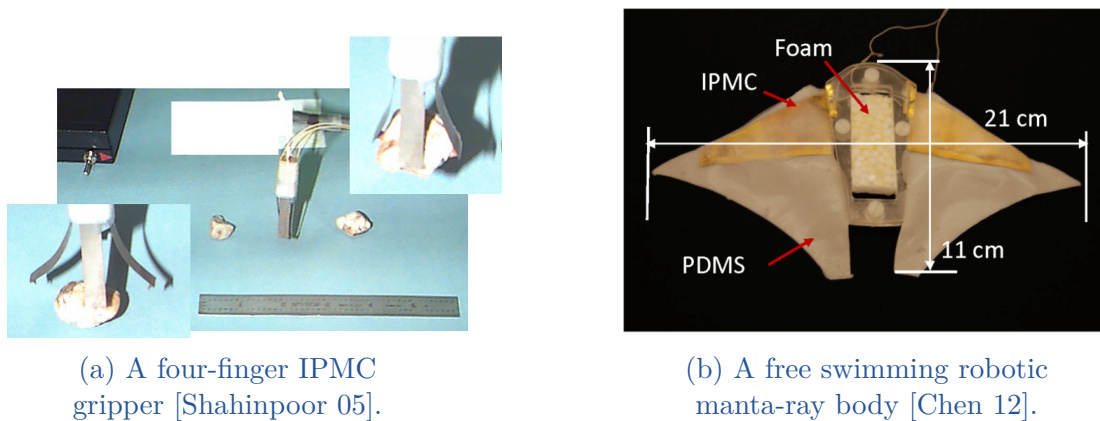


Figure I.8 – Applications of IPMC actuators.

Since the first design of IPMC actuators by [OGURO 92] in Japan and by [Shahinpoor 92] in the United States in 1992, the modeling of such actuators has been widely studied by many research groups. Various models have been proposed according to focused aspects, mainly sorted in three families: the black box model, the grey box model and the white box model. A brief description of the aforementioned models is presented in what follows.

As proposed in [Kanno 95, Bhandari 12], the black box approach, also termed as empirical approach, is the simplest modeling method that focuses on the relationship between the measured input (voltage or current) and output (endpoint displacement or force) of the system. The resulting model is derived in a case by case manner and depends on the experiment conditions. Consequently, it is not universal and may vary with respect to the considered IPMC and boundary conditions.

The white box model is at the opposite. The modeling is based on detailed physical and chemical principles. The established model is governed by multiscale PDEs. This is the precisest and most complex model type, as presented in [Nemat-Nasser 02, Shahinpoor 99, Branco 06, Zhu 13]. However, it is also difficult to use in simulation and for control design because many parameters at the molecular level, such as hydration coefficient and drag coefficient, are not precisely known and need to be identified [Nemat-Nasser 02].

The grey box model [Newbury 02, Bhandari 12], is more accurate than the black box model, and is easier to implement in simulation than the white box counterpart. It depends partly on empirical results and partly on physical principles [Bhandari 12]. As the modeling of IPMC actuators deals with electrical, chemical and mechanical phenomena, the coupling among these dynamics becomes an important research issue. [Nishida 08, Nishida 11] proposed a grey box model under the port-Hamiltonian framework, where the aforesaid multiphysical phenomena are modeled by three subsystems: the electrical system, the electro-stress diffusion system and the mechanical system. These subsystems are interconnected via boundary multiscale (BMS) coupling that will be detailed in Subsection II.2.4. In the model of [Nishida 08, Nishida 11] the mechanical contribution of the gel is considered through the internal material property of the overall mechanical structure, leading to a contradiction with respect to the assumptions that are made: locally symmetric deformation of the gel and distributed parameter model for the structure. This may cause a potential non-deformation problem when the gel generates a homogeneous bending moment, because the space derivative of the homogeneous bending moment exerted to the mechanical system will be zero.

In this thesis we use the port-Hamiltonian framework and propose to consider the gel as an external source that applies distributed bending moment densities to the IPMC strip. Meanwhile the gel deformation is connected to the mechanical deformation of the IPMC strip via Lagrange multipliers to deal with the intrinsic algebraic constraints. The detailed model is given in Section II.2, and a general explanation of the Lagrange multipliers in the port-Hamiltonian system (PHS) is presented in Subsection I.3.1.

I.3 PORT-HAMILTONIAN SYSTEMS

As previously mentioned, we shall apply the port-Hamiltonian framework to model the micro-endoscope embedded with IPMC actuators. In this section we give a detailed technical introduction of this modeling framework.

Firstly proposed in [Maschke 92], the port-Hamiltonian framework is an energy-based modeling framework, particularly suited for the modeling of multiphysical systems. An extensive review on PHS is presented in [van der Schaft 14]. The PHS is on the basis of Bond Graph representation (see details in Appendix A), where the dynamic equations are formulated through power conjugated flow variables f (e.g. velocity) and effort variables e (e.g. force). The time integration of the product of flow and effort variables gives the stored energy of the system, *i.e.* the Hamiltonian. The geometric structure, named Dirac structure which will be defined later, expresses the fact that the energy exchanged in the system and with the environment is preserved. Moreover, a PHS can interact with other PHSs through their ports in a power preserving way, and generates a new PHS [Duindam 09, van der Schaft 17].

Because energy is the common property of all physical system, the PHS gives a systematical framework for multiphysical system, and makes the coupling among different physical domains more clear. One can apply this port-based modeling to lumped parameter systems to get finite dimensional PHS, and to distributed parameter systems to get infinite dimensional PHS.

I.3.1 Finite dimensional PHSs

The general formulation of an autonomous finite dimensional Hamiltonian system without dissipation is given by:

$$\dot{x} = J(x) \frac{\partial H}{\partial x}(x), \quad (\text{I.1})$$

where $x \in \mathbb{R}^n$ denotes the state variables, also named as energy variables, $J(x) \in \mathbb{R}^{n \times n}$ is the interconnection matrix and is skew-symmetric representing the energy exchange in the system. H represents the Hamiltonian of the system. The time derivative of the Hamiltonian writes:

$$\frac{dH}{dt} = \frac{\partial^T H}{\partial x}(x) \dot{x}. \quad (\text{I.2})$$

According to (I.2), one can define a pair of power conjugated variables, flow variable f and effort variable e as:

$$f = \dot{x}, \quad e = \frac{\partial H}{\partial x}(x).$$

Because of the skew-symmetry of the matrix $J(x)$, (I.2) equals:

$$\frac{dH}{dt} = \frac{\partial^T H}{\partial x}(x) \dot{x}$$

$$\begin{aligned}
 &= \frac{\partial^T H}{\partial x}(x) J(x) \frac{\partial H(x)}{\partial x} \\
 &= 0.
 \end{aligned} \tag{I.3}$$

This indicates the power preservation of the system and is related to the intrinsic Dirac structure defined as follows:

Definition 1 (Dirac structure [Dalsmo 98, Duindam 09, van der Schaft 14]). *For a finite dimensional system, given an abstract linear subspace $\mathcal{F} = \mathbb{R}^n$ and \mathcal{E} with $\mathcal{E} = \mathcal{F}^*$ representing the duality, the subspace $\mathcal{D} \in \mathcal{F} \times \mathcal{E}$ is a Dirac structure if*

- $\langle e | f \rangle = 0$ for all $(f, e) \in \mathcal{D}$,
- $\dim \mathcal{D} = \dim \mathcal{F}$,

where $\langle e | f \rangle = e^T f$ is the duality product [Duindam 09] and \dim represents the dimension of the subspace.

One can find several representations of the Dirac structure in [Duindam 09] for finite dimensional systems. In this thesis, we use its image representation for the modeling and its kernel representation for the mixed finite element discretization. They are both given in what follows:

Image representation of Dirac structure [Duindam 09]:

$$\mathcal{D} = \left\{ (f, e) \in \mathcal{F} \times \mathcal{E} \mid f = E^T l, e = F^T l, l \in \mathbb{R}^n \right\}. \tag{I.4}$$

Kernel representation of Dirac structure [Duindam 09]:

$$\mathcal{D} = \{(f, e) \in \mathcal{F} \times \mathcal{E} \mid Ff + Ee = 0\} \tag{I.5}$$

with:

$$EF^T + FE^T = 0, \tag{I.6a}$$

$$\text{rank} \left(\begin{pmatrix} F & E \end{pmatrix} \right) = \dim \mathcal{F}. \tag{I.6b}$$

Linear maps F and E in (I.4) and (I.5) are defined as:

$$F : \mathcal{F} \rightarrow \mathcal{V}, \quad E : \mathcal{E} \rightarrow \mathcal{V},$$

with \mathcal{V} a linear space satisfying $\dim \mathcal{V} = \dim \mathcal{F}$. Similar Dirac structure can be defined in the non-homogeneous case including the boundary port variables and input and output, which will be presented in what follows.

The finite dimensional Hamiltonian formulation (I.1) is extended to the PHS by introducing the interconnection ports. A special case of the PHS is the input-state-output PHS with dissipation, which is given by:

$$f = (J(x) - R(x))e + B(x)u, \tag{I.7a}$$

$$y = B(x)^T e, \quad (\text{I.7b})$$

where $R(x) \in \mathbb{R}^{n \times n}$ is positive semidefinite given by $R(x) = g_R(x) S g_R(x)^T$ with $S \geq 0$, and $B(x) \in \mathbb{R}^{n \times m}$ is the input matrix. $u \in \mathbb{R}^m$ denotes the input and $y \in \mathbb{R}^m$ gives the power conjugated output.

The time derivative of the Hamiltonian here becomes:

$$\begin{aligned} \frac{dH}{dt} &= \frac{\partial^T H}{\partial x}(x) \dot{x} \\ &= e^T (J(x) - R(x)) e + \frac{\partial^T H}{\partial x}(x) B(x) u \\ &= -e^T R(x) e + y^T u, \end{aligned} \quad (\text{I.8})$$

which implies that the power change equals to the difference between the implied power and the dissipated power. If the Hamiltonian H is bounded from below, we can say that the system (I.7) is **passive**.

The dissipation in (I.7) opens a resistive port, with $e_R = S f_R$. Therefore, the associated Dirac structure of the input-state-output PHS with dissipation is:

$$\mathcal{D} = \left\{ (f, e, f_R, e_R, u, y) \mid y = B(x)^T e, \begin{pmatrix} f \\ f_R \end{pmatrix} = \begin{pmatrix} J & g_R \\ -g_R^T & 0 \end{pmatrix} \begin{pmatrix} e \\ e_R \end{pmatrix} + \begin{pmatrix} B(x) \\ 0 \end{pmatrix} u \right\}.$$

The PHS (I.7) can be extended to systems with constraints which are modeled with Lagrange multiplier [Duindam 09]:

$$f = (J(x) - R(x)) e + g_c \lambda_{\mathbf{L}} + B(x) u, \quad (\text{I.9a})$$

$$y = B(x)^T e, \quad (\text{I.9b})$$

$$0 = g_c^T e, \quad (\text{I.9c})$$

where $\lambda_{\mathbf{L}} \in \mathbb{R}^k$ denotes the Lagrange multiplier stemming from the modeling of mechanical constraints for example, and (I.9c) formulates the constraints. (I.9) herein defines a constrained PHS, with respect to a modulated Dirac structure:

$$\mathcal{D} = \left\{ (f, e, f_R, e_R, u, y) \mid 0 = g_c^T e, y = B(x)^T e, \lambda_{\mathbf{L}} \in \mathbb{R}^k, \begin{pmatrix} f \\ f_R \end{pmatrix} = \begin{pmatrix} J & g_R \\ -g_R^T & 0 \end{pmatrix} \begin{pmatrix} e \\ e_R \end{pmatrix} + \begin{pmatrix} g_c \\ 0 \end{pmatrix} \lambda_{\mathbf{L}} + \begin{pmatrix} B(x) \\ 0 \end{pmatrix} u \right\}.$$

Let us illustrate this constrained PHS with a simple example of two mass-spring systems, where two masses are glued as illustrated in Fig. I.9. It is supposed that the two systems have the same mass m and spring stiffness k . An external force F_{ext} is applied to one of the masses. The equations of motion without considering the constraints are written as:

$$\dot{p}_1 = -k q_1 + F_1 + F_{\text{ext}}, \quad (\text{I.10a})$$

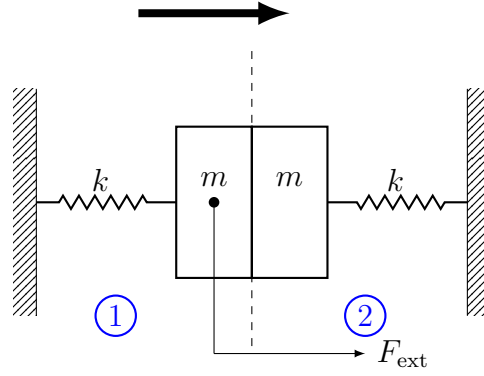


Figure I.9 – Schema of two glued mass-spring systems.

$$\dot{p}_2 = -kq_2 + F_2, \quad (\text{I.10b})$$

where q_1 , p_1 , q_2 and p_2 are related to positions and momentum of these two systems, respectively. F_1 and F_2 are the internal interaction forces, with $F_1 = -F_2$. The corresponding Bond Graphs (see details in Appendix A) of the two subsystems are given in Fig. I.10.



Figure I.10 – Bond Graph of two separate mass-spring systems.

The two glued mass-spring systems can be further interconnected by a Lagrange multiplier $\lambda_{\mathbf{L}} = F_1 = -F_2$, interpreted as the contact force acting at the constraint point with the same velocity constraint formulated as:

$$(1 \quad -1) \begin{pmatrix} \dot{q}_1 \\ \dot{q}_2 \end{pmatrix} = 0. \quad (\text{I.11})$$

The Hamiltonian writes:

$$H(q, p) = \frac{1}{2} \left(\frac{p_1^2}{m} + \frac{p_2^2}{m} \right) + \frac{1}{2} (kq_1^2 + kq_2^2). \quad (\text{I.12})$$

From (I.9)-(I.12), it follows that:

$$\underbrace{\begin{pmatrix} \dot{q}_1 \\ \dot{q}_2 \\ \dot{p}_1 \\ \dot{p}_2 \end{pmatrix}}_f = \underbrace{\begin{pmatrix} 0 & 0 & 1 & 0 \\ 0 & 0 & 0 & 1 \\ -1 & 0 & 0 & 0 \\ 0 & -1 & 0 & 0 \end{pmatrix}}_{\mathcal{J}} \underbrace{\begin{pmatrix} kq_1 \\ kq_2 \\ \frac{p_1}{m} \\ \frac{p_2}{m} \end{pmatrix}}_e + \underbrace{\begin{pmatrix} 0 \\ 0 \\ 1 \\ -1 \end{pmatrix}}_{g_c} \lambda_{\mathbf{L}} + \underbrace{\begin{pmatrix} 0 \\ 0 \\ 1 \\ 0 \end{pmatrix}}_B u, \quad (\text{I.13a})$$

$$y = B^T e = \frac{p_1}{m}, \quad (\text{I.13b})$$

$$0 = g_c^T e, \quad (\text{I.13c})$$

with $u = F_{\text{ext}}$.

In terms of the Bond Graph representation, the Lagrangian multiplier $\lambda_{\mathbf{L}}$ acts as a multi-port power preserving transformer [Karnopp 97], which helps to connect the two above Bond Graphs in Fig. I.10 together into Fig. I.11, where

$$A = \begin{pmatrix} 1 \\ -1 \end{pmatrix}.$$

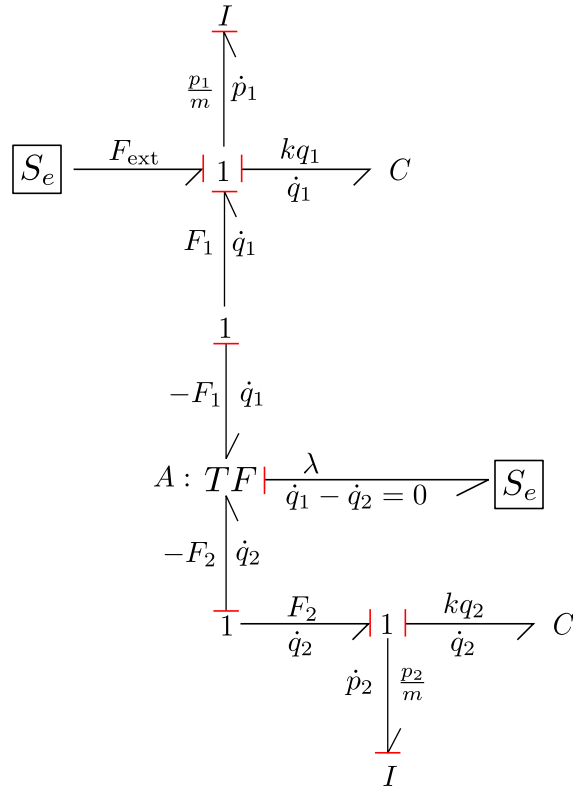


Figure I.11 – Bond Graph of two glued mass-spring systems.

For further simulation, the Lagrange multiplier in (I.9a) and (I.13a) should be eliminated. This elimination can be realized via the coordinate projection which is proposed in [van der Schaft 94] that preserves the port-Hamiltonian structure of the system. This projection approach has later been improved in [Wu 14] to get a descriptor formulation in the linear case where the effort variables $e = \mathcal{L}x$ with $\mathcal{L} \in \mathbb{R}^{n \times n}$ positive definite and symmetric. Here we give a short recall of the approach proposed in [Wu 14].

Given the matrix M that is formulated as:

$$M = \begin{pmatrix} s \\ (g_c^T g_c)^{-1} g_c^T \end{pmatrix}, \quad (\text{I.14})$$

with $s \in \mathbb{R}^{(n-k) \times n}$ satisfying $sg_c = 0$, one can transform the dynamic equation (I.9) into another coordinate:

$$\dot{\tilde{x}} = (\tilde{J} - \tilde{R}) \tilde{\mathcal{L}} \tilde{x} + \tilde{g}_c \lambda_{\mathbf{L}} + \tilde{B} u, \quad (\text{I.15a})$$

$$y = \tilde{B}^T \tilde{\mathcal{L}} \tilde{x}, \quad (\text{I.15b})$$

$$0 = \tilde{g}_c \tilde{\mathcal{L}} \tilde{x}, \quad (\text{I.15c})$$

with

$$\begin{aligned} \tilde{x} &= Mx, & \tilde{J} &= MJM^T, & \tilde{R} &= MRM^T, \\ \tilde{\mathcal{L}} &= M^{-T} \mathcal{L} M^{-1}, & \tilde{B} &= MB, & \tilde{g}_c &= Mg_c = \begin{pmatrix} 0 \\ I_k \end{pmatrix}. \end{aligned}$$

It is easy to find that the projected matrix \tilde{J} is still skew-symmetric, \tilde{R} is still symmetric and positive semidefinite, and $\tilde{\mathcal{L}}$ is still symmetric and positive definite. According to \tilde{g}_c in the new coordinate, one can decompose the state variable \tilde{x} into two parts, one of which does not depend on the Lagrange multiplier, and the other becomes a constraint. Let:

$$\tilde{x} = \begin{pmatrix} \tilde{x}_1 \\ \tilde{x}_2 \end{pmatrix}, \text{ with } \tilde{x}_1 \in \mathbb{R}^{n-k} \text{ and } \tilde{x}_2 \in \mathbb{R}^k,$$

(I.15a) is reformulated into [Wu 14]:

$$\begin{pmatrix} \dot{\tilde{x}}_1 \\ \dot{\tilde{x}}_2 \end{pmatrix} = \begin{pmatrix} \tilde{J}_{11} - \tilde{R}_{11} & \tilde{J}_{12} - \tilde{R}_{12} \\ \tilde{J}_{21} - \tilde{R}_{21} & \tilde{J}_{22} - \tilde{R}_{22} \end{pmatrix} \begin{pmatrix} \tilde{\mathcal{L}}_{11} & \tilde{\mathcal{L}}_{12} \\ \tilde{\mathcal{L}}_{21} & \tilde{\mathcal{L}}_{22} \end{pmatrix} \begin{pmatrix} \tilde{x}_1 \\ \tilde{x}_2 \end{pmatrix} + \begin{pmatrix} 0 \\ I_k \end{pmatrix} \lambda_{\mathbf{L}} + \begin{pmatrix} \tilde{B}_1 \\ \tilde{B}_2 \end{pmatrix} u. \quad (\text{I.16})$$

Replace the second line of (I.16) by (I.15c), one gets:

$$\begin{pmatrix} \dot{\tilde{x}}_1 \\ 0 \end{pmatrix} = \begin{pmatrix} \tilde{J}_{11} - \tilde{R}_{11} & \tilde{J}_{12} - \tilde{R}_{12} \\ 0 & I_k \end{pmatrix} \begin{pmatrix} \tilde{\mathcal{L}}_{11} & \tilde{\mathcal{L}}_{12} \\ \tilde{\mathcal{L}}_{21} & \tilde{\mathcal{L}}_{22} \end{pmatrix} \begin{pmatrix} \tilde{x}_1 \\ \tilde{x}_2 \end{pmatrix} + \begin{pmatrix} \tilde{B}_1 \\ 0 \end{pmatrix} u, \quad (\text{I.17})$$

which can be reformulated into a descriptor form [Wu 14] together with (I.15b):

$$\begin{pmatrix} I_{n-k} & 0 \\ 0 & 0 \end{pmatrix} \begin{pmatrix} \dot{\tilde{x}}_1 \\ \dot{\tilde{x}}_2 \end{pmatrix} = \begin{pmatrix} \tilde{J}_{11} - \tilde{R}_{11} & \tilde{J}_{12} - \tilde{R}_{12} \\ 0 & I_k \end{pmatrix} \begin{pmatrix} \tilde{\mathcal{L}}_{11} & \tilde{\mathcal{L}}_{12} \\ \tilde{\mathcal{L}}_{21} & \tilde{\mathcal{L}}_{22} \end{pmatrix} \begin{pmatrix} \tilde{x}_1 \\ \tilde{x}_2 \end{pmatrix} + \begin{pmatrix} \tilde{B}_1 \\ 0 \end{pmatrix} u, \quad (\text{I.18a})$$

$$y = \tilde{B}^T \tilde{\mathcal{L}} \tilde{x}. \quad (\text{I.18b})$$

Remark 1. *The established descriptor system (I.18) is a port-Hamiltonian system with respect to a Dirac structure [Wu 14]. One can formulate (I.18) in a kernel form by defining flow variables and effort variables as:*

$$\begin{aligned} f_1 &= \dot{\tilde{x}}_1, & f_2 &= \dot{\tilde{x}}_2, & f_p &= u, \\ e_1 &= \tilde{\mathcal{L}}_{11} \tilde{x}_1 + \tilde{\mathcal{L}}_{12} \tilde{x}_2, & e_2 &= \tilde{\mathcal{L}}_{21} \tilde{x}_1 + \tilde{\mathcal{L}}_{22} \tilde{x}_2, & e_p &= -y = - \begin{pmatrix} \tilde{B}_1^T & \tilde{B}_2^T \end{pmatrix} \begin{pmatrix} e_1 \\ e_2 \end{pmatrix}. \end{aligned}$$

The kernel formulation of (I.18) is therefore represented as:

$$\underbrace{\begin{pmatrix} -I_{n-k} & 0 & 0 \\ 0 & 0 & 0 \\ 0 & 0 & I \end{pmatrix}}_F \begin{pmatrix} f_1 \\ f_2 \\ -y \end{pmatrix} + \underbrace{\begin{pmatrix} \tilde{\mathcal{J}}_{11} & \tilde{\mathcal{J}}_{12} & \tilde{B}_1 \\ 0 & I_k & 0 \\ \tilde{B}_1^T & \tilde{B}_2^T & 0 \end{pmatrix}}_E \begin{pmatrix} e_1 \\ e_2 \\ u \end{pmatrix} = 0. \quad (\text{I.19})$$

With the two conditions satisfied in (I.6):

$$FE^T + EF^T = \begin{pmatrix} -\tilde{\mathcal{J}}_{11}^T - \tilde{\mathcal{J}}_{11} & 0 & 0 \\ 0 & 0 & 0 \\ 0 & 0 & 0 \end{pmatrix} = 0,$$

$$\text{rank}\left(\begin{pmatrix} F & E \end{pmatrix}\right) = n + m,$$

we can prove that (I.19) is a Dirac structure according to the kernel representation defined in (I.5).

I.3.2 Infinite dimensional PHSs

The infinite dimensional PHSs for distributed parameter systems have been firstly defined in [Maschke 00], and are extensively studied for the 1D linear case in [Le Gorrec 05] with applications to different fields of research such as fluid dynamics [Cardoso-Ribeiro 17], compliant robotics [Macchelli 04], chemical process control [Ramirez 13], vibroacoustic [Trenchant 18b], and also in higher dimensional cases as shell/plate vibrations [Macchelli 05, Brugnoli 19b], etc.

One can start with spatial 1D linear systems of the following dynamic form:

$$\begin{aligned} f(\zeta, t) &= \mathcal{J}e(\zeta, t) + B(\zeta)u_d(\zeta, t), \\ y_d(\zeta, t) &= B(\zeta)^*e(\zeta, t), \end{aligned} \quad (\text{I.20})$$

with flow and effort variables formulated by:

$$f(\zeta, t) = \frac{\partial x}{\partial t}(\zeta, t), \quad e(\zeta, t) = \frac{\partial \mathcal{H}}{\partial x}(\zeta, t), \quad (\text{I.21})$$

where $\zeta \in [a, b]$ is the spatial coordinate. $x \in L_2([a, b], \mathbb{R}^n)$ denotes the state of the system, also called the energy variable, with L_2 the Hilbert L2 space [Curtain 95, Yosida 95]. The N order differential operator $\mathcal{J} = \sum_{i=0}^N P_i \frac{\partial^i}{\partial \zeta^i}$, with $P_i = P_i^T(-1)^{i+1}$ and P_N full rank, is formally skew symmetric that guarantees the preservation of energy through the coupling among different subsystems and with their environment. $u_d \in L_2([a, b])$ and $y_d \in L_2([a, b])$ are related to power conjugated distributed input and output, with B^* the adjoint operator of B . The operator $B(\zeta)$ is bounded, denoting the in-domain input operator which maps the distributed input u_d (e.g. the exterior force density) to the state space x . $\mathcal{H}(\zeta, t)$ represents the energy density of the system.

Remark 2. For linear systems, the energy density \mathcal{H} is formulated as

$$\mathcal{H}(\zeta, t) = \frac{1}{2} x^*(\zeta, t) \mathcal{L}x(\zeta, t), \quad (\text{I.22})$$

with \mathcal{L} the energy bounded operator. Therefor, the effort variables in (I.21) becomes:

$$e(\zeta, t) = \mathcal{L}x(\zeta, t). \quad (\text{I.23})$$

The Hamiltonian $H(t)$ is the stored energy of the system (I.20), given as:

$$H(t) = \int_a^b \mathcal{H} \, d\zeta = \frac{1}{2} \int_a^b x^* \mathcal{L}x \, d\zeta. \quad (\text{I.24})$$

The boundary port variables of the system (I.20) can be defined as [Le Gorrec 05]:

$$\begin{pmatrix} f_\partial(t) \\ e_\partial(t) \end{pmatrix} = R_{ext} \begin{pmatrix} e(b, t) \\ \vdots \\ \frac{d^{N-1}e}{d\zeta^{N-1}}(b, t) \\ e(a, t) \\ \vdots \\ \frac{d^{N-1}e}{d\zeta^{N-1}}(a, t) \end{pmatrix}, \quad (\text{I.25})$$

such that $\frac{dH}{dt}(t) = f_\partial(t)^T e_\partial(t)$ with $u_d = 0$, where

$$R_{ext} = \frac{U}{\sqrt{2}} \begin{pmatrix} Q & -Q \\ I & I \end{pmatrix}, \quad \text{with } Q = \begin{pmatrix} P_1 & P_2 & \cdots & P_N \\ -P_2 & \cdots & -P_N & 0 \\ \vdots & \cdots & \cdots & \vdots \\ (-1)^{N-1}P_N & 0 & \cdots & 0 \end{pmatrix}, \quad (\text{I.26})$$

and U is a unitary matrix under the condition that $U^T \Sigma U = \Sigma$, with $\Sigma = \begin{pmatrix} 0 & I \\ I & 0 \end{pmatrix}$.

The inputs of the system (I.20) are divided into boundary input and distributed in-domain input. Distributed input u_d and output y_d have already been presented in (I.20). Boundary input u_b and output y_b are chosen from the boundary port variables as follows [Le Gorrec 05]:

$$u_b(t) = W \begin{pmatrix} f_\partial(t) \\ e_\partial(t) \end{pmatrix}, \quad y_b(t) = \tilde{W} \begin{pmatrix} f_\partial(t) \\ e_\partial(t) \end{pmatrix}, \quad (\text{I.27})$$

with $W \in \mathbb{R}^{nN \times 2nN}$ satisfying $W \Sigma W^T \geq 0$, $\tilde{W} \in \mathbb{R}^{nN \times 2nN}$ and $\begin{pmatrix} W \\ \tilde{W} \end{pmatrix}$ invertible.

In this case, it is shown in [Le Gorrec 05] that the domain of the operator \mathcal{J} defines a contraction semigroup. As a result, (I.20) and (I.27) defines a boundary control system.

When considering the distributed input and output, with the integration by part, the time derivative of the Hamiltonian (I.24) is¹:

$$\begin{aligned}
 \frac{dH}{dt} &= \int_a^b f^T e \, d\zeta + \int_a^b u_d^T y_d \, d\zeta \\
 &= \int_a^b (\mathcal{J}e)^T e \, d\zeta + \int_a^b u_d^T y_d \, d\zeta \\
 &= \int_a^b \left(P_0 e + P_1 \frac{\partial e}{\partial \zeta} + \cdots + P_N \frac{\partial^N e}{\partial \zeta^N} \right)^T e \, d\zeta + \int_a^b u_d^T y_d \, d\zeta \\
 &= \frac{1}{2} \left[e^T P_1^T e + \frac{\partial e^T}{\partial \zeta} P_2^T e - e^T P_2^T \frac{\partial e}{\partial \zeta} + \cdots + \sum_{i=0}^{N-1} (-1)^i \left(\frac{\partial^i e^T}{\partial \zeta^i} P_N^T \frac{\partial^{N-1-i} e}{\partial \zeta^{N-1-i}} \right) \right]_a^b \\
 &\quad + \int_a^b u_d^T y_d \, d\zeta \\
 &= \frac{1}{2} \begin{pmatrix} f^T & e^T \end{pmatrix} \Sigma \begin{pmatrix} f_\partial \\ e_\partial \end{pmatrix} + \int_a^b u_d^T y_d \, d\zeta \\
 &= \frac{1}{2} \begin{pmatrix} u_b^T & y_b^T \end{pmatrix} P_{W, \tilde{W}} \begin{pmatrix} u_b \\ y_b \end{pmatrix} + \int_a^b u_d^T y_d \, d\zeta, \tag{I.28}
 \end{aligned}$$

with $P_{W, \tilde{W}}^{-1} = \begin{pmatrix} W \Sigma W^T & W \Sigma \tilde{W}^T \\ \tilde{W} \Sigma W^T & \tilde{W} \Sigma \tilde{W}^T \end{pmatrix}$.

If W and \tilde{W} are chosen to satisfy the following conditions [Le Gorrec 05]:

$$\begin{aligned}
 W &= S \begin{pmatrix} I + V & I - V \end{pmatrix}, \\
 \tilde{W} &= \tilde{S} \begin{pmatrix} I + \tilde{V} & I - \tilde{V} \end{pmatrix}, \\
 I &= 2\tilde{S}(I - \tilde{V}V^T)S^T,
 \end{aligned}$$

with S and \tilde{S} invertible, and V and \tilde{V} unitary, (I.28) can be substituted into:

$$\frac{dH}{dt}(t) = u_b(t)^T y_b(t) + \int_a^b u_d(\zeta, t)^T y_d(\zeta, t) \, d\zeta. \tag{I.29}$$

Equation (I.29) reflects the power balance of a non-dissipative system. The variation of the energy is equal to the implied boundary energy and the implied in-domain distributed energy.

We have already defined the Dirac structure for finite dimensional PHSs in Subsection I.3.1, here we define the intrinsic geometric structure for infinite dimensional PHSs: the Stokes-Dirac structure. We first define the space of flow \mathcal{F} and the space of effort \mathcal{E} by the following equations [van der Schaft 02]:

$$\mathcal{F} = \left\{ \begin{pmatrix} f \\ f_\partial \\ u_d \end{pmatrix} \in L_2([a, b], \mathbb{R}^n) \times \mathbb{R}^{\{a, b\}} \times L_2([a, b]) \right\},$$

1. For the sake of compactness, the parameters ζ and t are omitted in this part.

$$\mathcal{E} = \left\{ \begin{pmatrix} e \\ e_\partial \\ y_d \end{pmatrix} \in H^N([a, b], \mathbb{R}^n) \times \mathbb{R}^{\{a, b\}} \times L_2([a, b]) \right\}, \quad (\text{I.30})$$

with $H^N([a, b], \mathbb{R}^n)$ denoting the Sobolev space [Curtain 95, Yosida 95] of N times differentiable functions on the interval $[a, b]$.

Definition 2 (Stokes-Dirac structure). *As for the infinite dimensional PHS, the Stokes's theorem is applied during the power conservation computation because of the presence of boundary variables (see details in [Maschke 00]). Therefore, the subspace $\mathcal{D} \in \mathcal{F} \times \mathcal{E}$ defined by*

$$\mathcal{D} = \left\{ \left(\begin{pmatrix} f \\ f_\partial \\ u_d \end{pmatrix}, \begin{pmatrix} e \\ e_\partial \\ y_d \end{pmatrix} \right) \in \mathcal{F} \times \mathcal{E} \mid f = \mathcal{J}e + B(\zeta)u_d, y_d = B^*e, \right. \\ \left. \text{and } \begin{pmatrix} f_\partial \\ e_\partial \end{pmatrix} \text{ calculated by (I.25)} \right\} \quad (\text{I.31})$$

is a Stokes-Dirac structure.

Here we take the example of a 1D vibrating string without dissipation on the coordinate $\zeta \in [0, L]$ to illustrate the aforementioned infinite dimensional port-Hamiltonian formulation. The dynamics of this string reads:

$$\frac{\partial^2 \omega}{\partial t^2}(\zeta, t) = \frac{T(\zeta)}{\rho(\zeta)} \frac{\partial^2 \omega}{\partial \zeta^2}(\zeta, t), \quad (\text{I.32})$$

where ω denotes the transversal displacement, T and ρ refer to the modulus of elasticity and the density, respectively.

Taking the energy, flow and effort variables as:

$$\begin{pmatrix} x_1(\zeta, t) \\ x_2(\zeta, t) \end{pmatrix} = \begin{pmatrix} \frac{\partial \omega}{\partial \zeta}(\zeta, t) \\ \rho(\zeta) \frac{\partial \omega}{\partial t}(\zeta, t) \end{pmatrix}, \quad \begin{pmatrix} f_1(\zeta, t) \\ f_2(\zeta, t) \end{pmatrix} = \frac{\partial}{\partial t} \begin{pmatrix} x_1(\zeta, t) \\ x_2(\zeta, t) \end{pmatrix}, \\ \begin{pmatrix} e_1(\zeta, t) \\ e_2(\zeta, t) \end{pmatrix} = \begin{pmatrix} T(\zeta) \frac{\partial \omega}{\partial \zeta}(\zeta, t) \\ \frac{\partial \omega}{\partial t}(\zeta, t) \end{pmatrix}, \quad (\text{I.33})$$

equation (I.32) is reformulated in the port-Hamiltonian framework:

$$\begin{pmatrix} f_1(\zeta, t) \\ f_2(\zeta, t) \end{pmatrix} = \begin{pmatrix} 0 & \frac{\partial}{\partial \zeta} \\ \frac{\partial}{\partial \zeta} & 0 \end{pmatrix} \begin{pmatrix} e_1(\zeta, t) \\ e_2(\zeta, t) \end{pmatrix}. \quad (\text{I.34})$$

Choosing

$$U = \frac{\sqrt{2}}{2} \begin{pmatrix} 0 & -1 & 1 & 0 \\ 0 & 1 & 1 & 0 \\ -1 & 0 & 0 & 1 \\ -1 & 0 & 0 & -1 \end{pmatrix}, \quad (\text{I.35})$$

boundary port variables are

$$\begin{pmatrix} f_{\partial}(t) \\ e_{\partial}(t) \end{pmatrix} = \begin{pmatrix} e_1(0, t) \\ e_1(L, t) \\ e_2(0, t) \\ -e_2(L, t) \end{pmatrix}. \quad (\text{I.36})$$

The Hamiltonian of the system expresses as:

$$H(x_1, x_2) = \frac{1}{2} \int_0^L \left(T(\zeta) (x_1(\zeta, t))^2 + \frac{1}{\rho(\zeta)} (x_2(\zeta, t))^2 \right) d\zeta, \quad (\text{I.37})$$

which is the sum of the potential energy and the kinetic energy.

Define the flow and effort space as:

$$\begin{aligned} \mathcal{F} &= \left\{ \begin{pmatrix} f \\ f_{\partial} \end{pmatrix} \in L_2([0, L], \mathbb{R}^2) \times \mathbb{R}^{\{0, L\}} \right\}, \\ \mathcal{E} &= \left\{ \begin{pmatrix} e \\ e_{\partial} \end{pmatrix} \in H^N([0, L], \mathbb{R}^2) \times \mathbb{R}^{\{0, L\}} \right\}, \end{aligned}$$

the linear subset $\mathcal{D} \in \mathcal{F} \times \mathcal{E}$ defined by

$$\mathcal{D} = \left\{ \left(\begin{pmatrix} f \\ f_{\partial} \end{pmatrix}, \begin{pmatrix} e \\ e_{\partial} \end{pmatrix} \right) \in \mathcal{F} \times \mathcal{E} \mid f = \mathcal{J}e, \text{ and } \begin{pmatrix} f_{\partial} \\ e_{\partial} \end{pmatrix} \text{ calculated by (I.36)} \right\} \quad (\text{I.38})$$

generates a Stokes-Dirac structure.

The system (I.20) can be extended to dissipative systems formulated as:

$$f(\zeta, t) = \left(\mathcal{J} - \underbrace{\mathcal{G}_R S_R \mathcal{G}_R^*}_{\mathcal{R}} \right) e(\zeta, t) + B(\zeta) u_d. \quad (\text{I.39})$$

The product \mathcal{R} is related to the dissipation, with operators S_R coercive and $\mathcal{G}_R = \sum_{i=0}^N G_i \frac{\partial^i}{\partial \zeta^i}$.

In order to formulate (I.39) in the port-Hamiltonian framework, a pair of flow and effort variables is added [Villegas 07]:

$$\begin{pmatrix} f(\zeta, t) \\ f_R(\zeta, t) \end{pmatrix} = \underbrace{\begin{pmatrix} \mathcal{J} & \mathcal{G}_R \\ -\mathcal{G}_R^* & 0 \end{pmatrix}}_{\mathcal{J}_e} \begin{pmatrix} e(\zeta, t) \\ e_R(\zeta, t) \end{pmatrix} + \begin{pmatrix} B(\zeta) \\ 0 \end{pmatrix} u_d, \quad (\text{I.40})$$

closed with

$$e_R(\zeta, t) = S_R f_R(\zeta, t). \quad (\text{I.41})$$

The extended operator \mathcal{J}_e is again skew-symmetric, indicating that we open another resistive port in the system while keeping the power conservation. The definition of boundary variables is quite similar to (I.25), with some modifications

because the matrix Q in (I.26) may now be singular. It is shown in [Villegas 07] that with a projection, the aforementioned singularity can be solved by choosing the boundary variables as:

$$\begin{pmatrix} \tilde{f}_\partial(t) \\ \tilde{e}_\partial(t) \end{pmatrix} = \tilde{R}_{ext} \begin{pmatrix} M_Q & 0 \\ 0 & M_Q \end{pmatrix} \begin{pmatrix} e(b, t) \\ \vdots \\ \frac{d^{N-1}e}{d\zeta^{N-1}}(b, t) \\ e(a, t) \\ \vdots \\ \frac{d^{N-1}e}{d\zeta^{N-1}}(a, t) \end{pmatrix}, \quad (\text{I.42})$$

with $\tilde{R}_{ext} = \frac{U}{\sqrt{2}} \begin{pmatrix} \tilde{Q} & -\tilde{Q} \\ I & I \end{pmatrix}$, $\tilde{Q} = M^T Q M$, $M_Q = (M^T M)^{-1} M^T$, $M \in \mathbb{R}^{nN \times r}$ and r denoting the rank of matrix Q . If Q is nonsingular, one can choose $M = I$ and $\tilde{Q} = Q$ in the sequel.

Let us consider an illustrative example of the 1D heat equation in an interval of $\zeta \in [a, b]$, which is given by:

$$\rho_h c \frac{\partial T_h}{\partial t}(\zeta, t) = \lambda_h \frac{\partial^2 T_h}{\partial \zeta^2}(\zeta, t), \quad (\text{I.43})$$

where T_h represents the temperature, ρ_h represents the density of the material, c denotes the specific heat capacity and λ_h refers to the thermal conductivity of the material.

Under the port-Hamiltonian framework, (I.43) is reformulated into:

$$\underbrace{\begin{pmatrix} \frac{\partial T_h}{\partial t} \\ \frac{\partial T_h}{\partial \zeta} \end{pmatrix}}_{f_e} = \underbrace{\begin{pmatrix} 0 & \frac{\partial}{\partial \zeta} \\ \frac{\partial}{\partial \zeta} & 0 \end{pmatrix}}_{\mathcal{J}_e} \underbrace{\begin{pmatrix} T_h \\ \frac{\lambda_h}{\rho_h c} \frac{\partial T_h}{\partial \zeta} \end{pmatrix}}_{e_e}, \quad (\text{I.44})$$

with $\mathcal{J} = 0$, $\mathcal{G}_R = \frac{\partial}{\partial \zeta}$ and $S_R = \frac{\lambda_h}{\rho_h c}$. According to (I.42), the boundary port variables are defined as:

$$\begin{pmatrix} f_\partial \\ e_\partial \end{pmatrix} = \begin{pmatrix} T_h(a) \\ T_h(b) \\ \frac{\lambda_h}{\rho_h c} \frac{\partial T_h}{\partial \zeta}(a) \\ -\frac{\lambda_h}{\rho_h c} \frac{\partial T_h}{\partial \zeta}(b) \end{pmatrix}, \quad (\text{I.45})$$

with extended $Q = P_1 = \begin{pmatrix} 0 & 1 \\ 1 & 0 \end{pmatrix}$ full rank, $\tilde{R}_{ext} = \frac{U}{\sqrt{2}} \begin{pmatrix} Q & -Q \\ I & I \end{pmatrix}$ and U the same as (I.35).

Moreover, the extension of (I.20) to n-dimensional systems has been proposed using the differential geometry in [Duindam 09]. But the analysis of existence of solution remains an open problem.

I.3.3 Control for PHSs

We have shown in the previous subsections that the Hamiltonian of a PHS is always semi-positive definite and its time derivative is semi-negative definite, making it a good Lyapunov candidate for nonlinear control. Furthermore, the intrinsic passivity of a PHS paves the way for passivity-based control (PBC) [Ortega 01].

The concept of PBC has initially been proposed in [Ortega 88], where the passivity of rigid robots was exploited to stabilize the system. Compared to other nonlinear control designs, such as nonlinearity cancellation or high gain, the PBC approach allows the controller to have physical meanings, and is largely applied to systems modeled by Euler-Lagrange equations [Ortega 98]. However, the Lagrange structure is not preserved for electrical and electro-mechanical systems, and the desired Lyapunov functions lacks the physical interpretation.

To solve this problem, the PBC has later been applied to PHSs in [Ortega 99a, Ortega 99b]. One can assign the equilibrium point, and improve the transient response with modified energy matrix using energy shaping methodology. The closed loop stability is guaranteed by Lyapunov arguments and damping injection methodology [Ortega 01]. Many dedicated PBC designs have been proposed for PHSs, see for instance [van der Schaft 17] for a general introduction. Among these controller designs, Control by Interconnection (CbI) is based on the passive interconnection of the plant system and the controller. The controller is also designed to be a PHS, such that the closed loop system is again a PHS [Ortega 08, van der Schaft 17]. A simple bloc diagram as presented in Fig. I.12 can clearly demonstrate this interconnection. The CbI consists in shaping the closed loop energy function (usually the closed loop potential energy part) by an appropriate choice of the controller parameters. The state variables of the plant system and those of the controller are related with an invariant set, *i.e.* the Casimir function, making the CbI equivalent to a state feedback [Ortega 08].

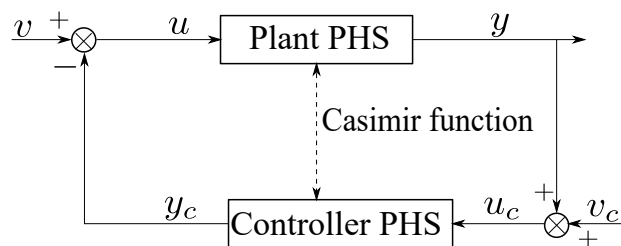


Figure I.12 – Schema bloc of CbI for PHS.

The CbI method has been generalized to 1D boundary controlled infinite dimensional PHS in [Machelli 17, Rodriguez 01]. A first result on ideal in-domain control that allows to take advantage of the distributed nature of the control action with the help of the Casimir function has been proposed in [Trenchant 17]. In this case the control action allows to modify the overall internal energy shape, and the dynamic properties of the closed loop system.

Remark 3. *Though it would not be a matter in our system, it is important to point out that the CbI has a disadvantage of dissipation obstacle, which means that we can not shape the energy on the coordinate where the plant system has dissipation. This dissipation obstacle could be tackled using another PBC approach: interconnection and damping assignment passivity-based control (IDA-PBC) [Ortega 00] and has been applied to PHS in [Ortega 02].*

I.4 CONTRIBUTIONS AND OUTLINE

I.4.1 Contributions

In this thesis, we propose mathematical models for both the IPMC actuators and for the flexible micro-endoscope under the infinite dimensional port-Hamiltonian framework, taking the electrical dynamics, the gel diffusion, the mechanical deformations and the mechanical constraints into considerations, using Lagrange multipliers. In a second stage, the established models are discretized using the finite difference method on staggered grids to preserve the Dirac structure of the PHS and to proceed in the simulations. Simulation results are then compared with experimental results in order to validate the proposed model of the IPMC actuators. Our control problem arises naturally from the application of IPMC actuator patches on the flexible structures. As the patches generate distributed bending moments to the compliant endoscope structure, distributed in-domain control for infinite dimensional PHS is investigated via an early lumping approach. More precisely, the number of patches and the number of elements used for the discretization lead to an ideal fully-actuated case and realistic under-actuated case, and the latter results in an optimization controller design. To take advantage of the passive property of PHS, the in-domain CbI is applied here, with the PBC methodologies of energy shaping and damping injection.

I.4.2 Outline of the thesis

This thesis is organized in four main chapters:

Chapter I This chapter addresses the research background and objectives of a control oriented modeling of a compliant micro-endoscope actuated by IPMC actuators. Different types of endoscopes and actuation approaches are reviewed, together with designing models of micro-endoscopes. The features of IPMC actuators and a literature review on existing mathematical models are detailed. The multiphysical and multiscale properties of the actuated endoscope model make the port-Hamiltonian formulation a powerful tool to deal with the interconnections. A brief introduction on port-Hamiltonian formulation of both finite dimensional and infinite dimensional systems are given, with the extension to dissipative systems and to systems with constraints that are formulated by Lagrange multipliers. An overview of PBC is then given, with the highlight of CbI specified to PHS.

Chapter II The designing model of the micro-endoscope with IPMC actuator are simplified into a flexible structure (beam or cylindrical shell) integrated with IPMC patches. The infinite dimensional PHS is applied to model the dynamics of IPMC actuator, generating the electrical, the electro-stress diffusion and the IPMC strip deformation subsystems. The Lagrange multiplier is used to deal with the algebraic constraints between the mechanical deformations of the gel and that of the IPMC strip. The infinite dimensional PHS is also employed to model the tubular endoscope, with examples of a 1D small deformation Timoshenko beam, a 1D large deformation beam, and a 2D cylindrical thin shell. The Lagrange multiplier is again applied to tackle the interconnection between the endoscope model and the IPMC actuator model.

Chapter III Two kinds of structure preserving discretization approaches are presented: the mixed finite element method and the finite difference method on staggered grids, with extension to dissipative systems with distributed input. Comparisons of these two discretization methods are investigated. The IPMC actuator model established in Chapter II is thus discretized with the finite difference method on staggered grids and simulated with Matlab. Experiments are carried out to measure the IPMC deformation to an applied step voltage and then a sinusoidal voltage, and the results are compared with simulation ones in order to validate our proposed mathematical model.

Chapter IV This part starts with an example of a linear vibrating string with dissipation, the CbI together with energy shaping and damping injection methodologies are used to design an in-domain distributed control. Two different cases are investigated: the ideal case where the system is fully-actuated and the more realistic under-actuated case where the control action is achieved using piecewise homogeneous inputs. In order to achieve the desired performances, the parameters of the controller matrix are determined using least square optimization. Finally, simulations are carried on to prove the effectiveness of the controller.

Chapter II

Port-Hamiltonian modeling of flexible bio-medical structures

II.1	Model descriptions and simplifications	28
II.1.1	1D beam model description	29
II.1.2	Shell model description	29
II.2	Port-Hamiltonian modeling of the IPMC actuator	30
II.2.1	Electrical system	32
II.2.2	Electro-stress diffusion system	35
II.2.3	Mechanical system	39
II.2.4	Multiscale coupling between subsystems	42
II.2.5	Overall IPMC model	46
II.3	1D port-Hamiltonian model of the actuated endoscope	51
II.4	2D port-Hamiltonian model of the actuated endoscope	55
II.5	Summary	63

II.1 MODEL DESCRIPTIONS AND SIMPLIFICATIONS

Before providing a mathematical model of the system depicted in Fig. I.6, we first need to make reasonable assumptions to simplify it. The design model in Fig. I.6 can be regarded as a clamped-free flexible tube equipped with IPMC patches, as illustrated in Fig. II.1. The IPMC patches are placed along the longitudinal axis of the endoscope. For the sake of simplicity, we consider firstly one IPMC patch. The IPMC actuator is controlled by the applied voltage, and provides distributed bending moments to the endoscope tube.

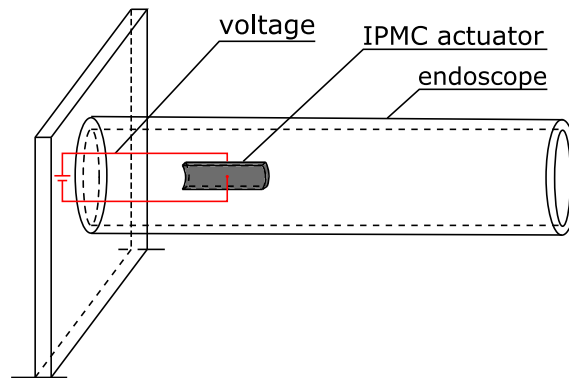


Figure II.1 – Model configuration of the micro-endoscope with the IPMC actuator.

In what follows we make the assumptions:

Assumption 1.a. *The temperature and humidity of the environment are constant, thus the deformation of the IPMC actuator is only caused by the applied voltage.*

Assumption 1.b. *The materials of both the endoscope and of the IPMC actuator are considered homogeneous and isotropic.*

Assumption 1.c. *The IPMC actuator is assumed to be perfectly connected to the endoscope.*

Assumption 1.d. *The width and thickness of the IPMC actuator are small enough so that it does not modify the geometric structure of the endoscope.*

Two main kinds of mechanical models will be proposed for the tube-like endoscope embedded with the IPMC actuator: the beam model and the shell model. The former is a simple 1D model that describes only the deformations of the neutral line and its cross section, while the shell model takes also into account the deformation on the width dimension, leading to a 2D model. We hereby present these two kinds of models and their coordinates descriptions.

II.1.1 1D beam model description

Various flexible beam models exist in the literature, ranging from the classical small deformation Euler-Bernoulli beam [Han 99], Timoshenko beam [Timoshenko 21] to large deformation beam models [Sandhu 90, Nada 10, Selig 01, Berzери 00, Simo 86]. For the small deformation models, the Timoshenko beam model takes the first-order shear deformation into consideration and is more precise than the Euler-Bernoulli beam model at high frequency vibrations. So in this thesis we will concentrate on the Timoshenko beam model for the small deformation of the mechanical structure. For the large deformation case, some typical models will be reviewed in Section II.3. We are going to apply one of these models, the inertial frame infinite dimensional model proposed by [Simo 86], which also contains the shear force, and which is easier to formulate the nonlinear terms resulting from the geometric nonlinearity.

The beam model configuration is illustrated in Fig. II.2. The IPMC actuator is placed over an interval $[X_1, X_2]$. L_o denotes the length of the IPMC actuator patch, while L_e represents that of the endoscope.

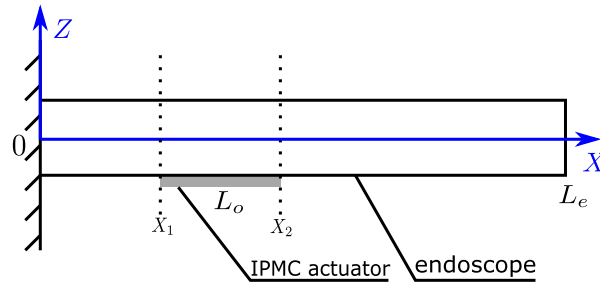


Figure II.2 – Beam model configuration.

II.1.2 Shell model description

The 2D shell model of the endoscope equipped with the IPMC patch, as depicted in Fig. II.3a, captures more accurate deformations of the structure, such as the rotations happening in the cross section.

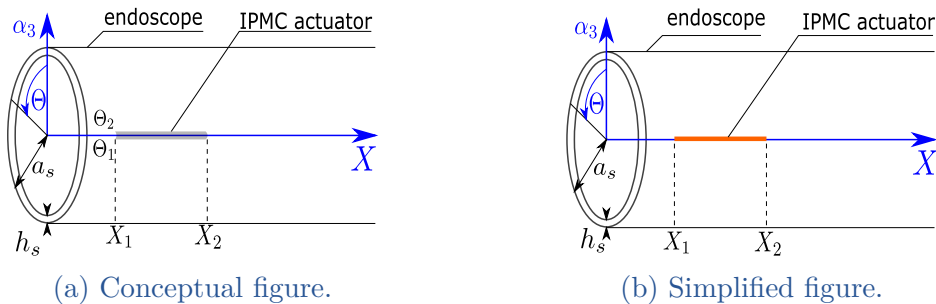


Figure II.3 – Shell model configuration.

Here we use the cylindrical coordinates X, Θ, α_3 to facilitate the calculations, where α_3 is normal to the reference surface generated by X and Θ , a_s denotes the cylinder radius and h_s is the thickness of the shell.

As a first attempt, the interconnection between the IPMC actuator and the endoscope is considered as the simplest scenario. Because of the symmetry about the X axis, the actuator is assumed to apply distributed line loading, *i.e.* distributed bending moment density, to the endoscope. As a result, compared to the endoscope, the IPMC strip can be simplified as a 1D string line, which is shown in Fig. II.3b.

In what follows, we first provide a detailed port-Hamiltonian model of the IPMC actuator, we then consider the port-Hamiltonian formulation of the two aforementioned mechanical structures, *i.e.* the beam and the shell, and then focus on the interconnections.

II.2 PORT-HAMILTONIAN MODELING OF THE IPMC ACTUATOR

In this section, we use infinite dimensional port-Hamiltonian formulations to model the IPMC actuator. The actuator under investigation is of length L_o , width b_o and thickness h_o . Its shape and structure are depicted in Fig. I.7a and I.7b (page 9). We shortly recall the working principles of an IPMC actuator as described in Subsection I.2.3. When subject to a step voltage, the free cations and water molecules inside the polyelectrolyte gel transport to the cathode side of the IPMC, generating a diffusion phenomena as pointed out in Fig. II.4b. This diffusion makes the cathode side of the IPMC swells and the anode side shrinks. Therefore, the actuator will have a quick bending motion towards the anode side. After the bending, free cations and water molecules will transport back to the anode side because of the solvent gradient. Then a slow back relaxation to the cathode side can be observed, as shown in Fig. II.4c.

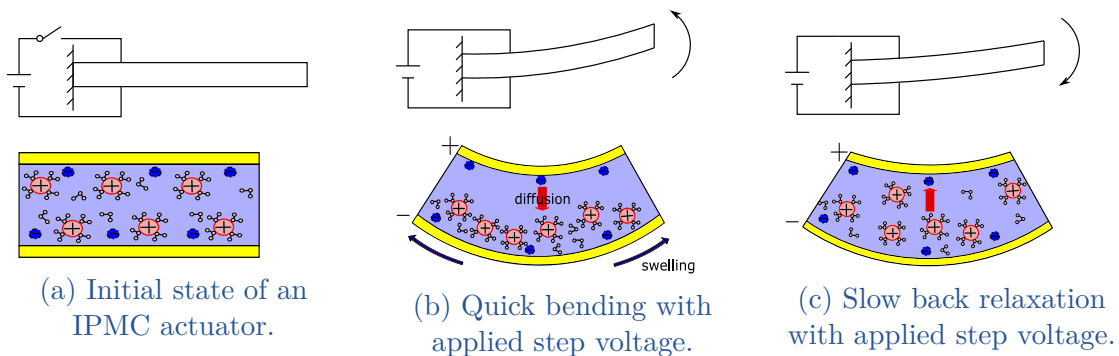


Figure II.4 – Diagram of the working principles of an IPMC actuator.

From the working principles, the IPMC model is composed of three parts: the electrical system for the electrodes and the interface with the polymer gel, the electro-stress diffusion system for the gel dynamics, and the mechanical system for the IPMC strip deformation. These three systems are modeled in ξ , z and x coordinates, as illustrated in Fig. II.5, which are at scales of nanometer, micrometer and centimeter [Nishida 11], respectively.

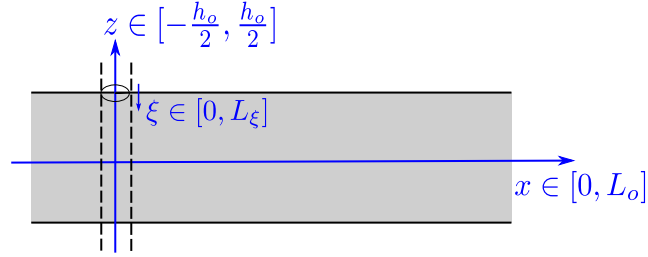


Figure II.5 – Coordinates representation of the IPMC actuator.

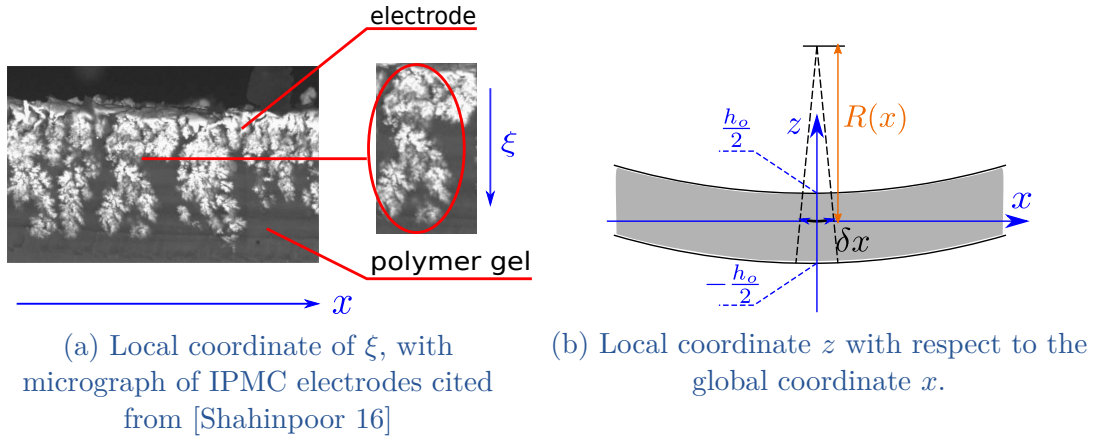


Figure II.6 – Local coordinates ξ and z with respect to the global coordinate x .

It is important to point out that the coordinate ξ of the electrical system is a virtual one [Nishida 08, Nishida 11]. This is due to the infinitesimal fractal-like structures on the interface between the electrodes and the polymer gel, because the electrodes are not perfectly coated, which is shown in Fig. II.6a. Moreover, both coordinates ξ and z are local and independent ones with respect to the global coordinate x . The former is related to infinite fractal-like structures along the electrodes. The latter is because of the assumption that the deformation of each infinitesimal slice of the gel is formulated by that of the mechanical system in x . As a result, each slice of the gel is supposed to have constant radius of curvature $R(x)$, which is illustrated in Fig. II.6b. The constant curvature of each z coordinate will generate a mechanical constraint between the electro-stress diffusion system and the mechanical system, which will be formulated as a Lagrange multiplier in (II.38) and (II.39). Two local coordinates ξ and z couple with each other through their boundaries. The local coordinate z and the global coordinate x interconnect

through the boundary of z and the domain of x . These multiscale interconnections and the mechanical constraint will be detailed in Subsection II.2.4. The local coordinates modelings are later related to the discretizations in Subsections III.2.1 and III.2.2.

II.2.1 Electrical system

Starting with the electrical part with the coordinate ξ presented in Fig. II.7, we assume that the supplied voltage V_1 is uniformly distributed on the electrode double layer. The micrograph of the electrodes (cf. Fig. II.6a) indicates that the electrodes are composed of fractal-like branches, which can be modeled as Fig. II.8a with a lumped parameter system, where $R_1(j)$ represents the resistance between two adjacent $(j - 1)$ th and j th branches, $R_2(j)$ and $C_2(j)$ correspond to the resistive and capacitive impedance of the j th branch [Bao 02], respectively. Furthermore, when the fractal-like branches tend to be infinite, the lumped parameter system turns to a be distributed parameter system, and the infinite dimensional electrodes model is depicted in Fig. II.8b with a virtual coordinate $\xi \in [0, L_\xi]$ as proposed in [Nishida 08, Nishida 11]. In this thesis, we shall use and study this infinite dimensional model for the electrodes interface.

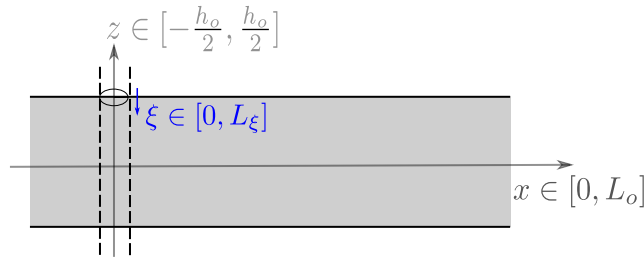


Figure II.7 – Coordinate representation of the electrical system.

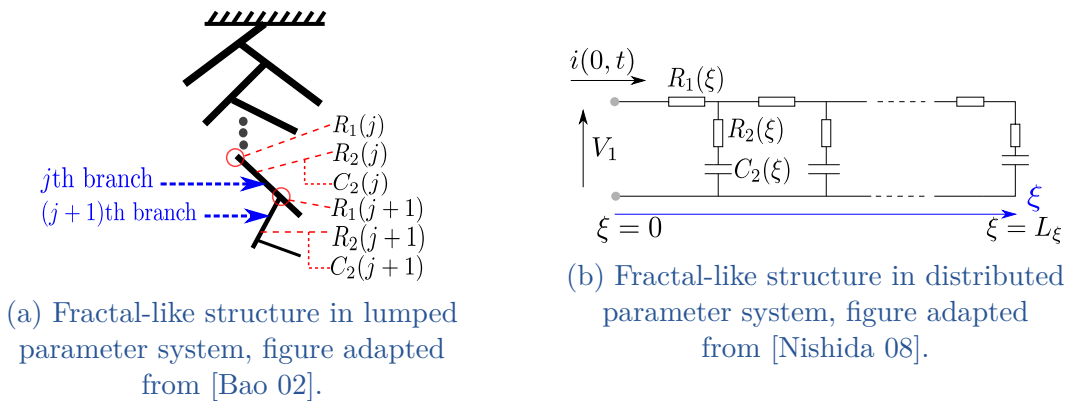


Figure II.8 – Models of IPMC electrodes interface.

The continuity equation and the Kirchhoff's current law yield:

$$\frac{\partial Q_e}{\partial t}(\xi, t) = -\frac{\partial i}{\partial \xi}(\xi, t), \quad (\text{II.1})$$

where $Q_e(\xi, t)$ is the charge density of each capacitor in Fig. II.8b and $i(\xi, t)$ gives the current.

By applying the Kirchhoff's voltage law, one gets:

$$\frac{\partial v}{\partial \xi}(\xi, t) + R_1(\xi)i(\xi, t) = 0, \quad (\text{II.2})$$

where $v(\xi, t)$ stands for the voltage that is formulated by:

$$v(\xi, t) = \frac{Q_e(\xi, t)}{C_2(\xi)} + R_2(\xi) \frac{\partial Q_e}{\partial t}(\xi, t). \quad (\text{II.3})$$

Combining (II.1)-(II.3), one gets:

$$\frac{\partial Q_e}{\partial t}(\xi, t) = \frac{\partial}{\partial \xi} \left(\frac{1}{R_1(\xi)} \frac{\partial}{\partial \xi} \left(\frac{Q_e(\xi, t)}{C_2(\xi)} + R_2(\xi) \frac{\partial Q_e}{\partial t}(\xi, t) \right) \right). \quad (\text{II.4})$$

Taking the flow and effort variables as:

$$\begin{aligned} f_1(\xi, t) &= \frac{\partial Q_e}{\partial t}(\xi, t), \\ e_1(\xi, t) &= \frac{Q_e(\xi, t)}{C_2(\xi)} + R_2(\xi) \frac{\partial Q_e}{\partial t}(\xi, t), \\ f_{r1}(\xi, t) &= \frac{\partial}{\partial \xi} \left(\frac{Q_e(\xi, t)}{C_2(\xi)} + R_2(\xi) \frac{\partial Q_e}{\partial t}(\xi, t) \right), \end{aligned}$$

one can express (II.4) as a dissipative PHS of the form:

$$\begin{pmatrix} f_1(\xi, t) \\ f_{r1}(\xi, t) \end{pmatrix} = \underbrace{\begin{pmatrix} 0 & \frac{\partial}{\partial \xi} \\ \frac{\partial}{\partial \xi} & 0 \end{pmatrix}}_{\mathcal{J}_{elec}} \begin{pmatrix} e_1(\xi, t) \\ e_{r1}(\xi, t) \end{pmatrix}, \quad (\text{II.5})$$

with the closure equation

$$e_{r1}(\xi, t) = \frac{f_{r1}(\xi, t)}{R_1(\xi)} = \frac{1}{R_1(\xi)} \frac{\partial}{\partial \xi} \left(\frac{Q_e(\xi, t)}{C_2(\xi)} + R_2(\xi) \frac{\partial Q_e}{\partial t}(\xi, t) \right). \quad (\text{II.6})$$

Assume that the the coordinate is infinitely long, so the current at the endpoint of each fractal structure is zero, namely $e_{r1}(L_\xi, t) = 0$.

According to [Villegas 07], the boundary port variables of (II.5) can be defined as:

$$\begin{pmatrix} f_{\partial \xi}(t) \\ e_{\partial \xi}(t) \end{pmatrix} = \begin{pmatrix} e_1(0, t) \\ e_1(L_\xi, t) \\ e_{r1}(0, t) \\ -e_{r1}(L_\xi, t) \end{pmatrix} = \begin{pmatrix} V_1 + V_c \\ e_1(L_\xi, t) \\ -I_e \\ 0 \end{pmatrix}, \quad (\text{II.7})$$

where V_c corresponds to the voltage generated in the gel, and I_e represents the output current.

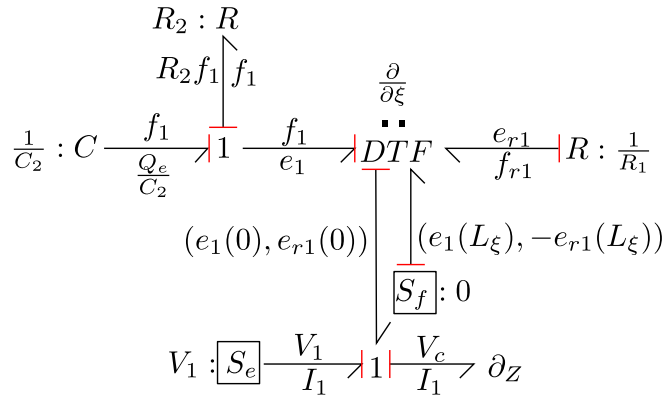


Figure II.9 – Bond Graph of the electrical system dynamics.

Equations (II.5) and the associated boundary port variables (II.7) can be represented by the Bond Graph of Fig. II.9. The applied voltage V_1 acts as an effort source, and the block DTF refers to the differential transformer that is related to the Stokes-Dirac structure in (II.5). One can find more details about this DTF in Appendix A.

The Hamiltonian of this system is the electrical energy and reads

$$H_{el}(t) = \frac{1}{2} \int_{\xi} \frac{(Q_e(\xi, t))^2}{C_2(\xi)} d\xi. \quad (\text{II.8})$$

Using the integration by parts, the energy balance equation is¹:

$$\begin{aligned} & \frac{\partial H_{el}}{\partial t}(t) \\ &= \int_{\xi} \left(\frac{\partial Q_e}{\partial t} \frac{Q_e}{C_2} \right) d\xi \\ &= \int_{\xi} \left(\frac{1}{R_1} \frac{\partial^2}{\partial \xi^2} \left(\frac{Q_e}{C_2} + R_2 \frac{\partial Q_e}{\partial t} \right) \frac{Q_e}{C_2} \right) d\xi \\ &= \frac{1}{R_1 C_2} \left(\left[Q_e \frac{\partial}{\partial \xi} \left(\frac{Q_e}{C_2} + R_2 \frac{\partial Q_e}{\partial t} \right) \right]_0^{L_{\xi}} - \int_{\xi} \frac{\partial}{\partial \xi} \left(\frac{Q_e}{C_2} + R_2 \frac{\partial Q_e}{\partial t} \right) \frac{\partial Q_e}{\partial \xi} d\xi \right) \\ &= \left[\frac{Q_e}{C_2} \frac{1}{R_1} \frac{\partial}{\partial \xi} \left(\frac{Q_e}{C_2} + R_2 \frac{\partial Q_e}{\partial t} \right) \right]_0^{L_{\xi}} - \int_{\xi} \frac{1}{R_1} \left(\frac{\partial}{\partial \xi} \left(\frac{Q_e}{C_2} + R_2 \frac{\partial Q_e}{\partial t} \right) \right)^2 d\xi \\ &\quad + \int_{\xi} \frac{1}{R_1} \frac{\partial}{\partial \xi} \left(\frac{Q_e}{C_2} + R_2 \frac{\partial Q_e}{\partial t} \right) \frac{\partial}{\partial \xi} \left(R_2 \frac{\partial Q_e}{\partial t} \right) d\xi \\ &\leq \left[\frac{Q_e}{C_2} \frac{1}{R_1} \frac{\partial}{\partial \xi} \left(\frac{Q_e}{C_2} + R_2 \frac{\partial Q_e}{\partial t} \right) \right]_0^{L_{\xi}} + \int_{\xi} \frac{1}{R_1} \frac{\partial}{\partial \xi} \left(\frac{Q_e}{C_2} + R_2 \frac{\partial Q_e}{\partial t} \right) \frac{\partial}{\partial \xi} \left(R_2 \frac{\partial Q_e}{\partial t} \right) d\xi \\ &= \left[\frac{Q_e}{C_2} \frac{1}{R_1} \frac{\partial}{\partial \xi} \left(\frac{Q_e}{C_2} + R_2 \frac{\partial Q_e}{\partial t} \right) \right]_0^{L_{\xi}} + \left[\frac{1}{R_1} \frac{\partial}{\partial \xi} \left(\frac{Q_e}{C_2} + R_2 \frac{\partial Q_e}{\partial t} \right) + R_2 \frac{\partial Q_e}{\partial t} \right]_0^{L_{\xi}} \end{aligned}$$

1. For the sake of compactness, the parameters ξ and t are omitted during the computation.

$$\begin{aligned}
 & - \int_{\xi} R_2 \frac{\partial Q_e}{\partial t} \frac{1}{R_1} \frac{\partial^2}{\partial \xi^2} \left(\frac{Q_e}{C_2} + R_2 \frac{\partial Q_e}{\partial t} \right) d\xi \\
 &= \left[\left(\frac{Q_e}{C_2} + R_2 \frac{\partial Q_e}{\partial t} \right) \frac{1}{R_1} \frac{\partial}{\partial \xi} \left(\frac{Q_e}{C_2} + R_2 \frac{\partial Q_e}{\partial t} \right) \right]_0^{L_\xi} \\
 & \quad - \int_{\xi} R_2 \frac{\partial Q_e}{\partial t} \frac{1}{R_1} \frac{\partial^2}{\partial \xi^2} \left(\frac{Q_e}{C_2} + R_2 \frac{\partial Q_e}{\partial t} \right) d\xi \\
 &= f_{\partial \xi}^T e_{\partial \xi} - \int_{\xi} R_2 \left(\frac{\partial Q_e}{\partial t} \right)^2 d\xi \\
 &\leq f_{\partial \xi}^T e_{\partial \xi}.
 \end{aligned} \tag{II.9}$$

The inequalities of (II.9) account for the dissipation of the electrical system through the resistances R_1 and R_2 .

II.2.2 Electro-stress diffusion system

In this part, the second subsystem stemming from the modeling of the electro-stress diffusion in the gel is studied. We recall the coordinate representation of this system in Fig. II.10.

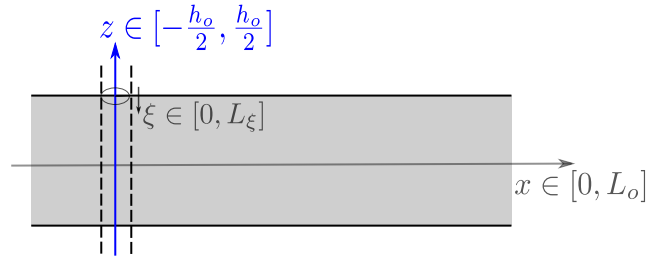


Figure II.10 – Coordinate representation of the electro-stress diffusion system.

The gel inside the IPMC actuator is composed of the solid and the liquid phases (cf. Fig. II.11). The former contains the polymer chain and fixed anions,

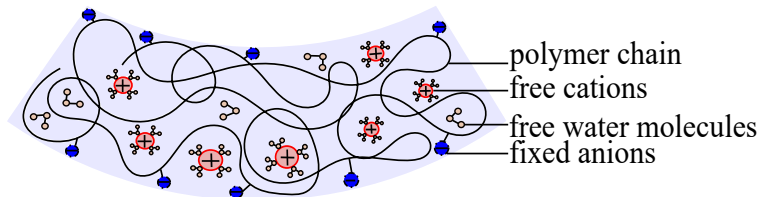


Figure II.11 – Solid and liquid phases of the gel.

whereas the later includes cations and water molecules [Zhu 12]. In the liquid phase, two coupled phenomena can be distinguished: the electro-osmosis (solvent transport caused by the electric field) and the electric field generated by the water transportation [Yamaue 05]. These phenomena have been modeled by Pierre-Gilles de Gennes in [de Gennes 00]. On the other hand, the solid phase is assumed to be

at a pseudo-equilibrium state and therefore form a **quasi-static electro-stress diffusion coupling model** [Yamaue 05, Nishida 08, Nishida 11]. The pseudo-equilibrium state means that the mechanical deformation of the solid phase is considered constant with time when the dynamics of the liquid phase occurs. This is due to the fact that the liquid dynamics is slower compared to the mechanical dynamics of the solid components. In what follows, we provide a detailed model of both solid and liquid phases.

Taking one slice of the gel as a case of study, besides the pseudo-equilibrium state assumption, the solid phase is also assumed to be symmetric, which is illustrated in Fig. II.6b (page 31). The radius of curvature $R(x, t)$ of each slice is assumed to stay constant. The displacement of each material point along the z -axis is given by $u_z(z, t)$, while along the x - and y - axis $u_x(z, x, t)$ and $u_y(z, x, t)$ are calculated according to [de Gennes 00, Yamaue 05]:

$$\mathbf{u}_o(x, y, z, t) = \begin{pmatrix} u_x(z, x, t) \\ u_y(z, x, t) \\ u_z(z, t) \end{pmatrix} = \begin{pmatrix} \frac{z}{R(x, t)}x \\ \frac{z}{R(x, t)}y \\ u_z(z, t) \end{pmatrix}, \quad (\text{II.10})$$

with $x \in [0, L_o]$, $y \in [0, b_o]$ and $z \in \left[-\frac{h_o}{2}, \frac{h_o}{2}\right]$.

The swelling ratio $f_s(z, x, t)$ is defined as the divergence of the displacement vector \mathbf{u}_o :

$$\begin{aligned} f_s(z, x, t) &= \nabla \cdot \mathbf{u}_o \\ &= \left(\frac{\partial}{\partial x} \quad \frac{\partial}{\partial y} \quad \frac{\partial}{\partial z} \right) (u_x \quad u_y \quad u_z)^T \\ &= \frac{2z}{R(x, t)} + \frac{\partial u_z}{\partial z}(z, t). \end{aligned} \quad (\text{II.11})$$

With the isotropic assumption made in Assumption 1.b, the components of the stress tensor are calculated according to the following formulation:

$$\sigma_{ij} = K \sum_k \frac{\partial u_k}{\partial x_k} \delta_{ij} + G \left(\frac{\partial u_i}{\partial x_j} + \frac{\partial u_j}{\partial x_i} - \frac{2}{3} \sum_k \frac{\partial u_k}{\partial x_k} \delta_{ij} \right), \quad (\text{II.12})$$

where K and G are the bulk modulus and the shear modulus of the gel, respectively. δ_{ij} is the Dirichlet function with $i = \{x, y, z\}$, $j = \{x, y, z\}$ and $k = \{x, y, z\}$.

As a result, (II.10) and (II.12) yield the following expressions [Yamaue 05]:

$$\sigma_{xx}(z, x, t) = \left(K - \frac{2}{3}G \right) f_s(z, x, t) + \frac{2G}{R(x, t)}z, \quad (\text{II.13a})$$

$$\sigma_{zz}(z, x, t) = \left(K + \frac{4}{3}G \right) f_s(z, x, t) - \frac{4G}{R(x, t)}z. \quad (\text{II.13b})$$

The pseudo-equilibrium state of the solid phase implies that the pressure p in the gel equals to the elastic stress in the z direction $\sigma_{zz}(z, x, t)$:

$$\begin{aligned} p(z, x, t) &= \sigma_{zz}(z, x, t) \\ &= \left(K + \frac{4}{3}G \right) f_s(z, x, t) - \frac{4G}{R(x, t)}z. \end{aligned} \quad (\text{II.14})$$

Remark 4. *The elastic stresses calculated in (II.12) and (II.13) are average values which do not take the eigen stress (stress generates in the liquid phase) into consideration. To the best of our knowledge, the eigen stress does not have exact formulation in the literature. One can find a more thorough explanation of detailed stresses in IPMC for example in [Zhu 12].*

In the liquid phase, it is supposed that the gel goes only in the z direction. This is consistent with the hypothesis of local homogeneity of the radius of curvature $R(x, t)$ in the solid phase. The conservation law reads [Yamaue 05]:

$$\frac{\partial f_s}{\partial t}(z, x, t) = -\frac{\partial \mathbf{j}_s}{\partial z}(z, x, t), \quad (\text{II.15})$$

where $\mathbf{j}_s(z, x, t)$ is the flux of solvent that follows the Pierre-Gilles de Gennes' model [de Gennes 00]:

$$\begin{cases} \mathbf{j}_e &= -\sigma_e \nabla \psi - \lambda \nabla p, \\ \mathbf{j}_s &= -\phi \frac{d^2}{\eta} \nabla p - \lambda \nabla \psi, \end{cases} \quad (\text{II.16})$$

where \mathbf{j}_e represents the electrical current density, σ_e is the conductance, λ stands for the Onsager's coupling constant and ψ is related to the electrical field. ϕ , d and η denote the water volume fraction, the effective pore size and the water viscosity, respectively. Their product $\phi d^2/\eta$ forms the constant of the Darcy's permeability [de Gennes 00].

Substituting (II.14) into (II.16), one gets:

$$\begin{aligned} \mathbf{j}_s(z, x, t) &= \frac{\lambda}{\sigma_e} \mathbf{j}_e(t) + \left(\frac{\lambda^2}{\sigma_e} - \phi \frac{d^2}{\eta} \right) \frac{\partial p}{\partial z}(z, x, t) \\ &= -\mathcal{R}_g \frac{\partial}{\partial z} (\mathcal{R}_f f_s(z, x, t)) + \mathbb{1}_Z \frac{\lambda}{\sigma_e} \mathbf{j}_e(t) + \mathbb{1}_Z \Phi(x, t), \end{aligned} \quad (\text{II.17})$$

with $\mathcal{R}_g = d \left(\frac{\phi}{\eta} - \frac{\lambda^2}{d^2 \sigma_e} \right)$, $\mathcal{R}_f = d \left(K + \frac{4}{3}G \right)$, and

$$\Phi(x, t) = \left(\phi \frac{d^2}{\eta} - \frac{\lambda^2}{\sigma_e} \right) \frac{4G}{R(x, t)} \quad (\text{II.18})$$

Remark 5. $\mathcal{R}_f f_s$ in (II.18) can be seen analogous to a compression force.

Remark 6. $\mathbb{1}_Z := 1, \forall z \in \left[-\frac{h_o}{2}, \frac{h_o}{2} \right]$ is the characteristic function. It is initially introduced in [Nishida 11] that is used for the multiscale and multiphysical coupling. This characteristic function distributes uniformly the boundary values $\frac{\lambda}{\sigma_e} \mathbf{j}_e(t)$ and $\Phi(x, t)$ into the z domain.

Similar to the electrical system, by defining

$$f_2(z, x, t) = \frac{\partial f_s}{\partial t}(z, x, t), \quad (\text{II.19a})$$

$$e_2(z, x, t) = \mathcal{R}_f f_s(z, x, t), \quad (\text{II.19b})$$

$$f_{r2}(z, x, t) = \mathcal{R}_f \frac{\partial f_s}{\partial z}(z, x, t), \quad (\text{II.19c})$$

(II.15) and (II.17) can then be reformulated in the dissipative port-Hamiltonian framework:

$$\begin{pmatrix} f_2(z, x, t) \\ f_{r2}(z, x, t) \end{pmatrix} = \begin{pmatrix} 0 & \frac{\partial}{\partial z} \\ \frac{\partial}{\partial z} & 0 \end{pmatrix} \begin{pmatrix} e_2(z, x, t) \\ e_{r2}(z, x, t) \end{pmatrix}, \quad (\text{II.20})$$

closed with

$$e_{r2}(z, x, t) = \mathcal{R}_g f_{r2}(z, x, t). \quad (\text{II.21})$$

The boundary port variables are chosen to be [Villegas 07]:

$$\begin{pmatrix} f_{\partial z}(t) \\ e_{\partial z}(t) \end{pmatrix} = \begin{pmatrix} e_{r2}\left(-\frac{h_o}{2}, t\right) \\ -e_{r2}\left(\frac{h_o}{2}, t\right) \\ e_2\left(-\frac{h_o}{2}, t\right) \\ e_2\left(\frac{h_o}{2}, t\right) \end{pmatrix}. \quad (\text{II.22})$$

Boundary conditions come from the impermeable assumption that [Nishida 08, Nishida 11]:

$$\mathbf{j}_s\left(\pm\frac{h_o}{2}\right) = -e_{r2}\left(\pm\frac{h_o}{2}\right) + \frac{\lambda}{\sigma_e} \mathbf{j}_e(t) + \Phi(x, t) = 0. \quad (\text{II.23})$$

The Bond Graph of the dynamics of the gel under the port-Hamiltonian formulation in (II.20) closed with (II.21) is given in Fig. II.12. It is also a diffusion system like Fig. II.9, with two external source flows $\frac{\lambda}{\sigma_e} \mathbf{j}_e(t)$ and $\Phi(x, t)$ from the boundary ∂_z to the domain z with the help of the characteristic function $\mathbb{1}_Z$.

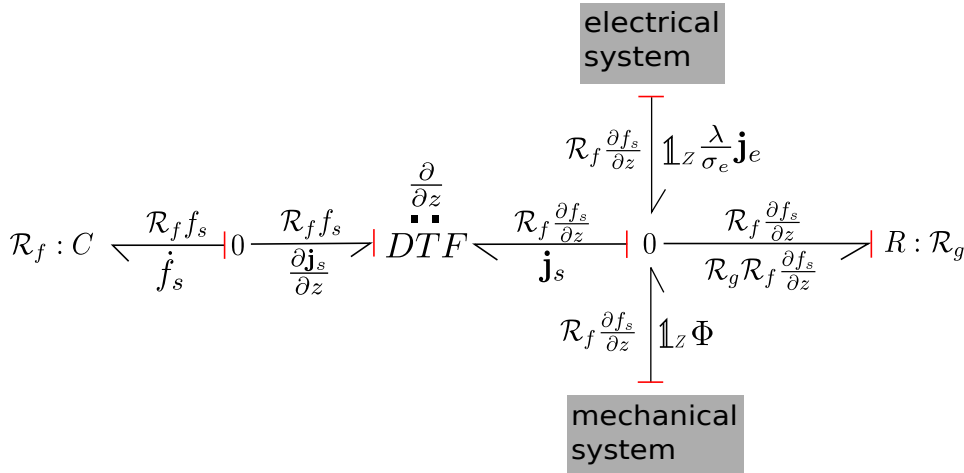


Figure II.12 – Bond Graph of the electro-stress diffusion system dynamics.

The Hamiltonian associated with the electro-stress diffusion system (II.20)-(II.22) is

$$H_{em}(x, t) = \frac{1}{2} \int_z \mathcal{R}_f f_s(z, x, t)^2 dz. \quad (\text{II.24})$$

With the integration by parts, the energy balance equation is calculated as ²:

$$\begin{aligned}
 \frac{\partial H_{em}}{\partial t} &= \int_z \left(\frac{\partial f_s}{\partial t} \mathcal{R}_f f_s \right) dz \\
 &= \int_z \left(\frac{\partial}{\partial z} \left(\mathcal{R}_g \frac{\partial}{\partial z} (\mathcal{R}_f f_s) \right) \right) \mathcal{R}_f f_s dz \\
 &= \mathcal{R}_g \mathcal{R}_f^2 \left(\left[f_s \left(\frac{\partial}{\partial z} f_s \right) \right]_{-\frac{h_o}{2}}^{\frac{h_o}{2}} - \int_z \left(\frac{\partial f_s}{\partial z} \right)^2 dz \right) \\
 &\leq f_{\partial z}^T e_{\partial z}.
 \end{aligned} \tag{II.25}$$

During the actuation of the IPMC, the swelling of the cathode side and the shrinking of the anode side are observed at a macro scale level. This is related to the bending moment locally generated in the gel which is formulated by:

$$M_o(x, t) = \int_z (\sigma_{xx} - p) b_o z dz. \tag{II.26}$$

Substituting the σ_{xx} and p formulated in (II.13a) and (II.14) to (II.26), one obtains the bending moment as:

$$M_o(x, t) = \underbrace{\int_z B_a(z) \mathcal{R}_f f_s(z, x, t) dz}_{M_{x1}(x, t)} + \underbrace{\frac{G b_o h_o^3}{2R(x, t)}}_{M_{x2}(x, t)}, \tag{II.27}$$

with $B_a(z) = -\frac{2G b_o z}{\mathcal{R}_f}$. The first term M_{x1} in (II.27) is related to the dynamics of the gel, and the second term M_{x2} is caused by the mechanical deformation of the solid phase.

II.2.3 Mechanical system

The mechanical system is modeled in x coordinate as depicted in Fig. II.13. We first model **only** the deformation of the IPMC actuator here. Afterwards, we

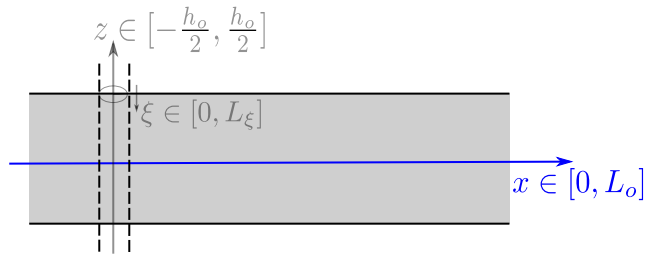


Figure II.13 – Coordinate representation of the mechanical system.

consider the same mechanical structure of both the endoscope and of the IPMC, and we propose various mechanical models in Section II.3. The IPMC actuator is considered to have a small deformation here, which can be modeled as a Timoshenko beam under the following assumptions:

2. For the sake of compactness, the parameters z and t are omitted during the computation.

Assumption 2.a. All the related deformations and strains are small, which guarantees the validity of the Hooke's law.

Assumption 2.b. Plane cross sections remain plane after the deformation, but do not need to be perpendicular to the neutral line.

Based on Assumption 2.b, unlike the Euler-Bernoulli beam, the shear force needs to be considered in the Timoshenko beam model. The force diagram is represented in Fig. II.14, where ω_o represents the transversal displacement, $\theta(x, t)$

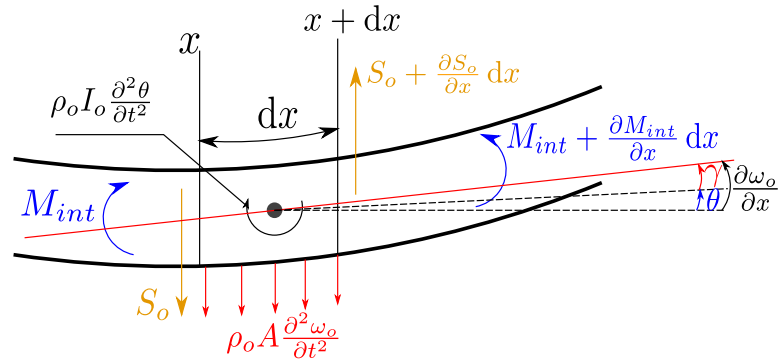


Figure II.14 – Force diagram of the Timoshenko beam.

refers to the bending angle, $\gamma(x, t) = \frac{\partial \omega_o}{\partial x}(x, t) - \theta(x, t)$ is related to the shear angle, ρ_o stands for the beam density, $A(x)$ is the cross section area of the beam, $I_o(x)$ denotes the cross section moment of inertia, and G and E are the shear modulus and Young's modulus of elasticity, respectively. $S_o(x, t) = GA(x)\gamma(x, t) = GA(x) \left(\frac{\partial \omega_o}{\partial x}(x, t) - \theta(x, t) \right)$ denotes the shear force, and $M_{int}(x, t) = EI_o(x) \frac{\partial \theta}{\partial x}(x, t)$ denotes the internal bending moment.

The Timoshenko beam model is given by the following equations [Timoshenko 21]:

$$\begin{aligned} \rho_o A(x) \frac{\partial^2 \omega_o}{\partial t^2}(x, t) &= \frac{\partial}{\partial x} \left(GA(x) \left(\frac{\partial \omega_o}{\partial x}(x, t) - \theta(x, t) \right) \right), \\ \rho_o I_o(x) \frac{\partial^2 \theta}{\partial t^2}(x, t) &= \frac{\partial}{\partial x} \left(EI_o(x) \frac{\partial \theta}{\partial x}(x, t) \right) + GA(x) \left(\frac{\partial \omega_o}{\partial x}(x, t) - \theta(x, t) \right) + m_{ext}, \end{aligned} \quad (\text{II.28})$$

where $m_{ext} = M_o(x, t)/L_o$ is the external bending moment per length, with $M_o(x, t)$ formulated by (II.27). Equation (II.28) can be reformulated in the infinite dimensional port-Hamiltonian form as:

$$\begin{pmatrix} f_3(x, t) \\ f_4(x, t) \\ f_5(x, t) \\ f_6(x, t) \end{pmatrix} = \begin{pmatrix} 0 & \frac{\partial}{\partial x} & 0 & -1 \\ \frac{\partial}{\partial x} & 0 & 0 & 0 \\ 0 & 0 & 0 & \frac{\partial}{\partial x} \\ 1 & 0 & \frac{\partial}{\partial x} & 0 \end{pmatrix} \begin{pmatrix} e_3(x, t) \\ e_4(x, t) \\ e_5(x, t) \\ e_6(x, t) \end{pmatrix} + \begin{pmatrix} 0 \\ 0 \\ 0 \\ 1 \end{pmatrix} m_{ext}, \quad (\text{II.29})$$

where

$$\begin{pmatrix} f_3(x, t) \\ f_4(x, t) \\ f_5(x, t) \\ f_6(x, t) \end{pmatrix} = \begin{pmatrix} \frac{\partial^2 \omega_o}{\partial t \partial x}(x, t) - \frac{\partial \theta}{\partial t}(x, t) \\ \rho_o A(x) \frac{\partial^2 \omega_o}{\partial t^2}(x, t) \\ \frac{\partial^2 \theta}{\partial t \partial x}(x, t) \\ \rho_o I_o(x) \frac{\partial^2 \theta}{\partial t^2}(x, t) \end{pmatrix}, \quad \begin{pmatrix} e_3(x, t) \\ e_4(x, t) \\ e_5(x, t) \\ e_6(x, t) \end{pmatrix} = \begin{pmatrix} GA(x) \left(\frac{\partial \omega_o}{\partial x}(x, t) - \theta(x, t) \right) \\ \frac{\partial \omega_o}{\partial t}(x, t) \\ EI_o(x) \frac{\partial \theta}{\partial x}(x, t) \\ \frac{\partial \theta}{\partial t}(x, t) \end{pmatrix}. \quad (\text{II.30})$$

The boundary port variables are given by [Le Gorrec 05]:

$$f_{\partial x}(t) = \begin{pmatrix} e_4(0, t) \\ e_3(L_o, t) \\ e_6(0, t) \\ e_5(L_o, t) \end{pmatrix}, \quad e_{\partial x}(t) = \begin{pmatrix} -e_3(0, t) \\ e_4(L_o, t) \\ -e_5(0, t) \\ e_6(L_o, t) \end{pmatrix}. \quad (\text{II.31})$$

The clamped-free boundary condition is applied, where is formulated as:

$$e_3(L_o) = 0, \quad e_4(0) = 0, \quad e_5(L_o) = 0, \quad e_6(0) = 0. \quad (\text{II.32})$$

The Hamiltonian of the beam is given by the sum of the potential elastic energy and the kinetic energy:

$$\begin{aligned} H_m(t) = \frac{1}{2} \int_x \left(GA(x) \left(\frac{\partial \omega_o}{\partial x}(x, t) - \theta(x, t) \right)^2 + EI_o(x) \left(\frac{\partial \theta}{\partial x}(x, t) \right)^2 \right. \\ \left. + \rho_o A(x) \left(\frac{\partial \omega_o}{\partial t}(x, t) \right)^2 + \rho_o I_o(x) \left(\frac{\partial \theta}{\partial t}(x, t) \right)^2 \right) dx. \end{aligned} \quad (\text{II.33})$$

Its time derivative yields³:

$$\begin{aligned} \frac{dH_m}{dt} &= \int_x \left(GA \left(\frac{\partial \omega_o}{\partial x} - \theta \right) \left(\frac{\partial^2 \omega_o}{\partial t \partial x} - \frac{\partial \theta}{\partial t} \right) + EI_o \frac{\partial \theta}{\partial x} \left(\frac{\partial^2 \theta}{\partial t \partial x} \right) + \rho_o A \frac{\partial \omega_o}{\partial t} \frac{\partial^2 \omega_o}{\partial t^2} \right. \\ &\quad \left. + \rho_o I_o \frac{\partial \theta}{\partial t} \frac{\partial^2 \theta}{\partial t^2} \right) dx \\ &= \int_x \left(e_3 \frac{\partial e_4}{\partial x} - e_3 e_6 + e_4 \frac{\partial e_3}{\partial x} + e_5 \frac{\partial e_6}{\partial x} + e_3 e_6 + e_6 \frac{\partial e_5}{\partial x} + e_6 m_{ext} \right) dx \\ &= \int_x \left(\frac{\partial (e_3 e_4)}{\partial x} + \frac{\partial (e_5 e_6)}{\partial x} \right) dx + \int_x m_{ext} e_6 dx \\ &= f_{\partial x}^T e_{\partial x} + \int_x m_{ext} \frac{\partial \theta}{\partial t} dx. \end{aligned}$$

The Bond Graph related to the mechanical deformation of the IPMC is given in Fig. II.15. One can notice that the mechanical system is a hyperbolic system without dissipation. In formulation (II.29) we consider that the boundary conditions are clamped-fixed as formulated in (II.32), and that the beam is applied by distributed bending moment m_{ext} , which plays as an external source in the Bond Graph Fig. II.15.

3. For the sake of compactness, the parameters x and t are omitted during the computation.

$$f_{r2}(z, t) = \mathcal{R}_f \frac{\partial f_s}{\partial z}(z, t),$$

$$e_{r2}(z, t) = \mathcal{R}_g f_{r2}(z, t) = \mathcal{R}_g \mathcal{R}_f \frac{\partial f_s}{\partial z}(z, t).$$

Given that these variables are of different scales and are defined in domains ξ and z separately, the ideas of the coupling are to distribute the boundary variables $e_{r1}(0, t)$ into the domain of z with the characteristic function $\mathbb{1}_Z$ to make it connected with $e_{r2}(z, t)$ according to (II.17) at page 37, and in return to integrate the flow variables $f_{r2}(z, t)$ to make it a boundary value of the domain z and then connect to $e_1(0, t)$ to guarantee the power conservation. This kind of interconnection, named **BMS**, was firstly introduced in [Nishida 11], and is briefly illustrated in Fig. II.17a.

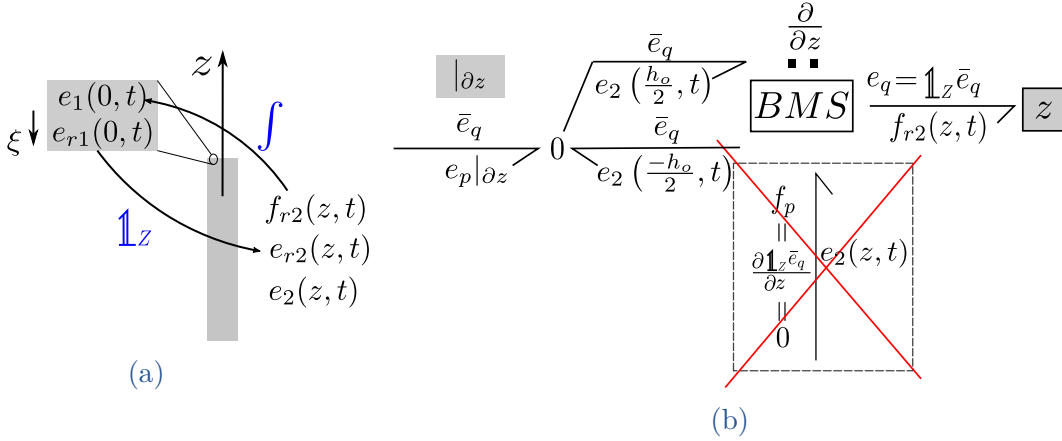


Figure II.17 – Diagram of the BMS explanation with $e_2|_{\partial z} = e_2(\frac{h_o}{2}) - e_2(-\frac{h_o}{2})$.

The BMS element works as a differential gyrator, whose complete structure is depicted in Fig. II.17b with an example formulated as follows:

$$\begin{pmatrix} f_p(z, t) \\ f_{r2}(z, t) \end{pmatrix} = \begin{pmatrix} 0 & \frac{\partial}{\partial z} \\ \frac{\partial}{\partial z} & 0 \end{pmatrix} \begin{pmatrix} e_2(z, t) \\ e_q(z, t) \end{pmatrix},$$

where $e_2(z, t) \in z$ and $f_{r2}(z, t) \in z$ are effort and flow variables in the domain of z . $e_q(z, t) = \mathbb{1}_Z \bar{e}_q(t)$ with $\bar{e}_q(t)$ a variable outside of the z domain coming from the boundary of ξ . We can therefore calculate f_p with:

$$f_p = \frac{\partial e_q}{\partial z} = \frac{\partial (\mathbb{1}_Z \bar{e}_q)}{\partial z} = 0, \quad (\text{II.34})$$

which corresponds to the rectangular block in Fig. II.17b. As a result, by applying the integration by parts, the power conservation at two sides of the BMS holds with the following equation:

$$\int_z e_q f_{r2} dz = \int_z \mathbb{1}_Z \bar{e}_q \frac{\partial e_2}{\partial z} dz$$

mechanical dynamics of the gel implicit and generates causality confusion between $\Phi(x, t)$ and $M_{x2}(x, t)$ formulated in (II.18) and (II.27) at page 37 and 39, respectively. The Bond Graph of this coupling is depicted in Fig. II.19. As shown on its right part, $\Phi(x, t)$ acts as a flow source for the electro-stress diffusion system and $M_{x2}(x, t)$ is the output of this system. From (II.18) and (II.27), they have a linear relation of the form:

$$M_{x2}(x, t) = B_p \Phi(x, t), \quad (\text{II.37})$$

with

$$B_p = \frac{b_o h_o^3}{4} \left(\phi \frac{d^2}{\eta} - \frac{\lambda^2}{\sigma_e} \right)^{-1}.$$

This coupling may cause the causal inconformity, which makes a Lagrange multiplier λ_L necessary, as presented by the red parts of Fig. II.19.

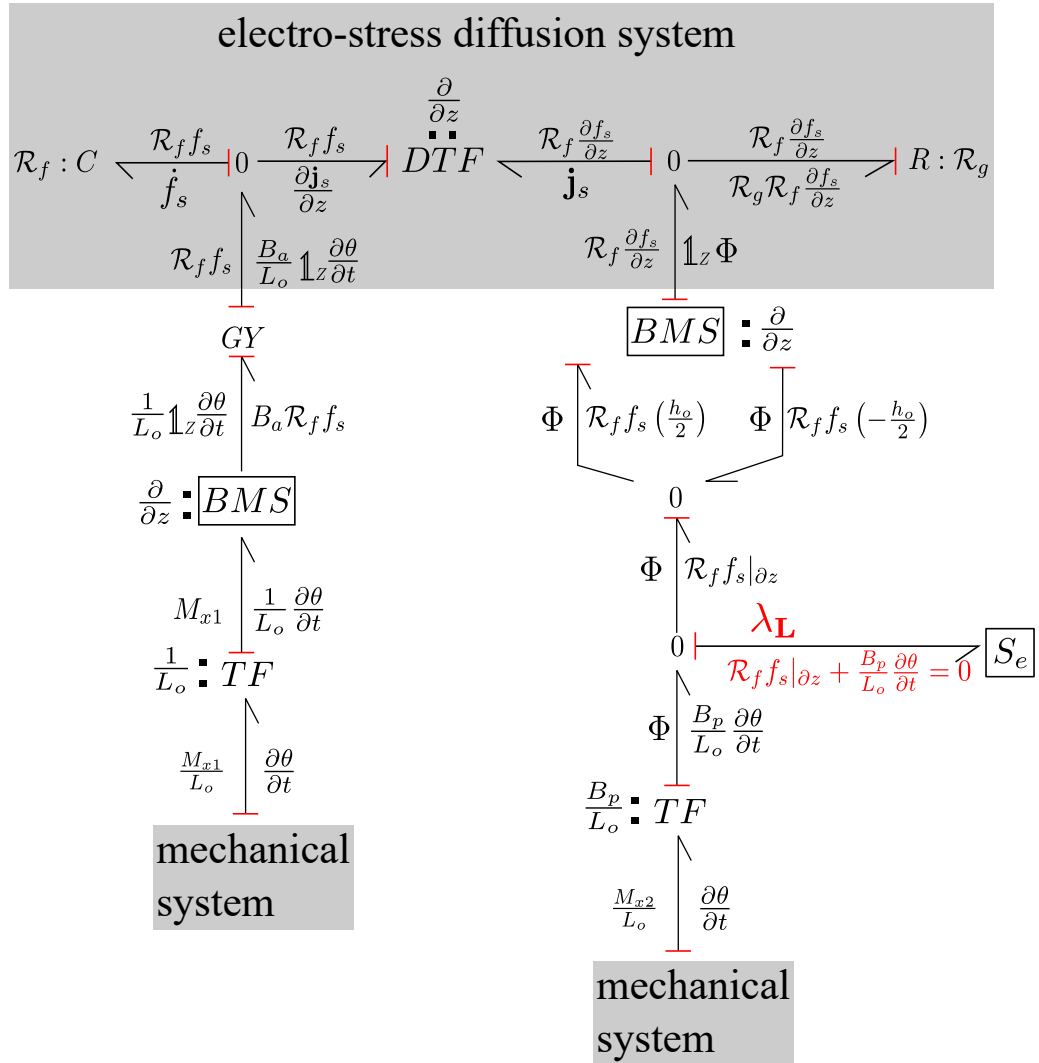


Figure II.19 – Bond graph of the coupling between the electro-stress diffusion system and the mechanical system, through $\frac{M_{x1}}{L_o}(x, t)$ (left column), $\frac{M_{x2}}{L_o}(x, t)$ (right column) and $\frac{\partial \theta}{\partial t}(x, t)$.

Therefore, one obtains:

$$\begin{pmatrix} 1 \\ \frac{B_p}{L_o} \end{pmatrix} \lambda_{\mathbf{L}} = \begin{pmatrix} \Phi \\ \frac{M_{x2}}{L_o} \end{pmatrix}. \quad (\text{II.38})$$

Furthermore, the physical constraint with respect to the Lagrange multiplier $\lambda_{\mathbf{L}}$ is:

$$\begin{pmatrix} 1 & \frac{B_p}{L_o} \end{pmatrix} \begin{pmatrix} \mathcal{R}_f f_s |_{\partial z} \\ \frac{\partial \theta}{\partial t} \end{pmatrix} = \mathcal{R}_f f_s |_{\partial z} + \frac{B_p}{L_o} \frac{\partial \theta}{\partial t} = 0. \quad (\text{II.39})$$

It reveals that the half arrow of the Lagrange multiplier in the Bond Graph Fig. II.19 is an effort source with the flow variable being to zero, such that by passing the '0' junction, the effort variable Φ remains unchanged, while the flow variables $\mathcal{R}_f f_s |_{\partial z}$ and $\frac{B_p}{L_o} \frac{\partial \theta}{\partial t}$ sum to zero, ensuring the power conservation. This is analogous to an interconnection of two glued mass-spring systems that illustrated in Subsection I.3.1 (at page 14), where two masses have the same velocity and inverse reaction forces.

On the other hand, the interconnection through $M_{x1}(x, t)$ is shown on the left column of Fig. II.19. An additional term $-\frac{B_a}{L_o} \mathbb{1}_Z \frac{\partial \theta}{\partial t}(x, t)$ is added into (II.15) to match the power conservation [Nishida 08, Nishida 11]. For the electro-stress diffusion system, this additional term can be seen as a distributed input coming from the mechanical system:

$$\begin{aligned} \frac{\partial f_s}{\partial t}(z, x, t) &= -\frac{\partial \mathbf{j}_s}{\partial z}(z, x, t) - \frac{B_a}{L_o} \mathbb{1}_Z \frac{\partial \theta}{\partial t}(x, t) \\ &= \mathcal{R}_g \frac{\partial}{\partial z} (\mathcal{R}_f f_s(z, x, t)) - \frac{B_a}{L_o} \mathbb{1}_Z \frac{\partial \theta}{\partial t}(x, t). \end{aligned} \quad (\text{II.40})$$

Accordingly, the dissipative PHS of the electro-stress diffusion system (II.20) changes to:

$$\begin{pmatrix} f_2(z, x, t) \\ f_{r2}(z, x, t) \end{pmatrix} = \begin{pmatrix} 0 & \frac{\partial}{\partial z} \\ \frac{\partial}{\partial z} & 0 \end{pmatrix} \begin{pmatrix} e_2(z, x, t) \\ e_{r2}(z, x, t) \end{pmatrix} + \begin{pmatrix} -\frac{B_a}{L_o} \mathbb{1}_Z \frac{\partial \theta}{\partial t}(x, t) \\ 0 \end{pmatrix}, \quad (\text{II.41})$$

closed with (II.21). With the boundary conditions (II.23), the boundary port variables (II.22) are written explicitly as:

$$\begin{pmatrix} f_{\partial z} \\ e_{\partial z} \end{pmatrix} = \begin{pmatrix} e_{r2} \left(-\frac{h_o}{2} \right) \\ -e_{r2} \left(\frac{h_o}{2} \right) \\ e_2 \left(-\frac{h_o}{2} \right) \\ e_2 \left(\frac{h_o}{2} \right) \end{pmatrix} = \begin{pmatrix} \frac{\lambda}{\sigma_e} \mathbf{j}_e + \lambda_{\mathbf{L}} \\ -\frac{\lambda}{\sigma_e} \mathbf{j}_e - \lambda_{\mathbf{L}} \\ e_2 \left(-\frac{h_o}{2} \right) \\ e_2 \left(\frac{h_o}{2} \right) \end{pmatrix}. \quad (\text{II.42})$$

II.2.5 Overall IPMC model

The three above subsystems (II.5), (II.41) and (II.29), with their closure equations (II.6) and (II.21), as well as their boundary variables defined in (II.7), (II.42), and (II.31), have to be coupled through relations (II.35), (II.36) and the Lagrange

multiplier formulated in (II.38) and (II.39), leading to the overall IPMC actuator system⁴:

$$\underbrace{\begin{pmatrix} f_1 \\ f_{r1} \\ f_2 \\ f_{r2} \\ f_3 \\ f_4 \\ f_5 \\ f_6 \end{pmatrix}}_f = \underbrace{\begin{pmatrix} 0 & \frac{\partial}{\partial \xi} & 0 & 0 & 0 & 0 & 0 & 0 \\ \frac{\partial}{\partial \xi} & 0 & 0 & 0 & 0 & 0 & 0 & 0 \\ 0 & 0 & 0 & \frac{\partial}{\partial z} & 0 & 0 & 0 & -\frac{B_a}{L_o} \mathbb{1}_Z \\ 0 & 0 & \frac{\partial}{\partial z} & 0 & 0 & 0 & 0 & 0 \\ 0 & 0 & 0 & 0 & 0 & \frac{\partial}{\partial x} & 0 & -1 \\ 0 & 0 & 0 & 0 & \frac{\partial}{\partial x} & 0 & 0 & 0 \\ 0 & 0 & 0 & 0 & 0 & 0 & 0 & \frac{\partial}{\partial x} \\ 0 & 0 & \int_Z \frac{B_a}{L_o}(\cdot) dz & 0 & 1 & 0 & \frac{\partial}{\partial x} & 0 \end{pmatrix}}_J \underbrace{\begin{pmatrix} e_1 \\ e_{r1} \\ e_2 \\ e_{r2} \\ e_3 \\ e_4 \\ e_5 \\ e_6 \end{pmatrix}}_e + \mathbf{A}_L \lambda_L, \quad (\text{II.43})$$

and $\mathbf{A}_L^* = \left(0 \ 0 \ (\cdot)|_{\frac{h_o}{2}} - (\cdot)|_{-\frac{h_o}{2}} \ 0 \ 0 \ 0 \ 0 \ \frac{B_p}{L_o}\right)$ with

$$\mathbf{A}_L^* e = e_2 \left(\frac{h_o}{2}\right) - e_2 \left(-\frac{h_o}{2}\right) + \frac{B_p}{L_o} e_6 = \mathcal{R}_f f_s|_{\partial z} + \frac{B_p}{L_o} \frac{\partial \theta}{\partial t} = 0, \quad (\text{II.44})$$

which is equivalent to the physical constraint (II.39).

Combining the Hamiltonians defined in each system (II.8), (II.24) and (II.33), the Hamiltonian of the overall IPMC actuator system (II.43) is written as:

$$\begin{aligned} H(t) &= \int_x (H_{el} + H_{em}) dx + H_m \\ &= \frac{1}{2} \int_x \int_\xi \frac{Q_e^2}{C_2} d\xi dx + \frac{1}{2} \int_x \int_z \mathcal{R}_f f_s^2 dz dx + \frac{1}{2} \int_x \left(GA \left(\frac{\partial \omega_o}{\partial x} - \theta \right)^2 \right. \\ &\quad \left. + EI_o \left(\frac{\partial \theta}{\partial x} \right)^2 + \rho_o A \left(\frac{\partial \omega_o}{\partial t} \right)^2 + \rho_o I_o \left(\frac{\partial \theta}{\partial t} \right)^2 \right) dx. \end{aligned} \quad (\text{II.45})$$

The overall model of the IPMC actuator formulated in (II.43) together with its physical constraint (II.44) can be illustrated in the following Fig. II.20, where the element \mathcal{R} denotes the dissipation port, \mathcal{S} is the energy storage port, \mathcal{D} refers to the Dirac structure, and the three blocs containing both \mathcal{D} and BMS stand for the multiscale interconnections we have illustrated in Fig. II.18 and II.19 at page 44 and 45, respectively. The circled numbers in Fig. II.20 represent the interconnection relationships, which are formulated as follows:

$$\begin{aligned} \textcircled{1} : \quad V_c &= \frac{-\lambda}{\sigma_e L_o b_o} e_2|_{\partial z} = \frac{-\lambda}{\sigma_e L_o b_o} \int_z f_{r2} dz, \\ \textcircled{2} : \quad \mathbb{1}_z \frac{\lambda}{\sigma_e} \mathbf{j}_e &= -\mathbb{1}_z \frac{\lambda}{\sigma_e L_o b_o} e_{r1}(0), \\ \textcircled{3} : \quad f_2 &= \frac{\partial e_{r2}}{\partial z} - \frac{B_a}{L_o} \mathbb{1}_Z e_6, \end{aligned}$$

4. For the sake of compactness, the coordinates ξ , z and x , as well as the time parameter t are omitted in the rest of this subsection.

$$\begin{aligned}
 \textcircled{4} : \quad & \frac{M_{x1}}{L_o} = \frac{\int_z B_a e_2 dz}{L_o}, \\
 \textcircled{5} : \quad & \mathbb{1}_Z \Phi = \mathbb{1}_Z \lambda_L, \\
 \textcircled{6} : \quad & \frac{M_{x2}}{L_o} = \frac{B_p}{L_o} \lambda_L, \\
 \textcircled{7} : \quad & \int_z f_{r2} dz + \frac{B_p}{L_o} e_6 = e_2|_{\partial z} + \frac{B_p}{L_o} e_6 = 0.
 \end{aligned}$$

The power preserving in Fig. II.20 indicates that the overall model of the IPMC

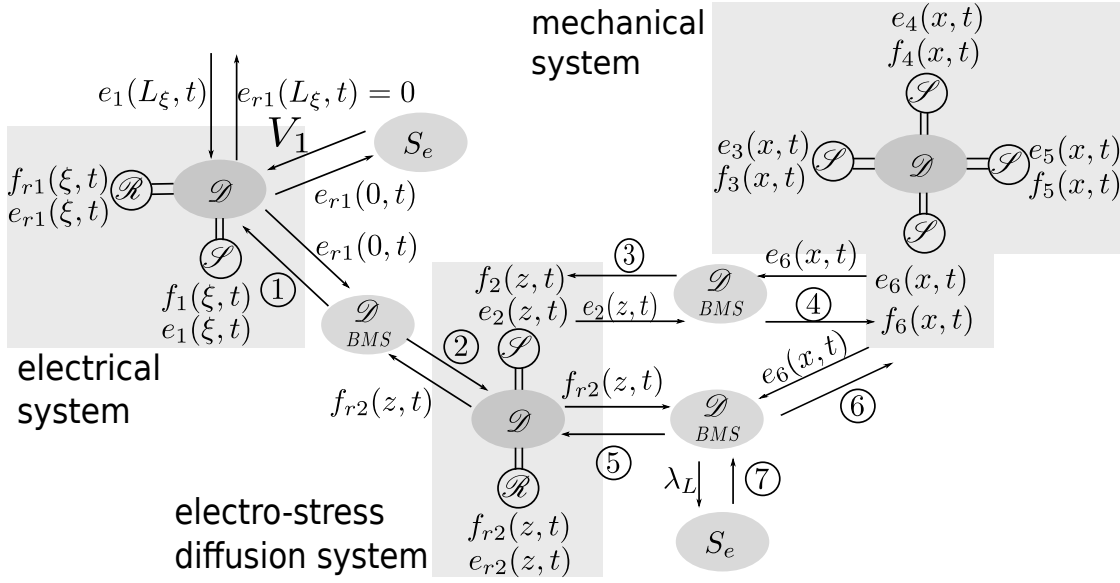


Figure II.20 – Schema of the overall IPMC actuator model.

actuator defines a modulated Dirac structure, which is formulated in the dual flow and effort spaces defined as follows.

The *space of flow variables* is defined as $\bar{\mathcal{F}} = \mathcal{F} \times \mathcal{F}_\partial$, with:

$$\begin{aligned}
 \mathcal{F} &= \mathcal{F}_{(0, L_\xi)} \times \mathcal{F}_{(-\frac{h_o}{2}, \frac{h_o}{2})} \times \mathcal{F}_{(0, L_o)} \\
 &= L_2 \left([0, L_\xi] \times [0, L_o], \mathbb{R}^2 \right) \times L_2 \left(\left[-\frac{h_o}{2}, \frac{h_o}{2} \right] \times [0, L_o], \mathbb{R}^2 \right) \times L_2 \left([0, L_o], \mathbb{R}^4 \right), \\
 \mathcal{F}_\partial &= \mathcal{F}_{\partial\xi} \times \mathcal{F}_{\partial z} \times \mathcal{F}_{\partial x} = \mathbb{R}^2 \times \mathbb{R}^2 \times \mathbb{R}^4.
 \end{aligned}$$

The *space of effort variables* is defined as $\bar{\mathcal{E}} = \mathcal{E} \times \mathcal{E}_\partial$, with:

$$\begin{aligned}
 \mathcal{E} &= \mathcal{E}_{(0, L_\xi)} \times \mathcal{E}_{(-\frac{h_o}{2}, \frac{h_o}{2})} \times \mathcal{E}_{(0, L_o)} \\
 &= H^1 \left([0, L_\xi] \times [0, L_o], \mathbb{R}^2 \right) \times H^1 \left(\left[-\frac{h_o}{2}, \frac{h_o}{2} \right] \times [0, L_o], \mathbb{R}^2 \right) \times H^1 \left([0, L_o], \mathbb{R}^4 \right), \\
 \mathcal{E}_\partial &= \mathcal{E}_{\partial\xi} \times \mathcal{E}_{\partial z} \times \mathcal{E}_{\partial x} = \mathbb{R}^2 \times \mathbb{R}^2 \times \mathbb{R}^4.
 \end{aligned}$$

Proposition 1. *The linear subset $\mathcal{D} \in \bar{\mathcal{F}} \times \bar{\mathcal{E}}$ defined by*

$$\mathcal{D} = \left\{ \begin{array}{l} \begin{pmatrix} f \\ f_\partial \\ e \\ e_\partial \end{pmatrix} \middle| f \in \mathcal{F}, e \in \mathcal{E}, \begin{pmatrix} f_\partial \\ e_\partial \end{pmatrix} \in \mathcal{F}_\partial \times \mathcal{E}_\partial, f = \mathcal{J}e + \mathbf{A}_L \lambda_L, \mathbf{A}_L^* e = 0, \\ \lambda_L \in H^1([0, L_o], \mathbb{R}), e_1(0) + \frac{\lambda}{\sigma_e L_o b_o} \left(e_2 \left(\frac{h_o}{2} \right) - e_2 \left(-\frac{h_o}{2} \right) \right) = V_1, \\ -e_{r2} \left(\pm \frac{h_o}{2} \right) - \frac{\lambda}{\sigma_e L_o b_o} e_{r1}(0) + \lambda_L = 0, e_{r1}(L_\xi) = 0, \\ e_3(L_o) = e_4(0) = e_5(L_o) = e_6(0) = 0 \end{array} \right\} \quad (\text{II.46})$$

is a modulated Stokes-Dirac structure.

Proof. (II.43) together with (II.44) can be reformulated with an extended Dirac structure :

$$\begin{pmatrix} f \\ 0 \end{pmatrix} = \underbrace{\begin{pmatrix} \mathcal{J} & \mathbf{A}_L \\ -\mathbf{A}_L^* & 0 \end{pmatrix}}_{\mathcal{J}_e} \begin{pmatrix} e \\ \lambda_L \end{pmatrix},$$

where the extended operator \mathcal{J}_e is formally skew-symmetric.

The skew symmetry of \mathcal{J}_e lies in the equality between $\langle e^1, \mathcal{J}_e e^2 \rangle$ and $\langle -\mathcal{J}_e e^1, e^2 \rangle$, where $\langle \cdot, \cdot \rangle$ denotes the inner product in the Hilbert space. e^1 and e^2 are two pairs of effort variables in \mathcal{E} .

$$\begin{aligned} \langle e^1, \mathcal{J}_e e^2 \rangle &= \int_x \int_\xi \left(e_1^1 \frac{\partial e_{r1}^2}{\partial \xi} \right) d\xi dx + \int_x \int_\xi \left(e_{r1}^1 \frac{\partial e_1^2}{\partial \xi} \right) d\xi dx + \int_x \int_z \left(e_2^1 \frac{\partial e_{r2}^2}{\partial z} \right) dz dx \\ &\quad - \int_x \int_z \left(e_2^1 \frac{B_a}{L_o} \mathbb{1}_z e_6^2 \right) dz dx + \int_x \int_z \left(e_{r2}^1 \frac{\partial e_2^2}{\partial z} \right) dz dx + \int_x \left(e_3^1 \left(\frac{\partial e_4^2}{\partial x} - e_6^2 \right) \right) dx \\ &\quad + \int_x \left(e_4^1 \frac{\partial e_3^2}{\partial x} \right) dx + \int_x \left(e_5^1 \frac{\partial e_6^2}{\partial x} \right) dx + \int_x \left(e_6^1 \left(\int_z \frac{B_a}{L_o} e_2^2 dz + e_3^2 + \frac{\partial e_5^2}{\partial x} \right) \right) dx \\ &\quad + \int_x \left(e_6^1 \frac{B_p}{L_o} \lambda_L^2 \right) dx + \int_x \left(\lambda_L^1 \left(-e_2 \left(\frac{h_o}{2} \right) + e_2 \left(\frac{h_o}{2} \right) - \frac{B_p}{L_o} e_6^2 \right) \right) dx. \end{aligned} \quad (\text{II.47})$$

Using the integration by parts, (II.47) becomes

$$\begin{aligned} \langle e^1, \mathcal{J}_e e^2 \rangle &= \int_x \left([e_1^1 e_{r1}^2]_0^{L_\xi} - \int_\xi \left(e_{r1}^2 \frac{\partial e_1^1}{\partial \xi} \right) d\xi \right) dx + \int_x \left([e_{r1}^1 e_1^2]_0^{L_\xi} - \int_\xi \left(e_1^2 \frac{\partial e_{r1}^1}{\partial \xi} \right) d\xi \right) dx \\ &\quad + \int_x \left([e_2^1 e_{r2}^2]_{-\frac{h_o}{2}}^{\frac{h_o}{2}} - \int_z \left(e_{r2}^2 \frac{\partial e_2^1}{\partial z} \right) dz \right) dx + \int_x \left([e_{r2}^1 e_2^2]_{-\frac{h_o}{2}}^{\frac{h_o}{2}} - \int_z \left(e_2^2 \frac{\partial e_{r2}^1}{\partial z} \right) dz \right) dx \end{aligned}$$

$$\begin{aligned}
 & - \int_x \int_z \left(e_2^1 \frac{B_a}{L_o} \mathbb{1}_z e_6^2 \right) dz dx + \int_x \left(e_6^1 \int_z \left(\frac{B_a}{L_o} e_2^2 \right) dz \right) dx \\
 & + \int_x \left(\lambda_{\mathbf{L}}^1 \left(-e_2 \left(\frac{h_o}{2} \right) + e_2 \left(\frac{h_o}{2} \right) \right) \right) dx + [e_3^1 e_4^2]_0^{L_o} - \int_x \left(e_4^2 \frac{\partial e_3^1}{\partial x} \right) dx \\
 & + [e_4^1 e_3^2]_0^{L_o} - \int_x \left(e_3^2 \frac{\partial e_4^1}{\partial x} \right) dx + [e_5^1 e_6^2]_0^{L_o} - \int_x \left(e_6^2 \frac{\partial e_5^1}{\partial x} \right) dx + [e_6^1 e_5^2]_0^{L_o} \\
 & - \int_x \left(e_5^2 \frac{\partial e_6^1}{\partial x} \right) dx - \int_x (e_3^1 e_6^2) dx + \int_x (e_6^1 e_3^2) dx + \int_x \left(e_6^1 \frac{B_p}{L_o} \lambda_{\mathbf{L}}^2 \right) dx \\
 & - \int_x \left(\lambda_{\mathbf{L}}^1 \frac{B_p}{L_o} e_6^2 \right) dx. \tag{II.48}
 \end{aligned}$$

By applying conditions of interconnection and boundary conditions expressed in Proposition 1, (II.48) is reformulated to:

$$\begin{aligned}
 \langle e^1, \mathcal{J}_e e^2 \rangle & = - \int_x (e_1^1(0) e_{r1}^2(0)) dx - \int_x (e_{r1}^1(0) e_1^2(0)) dx \\
 & + \int_x \left(e_2^1 \left(\frac{h_o}{2} \right) e_{r2}^2 \left(\frac{h_o}{2} \right) - e_2^1 \left(-\frac{h_o}{2} \right) e_{r2}^2 \left(-\frac{h_o}{2} \right) \right) dx \\
 & + \int_x \left(e_{r2}^1 \left(\frac{h_o}{2} \right) e_2^2 \left(\frac{h_o}{2} \right) - e_{r2}^1 \left(-\frac{h_o}{2} \right) e_2^2 \left(-\frac{h_o}{2} \right) \right) dx \\
 & - \int_x \int_\xi \left(e_{r1}^2 \frac{\partial e_1^1}{\partial \xi} \right) d\xi dx - \int_x \int_\xi \left(e_1^2 \frac{\partial e_{r1}^1}{\partial \xi} \right) d\xi dx - \int_x \int_z \left(e_{r2}^2 \frac{\partial e_2^1}{\partial z} \right) dz dx \\
 & - \int_x \int_z \left(e_2^2 \frac{\partial e_{r2}^1}{\partial z} \right) dz dx - \int_x \int_z \frac{B_a}{L_o} e_2^1 \mathbb{1}_z e_6^2 dz dx + \int_x \int_z \frac{B_a}{L_o} (\mathbb{1}_z e_6^1) e_2^2 dz dx \\
 & + \int_x \lambda_{\mathbf{L}}^1 \left(-e_2^2 \left(\frac{h_o}{2} \right) + e_2^2 \left(-\frac{h_o}{2} \right) \right) dx - \int_x \left(e_4^2 \frac{\partial e_3^1}{\partial x} \right) dx - \int_x \left(e_3^2 \frac{\partial e_4^1}{\partial x} \right) dx \\
 & - \int_x \left(e_6^2 \frac{\partial e_5^1}{\partial x} \right) dx - \int_x \left(e_5^2 \frac{\partial e_6^1}{\partial x} \right) dx - \int_x (e_6^2 e_3^1) dx + \int_x (e_3^2 e_6^1) dx \\
 & + \int_x \left(\lambda_{\mathbf{L}}^2 \frac{B_p}{L_o} e_6^1 \right) dx - \int_x \left(e_6^2 \frac{B_p}{L_o} \lambda_{\mathbf{L}}^1 \right) dx \\
 & = - \int_x (e_1^1(0) e_{r1}^2(0)) dx - \int_x (e_{r1}^1(0) e_1^2(0)) dx + \int_x (e_1^1(0) - V_1) e_{r1}^2(0) dx \\
 & + \int_x (e_1^2(0) - V_1) e_{r1}^1(0) dx - \int_x \int_\xi \left(e_{r1}^2 \frac{\partial e_1^1}{\partial \xi} \right) d\xi dx - \int_x \int_\xi \left(e_1^2 \frac{\partial e_{r1}^1}{\partial \xi} \right) d\xi dx \\
 & - \int_x \int_z \left(e_{r2}^2 \frac{\partial e_2^1}{\partial z} \right) dz dx - \int_x \int_z \left(e_2^2 \frac{\partial e_{r2}^1}{\partial z} \right) dz dx - \int_x \int_z \frac{B_a}{L_o} e_2^1 dz e_6^2 dx \\
 & + \int_x \int_z \frac{B_a}{L_o} (\mathbb{1}_z e_6^1) e_2^2 dz dx + \int_x \left(e_2^1 \left(\frac{h_o}{2} \right) - e_2^1 \left(-\frac{h_o}{2} \right) \right) \lambda_{\mathbf{L}}^2 dx \\
 & - \int_x \left(e_4^2 \frac{\partial e_3^1}{\partial x} \right) dx - \int_x \left(e_3^2 \frac{\partial e_4^1}{\partial x} \right) dx - \int_x \left(e_6^2 \frac{\partial e_5^1}{\partial x} \right) dx - \int_x \left(e_5^2 \frac{\partial e_6^1}{\partial x} \right) dx \\
 & - \int_x (e_6^2 e_3^1) dx + \int_x (e_3^2 e_6^1) dx + \int_x \left(\lambda_{\mathbf{L}}^2 \frac{B_p}{L_o} e_6^1 \right) dx - \int_x \left(e_6^2 \frac{B_p}{L_o} \lambda_{\mathbf{L}}^1 \right) dx
 \end{aligned}$$

$$= \langle -\mathcal{J}_e e^1, e^2 \rangle - V_1 \int_x (e_{r1}^2(0) + e_{r1}^1(0)) dx, \quad (\text{II.49})$$

where $-\int_x e_{r1}(0) dx$ is the output current $\int I_e dx$ along the IPMC electrodes. If the input voltage V_1 is considered to be 0, then $\langle e^1, \mathcal{J}_e e^2 \rangle = \langle -\mathcal{J}_e e^1, e^2 \rangle$, and Proposition 1 holds. \square

II.3 1D PORT-HAMILTONIAN MODEL OF THE ACTUATED ENDOSCOPE

We have established the overall model of the IPMC actuator with three subsystems: the electrical system, the electro-stress diffusion system and the mechanical system. In this section, we are going to extend the IPMC actuator model to the IPMC actuated endoscope model, which has been briefly introduced in Section II.1. From Assumption 1.d, we are going to model the deformation of both the actuator and the endoscope with the same mechanical system. And the interconnection between the IPMC and the endoscope is simplified through the electro-stress diffusion system and the integrated mechanical system.

Starting from the 1D small deformation case, which is modeled by the Timoshenko beam, the interconnection between the IPMC actuator and the endoscope is formulated as follows⁵:

$$\begin{pmatrix} f_I \\ f_{M1} \end{pmatrix} = \begin{pmatrix} \mathcal{J}_I & \mathcal{J}_{inter1} \\ -\mathcal{J}_{inter1}^* & \mathcal{J}_{M1} \end{pmatrix} \begin{pmatrix} e_I \\ e_{M1} \end{pmatrix} + \begin{pmatrix} A_{Lu} \\ A_{L1} \end{pmatrix} \lambda_L, \quad (\text{II.50})$$

where

$$f_I = \begin{pmatrix} f_1 \\ f_{r1} \\ f_2 \\ f_{r2} \end{pmatrix}, \quad e_I = \begin{pmatrix} e_1 \\ e_{r1} \\ e_2 \\ e_{r2} \end{pmatrix}, \quad \mathcal{J}_I = \begin{pmatrix} 0 & \frac{\partial}{\partial \xi} & 0 & 0 \\ \frac{\partial}{\partial \xi} & 0 & 0 & 0 \\ 0 & 0 & 0 & \frac{\partial}{\partial z} \\ 0 & 0 & \frac{\partial}{\partial z} & 0 \end{pmatrix}, \quad (\text{II.51})$$

$$f_{M1} = \begin{pmatrix} \frac{\partial^2 w_e}{\partial t \partial X} - \frac{\partial \theta_e}{\partial t} \\ \rho_e A_e \frac{\partial^2 w_e}{\partial t^2} \\ \frac{\partial^2 \theta_e}{\partial t \partial X} \\ \rho_e I_b \frac{\partial^2 \theta_e}{\partial t^2} \end{pmatrix}, \quad e_{M1} = \begin{pmatrix} G_e A_e \left(\frac{\partial w_e}{\partial X} - \theta_e \right) \\ \frac{\partial w_e}{\partial t} \\ E_e I_b \frac{\partial \theta_e}{\partial X} \\ \frac{\partial \theta_e}{\partial t} \end{pmatrix}, \quad \mathcal{J}_{M1} = \begin{pmatrix} 0 & \frac{\partial}{\partial X} & 0 & -1 \\ \frac{\partial}{\partial X} & 0 & 0 & 0 \\ 0 & 0 & 0 & \frac{\partial}{\partial X} \\ 1 & 0 & \frac{\partial}{\partial X} & 0 \end{pmatrix},$$

$$\mathcal{J}_{inter1} = \begin{pmatrix} 0 & 0 & 0 & 0 \\ 0 & 0 & 0 & 0 \\ 0 & 0 & 0 & -\mathbb{1}_Z B_a b_M \\ 0 & 0 & 0 & 0 \end{pmatrix}, \quad A_{Lu} = \begin{pmatrix} 0 \\ 0 \\ -\frac{\partial}{\partial z} \mathbb{1}_Z \\ 0 \end{pmatrix}, \quad A_{L1} = \begin{pmatrix} 0 \\ 0 \\ 0 \\ 0 \\ B_p b_M \end{pmatrix}, \quad (\text{II.52})$$

5. For the sake of compactness, the coordinates ξ , z and X , as well as the time parameter t are omitted in this section.

and $X \in [0, L_e]$ with L_e denoting the length of the endoscope. ρ_e , A_e , I_b , E_e and G_e relate to the mass density, cross section area, moment of inertial, Young's modulus and shear modulus of the mechanical structure, respectively. w_e and θ_e represent the transversal displacement and the rotational angle of the central line, respectively. b_M in (II.52) is formulated as:

$$b_M = \begin{cases} \frac{1}{X_2 - X_1}, & \text{for } X \in [X_1, X_2], \\ 0, & \text{else.} \end{cases} \quad (\text{II.53})$$

The aim of the rest part of this section is to generalize the previous model (II.50) to a mechanical structure operating over large deformations. In this case one needs to consider a mechanical model accounting for the geometric nonlinearity. There exist several models of 1D beams under large deformations in the literature, mainly sorted into the floating frame reference models and the inertial frame reference models. The former describes the large deformation of the beam with a rigid body motion and a small deformation with respect to the rigid body reference, while the latter does not make this distinction and models directly the deformation using nonlinear strain-displacement formulations. One can cite for example [Sandhu 90, Nada 10] for finite dimensional floating frame reference models, [Selig 01] for floating frame reference models with Lie algebra, which is later formulated into PHS in [Golo 03], and cite [Berzeri 00] for a finite dimensional inertial frame reference model named absolute nodal coordinate formulation, and [Simo 86] for infinite dimensional inertial frame reference models. In this thesis we focus on the infinite dimensional models because the considered structure is compliant. It was pointed out in [Simo 86] that the formulation under the floating frame reference generates coupling terms of the Coriolis and centrifugal effects together with the rotation inertia of the beam, making the kinetic energy not a standard quadratic form. On the other hand, the inertial frame reference formulation could tackle the aforementioned coupling problems and propose a much simpler model. So we will apply the infinite dimensional initial frame reference model proposed by [Simo 86], and reformulate it under the port-Hamiltonian framework.

The coordinate interpretation of the inertial frame reference is depicted in Fig. II.21, with \vec{t}_1 and \vec{t}_2 referring to the moving coordinates following the beam deformation, where \vec{t}_1 is perpendicular to the cross section and \vec{t}_2 is in the cross section. ω_1 and ω_2 represent the transversal displacements in the X and Z directions, respectively. The moving coordinates \vec{t}_1 and \vec{t}_2 are connected with the inertial coordinates X and Z by the following relationship [Simo 86]:

$$\begin{pmatrix} \vec{t}_1 \\ \vec{t}_2 \end{pmatrix} = \underbrace{\begin{pmatrix} \cos \theta_e & -\sin \theta_e \\ \sin \theta_e & \cos \theta_e \end{pmatrix}^T}_{\Lambda^T} \begin{pmatrix} X \\ Z \end{pmatrix}. \quad (\text{II.54})$$

The small deformation assumption is no longer valid here, still, the plane cross section Assumption 2.b remains valid. As we explained in the beginning of this part, the relations between the strain γ_e and the displacements ω_1 , ω_2 , θ_e are now

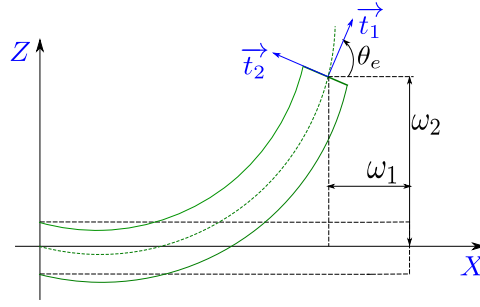


Figure II.21 – Diagram of the inertial frame reference model, figure adapted from [Simo 86].

nonlinear, which is formulated by the finite strain theory [Simo 86] as follows:

$$\gamma_e = \begin{pmatrix} \gamma_{Xe} \\ \gamma_{Ze} \end{pmatrix} = \begin{pmatrix} 1 + \frac{\partial \omega_1}{\partial X} - \cos \theta_e \\ \frac{\partial \omega_2}{\partial X} - \sin \theta_e \end{pmatrix}. \quad (\text{II.55})$$

Therefore, the equations of motion are formulated by:

$$\rho_e A_e \begin{pmatrix} \frac{\partial^2 \omega_1}{\partial t^2} \\ \frac{\partial^2 \omega_2}{\partial t^2} \end{pmatrix} = \frac{\partial}{\partial X} \left(\Lambda C_e \Lambda^T \begin{pmatrix} 1 + \frac{\partial \omega_1}{\partial X} - \cos \theta_e \\ \frac{\partial \omega_2}{\partial X} - \sin \theta_e \end{pmatrix} \right), \quad (\text{II.56a})$$

$$\rho_e I_b \frac{\partial^2 \theta_e}{\partial t^2} = E_e I_b \frac{\partial^2 \theta_e}{\partial X^2} + \begin{pmatrix} -\frac{\partial \omega_2}{\partial X} \\ 1 + \frac{\partial \omega_1}{\partial X} \end{pmatrix}^T \Lambda C_e \Lambda^T \begin{pmatrix} 1 + \frac{\partial \omega_1}{\partial X} - \cos \theta_e \\ \frac{\partial \omega_2}{\partial X} - \sin \theta_e \end{pmatrix} + m_{ext}, \quad (\text{II.56b})$$

where m_{ext} is the exerted bending moment density, and C_e is given by:

$$C_e = \begin{pmatrix} E_e A_e & 0 \\ 0 & G_e A_e \end{pmatrix}.$$

The Hamiltonian of the large deformation beam reads:

$$H_e = \frac{1}{2} \int_X \left(\rho_e A_e \left(\frac{\partial \omega_1}{\partial t} \right)^2 + \rho_e A_e \left(\frac{\partial \omega_2}{\partial t} \right)^2 + \rho_e I_b \left(\frac{\partial \theta_e}{\partial t} \right)^2 + E_e A_e \Gamma_1^2 + G_e A_e \Gamma_2^2 + E_e I_b \left(\frac{\partial \theta_e}{\partial x} \right)^2 \right) dX,$$

with

$$\Gamma = \begin{pmatrix} \Gamma_1 \\ \Gamma_2 \end{pmatrix} = \Lambda^T \gamma_e.$$

This inertial frame reference formulation has been reformulated as a PHS in [Nishida 05]. Choosing the flow and effort variables as:

$$f_{M2} = \begin{pmatrix} \frac{\partial^2 \omega_1}{\partial t \partial X} \\ \rho_e A_e \frac{\partial^2 \omega_1}{\partial t^2} \\ \frac{\partial^2 \omega_2}{\partial t \partial X} \\ \rho_e A_e \frac{\partial^2 \omega_2}{\partial t^2} \\ \frac{\partial \theta_e}{\partial t} \\ \frac{\partial^2 \theta_e}{\partial t \partial X} \\ \rho_e I_b \frac{\partial^2 \theta_e}{\partial t^2} \end{pmatrix}, \quad e_{M2} = \begin{pmatrix} (\Lambda C_e \Gamma)_1 \\ \frac{\partial \omega_1}{\partial t} \\ (\Lambda C_e \Gamma)_2 \\ \frac{\partial \omega_2}{\partial t} \\ \left(-\frac{\partial \omega_2}{\partial X}, 1 + \frac{\partial \omega_1}{\partial X}\right) \Lambda C_e \Gamma \\ E_e I_b \frac{\partial \theta_e}{\partial X} \\ \frac{\partial \theta_e}{\partial t} \end{pmatrix}, \quad (\text{II.57})$$

(II.56) becomes:

$$f_{M2} = \underbrace{\begin{pmatrix} 0 & \frac{\partial}{\partial X} & 0 & 0 & 0 & 0 & 0 \\ \frac{\partial}{\partial X} & 0 & 0 & 0 & 0 & 0 & 0 \\ 0 & 0 & 0 & \frac{\partial}{\partial X} & 0 & 0 & 0 \\ 0 & 0 & \frac{\partial}{\partial X} & 0 & 0 & 0 & 0 \\ 0 & 0 & 0 & 0 & 0 & 0 & 1 \\ 0 & 0 & 0 & 0 & 0 & 0 & \frac{\partial}{\partial X} \\ 0 & 0 & 0 & 0 & -1 & \frac{\partial}{\partial X} & 0 \end{pmatrix}}_{\mathcal{J}_{M2}} e_{M2} + \underbrace{\begin{pmatrix} 0 \\ 0 \\ 0 \\ 0 \\ 0 \\ 0 \\ 1 \end{pmatrix}}_{B_{M2}} m_{ext}. \quad (\text{II.58})$$

One can prove that the interconnection operator \mathcal{J}_{M2} is skew-symmetric. The non-linearity of this model lies in the energy matrix, which represents the constitutive relation between the effort and energy variables.

The boundary port variables are chosen to be [Nishida 05]:

$$f_{\partial M} = \begin{pmatrix} \frac{\partial \omega_1}{\partial t}(0) \\ \frac{\partial \omega_1}{\partial t}(L_e) \\ \frac{\partial \omega_2}{\partial t}(0) \\ \frac{\partial \omega_2}{\partial t}(L_e) \\ \frac{\partial \theta_e}{\partial t}(0) \\ \frac{\partial \theta_e}{\partial t}(L_e) \end{pmatrix}, \quad e_{\partial M} = \begin{pmatrix} -(\Lambda C_e \Gamma)_1(0) \\ (\Lambda C_e \Gamma)_1(L_e) \\ -(\Lambda C_e \Gamma)_2(0) \\ (\Lambda C_e \Gamma)_2(L_e) \\ -E_e I_b \frac{\partial \theta_e}{\partial X}(0) \\ E_e I_b \frac{\partial \theta_e}{\partial X}(L_e) \end{pmatrix}.$$

Remark 7. *The large deformation beam under the inertial frame reference model (II.56) reduces to the Timoshenko beam model (II.28) as soon as the small strain assumption $\cos \theta_e \approx 1$, $\sin \theta_e \approx \theta_e$ and the inextensible assumption that $\omega_1 = 0$ are made. As a result,*

$$\begin{aligned} \Gamma_1 &= 0, \text{ and} \\ \Gamma_2 &= \left(E_e A_e (\sin \theta_e)^2 + G_e A_e (\cos \theta_e)^2 \right) \left(\frac{\partial \omega_2}{\partial x} - \sin \theta_e \right) \\ &= \left(E_e A_e \frac{1 - \cos(2\theta_e)}{2} + G_e A_e \frac{\cos(2\theta_e) + 1}{2} \right) \left(\frac{\partial \omega_2}{\partial x} - \sin \theta_e \right) \end{aligned}$$

$$= G_e A_e \left(\frac{\partial \omega_2}{\partial x} - \theta_e \right),$$

which leads to the simplification.

This large deformation beam model (II.58) can be interconnected with the IPMC in a similar way as in (II.50), which is:

$$\begin{pmatrix} f_I \\ f_{M2} \end{pmatrix} = \begin{pmatrix} \mathcal{J}_I & \mathcal{J}_{inter2} \\ -\mathcal{J}_{inter2}^* & \mathcal{J}_{M2} \end{pmatrix} \begin{pmatrix} e_I \\ e_{M2} \end{pmatrix} + \begin{pmatrix} A_{Lu} \\ A_{L2} \end{pmatrix} \lambda_{\mathbf{L}}, \quad (\text{II.59})$$

where f_I , e_I , \mathcal{J}_I , and A_{Lu} are defined in (II.51) and (II.52),

$$\mathcal{J}_{inter2} = \begin{pmatrix} 0 & 0 & 0 & 0 & 0 & 0 & 0 \\ 0 & 0 & 0 & 0 & 0 & 0 & 0 \\ 0 & 0 & 0 & 0 & 0 & 0 & -\mathbb{1}_Z B_a b_M \\ 0 & 0 & 0 & 0 & 0 & 0 & 0 \end{pmatrix}, \text{ and } A_{L2} = B_{M2} B_p b_M,$$

with b_M defined in (II.53).

II.4 2D PORT-HAMILTONIAN MODEL OF THE ACTUATED ENDOSCOPE

In this section, we extend the dimension of the mechanical model to investigate the deformation of the middle referenced surface together with its normal section, leading to a 2D shell model. For the sake of simplicity, the model is presented in cylindrical coordinates with three directions X , Θ and α_3 , as illustrated in Fig. II.3.

Classical elastic thin shell models are based on Love's hypotheses [Leissa 73, Soedel 82]:

Assumption 3.a. *The thickness of the shell is small enough and is assumed to be constant.*

Assumption 3.b. *Deformations are small, and the Hooke's law applies.*

Assumption 3.c. *The cross section of the referenced surface remains un-stretched.*

Assumption 3.d. *The cross section of the referenced surface remains normal after deformation, so there is no shear deformation.*

Assumption 3.e. *The rotatory inertia is neglected.*

Assumption 3.f. $\alpha_3/a_s \ll 1$, with a_s denoting the radius of the cylindrical shell.

These assumptions give rise to the Love-Timoshenko models [Love 88, Timoshenko 59]. On the basis of the Love-Timoshenko models, there exist other models with several adjustments [Leissa 73], mainly proposed by: Flugge-Byrne-Lur'ye [Leissa 73, Kraus 67], Reissner-Naghdi-Berry [Reissner 41, Naghdi 64], Vlasov [Vlasov 51], Sanders [Sanders 60], Donnell-Mushtari [Donnell 33], etc. Here we give a short review on these models. Compared to the Love-Timoshenko one, Flugge-Byrne-Lur'ye applies Assumption 3.f after the calculations of resultant forces and bending moments, generating a higher-order model. Reissner-Naghdi-Berry applies Assumption 3.f before the calculations of strains. Vlasov neglects Assumption 3.f by expressing α_3/a_s with a geometric series expansion. Sanders improves the Love's model by proposing an eighth order approximation. And Donnell-Mushtari neglects the tangential terms of the middle referenced surface changes on the basis of Flugge-Byrne-Lur'ye's model. Readers are recommended to [Leissa 73, Qatu 02b, Qatu 02a] for detailed reviews of these various models.

However, these aforementioned models based on the Love's assumptions do not consider the shear deformation, nor the rotatory inertia. To deal with this issue and to get a more accurate linear model, Soedel released the Assumption 3.d and 3.e of Love's theory, and proposed a modified model in [Soedel 82]. This model can be reduced to 1D which is the Timoshenko beam [Timoshenko 09], and also be extended to 3D Mindlin plate [Mindlin 89], which will be detailed in Remark 8. For the rest part of this section, we center on the Soedel's model for the mechanical system of the actuated endoscope.

According to Assumption 3.c, the displacements are composed of u_{XX} , $u_{\Theta\Theta}$, w_3 , β_X and β_Θ , where u_{XX} , $u_{\Theta\Theta}$ and w_3 represent the deformations in the X , Θ and α_3 directions, respectively. β_X and β_Θ correspond to the rotations of tangents to the referenced surface oriented along the coordinates X and Θ . They are presented in Fig. II.22.

The displacement vectors are therefore formulated by [Kraus 67]:

$$\mathbf{U}_X(X, \Theta, \alpha_3) = u_{XX}(X, \Theta) + \alpha_3\beta_X(X, \Theta), \quad (\text{II.60a})$$

$$\mathbf{U}_\Theta(X, \Theta, \alpha_3) = u_{\Theta\Theta}(X, \Theta) + \alpha_3\beta_\Theta(X, \Theta), \quad (\text{II.60b})$$

$$\mathbf{W}(X, \Theta, \alpha_3) = w_3(X, \Theta). \quad (\text{II.60c})$$

The relations between the strains and deformations are ⁶ [Sokolnikoff 56, Kraus 67]:

$$\epsilon_{XX} = \frac{1}{\left(1 + \frac{\alpha_3}{r_1}\right)} \frac{\partial \mathbf{U}_X}{\partial X}, \quad (\text{II.61a})$$

$$\epsilon_{\Theta\Theta} = \frac{1}{a_s \left(1 + \frac{\alpha_3}{r_2}\right)} \left(\frac{\mathbf{U}_\Theta}{\partial \Theta} + \mathbf{W} \right), \quad (\text{II.61b})$$

$$\gamma_{X3} = \frac{1}{\left(1 + \frac{\alpha_3}{r_1}\right)} \frac{\partial \mathbf{W}}{\partial X} + \left(1 + \frac{\alpha_3}{r_1}\right) \frac{\partial}{\partial \alpha_3} \left(\frac{\mathbf{U}_X}{1 + \frac{\alpha_3}{r_1}} \right), \quad (\text{II.61c})$$

6. For the sake of compactness, the coordinates X and Θ , as well as the time parameter t are omitted in the rest of this section.

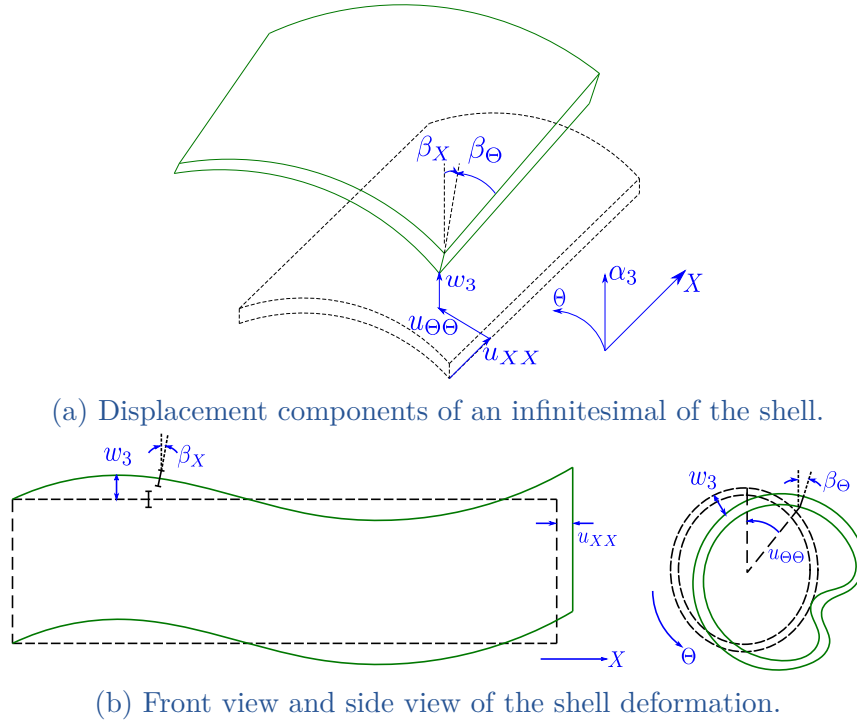


Figure II.22 – Deformation of the shell model.

$$\gamma_{\Theta 3} = \frac{1}{a_s \left(1 + \frac{\alpha_3}{r_2}\right)} \frac{\partial \mathbf{W}}{\partial \Theta} + a_s \left(1 + \frac{\alpha_3}{r_2}\right) \frac{\partial}{\partial \alpha_3} \left(\frac{\mathbf{U}_\Theta}{a_s \left(1 + \frac{\alpha_3}{r_2}\right)} \right), \quad (\text{II.61d})$$

$$\gamma_{X\Theta} = \frac{a_s \left(1 + \frac{\alpha_3}{r_2}\right)}{1 + \frac{\alpha_3}{r_1}} \frac{\partial}{\partial X} \left(\frac{\mathbf{U}_\Theta}{a_s \left(1 + \frac{\alpha_3}{r_2}\right)} \right) + \frac{1 + \frac{\alpha_3}{r_1}}{a_s \left(1 + \frac{\alpha_3}{r_2}\right)} \frac{\partial}{\partial \Theta} \left(\frac{\mathbf{U}_X}{\left(1 + \frac{\alpha_3}{r_1}\right)} \right), \quad (\text{II.61e})$$

where r_1 denotes the curvature radius of X axis and tends to infinity, and $r_2 = a_s$ is related to the curvature radius of Θ axis. Applying Assumption 3.f and substituting (II.60) to (II.61), one obtains:

$$\begin{aligned} \epsilon_{XX} &= \epsilon_{XX}^0 + \alpha_3 k_{XX}, & \epsilon_{\Theta\Theta} &= \epsilon_{\Theta\Theta}^0 + \alpha_3 k_{\Theta\Theta}, & \gamma_{X3} &= \frac{\partial w_3}{\partial X} + \beta_X, \\ \gamma_{\Theta 3} &= -\frac{u_{\Theta\Theta}}{a_s} + \frac{1}{a_s} \frac{\partial w_3}{\partial \Theta} + \beta_\Theta, & \gamma_{X\Theta} &= \gamma_{X\Theta}^0 + \alpha_3 k_{X\Theta}, \end{aligned} \quad (\text{II.62})$$

where ϵ_{XX}^0 , $\epsilon_{\Theta\Theta}^0$ and $\gamma_{X\Theta}^0$ are the membrane strains, and k_{XX} , $k_{\Theta\Theta}$ and $k_{X\Theta}$ are some curvature terms that are formulated as:

$$\begin{aligned} \epsilon_{XX}^0 &= \frac{\partial u_{XX}}{\partial X}, & \epsilon_{\Theta\Theta}^0 &= \frac{1}{a_s} \left(\frac{\partial u_{\Theta\Theta}}{\partial \Theta} + w_3 \right), & \gamma_{X\Theta}^0 &= \frac{\partial u_{\Theta\Theta}}{\partial X} + \frac{1}{a_s} \frac{\partial u_{XX}}{\partial \Theta}, \\ k_{XX} &= \frac{\partial \beta_X}{\partial X}, & k_{\Theta\Theta} &= \frac{1}{a_s} \frac{\partial \beta_\Theta}{\partial \Theta}, & k_{X\Theta} &= \frac{\partial \beta_\Theta}{\partial X} + \frac{1}{a_s} \frac{\partial \beta_X}{\partial \Theta}. \end{aligned}$$

Hooke's law gives the linear relation between the stresses and the strains as follows [Soedel 82]:

$$\begin{pmatrix} \sigma_{XX} \\ \sigma_{\Theta\Theta} \\ \tau_{X\Theta} \\ \tau_{X3} \\ \tau_{\Theta3} \end{pmatrix} = \begin{pmatrix} \frac{E_e}{1-\nu_s^2} & \frac{\nu_s E_e}{1-\nu_s^2} & 0 & 0 & 0 \\ \frac{\nu_s E_e}{1-\nu_s^2} & \frac{E_e}{1-\nu_s^2} & 0 & 0 & 0 \\ 0 & 0 & G_e & 0 & 0 \\ 0 & 0 & 0 & k'G_e & 0 \\ 0 & 0 & 0 & 0 & k'G_e \end{pmatrix} \begin{pmatrix} \epsilon_{XX} \\ \epsilon_{\Theta\Theta} \\ \gamma_{X\Theta} \\ \gamma_{X3} \\ \gamma_{\Theta3} \end{pmatrix}, \quad (\text{II.63})$$

where ν_s , and k' denote the Poisson ratio and the shear coefficient of the shell, respectively.

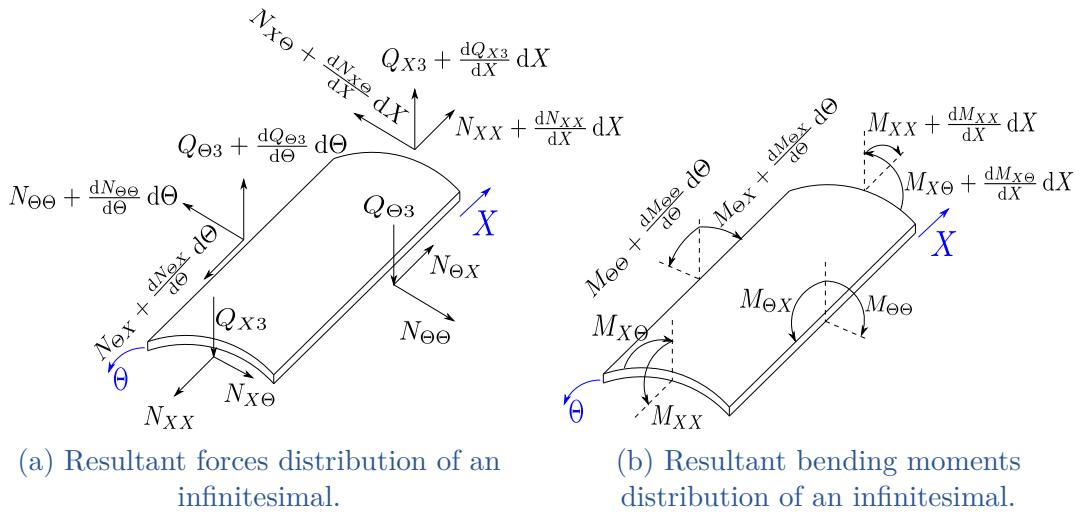


Figure II.23 – Resultant forces and bending moments diagram.

The resultant forces and bending moments diagram is depicted in Fig. II.23. Because of the symmetry, one has $N_{X\Theta} = N_{\Theta X}$, and $M_{X\Theta} = M_{\Theta X}$. These resultant forces and bending moments are calculated according to the stress tensors (II.63) as:

$$\begin{aligned} N_{XX} &= \int_{\alpha_3} \sigma_{XX} \left(1 + \frac{\alpha_3}{r_2}\right) d\alpha_3, & N_{\Theta\Theta} &= \int_{\alpha_3} \sigma_{\Theta\Theta} \left(1 + \frac{\alpha_3}{r_1}\right) d\alpha_3 \\ N_{X\Theta} &= \int_{\alpha_3} \tau_{X\Theta} \left(1 + \frac{\alpha_3}{r_2}\right) d\alpha_3, & Q_{X3} &= \int_{\alpha_3} \tau_{X3} \left(1 + \frac{\alpha_3}{r_2}\right) d\alpha_3, \\ Q_{\Theta3} &= \int_{\alpha_3} \tau_{\Theta3} \left(1 + \frac{\alpha_3}{r_1}\right) d\alpha_3, & M_{XX} &= \int_{\alpha_3} \sigma_{XX} \left(1 + \frac{\alpha_3}{r_2}\right) \alpha_3 d\alpha_3, \\ M_{\Theta\Theta} &= \int_{\alpha_3} \sigma_{\Theta\Theta} \left(1 + \frac{\alpha_3}{r_1}\right) \alpha_3 d\alpha_3, & M_{X\Theta} &= \int_{\alpha_3} \tau_{X\Theta} \left(1 + \frac{\alpha_3}{r_2}\right) \alpha_3 d\alpha_3. \end{aligned} \quad (\text{II.64})$$

Substituting (II.62) and (II.63) to (II.64), one gets:

$$N_{XX} = K_e \left(\epsilon_{XX}^0 + \nu_s \epsilon_{\Theta\Theta}^0 \right), \quad N_{\Theta\Theta} = K_e \left(\epsilon_{\Theta\Theta}^0 + \nu_s \epsilon_{XX}^0 \right),$$

$$\begin{aligned}
 N_{X\Theta} &= K_e \frac{1 - \nu_s}{2} \gamma_{X\Theta}^0, & Q_{X3} &= k' G_e h_s \gamma_{X3}, \\
 Q_{\Theta 3} &= k' G_e h_s \gamma_{\Theta 3}, & M_{XX} &= D_e (k_{XX} + \nu_s k_{\Theta\Theta}), \\
 M_{\Theta\Theta} &= D_e (k_{\Theta\Theta} + \nu_s k_{XX}), & M_{X\Theta} &= D_e \frac{1 - \nu_s}{2} k_{X\Theta},
 \end{aligned}$$

where h_s is the thickness of the shell, $K_e = \frac{E_e h_s}{1 - \nu_s^2}$, and $D_e = \frac{E_e h_s^3}{12(1 - \nu_s^2)}$ denotes the flexural rigidity.

The dynamic equations of the cylindrical shell are given by [Soedel 82]:

$$\rho_e h_s \frac{\partial^2 u_{XX}}{\partial t^2} = \frac{\partial N_{XX}}{\partial X} + \frac{1}{a_s} \frac{\partial N_{X\Theta}}{\partial \Theta}, \quad (\text{II.65a})$$

$$\rho_e h_s \frac{\partial^2 u_{\Theta\Theta}}{\partial t^2} = \frac{\partial N_{X\Theta}}{\partial X} + \frac{1}{a_s} \frac{\partial N_{\Theta\Theta}}{\partial \Theta} + \frac{1}{a_s} Q_{\Theta 3}, \quad (\text{II.65b})$$

$$\rho_e h_s \frac{\partial^2 w_3}{\partial t^2} = \frac{\partial Q_{X3}}{\partial X} + \frac{1}{a_s} \frac{\partial Q_{\Theta 3}}{\partial \Theta} - \frac{1}{a_s} N_{\Theta\Theta}, \quad (\text{II.65c})$$

$$\frac{\rho_e h_s^3}{12} \frac{\partial^2 \beta_X}{\partial t^2} = \frac{\partial M_{XX}}{\partial X} + \frac{1}{a_s} \frac{\partial M_{X\Theta}}{\partial \Theta} - Q_{X3} + m_X, \quad (\text{II.65d})$$

$$\frac{\rho_e h_s^3}{12} \frac{\partial^2 \beta_\Theta}{\partial t^2} = \frac{\partial M_{X\Theta}}{\partial X} + \frac{1}{a_s} \frac{\partial M_{\Theta\Theta}}{\partial \Theta} - Q_{\Theta 3}, \quad (\text{II.65e})$$

where m_X refers to the applied bending moment density in the X direction.

In order to reformulate the above dynamical equations (II.65) under the port-Hamiltonian framework, we first define the flow and effort variables in a similar way as in [Brugnoli 19a]:

$$f_{M3} = \frac{\partial}{\partial t} \underbrace{\begin{pmatrix} \rho_e h_s \frac{\partial \mathbf{u}}{\partial t} \\ \rho_e h_s \frac{\partial w_3}{\partial t} \\ \frac{\rho_e h_s^3}{12} \frac{\partial \beta}{\partial t} \\ \bar{k} \\ \bar{A} \\ \gamma \end{pmatrix}}_{x_{M3}}, \quad e_{M3} = \begin{pmatrix} \frac{\partial \mathbf{u}}{\partial t} \\ \frac{\partial w_3}{\partial t} \\ \frac{\partial \beta}{\partial t} \\ \bar{M} \\ \bar{N} \\ \mathbf{Q} \end{pmatrix},$$

with vectors:

$$\mathbf{u} = \begin{pmatrix} u_{XX} \\ u_{\Theta\Theta} \end{pmatrix}, \quad \beta = \begin{pmatrix} \beta_X \\ \beta_\Theta \end{pmatrix}, \quad \gamma = \begin{pmatrix} \gamma_{X3} \\ \gamma_{\Theta 3} \end{pmatrix}, \quad \mathbf{Q} = \begin{pmatrix} Q_{X3} \\ Q_{\Theta 3} \end{pmatrix},$$

and second order symmetric tensors:

$$\begin{aligned}
 \bar{k} &= \begin{pmatrix} k_{XX} & k_{X\Theta} \\ k_{\Theta X} & k_{\Theta\Theta} \end{pmatrix}, & \bar{A} &= \begin{pmatrix} \epsilon_{XX}^0 & \gamma_{X\Theta}^0 \\ \gamma_{\Theta X}^0 & \epsilon_{\Theta\Theta}^0 \end{pmatrix}, \\
 \bar{M} &= \begin{pmatrix} M_{XX} & M_{X\Theta} \\ M_{\Theta X} & M_{\Theta\Theta} \end{pmatrix}, & \bar{N} &= \begin{pmatrix} N_{XX} & N_{X\Theta} \\ N_{\Theta X} & N_{\Theta\Theta} \end{pmatrix}.
 \end{aligned}$$

The linear relation between the effort variables e_{M3} and the energy variables x_{M3} writes:

$$e_{M3} = \begin{pmatrix} \frac{1}{\rho_e h_s} & 0 & 0 & 0 & 0 & 0 \\ 0 & \frac{1}{\rho_e h_s} & 0 & 0 & 0 & 0 \\ 0 & 0 & \frac{12}{\rho_e h_s^3} & 0 & 0 & 0 \\ 0 & 0 & 0 & \overline{\overline{\overline{C^M}}} & 0 & 0 \\ 0 & 0 & 0 & 0 & \overline{\overline{\overline{C^N}}} & 0 \\ 0 & 0 & 0 & 0 & 0 & k' G_e h_s \end{pmatrix} x_{M3},$$

where the 4th order tensors $\overline{\overline{\overline{C^M}}}$, and $\overline{\overline{\overline{C^N}}}$ are composed of:

$$\begin{aligned} C_{XXXX}^M &= C_{\Theta\Theta\Theta\Theta}^M = D_e, & C_{XX\Theta\Theta}^M &= C_{\Theta\Theta XX}^M = D_e v_s, \\ C_{X\Theta X\Theta}^M &= C_{\Theta X \Theta X}^M = D_e \frac{1-v_s}{2}, & C_{XXXX}^N &= C_{\Theta\Theta\Theta\Theta}^N = K_e, \\ C_{XX\Theta\Theta}^N &= C_{\Theta\Theta XX}^N = K_e v_s, & C_{X\Theta X\Theta}^N &= C_{\Theta X \Theta X}^N = K_e \frac{1-v_s}{2}, \end{aligned}$$

and the rest of the components are equal to zero. The double dot operation $\overline{\overline{\overline{A}}} = \overline{\overline{\overline{C}}} : \overline{\overline{\overline{B}}}$ is computed as follows:

$$A_{ij} = C_{ijpq} B_{pq}, \text{ with } i, j, p, q = \{X, \Theta\}.$$

Hence, (II.65) is reformulated into a PHS in a 2D cylindrical domain $\Omega = [0, L_e] \times [0, 2\pi]$ as:

$$f_{M3} = \mathcal{J}_{M3} e_{M3} + B_{M3} m_X, \quad (\text{II.66})$$

where

$$\mathcal{J}_{M3} = \begin{pmatrix} 0 & 0 & 0 & 0 & Div & \begin{pmatrix} 0 & 0 \\ 0 & \frac{1}{a_s} \end{pmatrix} \\ 0 & 0 & 0 & 0 & -\begin{pmatrix} 0 & 0 \\ 0 & \frac{1}{a_s} \end{pmatrix} & div \\ 0 & 0 & 0 & Div & 0 & -1 \\ 0 & 0 & Grad & 0 & 0 & 0 \\ Grad & \begin{pmatrix} 0 & 0 \\ 0 & \frac{1}{a_s} \end{pmatrix} & 0 & 0 & 0 & 0 \\ -\begin{pmatrix} 0 & 0 \\ 0 & \frac{1}{a_s} \end{pmatrix} & grad & 1 & 0 & 0 & 0 \end{pmatrix}, \quad B_{M3} = \begin{pmatrix} \mathbf{0} \\ 0 \\ \begin{pmatrix} 1 \\ 0 \end{pmatrix} \\ \overline{\overline{\overline{0}}} \\ \overline{\overline{\overline{0}}} \\ \mathbf{0} \end{pmatrix},$$

where $\overline{\overline{\overline{0}}}$ is a 2nd order tensor of zero, the vector $\mathbf{0} = (0 \ 0)^T$. *Div* and *div* represent the divergence operators for tensors and for vectors, respectively. *Grad* and *grad* denote the gradient operators for vectors and for scalars, respectively.

The Hamiltonian of the 2D shell model yields:

$$H_M = \frac{1}{2} \int_{\Omega} \left(\rho_e h_s \frac{\partial \mathbf{u}}{\partial t} \cdot \frac{\partial \mathbf{u}}{\partial t} + \rho_e h_s \left(\frac{\partial w_3}{\partial t} \right)^2 + \frac{\rho_e h_s^3}{12} \frac{\partial \boldsymbol{\beta}}{\partial t} \cdot \frac{\partial \boldsymbol{\beta}}{\partial t} \right. \\ \left. \bar{k} : \bar{M} + \bar{A} : \bar{N} + \boldsymbol{\gamma} \cdot \mathbf{Q} \right) d\Omega. \quad (\text{II.67})$$

For an autonomous system, the time derivative of the Hamiltonian (II.67) is formulated as:

$$\frac{dH_M}{dt} = \int_{\Omega} \left(e_{M3}^T f_{M3} \right) d\Omega \\ = \int_{\Omega} \left(\frac{\partial \mathbf{u}}{\partial t} \left(\text{Div}(\bar{N}) \right) + \frac{\partial w_3}{\partial t} \left(\text{div}(\mathbf{Q}) \right) + \frac{\partial \boldsymbol{\beta}}{\partial t} \left(\text{Div}(\bar{M}) \right) + \bar{M} : \left(\text{Grad} \left(\frac{\partial \boldsymbol{\beta}}{\partial t} \right) \right) \right. \\ \left. + \bar{N} : \left(\text{Grad} \left(\frac{\partial \mathbf{u}}{\partial t} \right) \right) + \mathbf{Q} \left(\text{grad} \left(\frac{\partial w_3}{\partial t} \right) \right) \right) d\Omega \\ = \int_{\Omega} \left(\text{div} \left(\frac{\partial W}{\partial t} \mathbf{Q} \right) + \text{Div} \left(\bar{N} \cdot \frac{\partial \mathbf{u}}{\partial t} \right) + \text{Div} \left(\bar{M} \cdot \frac{\partial \boldsymbol{\beta}}{\partial t} \right) \right) d\Omega, \quad (\text{II.68})$$

with $\partial\Omega = (0, \Theta) \cup (L_e, \Theta)$ boundaries of the domain Ω .

Here we recall the Green Gauss's theorem:

$$\int_{\Omega} \text{div}(\mathbf{a}) d\Omega = \int_{\partial\Omega} \mathbf{a} \cdot \mathbf{n} ds, \quad (\text{II.69a}) \\ \int_{\Omega} \text{Div}(\bar{c} \cdot \mathbf{b}) d\Omega = \int_{\partial\Omega} (\bar{c} \cdot \mathbf{b}) \cdot \mathbf{n} ds \\ = \int_{\partial\Omega} (\bar{c} : (\mathbf{b} \otimes \mathbf{n})) ds \\ = \int_{\partial\Omega} (\bar{c} : [(b_n \cdot \mathbf{n} + b_s \cdot \mathbf{s}) \otimes \mathbf{n}]) ds \\ = \int_{\partial\Omega} (\bar{c} : (b_n \mathbf{n} \otimes \mathbf{n} + b_s \mathbf{s} \otimes \mathbf{n})) ds \\ = \int_{\partial\Omega} (b_n \bar{c} : (\mathbf{n} \otimes \mathbf{n}) + b_s \bar{c} : (\mathbf{s} \otimes \mathbf{n})) ds, \quad (\text{II.69b})$$

where \mathbf{n} and \mathbf{s} are the normal and tangent unit vectors with respect to the boundary $\partial\Omega$, and b_n and b_s denote the normal and tangent projections of the vector \mathbf{b} . The tensor product operation $\bar{A} = \mathbf{a} \otimes \mathbf{b}$ is formulated as:

$$A_{ij} = a_i b_j, \text{ with } i, j = \{X, \Theta\}.$$

Substituting (II.69) into (II.68), one gets:

$$\frac{dH_M}{dt} = \int_{\partial\Omega} \left(\frac{\partial w_3}{\partial t} (\mathbf{Q} \cdot \mathbf{n}) + \left(\frac{\partial \mathbf{u}}{\partial t} \cdot \mathbf{n} \right) (\bar{N} : (\mathbf{n} \otimes \mathbf{n})) + \left(\frac{\partial \mathbf{u}}{\partial t} \cdot \mathbf{s} \right) (\bar{N} : (\mathbf{s} \otimes \mathbf{n})) \right. \\ \left. + \left(\frac{\partial \boldsymbol{\beta}}{\partial t} \cdot \mathbf{n} \right) (\bar{M} : (\mathbf{n} \otimes \mathbf{n})) + \left(\frac{\partial \boldsymbol{\beta}}{\partial t} \cdot \mathbf{s} \right) (\bar{M} : (\mathbf{s} \otimes \mathbf{n})) \right) ds. \quad (\text{II.70})$$

Since the shell is closed and in cylindrical coordinates, we take $\mathbf{n} = \begin{pmatrix} 1 \\ 0 \end{pmatrix}$, and $\mathbf{s} = \begin{pmatrix} 0 \\ 1 \end{pmatrix}$. Therefore, one has:

$$\begin{aligned} \frac{\partial \mathbf{u}}{\partial t} \cdot \mathbf{n} &= \frac{\partial u_{XX}}{\partial t}, & \frac{\partial \mathbf{u}}{\partial t} \cdot \mathbf{s} &= \frac{\partial u_{\Theta\Theta}}{\partial t}, & \frac{\partial \boldsymbol{\beta}}{\partial t} \cdot \mathbf{n} &= \frac{\partial \beta_X}{\partial t}, \\ \frac{\partial \boldsymbol{\beta}}{\partial t} \cdot \mathbf{s} &= \frac{\partial \beta_\Theta}{\partial t}, & \mathbf{Q} \cdot \mathbf{n} &= Q_{X3}, & \mathbf{N} : (\mathbf{n} \otimes \mathbf{n}) &= N_{XX}, \\ \mathbf{N} : (\mathbf{s} \otimes \mathbf{n}) &= N_{X\Theta}, & \mathbf{M} : (\mathbf{n} \otimes \mathbf{n}) &= M_{XX}, & \mathbf{M} : (\mathbf{s} \otimes \mathbf{n}) &= M_{X\Theta}. \end{aligned} \quad (\text{II.71})$$

Applying (II.71) into the time derivative of the Hamiltonian (II.70), we obtain the boundary port variables:

$$f_\partial = \begin{pmatrix} \frac{\partial w_3}{\partial t} \\ \frac{\partial u_{XX}}{\partial t} \\ \frac{\partial u_{\Theta\Theta}}{\partial t} \\ \frac{\partial \beta_X}{\partial t} \\ \frac{\partial \beta_\Theta}{\partial t} \end{pmatrix} (0/L_e, \Theta), \quad e_\partial = \begin{pmatrix} Q_{X3} \\ N_{XX} \\ N_{X\Theta} \\ M_{XX} \\ M_{X\Theta} \end{pmatrix} (0/L_e, \Theta).$$

Remark 8. The 2D shell model (II.65) reduces to the Timoshenko beam model (II.28) when

$$\begin{aligned} u_{XX} = 0, \quad u_{\Theta\Theta} = 0, \quad \beta_\Theta = 0, \quad N_{XX} = 0, \quad N_{X\Theta} = 0, \quad N_{\Theta\Theta} = 0, \\ M_{X\Theta} = 0, \quad Q_{\Theta 3} = 0, \quad \text{and} \quad \frac{\partial(\cdot)}{\partial \Theta} = 0. \end{aligned}$$

On the other hand, (II.65) could be extended to the out-of-plane equations of the rectangular Mindlin plate [Soedel 82] with

$$\frac{1}{a_s} \frac{\partial}{\partial \theta} = \frac{\partial}{\partial y}, \quad \frac{1}{a_s} = 0, \quad \text{and} \quad \beta_\Theta = \beta_y.$$

The shell model (II.66) is interconnected with the electrical and electro-stress diffusion systems of the IPMC using the Lagrange multiplier $\lambda_{\mathbf{L}}$ accounting for the mechanical structure, leading to:

$$\begin{pmatrix} f_I \\ f_{M3} \end{pmatrix} = \begin{pmatrix} \mathcal{J}_I & \mathcal{J}_{inter3} \\ -\mathcal{J}_{inter3}^* & \mathcal{J}_{M3} \end{pmatrix} \begin{pmatrix} e_I \\ e_{M3} \end{pmatrix} + \begin{pmatrix} A_{Lu} \\ A_{L3} \end{pmatrix} \lambda_{\mathbf{L}},$$

with f_I , e_I , \mathcal{J}_I , A_{Lu} the same as formulated in (II.51) and (II.52), and

$$\mathcal{J}_{inter3} = \begin{pmatrix} 0 & 0 & 0 & 0 & 0 & 0 \\ 0 & 0 & 0 & 0 & 0 & 0 \\ 0 & 0 & (-\mathbb{1}_Z B_a b_M & 0) & 0 & 0 \\ 0 & 0 & 0 & 0 & 0 & 0 \end{pmatrix}, \quad A_{L3} = B_{M3} B_p b_M,$$

with b_M defined in (II.53).

II.5 SUMMARY

In this chapter, we first model the IPMC actuator under the infinite dimensional port-Hamiltonian framework. The multiscale coupling between the electrical, electro-stress diffusion and mechanical models inside the IPMC actuator is figured out. The Lagrange multiplier is used to deal with the mechanical constraints arising from the interconnection of the gel and the mechanical deformation of the actuator. Different from the model proposed in [Nishida 08, Nishida 11], where the bending moments are locally generated and are seen as modifications of the mechanical properties of the beam, we take the bending moments generated in the gel as external distributed inputs to the mechanical system, which can avoid singularities for homogeneous deformation. A list of differences with the model of [Nishida 08, Nishida 11] is illustrated in Table II.1. The global system

Table II.1 – Differences between our model with the model of *Nishida et al.*

	Model of <i>Nishida et al.</i>	Our model
Coupling through M_{x2}	Implicit causality	Explicit causality with the proposition of Lagrange multiplier as formulated in (II.38) and (II.39)
Input to the mechanical subsystem	Internal bending moment	Distributed external bending moment density $\frac{M_o}{L_o}$

is associated with a Stokes-Dirac structure, stemming from the expression of energy balances. This model will be further discretized in order to carry out the simulation in Chapter III.

Secondly, we have modeled the entire structure of the endoscope with the IPMC actuator. The deformation of the IPMC actuator is assumed to be the same as the endoscope, and is formulated by different mechanical models, *i.e.* the Timoshenko beam model for small deformation case, the infinite dimensional inertial frame beam model for large deformation case and the elastic thin shell model under cylindrical coordinates for 2D case. The interconnection between the endoscope and the IPMC actuator is simplified to be the interconnection between the electro-stress diffusion system in the gel and the mechanical system, which is also accomplished with the help of the Lagrange multipliers.

Chapter III

Numerical and experimental results

III.1	Structure preserving discretization methods	66
III.1.1	The mixed finite element approach	67
III.1.2	The finite difference method on staggered grids	77
III.1.3	Comparison of the mixed finite element method and the finite difference method on staggered grids	79
III.2	Application to the discretization of the IPMC actuator . .	81
III.2.1	Discretization of electric system	81
III.2.2	Discretization of electro-stress diffusion system	83
III.2.3	Discretization of the mechanical system	85
III.2.4	Descriptor form of the discretized global system	86
III.2.5	Elimination of the Lagrange multiplier	87
III.2.6	Simulation results and experimental validation	89
III.3	Summary	94

III.1 STRUCTURE PRESERVING DISCRETIZATION METHODS

The infinite dimensional PHS defined in Chapter II needs to be discretized in order to carry out the following simulation and control implementation. The discretization should be structure preserving in order to keep the Dirac structure and herein to guarantee the duality of discretized flow and effort variables and to realize the interconnections of discretized subsystems. In what follows, we focus on the structure preserving spatial discretization of the infinite dimensional PHS. For the time integration, we shall use the structure preserving implicit mid-point approach [Aoues 13] (explained afterwards in Appendix C), which is a special case of the Gauss-Legendre collocation studied in [Kotyczka 18a]. Traditional spatial discretization methods, like finite element, finite difference or finite volume, need to be modified in order to keep the intrinsic power conserving Dirac structure and to preserve the passivity of the original system, generating a finite dimensional PHS.

Golo *et al.* firstly proposed the mixed finite element methodology in [Golo 02]. The ‘mixed’ lies in the dual/mixed approximations of flow and effort variables on different geometric spaces (see the definition in Appendix B). Meanwhile, these variables are approximated by two parts which are only dependent on the time and on the space, respectively. The spatial dependent part is later approximated with k -form functions (named basis functions, see the definition in Appendix B) on sub-intervals according to their geometric spaces. After spatial integration of these basis functions, the dynamics of the system is divided into numerous sub-dynamics that interconnects through their boundaries. This mixed finite element method is suitable for both 1D hyperbolic systems like transmission line [Golo 04], and for parabolic systems like adsorption processes [Baaiu 09], as well as for 2D wave propagation in [Liu 20]. It was later generalized in [Moulla 12], with the use of pseudo-spectral formulations and higher order polynomial approximations on the whole space domain. Although it possesses good spectral properties, the pseudo-spectral approximation may cause Runge’s phenomenon when dealing with large intervals [Voss 10], where the approximations of the middle points in an interval are good but of the boundary points are worse.

These above mentioned approximation methodologies are based on the discretization of the solution, named strong form. On the other hand, partitioned finite element method [Cardoso-Ribeiro 18, Brugnoli 19a, Brugnoli 19b] and mixed Galerkin discretization [Kotyczka 18b] are investigated on the principle of weak form, which approximates the weak solution of PDEs.

The mixed finite volume method [Kotyczka 16] and finite difference method on staggered grids [Trenchant 18b] have been investigated most recently. The latter approach approximates the spatial derivatives through a Taylor series expansion and can be applied to both 1D and 2D hyperbolic [Trenchant 18b] and parabolic systems [Trenchant 18a] due to its simplicity. It is reported in [Kotyczka 18b] that

the finite difference method on staggered grids can be viewed as a special case of the mixed Galerkin method when the flow mapping parameter is chosen to be zero.

In the following of this chapter, we concentrate on the mixed finite element method and on the finite difference method on staggered grids, as these two approaches are easy to implement in our application cases. Brief introductions of these two methods will be explained with the example of a 1D vibrating string formulated in (I.34) at page 20, and then the finite difference method on staggered grids will be applied to the discretization of the IPMC actuator model given in (II.43) at page 47 because of its simplicity.

III.1.1 The mixed finite element approach

To apply the mixed finite element approximation, we reformulate the infinite dimensional PHS (I.34) at page 20 using differential forms, and approximate the effort and flow variables with appropriate k -forms.

III.1.1.a A reminder on mixed finite element approach

Formulations in differential forms Given $\Omega^1(\zeta)$ the space of one-form, the energy variables in (I.33) (i.e. the transversal strain $x_1(\zeta, t) \in \Omega^1$ and the momentum $x_2(\zeta, t) \in \Omega^1$) are represented in one-form densities as:

$$x_1(\zeta, t) = \frac{\partial \omega}{\partial \zeta} d\zeta, \quad x_2(\zeta, t) = \rho \frac{\partial \omega}{\partial t} d\zeta. \quad (\text{III.1})$$

Flow variables $f_1(\zeta, t) \in \Omega^1$ and $f_2(\zeta, t) \in \Omega^1$ are the time derivative of $x_1(\zeta, t)$ and $x_2(\zeta, t)$, formulated by:

$$f_1(\zeta, t) = \frac{\partial^2 \omega}{\partial t \partial \zeta} d\zeta, \quad f_2(\zeta, t) = \rho \frac{\partial^2 \omega}{\partial t^2} d\zeta. \quad (\text{III.2})$$

The Hamiltonian H in (I.37) at page 21 is reformulated by:

$$H = \frac{1}{2} \int_{\zeta} x_1 \wedge (T(*x_1)) + x_2 \wedge \left(\frac{*x_2}{\rho} \right), \quad (\text{III.3})$$

with \wedge denoting the wedge product that maps the product of Ω^k and Ω^l to Ω^{k+l} , and $*$ representing the Hodge star that maps the one-form state variables in $\Omega^1(\zeta)$ to zero-form effort functions in $\Omega^0(\zeta)$.

Effort variables $e_1(\zeta, t) \in \Omega^0(\zeta)$ and $e_2(\zeta, t) \in \Omega^0(\zeta)$ are zero-form functions that derived from the Hamiltonian (III.3):

$$e_1(\zeta, t) = \delta_{x_1} H = T(*x_1(\zeta, t)), \quad e_2(\zeta, t) = \delta_{x_2} H = \frac{1}{\rho} (*x_2(\zeta, t)), \quad (\text{III.4})$$

As a result, (I.34) at page 20 is reformulated in the differential forms as:

$$\begin{pmatrix} f_1(\zeta, t) \\ f_2(\zeta, t) \end{pmatrix} = \begin{pmatrix} 0 & d \\ d & 0 \end{pmatrix} \begin{pmatrix} e_1(\zeta, t) \\ e_2(\zeta, t) \end{pmatrix}, \quad (\text{III.5})$$

with boundary port variables (I.36) at page 21, where d stands for the exterior derivative that defined in Definition 6 in Appendix B at page 129.

Approximation of the Dirac structure The vibrating string are firstly discretized into several elements. In an interval of $[a, b]$, the 1-form energy variables and flow variables are approximated as:

$$x_1(\zeta, t) = x_1^{ab}(t)w_1^{ab}(\zeta), \quad (\text{III.6a})$$

$$x_2(\zeta, t) = x_2^{ab}(t)w_2^{ab}(\zeta), \quad (\text{III.6b})$$

$$f_1(\zeta, t) = f_1^{ab}(t)w_1^{ab}(\zeta), \quad (\text{III.6c})$$

$$f_2(\zeta, t) = f_2^{ab}(t)w_2^{ab}(\zeta), \quad (\text{III.6d})$$

and 0-form effort variables are approximated as:

$$e_1(\zeta, t) = e_1^a(t)w_1^a(\zeta) + e_1^b(t)w_1^b(\zeta), \quad (\text{III.7a})$$

$$e_2(\zeta, t) = e_2^a(t)w_2^a(\zeta) + e_2^b(t)w_2^b(\zeta), \quad (\text{III.7b})$$

where the 1-form $w_i^{ab}(\zeta)$ ($i = \{1, 2\}$) and 0-form $w_i^a(\zeta)$ and $w_i^b(\zeta)$ satisfy the following conditions:

$$\int_{\mathcal{L}_{ab}} w_i^{ab} = 1, \quad w_i^a(a) = 1, \quad w_i^a(b) = 0, \quad w_i^b(a) = 0, \quad w_i^b(b) = 1, \quad (\text{III.8})$$

with $\mathcal{L}_{ab} = b - a$ the element length.

These conditions state that the flow variables $f_1(\zeta, t)$ and $f_2(\zeta, t)$ coincide with the time dependent variables f_1^{ab} and f_2^{ab} after the integration over the interval $[a, b]$, and the effort variables $e_1(\zeta, t)$ and $e_2(\zeta, t)$ coincide with the time dependent variables $e_1^a, e_1^b, e_2^a, e_2^b$ on the two extremities a and b of the interval.

Substituting (III.6c) - (III.7) into (III.5), one gets:

$$f_1^{ab}(t)w_1^{ab}(\zeta) = e_2^a(t)dw_2^a(\zeta) + e_2^b(t)dw_2^b(\zeta), \quad (\text{III.9a})$$

$$f_2^{ab}(t)w_2^{ab}(\zeta) = e_1^a(t)dw_1^a(\zeta) + e_1^b(t)dw_1^b(\zeta). \quad (\text{III.9b})$$

Now we need to find relations between the approximated 1-form flow variables and 0-form effort variables such that (III.9) validates at all times, which is called the **compatibility**.

For equation (III.9a), if $e_2^a(t) = 0$, one gets:

$$w_1^{ab}(\zeta) = dw_2^b(\zeta). \quad (\text{III.10})$$

If $e_2^b(t) = 0$, one obtains:

$$w_1^{ab}(\zeta) = -dw_2^a(\zeta). \quad (\text{III.11})$$

Similarly, from equation (III.9b), we have:

$$w_2^{ab}(\zeta) = dw_1^b(\zeta), \quad (\text{III.12a})$$

$$w_2^{ab}(\zeta) = -dw_2^a(\zeta). \quad (\text{III.12b})$$

The aforesaid equations (III.10) - (III.12) give rise to the following compatibility equations¹:

$$\int_{\mathcal{L}_{ab}} w_1^{ab} \wedge w_1^a + \int_{\mathcal{L}_{ab}} w_1^{ab} \wedge w_1^b = 1, \quad (\text{III.13a})$$

$$\int_{\mathcal{L}_{ab}} w_2^{ab} \wedge w_2^a + \int_{\mathcal{L}_{ab}} w_2^{ab} \wedge w_2^b = 1, \quad (\text{III.13b})$$

$$\int_{\mathcal{L}_{ab}} w_1^{ab} \wedge w_1^a + \int_{\mathcal{L}_{ab}} w_2^{ab} \wedge w_2^a = 1, \quad (\text{III.13c})$$

Afterwards, with the integration, (III.9) yields:

$$f_1^{ab}(t) = -e_2^a(t) + e_2^b(t), \quad (\text{III.14a})$$

$$f_2^{ab}(t) = -e_1^a(t) + e_1^b(t), \quad (\text{III.14b})$$

With the obtained compatibility equations (III.13a) - (III.13c), the net power of element ab is:

$$\begin{aligned} P_{ab}(t) &= \sum_{i=1}^2 \int_{\mathcal{L}_{ab}} f_i(\zeta, t) \wedge e_i(\zeta, t) + f^B(t)e^B(t), \\ &= f_1^{ab}(t) \left(e_1^a(t) \int_{\mathcal{L}_{ab}} w_1^{ab} \wedge w_1^a + e_1^b(t) \int_{\mathcal{L}_{ab}} w_1^{ab} \wedge w_1^b \right) \\ &\quad + f_2^{ab}(t) \left(e_2^a(t) \int_{\mathcal{L}_{ab}} w_2^{ab} \wedge w_2^a + e_2^b(t) \int_{\mathcal{L}_{ab}} w_2^{ab} \wedge w_2^b \right) + f^B(t)e^B(t) \\ &= f_1^{ab}(t) \left(\beta_{ab}e_1^a(t) + (1 - \beta_{ab})e_1^b(t) \right) + f_2^{ab}(t) \left((1 - \beta_{ab})e_2^a(t) + \beta_{ab}e_2^b(t) \right) \\ &\quad + f^B(t)e^B(t), \end{aligned} \quad (\text{III.15})$$

where $\beta_{ab} = \int_{\mathcal{L}_{ab}} w_1^{ab} \wedge w_1^a$ refers to the effort mapping parameter, $f^B e^B = f^{Ba}(t)e^{Ba}(t) - f^{Bb}(t)e^{Bb}(t)$, with

$$f^B(t) = \begin{pmatrix} f^{Ba}(t) \\ f^{Bb}(t) \end{pmatrix} = \begin{pmatrix} e_1^a(t) \\ e_2^b(t) \end{pmatrix}, \quad e^B(t) = \begin{pmatrix} e^{Ba}(t) \\ -e^{Bb}(t) \end{pmatrix} = \begin{pmatrix} e_2^a(t) \\ -e_1^b(t) \end{pmatrix}.$$

Equation (III.15) leads to the definition of the only time-dependent effort variables of element ab as:

$$e_1^{ab}(t) = \beta_{ab}e_1^a(t) + \beta'_{ab}e_1^b(t), \quad (\text{III.16a})$$

$$e_2^{ab}(t) = \beta'_{ab}e_2^a(t) + \beta_{ab}e_2^b(t), \quad (\text{III.16b})$$

with $\beta'_{ab} = 1 - \beta_{ab}$.

Proposition 2. *One can then define a Dirac structure in the discretized element ab :*

1. For the sake of compactness, the parameter ζ is omitted in the rest of this part.

$$\underbrace{\begin{pmatrix} 1 & 0 & 0 & -1 \\ 0 & 1 & 1 & 0 \\ 0 & 0 & -\beta_{ab} & 0 \\ 0 & 0 & 0 & -\beta_{ab} \end{pmatrix}}_{F_{ab}} \begin{pmatrix} f_1^{ab}(t) \\ f_2^{ab}(t) \\ e_1^a(t) \\ e_2^b(t) \end{pmatrix} + \underbrace{\begin{pmatrix} 0 & 0 & 1 & 0 \\ 0 & 0 & 0 & 1 \\ 1 & 0 & 0 & \beta'_{ab} \\ 0 & 1 & -\beta'_{ab} & 0 \end{pmatrix}}_{E_{ab}} \begin{pmatrix} e_1^{ab}(t) \\ e_2^{ab}(t) \\ e_2^a(t) \\ -e_1^b(t) \end{pmatrix} = 0, \quad (\text{III.17})$$

Proof. $E_{ab}F_{ab}^T + F_{ab}E_{ab}^T = 0$, and $\text{rank}((F_{ab} \ E_{ab})) = 4$, which is the order of the discretized finite dimensional PHS. According to (I.5) at page 12, these two necessary conditions conclude that (III.17) is the kernel representation of the Dirac structure. \square

Explicit form for the Dirac structure According to the boundary port variables defined in (I.36) at page 21, and to the clamped-free boundary conditions, one defines the input and output of the element ab as follows:

$$u_{ab}(t) = W \begin{pmatrix} f^B(t) \\ e^B(t) \end{pmatrix} = \begin{pmatrix} e_1^b(t) \\ e_2^a(t) \end{pmatrix}, \quad y_{ab}(t) = \tilde{W} \begin{pmatrix} f^B(t) \\ e^B(t) \end{pmatrix} = \begin{pmatrix} e_2^b(t) \\ -e_1^a(t) \end{pmatrix}, \quad (\text{III.18})$$

with $W = \begin{pmatrix} 0 & 0 & 0 & -1 \\ 0 & 0 & 1 & 0 \end{pmatrix}$, $\tilde{W} = \begin{pmatrix} 0 & 1 & 0 & 0 \\ -1 & 0 & 0 & 0 \end{pmatrix}$, and $\begin{pmatrix} W \\ \tilde{W} \end{pmatrix}$ invertible.

Hence, the Dirac structure (III.17) can be reformulated in an explicit form as:

$$\begin{pmatrix} \dot{x}_1^{ab}(t) \\ \dot{x}_2^{ab}(t) \end{pmatrix} = \begin{pmatrix} 0 & \frac{1}{\beta_{ab}} \\ -\frac{1}{\beta_{ab}} & 0 \end{pmatrix} \begin{pmatrix} e_1^{ab}(t) \\ e_2^{ab}(t) \end{pmatrix} + \begin{pmatrix} 0 & -\frac{1}{\beta_{ab}} \\ \frac{1}{\beta_{ab}} & 0 \end{pmatrix} \begin{pmatrix} e_1^b(t) \\ e_2^a(t) \end{pmatrix}, \quad (\text{III.19a})$$

$$\begin{pmatrix} e_2^b(t) \\ -e_1^a(t) \end{pmatrix} = \begin{pmatrix} 0 & \frac{1}{\beta_{ab}} \\ -\frac{1}{\beta_{ab}} & 0 \end{pmatrix} \begin{pmatrix} e_1^{ab}(t) \\ e_2^{ab}(t) \end{pmatrix} + \begin{pmatrix} 0 & -\frac{\beta'_{ab}}{\beta_{ab}} \\ \frac{\beta'_{ab}}{\beta_{ab}} & 0 \end{pmatrix} \begin{pmatrix} e_1^b(t) \\ e_2^a(t) \end{pmatrix}, \quad (\text{III.19b})$$

Interconnection of adjacent elements The idea is to connect each adjacent element together with the power preserving interconnection relationships. The schema is depicted in Fig.III.1, where j_{ab} represents the j th element of length (b_a) ($j \in \{1, \dots, n\}$). Same as (III.19), we write the PHS of two adjacent elements j_{ab}

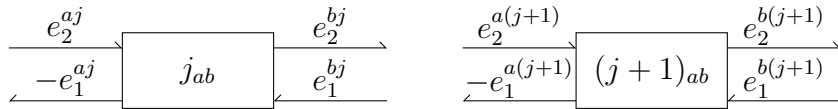


Figure III.1 – Interconnection of adjacent elements.

and $(j+1)_{ab}$ as:

$$\begin{pmatrix} \dot{x}_1^j(t) \\ \dot{x}_2^j(t) \end{pmatrix} = \begin{pmatrix} 0 & \frac{1}{\beta_{ab}} \\ -\frac{1}{\beta_{ab}} & 0 \end{pmatrix} \begin{pmatrix} e_1^j(t) \\ e_2^j(t) \end{pmatrix} + \begin{pmatrix} 0 & -\frac{1}{\beta_{ab}} \\ \frac{1}{\beta_{ab}} & 0 \end{pmatrix} \begin{pmatrix} e_1^{bj}(t) \\ e_2^{aj}(t) \end{pmatrix}, \quad (\text{III.20a})$$

$$\begin{pmatrix} e_2^{bj}(t) \\ -e_1^{aj}(t) \end{pmatrix} = \begin{pmatrix} 0 & \frac{1}{\beta_{ab}} \\ -\frac{1}{\beta_{ab}} & 0 \end{pmatrix} \begin{pmatrix} e_1^j(t) \\ e_2^j(t) \end{pmatrix} + \begin{pmatrix} 0 & -\frac{\beta'_{ab}}{\beta_{ab}} \\ \frac{\beta'_{ab}}{\beta_{ab}} & 0 \end{pmatrix} \begin{pmatrix} e_1^{bj}(t) \\ e_2^{aj}(t) \end{pmatrix}, \quad (\text{III.20b})$$

$$\begin{pmatrix} \dot{x}_1^{j+1}(t) \\ \dot{x}_2^{j+1}(t) \end{pmatrix} = \begin{pmatrix} 0 & \frac{1}{\beta_{ab}} \\ -\frac{1}{\beta_{ab}} & 0 \end{pmatrix} \begin{pmatrix} e_1^{j+1}(t) \\ e_2^{j+1}(t) \end{pmatrix} + \begin{pmatrix} 0 & -\frac{1}{\beta_{ab}} \\ \frac{1}{\beta_{ab}} & 0 \end{pmatrix} \begin{pmatrix} e_1^{b(j+1)}(t) \\ e_2^{a(j+1)}(t) \end{pmatrix}, \quad (\text{III.20c})$$

$$\begin{pmatrix} e_2^{b(j+1)}(t) \\ -e_1^{a(j+1)}(t) \end{pmatrix} = \begin{pmatrix} 0 & \frac{1}{\beta_{ab}} \\ -\frac{1}{\beta_{ab}} & 0 \end{pmatrix} \begin{pmatrix} e_1^{j+1}(t) \\ e_2^{j+1}(t) \end{pmatrix} + \begin{pmatrix} 0 & -\frac{\beta'_{ab}}{\beta_{ab}} \\ \frac{\beta'_{ab}}{\beta_{ab}} & 0 \end{pmatrix} \begin{pmatrix} e_1^{b(j+1)}(t) \\ e_2^{a(j+1)}(t) \end{pmatrix}. \quad (\text{III.20d})$$

The input and output relations between i_{ab} and $(i+1)_{ab}$ are given as:

$$e_1^{bi}(t) = e_1^{a(i+1)}(t), \quad e_2^{bi}(t) = e_2^{a(i+1)}(t). \quad (\text{III.21})$$

Substituting (III.21) into (III.20), one obtains:

$$\begin{pmatrix} \dot{x}_1^j(t) \\ \dot{x}_1^{j+1}(t) \\ \dot{x}_2^j(t) \\ \dot{x}_2^{j+1}(t) \end{pmatrix} = \begin{pmatrix} 0 & 0 & \frac{1}{\beta_{ab}} & 0 \\ 0 & 0 & -\frac{1}{\beta_{ab}^2} & \frac{1}{\beta_{ab}} \\ -\frac{1}{\beta_{ab}} & \frac{1}{\beta_{ab}^2} & 0 & 0 \\ 0 & -\frac{1}{\beta_{ab}} & 0 & 0 \end{pmatrix} \begin{pmatrix} e_1^j(t) \\ e_1^{j+1}(t) \\ e_2^j(t) \\ e_2^{j+1}(t) \end{pmatrix} + \begin{pmatrix} -\frac{1}{\beta_{ab}} & 0 \\ \frac{\beta'_{ab}}{\beta_{ab}^2} & 0 \\ 0 & -\frac{\beta'_{ab}}{\beta_{ab}^2} \\ 0 & \frac{1}{\beta_{ab}} \end{pmatrix} \begin{pmatrix} e_2^{aj}(t) \\ e_1^{b(j+1)}(t) \end{pmatrix}, \quad (\text{III.22a})$$

$$\begin{pmatrix} -e_1^{aj}(t) \\ e_2^{bj+1}(t) \end{pmatrix} = \begin{pmatrix} -\frac{1}{\beta_{ab}} & \frac{\beta'_{ab}}{\beta_{ab}^2} & 0 & 0 \\ 0 & 0 & -\frac{\beta'_{ab}}{\beta_{ab}^2} & \frac{1}{\beta_{ab}} \end{pmatrix} \begin{pmatrix} e_1^j(t) \\ e_1^{j+1}(t) \\ e_2^j(t) \\ e_2^{j+1}(t) \end{pmatrix} + \begin{pmatrix} 0 & -\frac{\beta'^2_{ab}}{\beta_{ab}^2} \\ \frac{\beta'^2_{ab}}{\beta_{ab}^2} & 0 \end{pmatrix} \begin{pmatrix} e_2^{aj}(t) \\ e_1^{b(j+1)}(t) \end{pmatrix}. \quad (\text{III.22b})$$

Consequently, the discretized finite dimensional representation of (III.5) at page 67 with n elements yields:

$$\begin{pmatrix} \dot{x}_{1d}(t) \\ \dot{x}_{2d}(t) \end{pmatrix} = \begin{pmatrix} 0 & J_1 \\ -J_1^T & 0 \end{pmatrix} \begin{pmatrix} e_{1d}(t) \\ e_{2d}(t) \end{pmatrix} + \underbrace{\begin{pmatrix} b_1 & 0 \\ 0 & b_2 \end{pmatrix}}_{B_b} \begin{pmatrix} e_2(0, t) \\ e_1(L, t) \end{pmatrix}, \quad (\text{III.23a})$$

$$\begin{pmatrix} -e_1(0, t) \\ e_2(L, t) \end{pmatrix} = \begin{pmatrix} b_1^T & 0 \\ 0 & b_2^T \end{pmatrix} \begin{pmatrix} e_{1d}(t) \\ e_{2d}(t) \end{pmatrix} + \underbrace{\begin{pmatrix} 0 & (-1)^{n-1} \left(\frac{\beta'_{ab}}{\beta_{ab}}\right)^n \\ (-1)^n \left(\frac{\beta'_{ab}}{\beta_{ab}}\right)^n & 0 \end{pmatrix}}_{D_b} \begin{pmatrix} e_2(0, t) \\ e_1(L, t) \end{pmatrix}, \quad (\text{III.23b})$$

with

$$x_{id}(t) = \begin{pmatrix} x_i^1(t) \\ \vdots \\ x_i^n(t) \end{pmatrix}, \quad e_{id}(t) = \begin{pmatrix} e_i^1(t) \\ \vdots \\ e_i^n(t) \end{pmatrix}, \quad i = \{1, 2\}, \quad b_1 = \begin{pmatrix} -\frac{1}{\beta_{ab}} \\ \frac{\beta'_{ab}}{\beta_{ab}^2} \\ \frac{\beta'_{ab}}{\beta_{ab}^2} \\ \vdots \\ (-1)^n \frac{(\beta'_{ab})^{n-1}}{\beta_{ab}^n} \end{pmatrix}, \quad (\text{III.23c})$$

III.1.1.b Extension to system with dissipation and distributed input

In this part, we want to generalize the mixed finite element method to the system with dissipation and with distributed in-domain control. We take always the vibrating string for example, but here we add the dissipation, which is assumed to be proportional to the transversal velocity, together with the distributed force density. The dynamic equation is formulated as:

$$\frac{\partial^2 \omega}{\partial t^2}(\zeta, t) = \frac{T}{\rho} \frac{\partial^2 \omega}{\partial \zeta^2}(\zeta, t) - R \frac{\partial \omega}{\partial t}(\zeta, t) + u_d(\zeta, t), \quad (\text{III.30})$$

where R is related to the dissipation, and $u_d(\zeta, t)$ denotes the applied force density. Thus, the port-Hamiltonian formulation of the vibrating string in (I.34) at page 20 is modified to:

$$\begin{pmatrix} f_1(\zeta, t) \\ f_2(\zeta, t) \end{pmatrix} = \begin{pmatrix} 0 & \frac{\partial}{\partial \zeta} \\ \frac{\partial}{\partial \zeta} & -R \end{pmatrix} \begin{pmatrix} e_1(\zeta, t) \\ e_2(\zeta, t) \end{pmatrix} + \begin{pmatrix} 0 \\ 1 \end{pmatrix} u_d(\zeta, t), \quad (\text{III.31a})$$

$$y_d(\zeta, t) = \begin{pmatrix} 0 & 1 \end{pmatrix} \begin{pmatrix} e_1(\zeta, t) \\ e_2(\zeta, t) \end{pmatrix}, \quad (\text{III.31b})$$

where $y_d(\zeta, t)$ stands for the velocity which is the power conjugated variable of the distributed input $u_d(\zeta, t)$.

To better express (III.31) in the form of power conservation, we open the dissipation ports and the distributed input-output ports, and reformulate (III.31) into:

$$\begin{pmatrix} f_1(\zeta, t) \\ f_2(\zeta, t) \\ y_R(\zeta, t) \\ -y_d(\zeta, t) \end{pmatrix} = \begin{pmatrix} 0 & \frac{\partial}{\partial \zeta} & 0 & 0 \\ \frac{\partial}{\partial \zeta} & 0 & -1 & 1 \\ 0 & 1 & 0 & 0 \\ 0 & -1 & 0 & 0 \end{pmatrix} \begin{pmatrix} e_1(\zeta, t) \\ e_2(\zeta, t) \\ u_R(\zeta, t) \\ u_d(\zeta, t) \end{pmatrix}, \quad (\text{III.32})$$

with additional closure equation:

$$y_R(\zeta, t) = \frac{1}{R} u_R(\zeta, t).$$

The differential form of (III.32) is given by:

$$\begin{pmatrix} f_1(\zeta, t) \\ f_2(\zeta, t) \\ y_R(\zeta, t) \\ -y_d(\zeta, t) \end{pmatrix} = \begin{pmatrix} 0 & d & 0 & 0 \\ d & 0 & -1 & 1 \\ 0 & 1 & 0 & 0 \\ 0 & -1 & 0 & 0 \end{pmatrix} \begin{pmatrix} e_1(\zeta, t) \\ e_2(\zeta, t) \\ u_R(\zeta, t) \\ u_d(\zeta, t) \end{pmatrix}, \quad (\text{III.33})$$

with the closure equation represented by the differential form as:

$$y_R(\zeta, t) = \frac{1}{R} (*u_R(\zeta, t)). \quad (\text{III.34})$$

The 1-forms $x_1(\zeta, t)$, $x_2(\zeta, t)$, $f_1(\zeta, t)$ and $f_2(\zeta, t)$ are already defined in (III.1) at page 67 and approximated in (III.6) at page 68. The 0-forms $e_1(\zeta, t)$ and $e_2(\zeta, t)$ are defined in (III.4) and approximated in (III.7). Moreover, we have another 1-forms $u_R(\zeta, t)$, and $u_d(\zeta, t)$ and 0-forms $y_R(\zeta, t)$ and $y_d(\zeta, t)$ defined by:

$$\begin{aligned} u_R(\zeta, t) &= R \frac{\partial \omega}{\partial t}(\zeta, t) d\zeta, & u_d(\zeta, t) &= f_u(t) d\zeta, \\ y_R(\zeta, t) &= e_2(\zeta, t), & y_d(\zeta, t) &= e_2(\zeta, t), \end{aligned} \quad (\text{III.35})$$

with f_u the applied force density.

These 1-forms and 0-forms in (III.35) are later approximated as:

$$u_R(\zeta, t) = u_R^{ab}(t) w_R^{ab}(\zeta), \quad (\text{III.36a})$$

$$u_d(\zeta, t) = u_d^{ab}(t) w_d^{ab}(\zeta), \quad (\text{III.36b})$$

$$y_R(\zeta, t) = e_2(\zeta, t) = e_2^a(t) w_2^a(\zeta) + e_2^b(t) w_2^b(\zeta), \quad (\text{III.36c})$$

$$y_d(\zeta, t) = e_2(\zeta, t) = e_2^a(t) w_2^a(\zeta) + e_2^b(t) w_2^b(\zeta). \quad (\text{III.36d})$$

By integrating (III.36b), one gets:

$$u_d^{ab}(t) = (b - a) f_u(t). \quad (\text{III.37})$$

Substituting the approximation equations (III.6), (III.7), and (III.36) into (III.33), one obtains:

$$f_1^{ab}(t) w_1^{ab}(\zeta) = e_2^a(t) dw_2^a(\zeta) + e_2^b(t) dw_2^b(\zeta), \quad (\text{III.38a})$$

$$f_2^{ab}(t) w_2^{ab}(\zeta) = e_1^a(t) dw_1^a(\zeta) + e_1^b(t) dw_1^b(\zeta) - u_R^{ab}(t) w_R^{ab}(\zeta) + u_d^{ab}(t) w_d^{ab}(\zeta). \quad (\text{III.38b})$$

The **compatibility** equations are the same as that in (III.10)-(III.13c). Furthermore, for (III.38b), if $e_1^a(t) = 0$, $e_1^b(t) = 0$, and $u_d^{ab}(t) = 0$ one gets:

$$c_1 w_2^{ab}(\zeta) = -w_R^{ab}(\zeta). \quad (\text{III.39})$$

By integration of (III.39), one has $c_1 = -1$, which gives the additional **compatibility** equation:

$$w_2^{ab}(\zeta) = w_R^{ab}(\zeta). \quad (\text{III.40})$$

Similarly, if $e_1^a(t) = 0$, $e_1^b(t) = 0$, and $u_R^{ab}(t) = 0$, (III.38b) yields the **compatibility** equation:

$$w_2^{ab}(\zeta) = w_d^{ab}(\zeta). \quad (\text{III.41})$$

Integrating (III.38), one gets:

$$f_1^{ab}(t) = -e_2^a(t) + e_2^b(t), \quad (\text{III.42a})$$

$$f_2^{ab}(t) = -e_1^a(t) + e_1^b(t) - u_R^{ab}(t) + u_d^{ab}(t). \quad (\text{III.42b})$$

The net power of the element ab is expressed as²:

$$\begin{aligned}
 P_{ab}(t) &= \int_{\mathcal{L}_{ab}} (f_1(\zeta, t) \wedge e_1(\zeta, t) + f_2(\zeta, t) \wedge e_2(\zeta, t) - u_R(\zeta, t) \wedge y_R(\zeta, t) \\
 &\quad + u_d(\zeta, t) \wedge y_d(\zeta, t)) \\
 &= f_1^{ab}(t) \left(e_1^a(t) \int_{\mathcal{L}_{ab}} w_1^{ab} \wedge w_1^a + e_1^b(t) \int_{\mathcal{L}_{ab}} w_1^{ab} \wedge w_1^b \right) \\
 &\quad + f_2^{ab}(t) \left(e_2^a(t) \int_{\mathcal{L}_{ab}} w_2^{ab} \wedge w_2^a + e_2^b(t) \int_{\mathcal{L}_{ab}} w_2^{ab} \wedge w_2^b \right) \\
 &\quad - u_R^{ab}(t) \left(e_2^a(t) \int_{\mathcal{L}_{ab}} w_R^{ab} \wedge w_2^a + e_2^b(t) \int_{\mathcal{L}_{ab}} w_R^{ab} \wedge w_2^b \right) \\
 &\quad - u_d^{ab}(t) \left(e_2^a(t) \int_{\mathcal{L}_{ab}} w_d^{ab} \wedge w_2^a + e_2^b(t) \int_{\mathcal{L}_{ab}} w_d^{ab} \wedge w_2^b \right).
 \end{aligned} \tag{III.43}$$

According to the compatibility equations (III.40) and (III.41),

$$\begin{aligned}
 \int_{\mathcal{L}_{ab}} w_R^{ab} \wedge w_2^a &= \int_{\mathcal{L}_{ab}} w_2^{ab} \wedge w_2^a = 1 - \beta_{ab}, \\
 \int_{\mathcal{L}_{ab}} w_R^{ab} \wedge w_2^b &= \int_{\mathcal{L}_{ab}} w_2^{ab} \wedge w_2^b = \beta_{ab}, \\
 \int_{\mathcal{L}_{ab}} w_d^{ab} \wedge w_2^a &= \int_{\mathcal{L}_{ab}} w_2^{ab} \wedge w_2^a = 1 - \beta_{ab}, \\
 \int_{\mathcal{L}_{ab}} w_d^{ab} \wedge w_2^b &= \int_{\mathcal{L}_{ab}} w_2^{ab} \wedge w_2^b = \beta_{ab}.
 \end{aligned}$$

Therefore,

$$y_R^{ab}(t) = (1 - \beta_{ab}) e_2^a(t) + \beta_{ab} e_2^b(t) = e_2^{ab}(t), \tag{III.44a}$$

$$y_d^{ab}(t) = (1 - \beta_{ab}) e_2^a(t) + \beta_{ab} e_2^b(t) = e_2^{ab}(t). \tag{III.44b}$$

Proposition 3. From equations (III.42), (III.16a), (III.16b), and (III.44), one can create a Dirac structure:

$$\begin{aligned}
 &\underbrace{\begin{pmatrix} -1 & 0 & 0 & 0 & 0 & 1 \\ 0 & -1 & -1 & 1 & -1 & 0 \\ 0 & 0 & 0 & 0 & \beta_{ab} & 0 \\ 0 & 0 & 0 & 0 & 0 & \beta_{ab} \\ 0 & 0 & 0 & 0 & 0 & \beta_{ab} \\ 0 & 0 & 0 & 0 & 0 & \beta_{ab} \end{pmatrix}}_{F_{ab}} \begin{pmatrix} f_1^{ab}(t) \\ f_2^{ab}(t) \\ u_R^{ab}(t) \\ u_d^{ab}(t) \\ e_1^a(t) \\ e_2^b(t) \end{pmatrix} \\
 &+ \underbrace{\begin{pmatrix} 0 & 0 & 0 & 0 & -1 & 0 \\ 0 & 0 & 0 & 0 & 0 & -1 \\ -1 & 0 & 0 & 0 & 0 & -(1 - \beta_{ab}) \\ 0 & -1 & 0 & 0 & 1 - \beta_{ab} & 0 \\ 0 & 0 & -1 & 0 & 1 - \beta_{ab} & 0 \\ 0 & 0 & 0 & 1 & 1 - \beta_{ab} & 0 \end{pmatrix}}_{E_{ab}} \begin{pmatrix} e_1^{ab}(t) \\ e_2^{ab}(t) \\ y_R^{ab}(t) \\ -y_d^{ab}(t) \\ e_2^a(t) \\ -e_1^b(t) \end{pmatrix} = 0.
 \end{aligned} \tag{III.45}$$

2. For the sake of compactness, the parameter ζ is omitted in the rest of this part.

Proof. $E_{ab}F_{ab}^T + F_{ab}E_{ab}^T = 0$, and $\text{rank}\left(\begin{pmatrix} F_{ab} & E_{ab} \end{pmatrix}\right) = 6$, which is the order of the extended finite dimensional PHS with the dissipation ports and distributed input-output ports open. According to (I.5) at page 12, these two necessary conditions conclude that (III.45) is the kernel representation of the Dirac structure. \square

With the same boundary input and output as defined in (III.18), the Dirac structure (III.45) can be expressed in the explicit form:

$$\begin{pmatrix} f_1^{ab}(t) \\ f_2^{ab}(t) \\ y_R^{ab}(t) \\ -y_d^{ab}(t) \end{pmatrix} = \begin{pmatrix} 0 & \frac{1}{\beta_{ab}} & 0 & 0 \\ -\frac{1}{\beta_{ab}} & 0 & -1 & 1 \\ 0 & 1 & 0 & 0 \\ 0 & -1 & 0 & 0 \end{pmatrix} \begin{pmatrix} e_1^{ab}(t) \\ e_2^{ab}(t) \\ u_R^{ab}(t) \\ u_d^{ab}(t) \end{pmatrix} + \begin{pmatrix} 0 & -\frac{1}{\beta_{ab}} \\ \frac{1}{\beta_{ab}} & 0 \\ 0 & 0 \\ 0 & 0 \end{pmatrix} \begin{pmatrix} e_1^b(t) \\ e_2^a(t) \end{pmatrix}, \quad (\text{III.46a})$$

$$\begin{pmatrix} e_2^b(t) \\ -e_1^a(t) \end{pmatrix} = \begin{pmatrix} 0 & \frac{1}{\beta_{ab}} & 0 & 0 \\ -\frac{1}{\beta_{ab}} & 0 & 0 & 0 \end{pmatrix} \begin{pmatrix} e_1^{ab}(t) \\ e_2^{ab}(t) \end{pmatrix} + \begin{pmatrix} 0 & -\frac{\beta'_{ab}}{\beta_{ab}} \\ \frac{\beta'_{ab}}{\beta_{ab}} & 0 \end{pmatrix} \begin{pmatrix} e_1^b(t) \\ e_2^a(t) \end{pmatrix}. \quad (\text{III.46b})$$

To eliminate u_R^{ab} and y_R^{ab} in (III.46), we substitute the closure equation (III.34) into the dissipation power of one element ab :

$$\begin{aligned} P_{Rab} &= \int_{\mathcal{L}_{ab}} u_R(\zeta, t) \wedge y_R(\zeta, t) \\ &= \int_{\mathcal{L}_{ab}} u_R(\zeta, t) \wedge \left(\frac{1}{R} (*u_R(\zeta, t)) \right) \\ &= \frac{(u_R^{ab}(t))^2}{R} \int_{\mathcal{L}_{ab}} w_R^{ab}(t) \wedge (*w_R^{ab}(t)) \\ &= u_R^{ab} e_R^{ab}. \end{aligned}$$

Therefore,

$$u_R^{ab}(t) = R_{ab} e_R^{ab}(t) = R_{ab} e_2^{ab}(t), \quad (\text{III.47})$$

with

$$R_{ab} = \frac{R}{\int_{\mathcal{L}_{ab}} w_R^{ab}(t) \wedge (*w_R^{ab}(t))}. \quad (\text{III.48})$$

Substituting (III.47) into (III.46), one obtains the simplified explicit form of the Dirac structure with dissipation and with distributed input for the element ab as follows:

$$\begin{pmatrix} f_1^{ab}(t) \\ f_2^{ab}(t) \end{pmatrix} = \begin{pmatrix} 0 & \frac{1}{\beta_{ab}} \\ -\frac{1}{\beta_{ab}} & -R_{ab} \end{pmatrix} \begin{pmatrix} e_1^{ab}(t) \\ e_2^{ab}(t) \end{pmatrix} + \begin{pmatrix} 0 & -\frac{1}{\beta_{ab}} \\ \frac{1}{\beta_{ab}} & 0 \end{pmatrix} \begin{pmatrix} e_1^b(t) \\ e_2^a(t) \end{pmatrix} + \begin{pmatrix} 0 \\ 1 \end{pmatrix} u_d^{ab}(t),$$

$$\begin{pmatrix} e_2^b(t) \\ -e_1^a(t) \end{pmatrix} = \begin{pmatrix} 0 & \frac{1}{\beta_{ab}} \\ -\frac{1}{\beta_{ab}} & 0 \end{pmatrix} \begin{pmatrix} e_1^{ab}(t) \\ e_2^{ab}(t) \end{pmatrix} + \begin{pmatrix} 0 & -\frac{\beta'_{ab}}{\beta_{ab}} \\ \frac{\beta'_{ab}}{\beta_{ab}} & 0 \end{pmatrix} \begin{pmatrix} e_1^b(t) \\ e_2^a(t) \end{pmatrix},$$

$$y_d^{ab}(t) = \begin{pmatrix} 0 & 1 \end{pmatrix} \begin{pmatrix} e_1^{ab}(t) \\ e_2^{ab}(t) \end{pmatrix},$$

where $u_d^{ab}(t)$ is defined in (III.37), and R_{ab} is defined in (III.48).

Similar as what we have done in Subsection III.1.1.a to interconnect the adjacent elements through their inputs and outputs, at last, the structure preserving discretization of (III.31) yields:

$$\begin{pmatrix} \dot{x}_{1d}(t) \\ \dot{x}_{2d}(t) \end{pmatrix} = \left(\begin{pmatrix} 0 & J_1 \\ -J_1^T & 0 \end{pmatrix} - \begin{pmatrix} 0 & 0 \\ 0 & R_d \end{pmatrix} \right) \begin{pmatrix} e_{1d}(t) \\ e_{2d}(t) \end{pmatrix} + B_b \begin{pmatrix} e_2(0, t) \\ e_1(L, t) \end{pmatrix} + \underbrace{\begin{pmatrix} 0 \\ I \end{pmatrix}}_{B_d} \mathbf{u}_d(t), \quad (\text{III.49a})$$

$$\begin{pmatrix} -e_1(0, t) \\ e_2(L, t) \end{pmatrix} = B_b^T \begin{pmatrix} e_{1d}(t) \\ e_{2d}(t) \end{pmatrix} + D_b \begin{pmatrix} e_2(0, t) \\ e_1(L, t) \end{pmatrix}, \quad (\text{III.49b})$$

$$\mathbf{y}_d(t) = B_d^T \begin{pmatrix} e_{1d}(t) \\ e_{2d}(t) \end{pmatrix}, \quad (\text{III.49c})$$

with x_{id} , e_{id} , $i = \{1, 2\}$, J_1 , B_b , and D_b the same as in (III.23) at page 71,

$$e_{1d} = T_d x_{1d}, \quad e_{2d} = \frac{1}{\rho_d} x_{2d}, \quad (\text{III.50a})$$

$$T_d = \begin{pmatrix} T_{ab} & & \\ & \ddots & \\ & & T_{ab} \end{pmatrix}, \quad \frac{1}{\rho_d} = \begin{pmatrix} \frac{1}{\rho_{ab}} & & \\ & \ddots & \\ & & \frac{1}{\rho_{ab}} \end{pmatrix}, \quad (\text{III.50b})$$

$$R_d = \begin{pmatrix} R_{ab} & & \\ & \ddots & \\ & & R_{ab} \end{pmatrix}, \quad \text{and } \mathbf{u}_d(t) = (b - a) \begin{pmatrix} f_u^1(t) \\ \vdots \\ f_u^n(t) \end{pmatrix}, \quad (\text{III.50c})$$

where T_{ab} and ρ_{ab} are defined in (III.29) at page 72, and if we choose the same shape function of w_R^{ab} as in (III.28), then $R_{ab} = R(b - a)$.

Remark 9. *The distributed input in (III.31) and (III.49) is a fully-actuated case, where each element is applied with an independent input. We will discuss the case where we can not actuate the string independently in Chapter IV.*

III.1.2 The finite difference method on staggered grids

Different from the mixed finite element method, which mainly focuses on the approximation of the solutions, here the finite difference method on staggered grids deals directly with the approximation of equations [Villadsen 78, Baaiu 09], using the Taylor series expansion to approximate the space derivative $\frac{\partial}{\partial \zeta}$ [Trenchant 18b]. The principle of this approach is to place different pairs of power conjugated variables with a step distance, which makes the operator $\frac{\partial}{\partial \zeta}$ be discretized into the difference of two adjacent values over their step distance.

We take the same example of a vibrating string with dissipation and distributed input which is formulated in (III.31) at page 73, with clamped-free boundary conditions. The boundary variables $e_2(0, t)$ and $e_1(L, t)$ are placed at two ends of the string, as depicted in Fig. III.2.



Figure III.2 – Schema of the finite difference method on staggered grids.

To implement the Taylor series approximations, the effort variables $e_1(\zeta, t)$ and $e_2(\zeta, t)$ are not placed at the same position. In fact, they have a distance of $h/2$ for every element (h stands for the length of each element), as is shown in Fig. III.3 (divided with n elements, $L = (n + \frac{1}{2})h$):

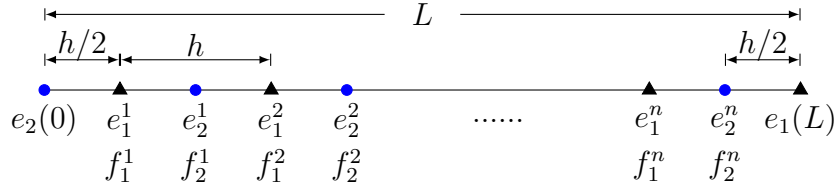


Figure III.3 – The finite difference method on staggered grids for clamped-free vibrating string.

As a result, equation (III.31a) is discretized as follows:

$$\begin{aligned} f_1^1(t) &= \frac{e_2^1(t) - e_2(0, t)}{h}, & f_2^1(t) &= \frac{e_1^2(t) - e_1^1(t)}{h} - Re_2^1(t) + u_d^1(t), \\ f_1^2(t) &= \frac{e_2^2(t) - e_2^1(t)}{h}, & f_2^2(t) &= \frac{e_1^3(t) - e_1^2(t)}{h} - Re_2^2(t) + u_d^2(t), \\ &\vdots & &\vdots \\ f_1^n(t) &= \frac{e_2^n(t) - e_2^{n-1}(t)}{h}, & f_2^n(t) &= \frac{e_1(L, t) - e_1^n(t)}{h} - Re_2^n(t) + u_d^n(t). \end{aligned}$$

And one obtains the approximation of (III.31) at page 73 as follows:

$$\begin{pmatrix} \dot{x}_{1d}(t) \\ \dot{x}_{2d}(t) \end{pmatrix} = \begin{pmatrix} 0 & J_2 \\ -J_2^T & -R_{d2} \end{pmatrix} \begin{pmatrix} e_{1d}(t) \\ e_{2d}(t) \end{pmatrix} + \begin{pmatrix} g_1 \\ g_2 \end{pmatrix} \begin{pmatrix} e_2(0, t) \\ e_1(L, t) \end{pmatrix} + \begin{pmatrix} 0 \\ I \end{pmatrix} u_d(t), \quad (\text{III.51a})$$

$$y_d(t) = \begin{pmatrix} 0 & I \end{pmatrix} \begin{pmatrix} e_{1d}(t) \\ e_{2d}(t) \end{pmatrix}, \quad (\text{III.51b})$$

with

$$J_2 = \begin{pmatrix} \frac{1}{h} & & & \\ -\frac{1}{h} & \frac{1}{h} & & \\ & \ddots & \ddots & \\ & & -\frac{1}{h} & \frac{1}{h} \end{pmatrix}, \quad R_{d2} = \begin{pmatrix} R & & \\ & \ddots & \\ & & R \end{pmatrix}, \quad \begin{pmatrix} e_{1d}(t) \\ e_{2d}(t) \end{pmatrix} = \begin{pmatrix} T x_{1d}(t) \\ \frac{1}{\rho} x_{2d}(t) \end{pmatrix},$$

$$g_1 = \begin{pmatrix} -\frac{1}{h} & 0 \\ 0 & 0 \\ \vdots & \vdots \\ 0 & 0 \end{pmatrix}, \quad g_2 = \begin{pmatrix} 0 & 0 \\ \vdots & \vdots \\ 0 & 0 \\ 0 & \frac{1}{h} \end{pmatrix}, \quad u_d(t) = \begin{pmatrix} u_d^1(t) \\ \vdots \\ u_d^n(t) \end{pmatrix} = \begin{pmatrix} f_u^1(t) \\ \vdots \\ f_u^n(t) \end{pmatrix}.$$

III.1.3 Comparison of the mixed finite element method and the finite difference method on staggered grids

Based on the computations of the mixed finite element method and the finite difference method on staggered grids, it is obvious to find that the latter is much easier in terms of calculations. Here we would like to investigate the effectiveness of these two approaches. The simulation is carried out with a clamped free vibrating string with dissipation, whose length $L = 2\text{m}$, modulus of elasticity $T = 1.4 \times 10^6\text{N}$, density $\rho = 1.225\text{kg/m}$, dissipation parameter $R = 10^6\text{kg}/(\text{ms})$, and initial conditions are zero. A distributed force density $f_u = 10^6\text{N/m}$ is applied along the vibrating string. The vibrating string is approximated by $n = 10, 50$ and 100 elements, with the two aforementioned different discretization methods. The simulation results of the endpoint position with the two discretization approaches are presented in Fig. III.4a and Fig. III.5a, respectively. Simulation results of the Hamiltonian with these two discretization methods are illustrated in Fig. III.4b and Fig. III.5b, respectively. One can notice from these comparisons that, the simulation results with the mixed finite element methods can have a more precise solution with only 50 element, whereas the finite difference method on staggered grids needs 100 or even greater elements.

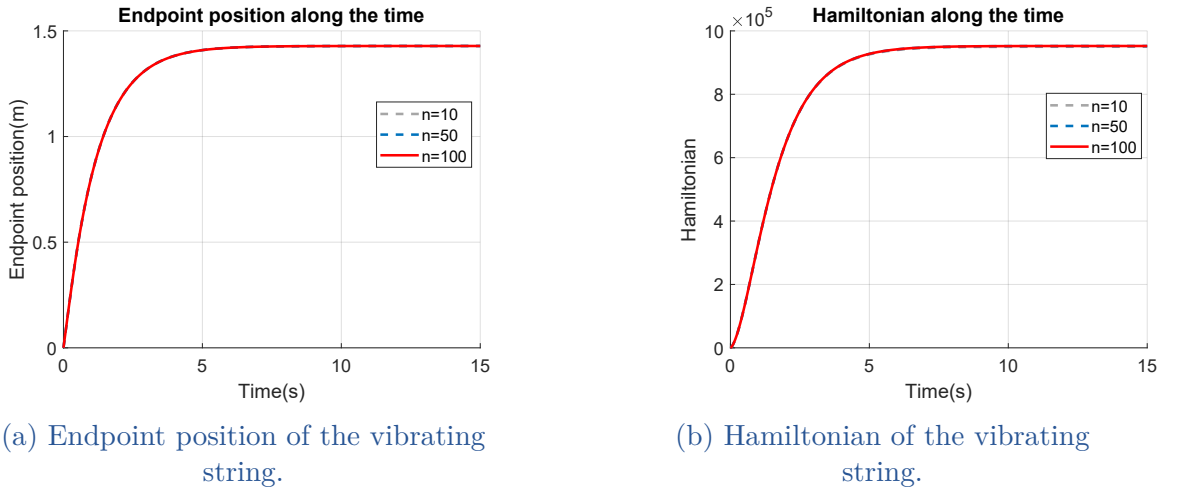
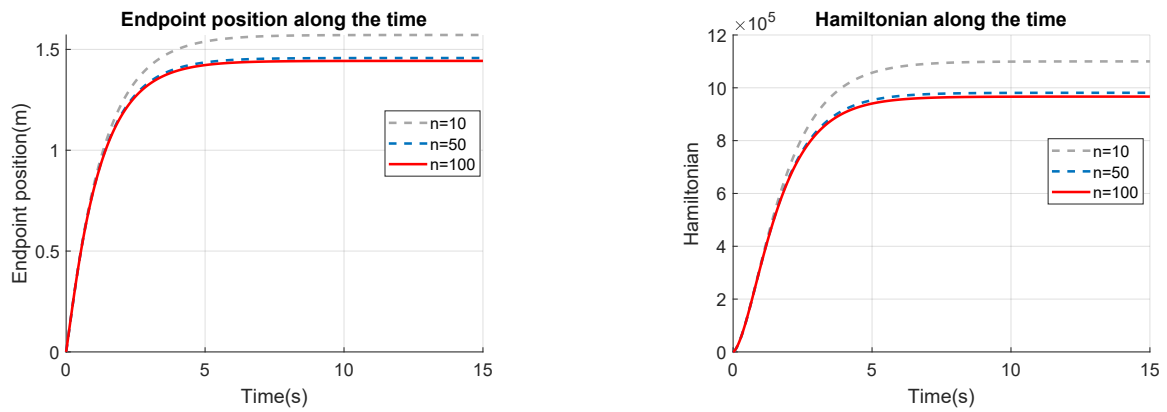


Figure III.4 – Simulation results of the vibrating string, with the approximation method of mixed finite element.

Given the analytic solution of $T \frac{\partial^2 \omega}{\partial \zeta^2} = f_u$ with clamped-free boundary conditions as:

$$\omega(L) = \frac{f_u L^2}{2T} = 1.4286\text{m}, \quad (\text{III.52})$$

we compare the error of the endpoint displacement at equilibrium between the approximated solution and the analytic one (III.52) with these two discretization approaches, and the results are depicted in Fig. III.6. This error analysis is consistent with our simulation results depicted in Fig. III.4 and Fig. III.5. As a result,



(a) Endpoint position of the vibrating string.

(b) Hamiltonian of the vibrating string.

Figure III.5 – Simulation results of the vibrating string, with the approximation method of finite difference on staggered grids.

we conclude that the finite difference method on staggered grids has the advantage of calculation simplicity, on the other hand, the mixed finite element method can approximate the analytic solution with very less discretization numbers.

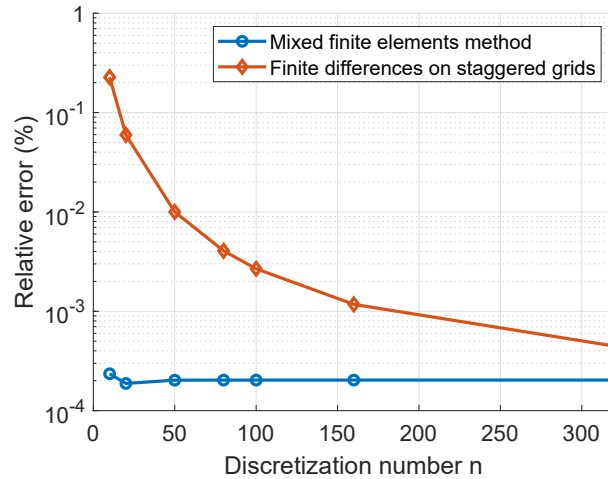


Figure III.6 – Relative approximation error of the mixed finite element method and of the finite difference method on staggered grids with different discretized number $n = 10, 20, 50, 80, 100, 160, 320$.

III.2 APPLICATION TO THE DISCRETIZATION OF THE IPMC ACTUATOR

After introducing the structure preserving discretization methods for the infinite dimensional PHS, we are going to apply them to our proposed model of the IPMC actuator (II.43) at page 47 in order to compare it with the experimental results and validate the model. Here we choose the finite difference method on staggered grids to approximate the multiscale IPMC actuator model as represented in (II.43) because of its simplicity. Under the fact of multiscale modeling, ξ and z are local coordinates with respect to the global coordinate x , which means that each point in x possesses one corresponding ξ and z . Hence, there are $N_e (= N_\xi \times N_b)$ elements for the electrical system, $N_g (= N_z \times N_b)$ elements for the electro-stress diffusion system, and N_b elements for the mechanical system, where N_ξ and N_z are discretization numbers along each ξ and z coordinates, respectively. It is assumed that the physical parameters, *i.e.* $R_1(\xi)$, $R_2(\xi)$, $C_2(\xi)$, \mathcal{R}_f , \mathcal{R}_g , G , E $A(x)$, and $I_o(x)$ are constant, so we will omit the coordinate variables of them.

III.2.1 Discretization of electric system

Before starting the discretization, (II.5) at page 33 has to be reformulated in order to handle its linear algebraic expression $e_1 = \frac{Q_e}{C_2} + R_2 \frac{\partial Q_e}{\partial t}$. Therefore, by defining $e_{1c} = \frac{Q_e}{C_2}$ and $e_{1R} = R_2 \frac{\partial Q_e}{\partial t} = R_2 f_1$, (II.5) is rewritten as:

$$\begin{pmatrix} f_1 \\ f_{r1} \\ f_1 \end{pmatrix} = \begin{pmatrix} 0 & \frac{\partial}{\partial \xi} & 0 \\ \frac{\partial}{\partial \xi} & 0 & \frac{\partial}{\partial \xi} \\ 0 & \frac{\partial}{\partial \xi} & 0 \end{pmatrix} \begin{pmatrix} e_{1c} \\ e_{r1} \\ e_{1R} \end{pmatrix}. \quad (\text{III.53})$$

The discretization scheme is shown in Fig. III.7, where $(f_1)_{1,j}$ represents the 1st element along ξ coordinate on the j^{th} element of x coordinate, with $j \in \{1, \dots, N_b\}$, and h_1 is the discretization step distance along the ξ direction.

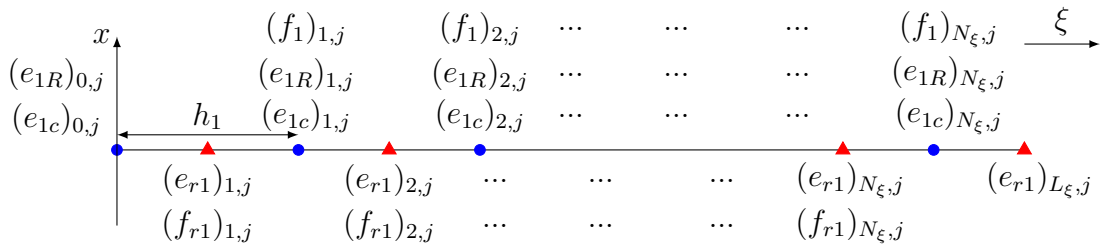


Figure III.7 – Discretization schema of the electrical system (III.53).

We take the discretization of $f_1 = \frac{\partial e_{r1}}{\partial \xi}$ for an example. According to the finite difference method on staggered grids presented in Subsection III.1.2, with the Taylor series expansion, one get:

$$\begin{aligned}
 (f_1)_{1,1} &= \frac{(e_{r1})_{2,1} - (e_{r1})_{1,1}}{h_1}, \\
 &\dots \\
 (f_1)_{1,N_b} &= \frac{(e_{r1})_{2,N_b} - (e_{r1})_{1,N_b}}{h_1}, \\
 &\dots \\
 (f_1)_{ii,j} &= \frac{(e_{r1})_{ii+1,j} - (e_{r1})_{ii,j}}{h_1}, \\
 &\dots \\
 (f_1)_{N_\xi,N_b} &= \frac{(e_{r1})_{L_\xi,N_b} - (e_{r1})_{N_\xi,N_b}}{h_1}.
 \end{aligned}$$

With the same approximation of f_{r1} , (III.53) is discretized into:

$$\begin{pmatrix} f_{1d} \\ f_{r1d} \\ f_{1d} \end{pmatrix} = \begin{pmatrix} \mathbf{0} & D_1 & \mathbf{0} \\ -D_1^T & \mathbf{0} & -D_1^T \\ \mathbf{0} & D_1 & \mathbf{0} \end{pmatrix} \begin{pmatrix} e_{1cd} \\ e_{r1d} \\ e_{1Rd} \end{pmatrix} + \begin{pmatrix} \mathbf{0} \\ g_1 \\ \mathbf{0} \end{pmatrix} e_{1b} + \begin{pmatrix} g_{11} \\ \mathbf{0} \\ g_{11} \end{pmatrix} e_{r1}(L_\xi), \quad (\text{III.54})$$

with

$$f_{id} = \begin{pmatrix} (f_i)_{1,1} \\ \vdots \\ (f_i)_{1,N_b} \\ \vdots \\ \vdots \\ (f_i)_{N_\xi,N_b} \end{pmatrix}, \quad e_{id} = \begin{pmatrix} (e_i)_{1,1} \\ \vdots \\ (e_i)_{1,N_b} \\ \vdots \\ \vdots \\ (e_i)_{N_\xi,N_b} \end{pmatrix}, \quad i = \{1, r1\}, \quad \iota = \{1c, r1, 1R\},$$

$$e_{1b} = \begin{pmatrix} (e_1)_{0,1} \\ \vdots \\ (e_1)_{0,N_b} \end{pmatrix} = \begin{pmatrix} V_1 + (V_c)_1 \\ \vdots \\ V_1 + (V_c)_{N_b} \end{pmatrix}, \quad D_1 = \begin{pmatrix} -\frac{1}{h_1} & \frac{1}{h_1} & & & \\ & \ddots & \ddots & & \\ & & \ddots & \ddots & \\ & & & \ddots & \frac{1}{h_1} \\ & & & & -\frac{1}{h_1} \end{pmatrix},$$

$$g_1 = \begin{pmatrix} -\frac{1}{h_1} \\ \mathbf{0} \\ \vdots \\ \mathbf{0} \end{pmatrix}, \quad g_{11} = \begin{pmatrix} \mathbf{0} \\ \vdots \\ \mathbf{0} \\ \frac{1}{h_1} \end{pmatrix}, \quad \mathbb{R}^{N_b \times N_b} \ni \frac{\mathbf{1}}{h_1} = \begin{pmatrix} \frac{1}{h_1} & & & \\ & \ddots & & \\ & & \ddots & \\ & & & \frac{1}{h_1} \end{pmatrix}$$

and $\mathbf{0}$ the zero matrix of appropriate size. Because of the boundary condition that $e_{r1}(L_\xi) = 0$, the part $(g_{11}^T \ \mathbf{0} \ g_{11}^T)^T e_{r1}(L_\xi)$ in (III.54) can be deleted from now on.

The closure equations $e_{r1} = \frac{f_{r1}}{R_1}$ and $e_{1R} = R_2 f_1$ are discretized into:

$$e_{r1d} = L_{r1} f_{r1d}, \quad (\text{III.55a})$$

$$e_{1Rd} = L_{r2} f_{1d}, \quad (\text{III.55b})$$

with $L_{r1} = \text{diag}(\frac{1}{R_1})$ and $L_{r2} = \text{diag}(R_2)$.

We discretize also the dynamic equation of f_1 and the constitutive equation of e_{1cd} :

$$f_{1d} = \dot{x}_{1d}, \quad (\text{III.56a})$$

$$e_{1cd} = L_{d1} x_{1d}, \quad (\text{III.56b})$$

with $L_{d1} = \text{diag}(\frac{1}{C_2})$.

Substituting (III.55) and (III.56) into (III.54), one obtains:

$$\begin{pmatrix} \dot{x}_{1d} \\ f_{r1d} \\ f_{1d} \end{pmatrix} = \begin{pmatrix} \mathbf{0} & D_1 & \mathbf{0} \\ -D_1^T & \mathbf{0} & -D_1^T \\ \mathbf{0} & D_1 & \mathbf{0} \end{pmatrix} \begin{pmatrix} L_{d1} & \mathbf{0} & \mathbf{0} \\ \mathbf{0} & L_{r1} & \mathbf{0} \\ \mathbf{0} & \mathbf{0} & L_{r2} \end{pmatrix} \begin{pmatrix} x_{1d} \\ f_{r1d} \\ f_{1d} \end{pmatrix} + \begin{pmatrix} \mathbf{0} \\ g_1 \\ \mathbf{0} \end{pmatrix} e_{1b}. \quad (\text{III.57})$$

The power conjugated output of this subsystem (III.57) is therefore the discretized current I_{ed} , which is formulated as:

$$I_{ed} = \begin{pmatrix} (I_e)_{11} \\ \vdots \\ (I_e)_{N_b} \end{pmatrix} = \begin{pmatrix} \mathbf{0} & g_1^T & \mathbf{0} \end{pmatrix} \begin{pmatrix} L_{d1} x_{1d} \\ L_{r1} f_{r1d} \\ L_{r2} f_{1d} \end{pmatrix} = g_1^T L_{r1} f_{r1d}. \quad (\text{III.58})$$

III.2.2 Discretization of electro-stress diffusion system

Recall equation (II.41) at page 46:

$$\begin{pmatrix} f_2 \\ f_{r2} \end{pmatrix} = \begin{pmatrix} \mathbf{0} & \partial_z \\ \partial_z & \mathbf{0} \end{pmatrix} \begin{pmatrix} e_2 \\ e_{r2} \end{pmatrix} + \begin{pmatrix} -\frac{B_a}{L_o} \mathbb{1}_z \frac{\partial \theta}{\partial t} \\ \mathbf{0} \end{pmatrix}.$$

According to the boundary condition (II.23) at page 38, we need to place the boundary variables $e_{r2}(\pm \frac{h_o}{2})$ at the extremities of each z coordinate, which is illustrated in Fig. III.8.

As a result, there are $N_z \times N_b$ elements for f_{2d} and e_{2d} , and $(N_z - 1) \times N_b$ elements for f_{r2d} and e_{r2d} . Equation (II.41) is herein discretized into:

$$\begin{pmatrix} f_{2d} \\ f_{r2d} \end{pmatrix} = \begin{pmatrix} \mathbf{0} & D_2 \\ -D_2^T & \mathbf{0} \end{pmatrix} \begin{pmatrix} e_{2d} \\ e_{r2d} \end{pmatrix} + \begin{pmatrix} D_{26} & g_2 \\ \mathbf{0} & \mathbf{0} \end{pmatrix} \begin{pmatrix} e_{6d} \\ e_{2b} \end{pmatrix}, \quad (\text{III.59})$$

$$e_{2d} = L_{d2}x_{2d}, \quad (\text{III.60b})$$

$$e_{r2d} = L_{r3}f_{r2d}, \quad (\text{III.60c})$$

with $L_{d2} = \text{diag}(\mathcal{R}_f)$ and $L_{r3} = \text{diag}(\mathcal{R}_g)$.

Substituting (III.60) into (III.59), and formulating e_{2b} explicitly with the coupling equation (II.35), one obtains:

$$\begin{pmatrix} \dot{x}_{2d} \\ f_{r2d} \end{pmatrix} = \begin{pmatrix} \mathbf{0} & D_2 \\ -D_2^T & \mathbf{0} \end{pmatrix} \begin{pmatrix} L_{d2} & \mathbf{0} \\ \mathbf{0} & L_{r3} \end{pmatrix} \begin{pmatrix} x_{2d} \\ f_{r2d} \end{pmatrix} + \begin{pmatrix} D_{26} \\ \mathbf{0} \end{pmatrix} e_{6d} + \begin{pmatrix} g_2 \\ \mathbf{0} \end{pmatrix} \left(\frac{\lambda}{\sigma_e L_o b_o} I_{ed} + \lambda_{\mathbf{L}d} \right). \quad (\text{III.61})$$

The power conjugated output voltage V_{cd} in terms of the input I_{ed} yields:

$$V_{cd} = \begin{pmatrix} (V_c)_1 \\ \vdots \\ (V_c)_{N_b} \end{pmatrix} = \frac{-\lambda}{\sigma_e L_o b} \begin{pmatrix} g_2^T & \mathbf{0} \end{pmatrix} \begin{pmatrix} L_{d2}x_{2d} \\ L_{r3}f_{r2d} \end{pmatrix} = \frac{-\lambda}{\sigma_e L_o b} g_2^T L_{d2}x_{2d}, \quad (\text{III.62})$$

which is consistent with the coupling equation (II.36).

III.2.3 Discretization of the mechanical system

We recall the equation of Timoshenko model formulated in (II.29):

$$\begin{pmatrix} f_3(x, t) \\ f_4(x, t) \\ f_5(x, t) \\ f_6(x, t) \end{pmatrix} = \begin{pmatrix} 0 & \frac{\partial}{\partial x} & 0 & -1 \\ \frac{\partial}{\partial x} & 0 & 0 & 0 \\ 0 & 0 & 0 & \frac{\partial}{\partial x} \\ 1 & 0 & \frac{\partial}{\partial x} & 0 \end{pmatrix} \begin{pmatrix} e_3(x, t) \\ e_4(x, t) \\ e_5(x, t) \\ e_6(x, t) \end{pmatrix} + \begin{pmatrix} 0 \\ 0 \\ 0 \\ 1 \end{pmatrix} m_{ext},$$

with $m_{ext} = \frac{M_o}{L_o} = \frac{\int_z B_a e_2 dz}{L_o} + \frac{B_p}{L_o} \lambda_{\mathbf{L}d}$. For a clamped-free cantilever beam, the discretization scheme is illustrated in Fig. III.9.

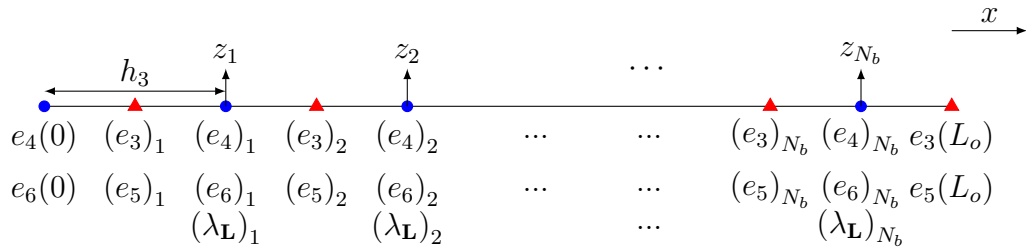


Figure III.9 – Discretization schema of the mechanical system (II.29).

Therefore, (II.29) is discretized into:

$$\begin{pmatrix} f_{3d} \\ f_{4d} \\ f_{5d} \\ f_{6d} \end{pmatrix} = \underbrace{\begin{pmatrix} \mathbf{0} & D_3 & \mathbf{0} & S_1 \\ -D_3^T & \mathbf{0} & \mathbf{0} & \mathbf{0} \\ \mathbf{0} & \mathbf{0} & \mathbf{0} & D_3 \\ -S_1^T & \mathbf{0} & -D_3^T & \mathbf{0} \end{pmatrix}}_{J_{md}} \begin{pmatrix} e_{3d} \\ e_{4d} \\ e_{5d} \\ e_{6d} \end{pmatrix} + \underbrace{\begin{pmatrix} \mathbf{0} \\ \mathbf{0} \\ \mathbf{0} \\ -D_{26}^T \end{pmatrix}}_{S_2} e_{2d} + \underbrace{\begin{pmatrix} \mathbf{0} \\ \mathbf{0} \\ \mathbf{0} \\ \text{diag}\left(\frac{B_p}{L_o}\right) \end{pmatrix}}_{S_\lambda} \lambda_{\mathbf{L}d}$$

$$+ \begin{pmatrix} g_3 & g_4 & \mathbf{0} & \mathbf{0} \\ \mathbf{0} & \mathbf{0} & g_5 & \mathbf{0} \\ \mathbf{0} & g_3 & \mathbf{0} & \mathbf{0} \\ \mathbf{0} & \mathbf{0} & g_6 & g_5 \end{pmatrix} \begin{pmatrix} e_4(0) \\ e_6(0) \\ e_3(L_o) \\ e_5(L_o) \end{pmatrix}, \quad (\text{III.63})$$

with $f_{id} = ((f_i)_1 \cdots (f_i)_{N_b})^T$, $e_{id} = ((e_i)_1 \cdots (e_i)_{N_b})^T$, $i = \{3, 4, 5, 6\}$, and:

$$D_3 = \begin{pmatrix} \frac{1}{h_3} & & & & & \\ -\frac{1}{h_3} & \ddots & & & & \\ & \ddots & \ddots & & & \\ & & \ddots & \ddots & & \\ & & & -\frac{1}{h_3} & \frac{1}{h_3} & \end{pmatrix}, \quad S_1 = \begin{pmatrix} -\frac{1}{2} & & & & & \\ -\frac{1}{2} & \ddots & & & & \\ & \ddots & \ddots & & & \\ & & \ddots & \ddots & & \\ & & & -\frac{1}{2} & -\frac{1}{2} & \end{pmatrix}, \quad g_3 = \begin{pmatrix} -\frac{1}{h_3} \\ 0 \\ \vdots \\ 0 \end{pmatrix},$$

$$g_4 = \begin{pmatrix} -\frac{1}{2} \\ 0 \\ \vdots \\ 0 \end{pmatrix}, \quad g_5 = \begin{pmatrix} 0 \\ \vdots \\ 0 \\ \frac{1}{h_3} \end{pmatrix}, \quad \text{and} \quad g_6 = \begin{pmatrix} 0 \\ \vdots \\ 0 \\ \frac{1}{2} \end{pmatrix}.$$

Because of the clamped-free boundary conditions, $e_3(L_o) = e_4(0) = e_5(L_o) = e_6(0) = 0$, we can delete the last part in (III.63). The dynamic equation of f_3 , f_4 , f_5 and f_6 , and the constitutive equations of effort variables e_3 , e_4 , e_5 and e_6 yield:

$$\begin{pmatrix} f_{3d} \\ f_{4d} \\ f_{5d} \\ f_{6d} \end{pmatrix} = \begin{pmatrix} \dot{x}_{3d} \\ \dot{x}_{4d} \\ \dot{x}_{5d} \\ \dot{x}_{6d} \end{pmatrix}, \quad \begin{pmatrix} e_{3d} \\ e_{4d} \\ e_{5d} \\ e_{6d} \end{pmatrix} = \underbrace{\begin{pmatrix} L_{d3} & \mathbf{0} & \mathbf{0} & \mathbf{0} \\ \mathbf{0} & L_{d4} & \mathbf{0} & \mathbf{0} \\ \mathbf{0} & \mathbf{0} & L_{d5} & \mathbf{0} \\ \mathbf{0} & \mathbf{0} & \mathbf{0} & L_{d6} \end{pmatrix}}_{L_{md}} \underbrace{\begin{pmatrix} x_{3d} \\ x_{4d} \\ x_{5d} \\ x_{6d} \end{pmatrix}}_{x_{md}}, \quad (\text{III.64})$$

with $L_{d3} = \text{diag}(GA)$, $L_{d4} = \text{diag}\left(\frac{1}{\rho_o A}\right)$, $L_{d5} = \text{diag}(EI_o)$ and $L_{d6} = \text{diag}\left(\frac{1}{\rho_o I_o}\right)$.

Substituting (III.64) into (III.63), one obtains:

$$\dot{x}_{md} = J_{md} L_{md} x_{md} + S_2 e_{2d} + S_\lambda \lambda_{Ld}. \quad (\text{III.65})$$

III.2.4 Descriptor form of the discretized global system

The discretized coupling relations between the electrical subsystem and the electro-stress diffusion subsystem (III.58) and (III.62) permit to interconnect (III.57) and (III.61) through e_{1b} and e_{2b} . Equations (III.61) and (III.65) are interconnected through e_{2d} , e_{6d} and λ_{Ld} . As a result, the discretization of the overall IPMC actuator system (II.43) at page 47 is formulated as follows:

$$\begin{pmatrix} \dot{x}_{1d} \\ f_{r1d} \\ f_{1d} \\ \dot{x}_{2d} \\ f_{r2d} \\ \dot{x}_{md} \end{pmatrix} = \begin{pmatrix} \mathbf{0} & D_1 & \mathbf{0} & \mathbf{0} & \mathbf{0} & \mathbf{0} \\ -D_1^T & \mathbf{0} & -D_1^T & -S_3^T & \mathbf{0} & \mathbf{0} \\ \mathbf{0} & D_1 & \mathbf{0} & \mathbf{0} & \mathbf{0} & \mathbf{0} \\ \mathbf{0} & S_3 & \mathbf{0} & \mathbf{0} & D_2 & -S_2^T \\ \mathbf{0} & \mathbf{0} & \mathbf{0} & -D_2^T & \mathbf{0} & \mathbf{0} \\ \mathbf{0} & \mathbf{0} & \mathbf{0} & S_2 & \mathbf{0} & J_{md} \end{pmatrix} \begin{pmatrix} L_{d1} x_{1d} \\ L_{r1} f_{r1d} \\ L_{r2} f_{1d} \\ L_{d2} x_{2d} \\ L_{r3} f_{r2d} \\ L_{md} x_{md} \end{pmatrix} + \begin{pmatrix} \mathbf{0} \\ \mathbf{0} \\ \mathbf{0} \\ g_2 \\ \mathbf{0} \\ S_\lambda \end{pmatrix} \lambda_{Ld} + \begin{pmatrix} \mathbf{0} \\ g \\ \mathbf{0} \\ \mathbf{0} \\ \mathbf{0} \\ \mathbf{0} \end{pmatrix} V_1, \quad (\text{III.66})$$

with $S_3 = g_2 \frac{\lambda}{\sigma_e L_o b} g_1^T$, enclosed with the discretized constraint equation (II.44) at page 47:

$$\begin{pmatrix} \mathbf{0} & \mathbf{0} & \mathbf{0} & g_2^T & \mathbf{0} & S_\lambda^T \end{pmatrix} \begin{pmatrix} L_{d1}x_{1d} \\ L_{r1}f_{r1d} \\ L_{r2}f_{1d} \\ L_{d2}x_{2d} \\ L_{r3}f_{r2d} \\ L_{md}x_{md} \end{pmatrix} = g_2^T e_{2d} + \text{diag} \left(\frac{B_p}{L_o} \right) e_{6d} = 0. \quad (\text{III.67})$$

Equation (III.66) together with the discretized constraint (III.67) and closure equations (III.55a), (III.55b) and (III.60c) need to be expressed in a descriptor form in order to eliminate f_{r1d} , f_{1d} and f_{r2} , leading to:

$$\mathbf{E} \begin{pmatrix} \dot{x}_{1d} \\ \dot{x}_{2d} \\ \dot{x}_{md} \end{pmatrix} = (J_d - R_d) \underbrace{\begin{pmatrix} L_{d1} & \mathbf{0} & \mathbf{0} \\ \mathbf{0} & L_{d2} & \mathbf{0} \\ \mathbf{0} & \mathbf{0} & L_{md} \end{pmatrix}}_{L_d} \underbrace{\begin{pmatrix} x_{1d} \\ x_{2d} \\ x_{md} \end{pmatrix}}_{x_d} + \underbrace{\begin{pmatrix} B_1 \\ B_2 \\ \mathbf{0} \end{pmatrix}}_B V + \underbrace{\begin{pmatrix} \mathbf{0} \\ g_2 \\ S_\lambda \end{pmatrix}}_{g_c} \lambda_{\mathbf{L}_d}, \quad (\text{III.68})$$

closed with

$$g_c^T L_d x_d = 0, \quad (\text{III.69})$$

with

$$\mathbf{E} = \begin{pmatrix} \mathbf{I} + D_1 L_{r1} D_1^T L_{r2} & \mathbf{0} & \mathbf{0} \\ S_3 L_{r1} D_1^T L_{r2} & \mathbf{I} & \mathbf{0} \\ \mathbf{0} & \mathbf{0} & \mathbf{I} \end{pmatrix}, \quad J_d = \begin{pmatrix} \mathbf{0} & \mathbf{0} & \mathbf{0} \\ \mathbf{0} & \mathbf{0} & -S_2^T \\ \mathbf{0} & S_2 & J_{md} \end{pmatrix},$$

$$R_d = \begin{pmatrix} D_1 L_{r1} D_1^T & D_1 L_{r1} S_3^T & \mathbf{0} \\ S_3 L_{r1} D_1^T & S_3 L_{r1} S_3^T + D_2 L_{r3} D_2^T & \mathbf{0} \\ \mathbf{0} & \mathbf{0} & \mathbf{0} \end{pmatrix}, \quad B_1 = D_1 L_{r1} g_1, \quad B_2 = S_3 L_{r1} g_1,$$

where \mathbf{I} is the identity matrix of appropriate size.

III.2.5 Elimination of the Lagrange multiplier

The Lagrange multiplier $\lambda_{\mathbf{L}_d}$ in (III.68) has to be eliminated in order to perform the simulation and apply the control strategies afterwards. We follow the coordinate projection [Wu 14] as we introduced in Subsection I.3.1. Choose the projection matrix M as formulated in (I.14) at page 15 with

$$s = \begin{pmatrix} \mathbf{I} & \mathbf{0} & \mathbf{0} \\ \mathbf{0} & X_1 & \mathbf{0} \\ \mathbf{0} & X_2 & X_3 \end{pmatrix} \in \mathbb{R}^{(N_e + N_g + 3N_b) \times (N_e + N_g + 4N_b)}, \quad (\text{III.70a})$$

$$X_1 = \begin{pmatrix} \mathbf{I}_{N_b \times N_b} & \mathbf{0}_{(N_g-2N_b) \times N_b} & \mathbf{I}_{N_b \times N_b} \\ \mathbf{0}_{(N_g-2N_b) \times N_b} & \mathbf{I}_{(N_g-2N_b) \times (N_g-2N_b)} & \mathbf{0}_{(N_g-2N_b) \times N_b} \end{pmatrix}, \quad (\text{III.70b})$$

$$X_2 = \begin{pmatrix} \mathbf{0}_{3N_b \times N_g} \\ \text{diag} \left(\frac{B_p h_2}{L_o} \right)_{N_b \times N_b} & \mathbf{0}_{(N_g-N_b) \times N_b} \end{pmatrix}, \quad (\text{III.70c})$$

$$X_3 = \mathbf{I} \in \mathbb{R}^{4N_b \times 4N_b}, \quad (\text{III.70d})$$

satisfying $X_1 g_2 = 0$, $(X_2 \ X_3) \begin{pmatrix} g_2 \\ S_\lambda \end{pmatrix} = 0$, and herein $sg_c = 0$. Therefore, by multiplying M , (III.68) is transformed into:

$$M\mathbf{E}\dot{x}_d = M(J_d - R_d)L_d x_d + MBV + Mg_c \lambda_{L_d}, \quad (\text{III.71})$$

closed with the same constraint equation (III.69).

Define:

$$\tilde{z}_d = Mx_d = \begin{pmatrix} \tilde{z}_{1d} \\ \tilde{z}_{2d} \end{pmatrix}, \quad (\text{III.72a})$$

$$\tilde{J}_d = MJ_d M^T = \begin{pmatrix} \tilde{J}_{11d} & \tilde{J}_{12d} \\ \tilde{J}_{21d} & \tilde{J}_{22d} \end{pmatrix}, \quad (\text{III.72b})$$

$$\tilde{R}_d = MR_d M^T = \begin{pmatrix} \tilde{R}_{11d} & \tilde{R}_{12d} \\ \tilde{R}_{21d} & \tilde{R}_{22d} \end{pmatrix}, \quad (\text{III.72c})$$

$$\tilde{L}_d = M^{-T} L_d M^{-1} = \begin{pmatrix} \tilde{L}_{11d} & \tilde{L}_{12d} \\ \tilde{L}_{21d} & \tilde{L}_{22d} \end{pmatrix}, \quad (\text{III.72d})$$

$$\tilde{B} = MB = \begin{pmatrix} \tilde{B}_1 \\ \tilde{B}_2 \end{pmatrix}, \quad (\text{III.72e})$$

$$\tilde{M} = M\mathbf{E}M^{-1} = \begin{pmatrix} \tilde{M}_{11d} & \tilde{M}_{12d} \\ \tilde{M}_{21d} & \tilde{M}_{22d} \end{pmatrix}, \quad (\text{III.72f})$$

with $\tilde{z}_{1d} \in \mathbb{R}^{N_e + N_g + 3N_b}$ and $\tilde{z}_{2d} \in \mathbb{R}^{N_b}$, (III.71) with the constraint equation (III.69) can be reformulated as:

$$\begin{pmatrix} \tilde{M}_{11d} & \tilde{M}_{12d} \\ \tilde{M}_{21d} & \tilde{M}_{22d} \end{pmatrix} \begin{pmatrix} \dot{\tilde{z}}_{1d} \\ \dot{\tilde{z}}_{2d} \end{pmatrix} = \left(\begin{pmatrix} \tilde{J}_{11d} & \tilde{J}_{12d} \\ \tilde{J}_{21d} & \tilde{J}_{22d} \end{pmatrix} - \begin{pmatrix} \tilde{R}_{11d} & \tilde{R}_{12d} \\ \tilde{R}_{21d} & \tilde{R}_{22d} \end{pmatrix} \right) \begin{pmatrix} \tilde{L}_{11d} & \tilde{L}_{12d} \\ \tilde{L}_{21d} & \tilde{L}_{22d} \end{pmatrix} \begin{pmatrix} \tilde{z}_{1d} \\ \tilde{z}_{2d} \end{pmatrix} + \begin{pmatrix} \tilde{B}_1 \\ \tilde{B}_2 \end{pmatrix} V + \begin{pmatrix} \mathbf{0} \\ \mathbf{I} \end{pmatrix} \lambda_{L_d}, \quad (\text{III.73a})$$

$$(Mg_c)^T \tilde{L}_d \tilde{z}_d = 0. \quad (\text{III.73b})$$

Replace the second line of (III.73a) by (III.73b) as we have introduced in (I.17) at page 16, we finally obtain:

$$\begin{pmatrix} \tilde{M}_{11d} & \tilde{M}_{12d} \\ \mathbf{0} & \mathbf{0} \end{pmatrix} \begin{pmatrix} \dot{\tilde{z}}_{1d} \\ \dot{\tilde{z}}_{2d} \end{pmatrix} = \begin{pmatrix} \tilde{J}_{11d} - \tilde{R}_{11d} & \tilde{J}_{12d} - \tilde{R}_{12d} \\ \mathbf{0} & \mathbf{I} \end{pmatrix} \tilde{L}_d \begin{pmatrix} \tilde{z}_{1d} \\ \tilde{z}_{2d} \end{pmatrix} + \begin{pmatrix} \tilde{B}_1 \\ \mathbf{0} \end{pmatrix} V. \quad (\text{III.74})$$

III.2.6 Simulation results and experimental validation

The experimental set-up is shown in Fig. III.10. The IPMC patch is controlled through a computer equipped with a dSPACE controller board. It helps to send the input voltage generated from the Simulink to the IPMC strip and receive the measured signals from the sensors. The amplifier is used to regulate the input current in order to guarantee the power. The current conditioner is used to transform the measured current to signals. The laser position sensor (Keyence LK-G152) and the current sensor (HIOKI CT6700) are used to measure the tip displacement of IPMC and the output current, respectively.

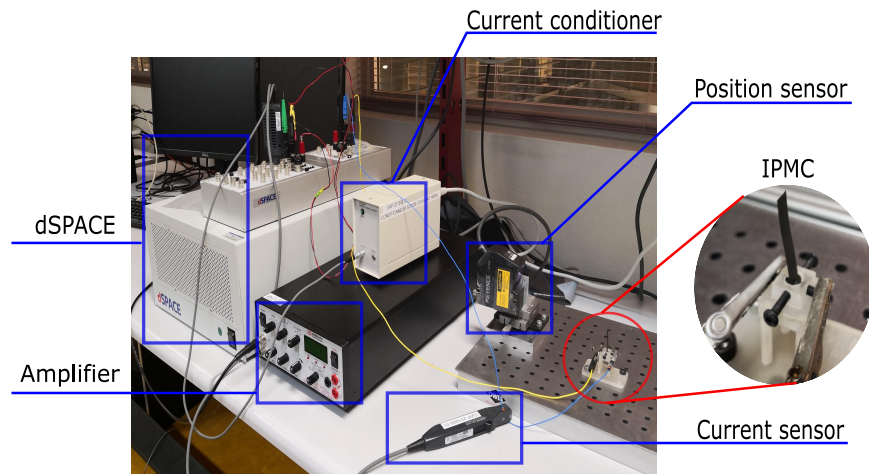


Figure III.10 – Experimental setup of the IPMC actuator.

The considered IPMC is a Nafion[®] based IPMC. Its dimensions and mechanical parameters are listed in Table III.1. According to [Paquette 03], the water volume fraction $\phi = 0.34$ and the water viscosity $\eta = 0.010\text{Pa} \cdot \text{s}$. The identified parameters are listed in Table III.2. It is important to point out that the identified values are chosen arbitrarily in a certain interval according to the references [Nishida 11, Paquette 03].

Table III.1 – Dimensions and mechanical parameters of the IPMC.

Name	Parameters	Value	Unit
Length	L_o	45	mm
Width	b_o	5	mm
Thickness	h_o	0.2	mm
Young's modulus	E	9×10^7	Pa
Density	ρ_o	1.633×10^3	kg/m^3
Poisson ratio	ν	0.3	1

Table III.2 – Identified parameters.

Name	Parameters	Value	Unit
Resistance	$R_{1\text{total}}$	460.54	Ω
Resistance	$R_{2\text{total}}$	3	Ω
Capacitance	$C_{2\text{total}}$	0.021	F
Onsager's coefficient	λ	16.6×10^{-9}	$\text{m}^2(\text{Vs})$
Conductance	σ_e	13.10	$1/(\Omega \text{ m})$
Effective pore size	d	10	nm

The temporal evolution of the currents obtained in the simulation with a step voltage of 1V is depicted and compared to the experimental one in Fig. III.11. The simulations correspond to four different values of the discretization number in ξ coordinate with $N_\xi = 10, 50, 100$ and 200 . The discretization numbers in z and x coordinates N_z and N_b are fixed to 10. As N_ξ increases, the peak responses of the output current obtained in the simulation approach gradually to the experimental one (marked by the black solid line), while the settling time remains similar.

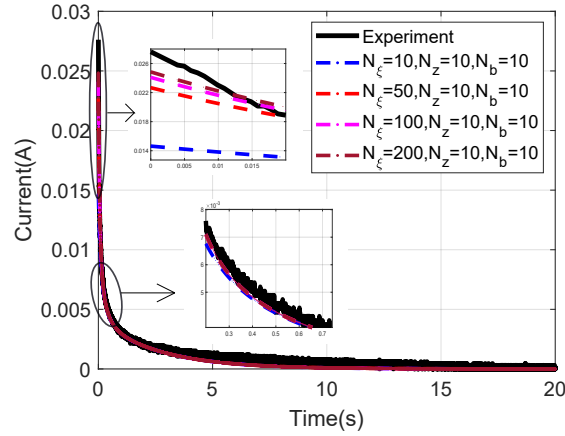


Figure III.11 – Variation of output current according to different discretization numbers N_ξ of the electrical system, compared with experimental data.

This temporal evolution of the output current is in accordance with the frequency responses of the transfer functions between the input voltage and the output current associated to different values of N_ξ . From the Bode diagram in Fig. III.12, the transfer functions between the input voltage and output current have similar shapes at low frequencies but are slightly different at high frequencies. These differences at high frequencies tend to zero when N_ξ tends to infinity. However, one can notice both from Fig. III.11 and Fig. III.12 that for the considered example, the difference is minor for N_ξ greater than 50.

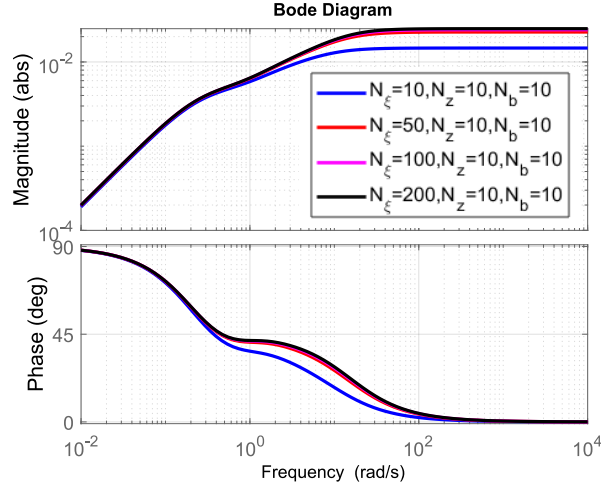
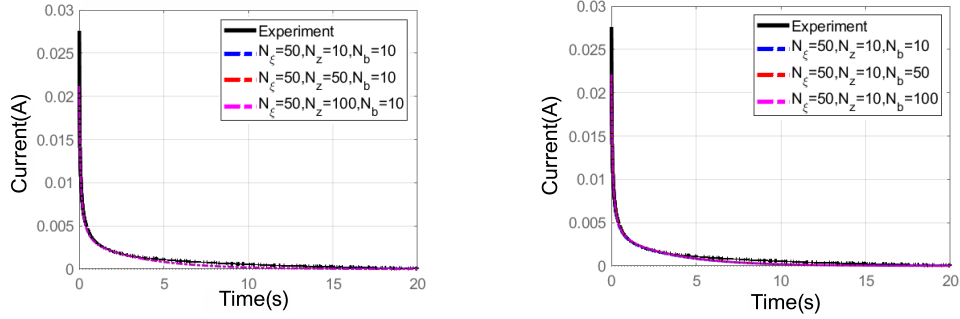


Figure III.12 – Bode diagram of the impedance relevant to each discretized number N_ξ .

The influences of the discretization numbers N_z and N_b on output the current have also been investigated in Fig. III.13a and III.13b, respectively. One can conclude that these parameters N_z and N_b have a minor effect on the current responses compared to that of N_ξ .



(a) Output current with respect to different discretization numbers N_z , compared with experimental data.

(b) Output current with respect to different discretization numbers N_b , compared with experimental data.

Figure III.13 – Variation of the output current according to different discretization numbers N_z and N_b .

We consider now the consistency between the simulation and experimental results for the tip deflection of the IPMC strip. Preliminary works suggest that the deflection does not change with N_z . Meanwhile, its variation is negligible as soon as N_ξ is greater than 50. So we concentrate on the analysis of the influence of the discretization number N_b , with the other two discretization numbers $N_\xi = 50$ and $N_z = 10$. As shown in Fig. III.14, N_b has a significant influence on the predicted response. The simulation results get close to the experimental data with the

increase of the discretization number N_b , which is consistent to the example of the vibrating string with dissipation presented in Fig. III.5a at page 80. One can see that $N_b = 100$ leads to a very good approximation of the measured experimental behavior.

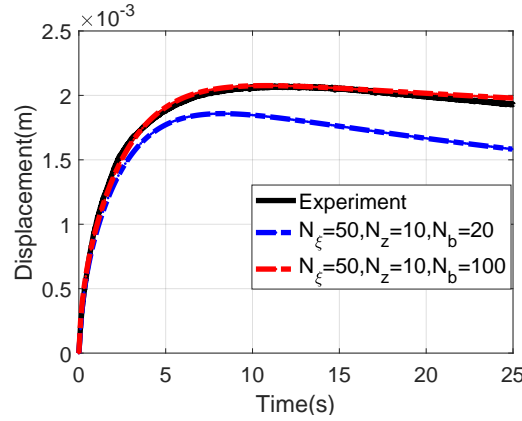


Figure III.14 – Tip deflection of IPMC strip according to different discretization numbers N_b of the mechanical system, compared with experimental data.

The two bending moments M_{x_1} and M_{x_2} generated by the gel are therefore simulated in Fig. III.15 for $N_\xi = 50$, $N_z = 10$ and $N_b = 100$. Fig. III.15a shows the distribution along the beam and the temporal evolution of the bending moment M_{x_1} , while Fig. III.15b illustrates those related to M_{x_2} . At each time, the bending moment M_{x_1} is constant along the beam. Nevertheless, as illustrated by the dashed light blue line in Fig. III.15b, M_{x_2} has a larger value at the clamped point and is equal to zero at the free end point, which is in accordance with the considered clamped-free boundary conditions for the cantilever. The sum of the two bending moments M_{x_1} and M_{x_2} forms the total bending moment that applies to the beam model, whose simulation result is given in Fig. III.15c. One can notice a diffusion phenomenon in Fig. III.15, as illustrated by the red solid lines. This diffusion effect of the bending moment explains the back relaxation of the displacement in our model, as shown in Fig. III.14. Considered as the main drawback of the IPMC actuators, this back relaxation exists in almost all Nafion[®] based IPMCs. More thorough studies on this phenomenon are referred to some recent references, e.g. [Porfiri 17]. Some new materials of the IPMC actuator have been proposed to reduce and eventually eliminate the back relaxation in [Panwar 12, Luqman 11].

Apart from the step response, we have also compared the experimental result and the simulation one with a sinusoidal input voltage of amplitude 1V and frequency of 1Hz. The results are illustrated in Fig. III.16 with two different discretization numbers $N_b = 20$ and $N_b = 100$. The simulation results are consistent with the experimental one.

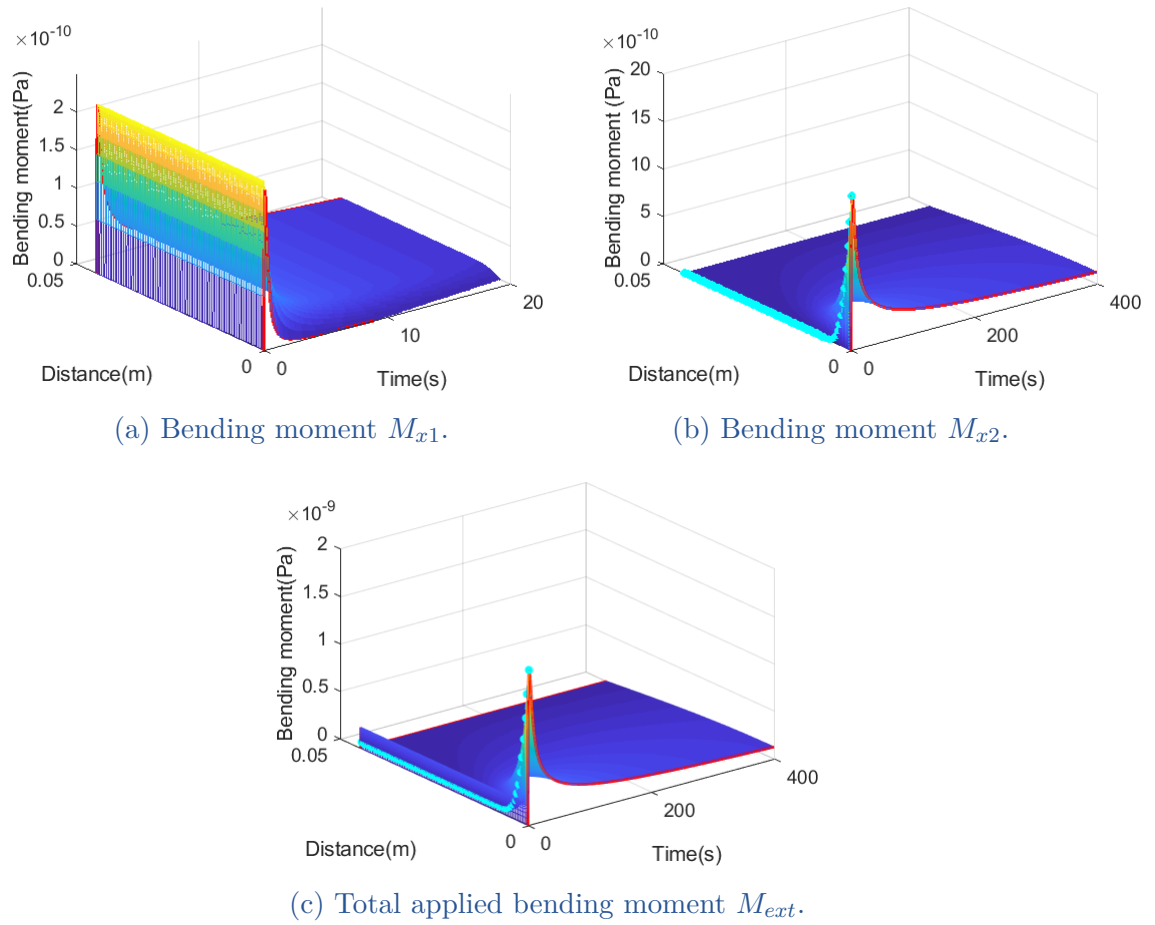


Figure III.15 – Simulation results for M_{x1} , M_{x2} and M_{ext} along x-axis and the time ($N_\xi = 50$, $N_z = 10$ and $N_b = 100$).

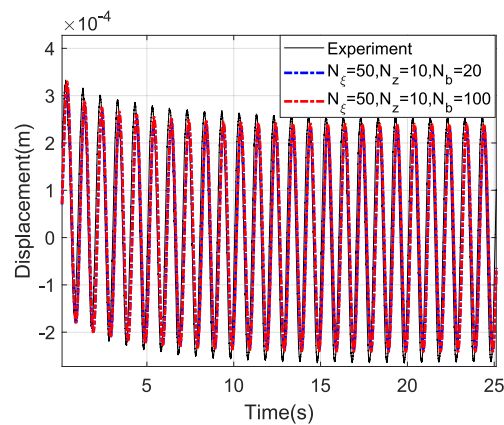


Figure III.16 – Tip deflection of IPMC strip with a sinusoidal input voltage.

III.3 SUMMARY

In this Chapter, structure preserving spatial discretization methods for 1D infinite dimensional PHS are presented. As many structure preserving approximation methods have been proposed in the literature, we apply the most common used the mixed finite element method and the finite difference method on staggered grids, and extend them to systems with dissipation and distributed input with an example of a vibrating string. The Dirac structure and the passivity of the infinite dimensional PHS are preserved after the discretization. A comparison of these two discretization approaches is then investigated. The mixed finite element method can get more precise approximated solution with less discretization numbers compared to the finite difference method on staggered grids. On the other hand, the finite difference method on staggered grids has the benefit of simplicity in terms of calculation.

The finite difference method on staggered grids is later applied to approximate the IPMC actuator model that proposed in Chapter II. The simulation results are compared with the experimental measurements with a step voltage as well as a sinusoidal voltage. It has been shown that with enough discretization numbers the simulations of the output current and the tip displacement of the IPMC actuator match with the experimental data. We have also analyzed the frequency response of the electrical system of the IPMC actuator by plotting the Bode diagram, and the back relaxation of the IPMC by plotting the bending moments generated in the gel.

Still some open questions remain to be solved, especially the large discretization numbers required in the simulation of the IPMC actuator, which will make it difficult for the controller design. Based on the simulation results presented in Subsection III.1.3, the mixed finite element method provide a better convergence with much fewer discretization elements for the infinite dimensional port-Hamiltonian system. One solution is to apply the mixed finite element method to the IPMC actuated endoscope model. The second choice is to use the finite dimensional structure preserving reduction method to reduce the obtained high order discretized model in order to get a suitable low order model for the control design purpose.

Chapter IV

In-domain distributed control

IV.1	Control problem formulation	98
IV.2	In-domain distributed CbI with early lumping approach. ..	99
	IV.2.1 Fully-actuated case	104
	IV.2.2 Under-actuated case	105
	IV.2.3 Closed loop stability	108
IV.3	Numerical simulations	109
	IV.3.1 Fully-actuated case	110
	IV.3.2 Under-actuated case	113
IV.4	Summary	115

In Section I.1 and Subsection I.2.1 are presented the general control objectives for an efficient use of micro- endoscopes for medical applications. Here we briefly recall these objectives and make some reasonable assumptions and simplifications. The compliant micro-endoscope is controlled through an in-domain network of IPMC actuators and the aim of the control design is twofold:

- Change as fast as possible the shape of the endoscope without too much overshoot and vibrations,
- Avoid vibrations during imaging of surgery operations.

In what follows we concentrate on the stabilization of the flexible structure around its natural equilibrium positions and consider the shape of the structure can be modified using appropriated input shaping. We then make the assumption that the deformation of the structure is small enough and we restrict our study to the 1D longitudinal domain. For the sake of simplicity and the clarity of the presentation, the proposed control design is illustrated with the help of the vibrating string example considering that the actuator patches deliver a piecewise homogeneous force density (cf Fig. IV.1). It means that the IPMC dynamics is first neglected. The extension of the proposed control design strategy to more complex dynamic structures (Timoshenko beam, shell models, etc.) and to the use of non-ideal actuators require attention but does not raise any serious difficulty.

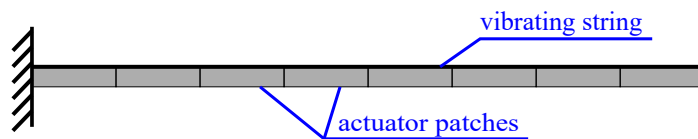


Figure IV.1 – Simplified model for the control design.

As the dynamics of the vibrating string is formulated by hyperbolic PDEs, the control problem is to design a controller for the hyperbolic PDEs. Two main categories exist for such kind of problem, the late lumping approach [Curtain 95, Meurer 13, Trenchant 17] and the early lumping approach [Morris 10, Wu 20]. The former designs the infinite dimensional controller directly according to the infinite dimensional plant system without loss of information about the infinite dimensional system. The main problem of such kind of approach comes from the infinite dimensional aspect of the controller structure that needs to be reduced for practical and real time implementation [Morris 10]. The early lumping approach consists in first approximating the infinite dimensional system by a finite dimensional system and then designing a finite dimensional controller based on the discretized system. This approach is largely used in the practical implementation, but as the controller is designed on the basis of the approximated plant system and the high frequency modes of the infinite dimensional plant system are neglected, it may lead to spillover effect [Balas 78, Bontsema 88]. The spillover effect talks about the lack of robustness when applying the controller designed from the approximated system to the infinite-dimensional system, making the closed loop system unstable. One needs to carefully deal with the stability of the closed loop system with early lumping approach.

Back to our plant system formulated under the port-Hamiltonian framework, we would like to take advantage of the passivity of the PHS and design a passivity based controller which has clear physical interpretation [Ortega 99b, Ortega 01], especially the control by interconnection (CbI) approach [Ortega 08] introduced in Subsection I.3.3. The controller is also designed to be a PHS and connected with the plant PHS through a power preserving way, making the closed loop again a PHS [van der Schaft 17] as illustrated in Fig. I.12. [Trenchant 17] has proposed an in-domain distributed CbI strategy based on the late lumping approach with a positive feedback, which can convert a hyperbolic PDE into a parabolic one. In this thesis, we would like to extend this control strategy with the **early lumping approach** to implement the in-domain distributed CbI. The main idea is depicted in Fig. IV.2, where $BC(0)$ and $BC(L)$ relate to the boundary conditions that are set to be zero. Different from a local control, the controller takes the distributed information of the plant system into consideration. This control strategy takes advantage of the early lumping approach, leading to a directly implementable controller with guaranteed performances on the discretized model, and herein on the infinite dimensional system over a given range of frequencies. Moreover, the asymptotic stability is guaranteed with controller being a PHS and strictly input passive.

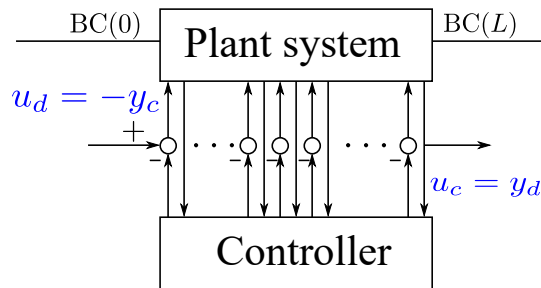


Figure IV.2 – In-domain distributed CbI schema.

After the discretization of the infinite dimensional PHS, two different cases will be investigated: the ideal *fully-actuated case* where the control input works independently on each element of the discretized model and the *under-actuated case* where the input of each IPMC actuator patch acts identically on sets of elements, providing less degrees of freedom. This latter case is closer to the real implementation case as the control is usually carried out through patches that act similarly over spatial elements. In the fully-actuated case, the closed loop performances can be ideally assigned since each discretized element is actuated independently. However, an optimal problem will be addressed in the under-actuated case to choose the control parameters such that similar closed loop performance can be guaranteed.

In the following sections, we first state the control problem with the formulation of the vibrating string, and then design our controller in an early lumping way under the *fully-actuated case* and the *under-actuated case*. The stability of the closed loop between the infinite dimensional system and the finite dimensional

system is studied. Finally, in the fully-actuated and under-actuated cases simulations are undertaken to compare the dynamic performances with different choices of controller matrices.

IV.1 CONTROL PROBLEM FORMULATION

The weakly damped vibrating string with distributed control on the 1D spatial domain $\zeta \in [0, L]$ is modeled in (III.30) at page 73, which is reformulated under the port-Hamiltonian framework as:

$$\underbrace{\frac{\partial}{\partial t} \begin{pmatrix} x_1(\zeta, t) \\ x_2(\zeta, t) \end{pmatrix}}_{x(\zeta, t)} = \underbrace{\begin{pmatrix} 0 & \frac{\partial}{\partial \zeta} \\ \frac{\partial}{\partial \zeta} & -R \end{pmatrix}}_{\mathcal{J}-\mathcal{R}} \underbrace{\begin{pmatrix} T(\zeta) & 0 \\ 0 & \frac{1}{\rho(\zeta)} \end{pmatrix}}_{\mathcal{Q}} \begin{pmatrix} x_1(\zeta, t) \\ x_2(\zeta, t) \end{pmatrix} + \underbrace{\begin{pmatrix} 0 \\ b \end{pmatrix}}_B u_d, \quad (\text{IV.1})$$

$$y_d = B^* \mathcal{Q} \begin{pmatrix} x_1(\zeta, t) \\ x_2(\zeta, t) \end{pmatrix},$$

with $x_1(\zeta, t)$, and $x_2(\zeta, t)$ defined in (I.33) at page 20. $T(\zeta)$ and $\rho(\zeta)$ denotes the modulus of elasticity and the density, respectively. The distributed input u_d stands for the exterior force density and the conjugated output y_d is the mean velocity over the domain. R is related to the dissipation and B stands for the bounded in-domain input operator that maps the input u_d to the state space. Define effort variables $e_1(\zeta, t) = T(\zeta)x_1(\zeta, t)$ and $e_2(\zeta, t) = \frac{1}{\rho(\zeta)}x_2(\zeta, t)$. The boundary port variables and the Hamiltonian of the system are formulated in (I.36) and in (I.37) at page 21 and are such that:

$$\frac{dH}{dt}(t) = f_{\partial}^T(t)e_{\partial}(t) + \int_{\zeta} y_d(\zeta, t)^T u_d(\zeta, t) d\zeta - \int_{\zeta} e_2(\zeta, t)^T R e_2(\zeta, t) d\zeta. \quad (\text{IV.2})$$

Remark 10. *For the infinite dimensional controller, the operator b equals to 1. For the finite dimensional controller, b is a piecewise homogeneous operator that maps the same input of one patch to its applied interval on the vibrating string.*

Clamped-free boundary conditions are considered, so the boundary input and output u_b and y_b are chosen to be:

$$u_b(t) = W \begin{pmatrix} f_{\partial}(t) \\ e_{\partial}(t) \end{pmatrix} = \begin{pmatrix} \frac{1}{\rho(0)}x_2(0, t) \\ T(L)x_1(L, t) \end{pmatrix} = \begin{pmatrix} 0 \\ 0 \end{pmatrix}, \quad (\text{IV.3a})$$

$$y_b = \tilde{W} \begin{pmatrix} f_{\partial}(t) \\ e_{\partial}(t) \end{pmatrix} = \begin{pmatrix} -T(0)x_1(0, t) \\ \frac{1}{\rho(L)}x_2(L, t) \end{pmatrix}, \quad (\text{IV.3b})$$

where $W = \begin{pmatrix} 0 & 0 & 1 & 0 \\ 0 & 1 & 0 & 0 \end{pmatrix}$, $\tilde{W} = \begin{pmatrix} -1 & 0 & 0 & 0 \\ 0 & 0 & 0 & -1 \end{pmatrix}$ with $\begin{pmatrix} W \\ \tilde{W} \end{pmatrix}$ invertible. As a result, (IV.2) becomes:

$$\frac{dH}{dt}(t) = \int_{\zeta} y_d(\zeta, t)^T u_d(\zeta, t) d\zeta - \int_{\zeta} e_2(\zeta, t)^T R e_2(\zeta, t) d\zeta. \quad (\text{IV.4})$$

The controller for the system (IV.1) is looked for under a PHS form:

$$\begin{aligned}\frac{\partial x_c}{\partial t}(\zeta, t) &= (\mathcal{J}_c - \mathcal{R}_c) \frac{\partial H_c}{\partial x_c}(\zeta, t) + \mathcal{B}_c u_c(\zeta, t), \\ y_c &= \mathcal{B}_c^* \frac{\partial H_c}{\partial x_c}(\zeta, t),\end{aligned}\tag{IV.5}$$

with $x_c(\zeta, t)$ the state variable of the controller, \mathcal{J}_c the skew-symmetric operator, \mathcal{R}_c the symmetric positive semi-definite operator and $H_c(x_c)$ the Hamiltonian of the controller. The controller is interconnected to the plant system (IV.1) in a power preserving way:

$$\begin{aligned}u_d(\zeta, t) &= -y_c(\zeta, t), \\ u_c(\zeta, t) &= y_d(\zeta, t).\end{aligned}\tag{IV.6}$$

The Hamiltonian of closed loop then writes:

$$H_{cl}(x, x_c) = H(x) + H_c(x_c).\tag{IV.7}$$

The aim of the CbI is to shape the closed loop energy function H_{cl} with the choice of H_c . This energy shaping is realized with the structural invariant Casimir function [Duindam 09, Ortega 08] $C(x, x_c)$, which remains invariant along the trajectories of the system and is independent of the energy function such that:

$$\frac{dC}{dt} = 0, \quad \forall H_c(x_c).\tag{IV.8}$$

By taking the Casimir function of the form:

$$C(x, x_c) = F(x) - x_c,\tag{IV.9}$$

where $F(x)$ is a differentiable function and has the same dimension as x_c , the Hamiltonian in closed loop (IV.7) becomes:

$$H_{cl}(x) = H(x) + H_c(F(x) - C).\tag{IV.10}$$

As a result, the state variable of the controller is connected with that of the plant system, and H_c can be chosen to shape the closed loop energy.

IV.2 IN-DOMAIN DISTRIBUTED CBI WITH EARLY LUMPING APPROACH

The controller designed in Section IV.1 is an infinite dimensional controller. When it comes to the real case, the vibrating string is controlled by finite dimensional patches that delivered the same input $\mathbf{u}_d(t)$ over the applied interval. As a result, the operator b now becomes a piecewise homogeneous function as we

pointed out in Remark 10. And the Hamiltonian of the open loop system (IV.4) becomes:

$$\frac{dH}{dt}(t) = \mathbf{y}_d(t)^T \mathbf{u}_d(t) - \int_{\zeta} e_2(\zeta, t)^T Re_2(\zeta, t) d\zeta, \quad (\text{IV.11})$$

where \mathbf{y}_d is the sum of velocity.

We first proceed to the spatial discretization of the system in order to approximate the infinite dimensional system (IV.1) into finite dimensional system. For a sake of simplicity we consider here the homogeneous case, *i.e.* the physical parameters T and ρ do not depend on ζ . Since the passivity based control (PBC) is considered, the discretization has to preserve the structure and the passivity of the system to take advantage of the system properties. Moreover, we want to consider the elements interconnections of the discretized system. To this aim we use the mixed finite element method proposed in [Golo 04] and detailed in Subsection III.1.1.b. The discretization of the plant system (IV.1) in n elements leads to the finite dimensional system similar to (III.49) at page 77:

$$\frac{d}{dt} \begin{pmatrix} x_{1d}(t) \\ x_{2d}(t) \end{pmatrix} = \left(\begin{pmatrix} 0 & J_i \\ -J_i^T & 0 \end{pmatrix} - \begin{pmatrix} 0 & 0 \\ 0 & R_d \end{pmatrix} \right) \begin{pmatrix} Q_1 x_{1d}(t) \\ Q_2 x_{2d}(t) \end{pmatrix} + B_b u_b(t) + \underbrace{\begin{pmatrix} 0 \\ b_d \end{pmatrix}}_{B_d} \mathbf{u}_d(t), \quad (\text{IV.12a})$$

$$y_b(t) = B_b^T \begin{pmatrix} Q_1 x_{1d}(t) \\ Q_2 x_{2d}(t) \end{pmatrix} + D_b u_b(t), \quad (\text{IV.12b})$$

$$\mathbf{y}_d(t) = \begin{pmatrix} 0 & b_d^T \end{pmatrix} \begin{pmatrix} Q_1 x_{1d}(t) \\ Q_2 x_{2d}(t) \end{pmatrix}, \quad (\text{IV.12c})$$

with J_i , B_b and D_b formulated in (III.23) at page 71, R_d calculated in (III.50c) at page 77, $Q_1 = \text{diag}(T_{ab}) \in \mathbb{R}^{n \times n}$, $Q_2 = \text{diag}\left(\frac{1}{\rho_{ab}}\right) \in \mathbb{R}^{n \times n}$ and T_{ab} and ρ_{ab} calculated in (III.29) at page 72. $\mathbf{u}_d(t) \in \mathbb{R}^{m \times 1}$ and $\mathbf{y}_d(t) \in \mathbb{R}^{m \times 1}$ correspond to the power conjugated distributed input and output, with m denoting the number of independent input and output satisfying $m \leq n$.

With the clamped-free boundary conditions (IV.3a), (IV.12) can be simplified as:

$$\frac{d}{dt} \begin{pmatrix} x_{1d}(t) \\ x_{2d}(t) \end{pmatrix} = \left(\begin{pmatrix} 0 & J_i \\ -J_i^T & 0 \end{pmatrix} - \begin{pmatrix} 0 & 0 \\ 0 & R_d \end{pmatrix} \right) \begin{pmatrix} Q_1 x_{1d}(t) \\ Q_2 x_{2d}(t) \end{pmatrix} + B_d \mathbf{u}_d(t), \quad (\text{IV.13a})$$

$$\mathbf{y}_d(t) = B_d^T \begin{pmatrix} Q_1 x_{1d}(t) \\ Q_2 x_{2d}(t) \end{pmatrix}. \quad (\text{IV.13b})$$

Remark 11. *The choice of mixed finite element method rather than the finite difference method on staggered grids for the structure preserving discretization is that we focus now on each element of the model, and the mixed finite element method can attain a more precise simulation results with less discretization number as*

investigated in Subsection III.1.3. Yet some other approaches such as the pseudo-spectral scheme [Moulla 12], and the mixed Galerkin method [Kotyczka 18b] that also guarantee the existence of a finite Dirac structure and structural invariant are suitable for control design purposes.

The Hamiltonian of the discretized model (IV.13) is given as follows:

$$H_d(x_{1d}, x_{2d}) = \frac{1}{2} \left(x_{1d}(t)^T Q_1 x_{1d}(t) + x_{2d}(t)^T Q_2 x_{2d}(t) \right). \quad (\text{IV.14})$$

We have not explicitly expressed the discretized matrix B_d here, because the dimension of the matrix B_d depends on the numbers of independent inputs, which is whether the system is fully- or under-actuated. These two cases will be presented in Subsection IV.2.1 and IV.2.2, respectively.

As mentioned in Section IV.1, we are going to shape the distributed energy function all over the system by choosing appropriately the controller parameters and by using the closed loop structural invariant *i.e.* Casimir functions. As introduced in Subsection I.3.3, the Casimir function helps to interconnect the state variables x_{1d} and x_{2d} in open loop and the state variables in the controller, resulting in a state feedback control.

The controller is formulated as a linear finite dimensional PHS of the form:

$$\begin{aligned} \dot{x}_{cd}(t) &= (J_c - R_c) Q_c x_{cd}(t) + B_c \mathbf{u}_c(t), \\ \mathbf{y}_c(t) &= B_c^T Q_c x_{cd}(t) + D_c \mathbf{u}_c(t), \end{aligned} \quad (\text{IV.15})$$

where $x_{cd}(t) \in \mathbb{R}^{m \times 1}$ is the state variables of the controller, $J_c \in \mathbb{R}^{m \times m}$ is skew-symmetric, $R_c \in \mathbb{R}^{m \times m}$ is symmetric and positive semi-definite, $Q_c \in \mathbb{R}^{m \times m}$ is also symmetric and positive semi-definite, $B_c \in \mathbb{R}^{m \times m}$, $\mathbf{u}_c(t) \in \mathbb{R}^{m \times 1}$ and $\mathbf{y}_c(t) \in \mathbb{R}^{m \times 1}$. $D_c \in \mathbb{R}^{m \times m}$ is positive semi-definite and works as the damping injection or the diffusion operator.

The Hamiltonian of the finite dimensional controller writes:

$$H_{cd}(x_{cd}) = \frac{1}{2} x_{cd}(t)^T Q_c x_{cd}(t). \quad (\text{IV.16})$$

Without considering external signals, the interconnection between the discretized plant system (IV.13) and the controller (IV.15) is:

$$\begin{aligned} \mathbf{u}_d(t) &= -\mathbf{y}_c(t), \\ \mathbf{u}_c(t) &= \mathbf{y}_d(t), \end{aligned} \quad (\text{IV.17})$$

which makes the passivity preserved in closed loop.

Combing the discretized plant system (IV.13), and the controller (IV.15) via the interconnection (IV.17), one gets a new PHS in closed-loop:

$$\dot{x}_{cl}(t) = (J_{cl} - R_{cl}) Q_{cl} x_{cl}(t), \quad (\text{IV.18})$$

where

$$\begin{aligned}
 x_{cl}(t) &= \begin{pmatrix} x_{1d}(t) \\ x_{2d}(t) \\ x_{cd}(t) \end{pmatrix}, & J_{cl} &= \begin{pmatrix} 0 & J_i & 0 \\ -J_i^T & 0 & -b_d B_c^T \\ 0 & B_c b_d^T & J_c \end{pmatrix}, \\
 R_{cl} &= \begin{pmatrix} 0 & 0 & 0 \\ 0 & R_d + b_d D_c b_d^T & 0 \\ 0 & 0 & R_c \end{pmatrix}, & Q_{cl} &= \begin{pmatrix} Q_1 & 0 & 0 \\ 0 & Q_2 & 0 \\ 0 & 0 & Q_c \end{pmatrix}.
 \end{aligned} \tag{IV.19}$$

Combing (IV.14) and (IV.16), the closed-loop Hamiltonian function reads:

$$\begin{aligned}
 H_{cl}(x_{1d}, x_{2d}, x_{cd}) &= H_d(x_{1d}, x_{2d}) + H_{cd}(x_{cd}) \\
 &= \frac{1}{2} \left(x_{1d}(t)^T Q_1 x_{1d}(t) + x_{2d}(t)^T Q_2 x_{2d}(t) + x_{cd}(t)^T Q_c x_{cd}(t) \right).
 \end{aligned} \tag{IV.20}$$

The idea of the control is to shape the Hamiltonian in closed loop to a desired value in order to modify the desired equilibrium point or to modify the closed loop performances. The following Proposition 4 characterizes how the closed-loop energy can be shaped by using structural invariants, *i.e.* the Casimir function.

Proposition 4. *Choosing $J_c = 0$, $R_c = 0$, the closed-loop system (IV.18) admits the Casimir function $C(x_{1d}, x_{cd})$ defined by:*

$$C(x_{1d}, x_{cd}) = B_c b_d^T J_i^{-1} x_{1d}(t) - x_{cd}(t), \tag{IV.21}$$

as structural invariant, i.e. $\frac{dC(x_{1d}, x_{cd})}{dt} = 0$ along the closed loop trajectories. If the initial conditions $x_{1d}(0)$ and $x_{cd}(0)$ satisfy $C(x_{1d}(0), x_{cd}(0)) = 0$, the control law (IV.17) is equivalent to the state feedback:

$$\mathbf{u}_d(t) = -B_c^T Q_c B_c b_d^T J_i^{-1} x_{1d}(t) - D_c \mathbf{y}_d(t), \tag{IV.22a}$$

$$\mathbf{y}_d(t) = b_d^T Q_2 x_{2d}(t). \tag{IV.22b}$$

Therefore, the closed-loop system becomes

$$\begin{pmatrix} \dot{x}_{1d}(t) \\ \dot{x}_{2d}(t) \end{pmatrix} = \begin{pmatrix} 0 & J_i \\ -J_i^T & -R_d - b_d D_c b_d^T \end{pmatrix} \begin{pmatrix} \tilde{Q}_1 x_{1d}(t) \\ Q_2 x_{2d}(t) \end{pmatrix}, \tag{IV.23}$$

where

$$\tilde{Q}_1 = Q_1 + J_i^{-T} b_d B_c^T Q_c B_c b_d^T J_i^{-1} \tag{IV.24}$$

is the new closed loop energy matrix associated to x_{1d} .

Proof. Given the Casimir function in its general form similar to (IV.9):

$$C(x_{1d}, x_{2d}, x_{cd}) = F(x_{1d}, x_{2d}) - x_{cd}, \tag{IV.25}$$

from its structure invariant property, *i.e.* $\dot{C}(x_{1d}, x_{2d}, x_{cd}) = 0$, one gets

$$\frac{dC}{dt} = \frac{\partial C}{\partial x_{cl}}^T \frac{\partial x_{cl}}{\partial t} = \left(\frac{\partial F}{\partial x_{1d}}^T, \frac{\partial F}{\partial x_{2d}}^T, -I \right) (J_{cl} - R_{cl}) e_{cl} = 0, \tag{IV.26}$$

where $x_{cl}(t)$ is defined in (IV.19) and $e_{cl}(t) = \frac{\partial H_{cl}(x_{cl})}{\partial x_{cl}} = Q_{cl}x_{cl}$.

As the Casimir function should not depend on the trajectories of the system *i.e.* on the Hamiltonian, (IV.26) gives rise to the following matching equations:

$$\frac{\partial F}{\partial x_{2d}} \left(-J_i^T \right) = 0, \quad (\text{IV.27a})$$

$$\frac{\partial F}{\partial x_{1d}} J_i - \frac{\partial F}{\partial x_{2d}} \left(R_d + b_d D_c b_d^T \right) - B_c b_d^T = 0, \quad (\text{IV.27b})$$

$$\frac{\partial F}{\partial x_{2d}} \left(-b_d B_c^T \right) - (J_c - R_c) = 0. \quad (\text{IV.27c})$$

Solving (IV.27a), one gets

$$\frac{\partial F}{\partial x_{2d}} = 0, \quad (\text{IV.28})$$

which indicates that x_{cd} does not hinge on x_{2d} , and that the controller allows to modify the potential energy only. Therefore, substituting (IV.28) into (IV.27c), one obtains

$$J_c = 0, \quad (\text{IV.29})$$

$$R_c = 0. \quad (\text{IV.30})$$

Since the matrix J_i in (IV.13) is full rank and with (IV.28), from (IV.27b) one gets (IV.21) as the structural invariant as soon as the initial condition of $x_{cd}(t)$ has been chosen properly.

Taking the initial conditions of $x_{1d}(0)$ and $x_{cd}(0)$ such that $C(x_{1d}(0), x_{cd}(0)) = 0$, (IV.21) becomes

$$x_{cd}(t) = B_c b_d^T J_i^{-1} x_{1d}(t), \quad (\text{IV.31})$$

that links the state of the controller with the state of the system. Replacing the state variable of the controller $x_{cd}(t)$ in (IV.18) by (IV.31), the control law (IV.15) becomes a state feedback (IV.22a) with $\mathbf{u}_c(t) = \mathbf{y}_d(t) = b_d^T Q_2 x_{2d}(t)$. Thus the closed loop system (IV.18) becomes (IV.23) which concludes the proof. \square

Substituting (IV.29) and (IV.30) into the controller (IV.15), the controller thus becomes:

$$\begin{aligned} \dot{x}_{cd}(t) &= B_c \mathbf{u}_c(t), \\ \mathbf{y}_c(t) &= B_c^T Q_c x_{cd}(t) + D_c \mathbf{u}_c(t), \\ &= B_c^T Q_c \int B_c \mathbf{u}_c(t) dt + D_c \mathbf{u}_c(t), \end{aligned} \quad (\text{IV.32})$$

which is a propositional-integral (PI) control if (IV.17) holds.

From Proposition 4, the closed-loop Hamiltonian function (IV.20) becomes:

$$H_{cl}(x_{1d}, x_{2d}) = \frac{1}{2} \left(x_{1d}(t)^T \tilde{Q}_1 x_{1d}(t) + x_{2d}(t)^T Q_2 x_{2d}(t) \right), \quad (\text{IV.33})$$

and satisfies

$$\frac{dH_{cl}}{dt}(t) = -x_{2d}(t)^T Q_2 \left(R_d + b_d D_c b_d^T \right) Q_2 x_{2d}(t) \leq 0. \quad (\text{IV.34})$$

From a physical point of view, (IV.33) implies that with the dynamic controller (IV.15) equivalent to the state feedback (IV.22a), it is possible to change, at least partially, the distributed modulus of elasticity of the string, thereby achieving desired performances in closed loop. According to (IV.24), the degrees of freedom available for this energy shaping depend on the range of controller matrices B_c and Q_c *i.e.* the number of distributed independent actuators. For a given problem *i.e.* for a given number of independent control variables, the objective is to find the matrices B_c and Q_c such that the *distance*¹ between the closed loop potential energy matrix $J_i^{-T} b_d B_c^T Q_c B_c b_d^T J_i^{-1} + Q_1$ and the desired one \tilde{Q}_1 is minimal *i.e.*

$$\min_{B_c^T Q_c B_c} \|J_i^{-T} b_d B_c^T Q_c B_c b_d^T J_i^{-1} + Q_1 - \tilde{Q}_1\|_F \quad (\text{IV.35})$$

This problem can be formalized by the optimization Problem 1.

Problem 1. *The potential energy of the closed loop system (IV.33) is shaped in an optimal way if and only if $X = B_c^T Q_c B_c \in SR_0^{m \times m}$ minimizes the criterion*

$$f(X) = \|AXA^T - Q_m\|_F \quad (\text{IV.36})$$

where $A = J_i^{-T} b_d \in \mathbb{R}^{n \times m}$, and $Q_m = \tilde{Q}_1 - Q_1 \in D_0^{n \times n}$, with $SR_0^{m \times m}$ representing the set of symmetric positive semi-definite matrices, and $D_0^{n \times n}$ standing for diagonal positive semi-definite matrices.

To solve Problem 1, we consider two different cases: the *ideal* fully-actuated case ($m = n$) and the under-actuated case ($m < n$).

IV.2.1 Fully-actuated case

We first consider the ideal case where each discretized string element is actuated by an independent input force, *i.e.* $u_d(t) \in \mathbb{R}^m$ and $m = n$, as illustrated in Fig. IV.3. In this case, the input matrix can be written as:

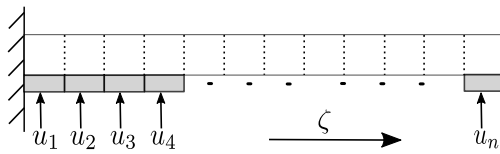


Figure IV.3 – Clamped-free vibrating string with fully-actuated case.

$$b_d = I \in \mathbb{R}^{n \times n}. \quad (\text{IV.37})$$

The power conjugated output vector $y_d(t)$ contains all the velocities of the discretized system. In this case the optimization Problem 1 admits an exact solution that is given in the following Proposition 5.

1. The distance is considered here in the Frobenius norm sense. The definition of the Frobenius norm can be found in Definition 6.4 of [Shores 07]: for a matrix $\mathbb{R}^{m \times n} \ni A = [a_{ij}]$, $\|A\|_F = \left(\sum_{i=1}^m \sum_{j=1}^n |a_{ij}|^2\right)^{1/2}$.

Proposition 5. *In the fully-actuated case, i.e. $m = n$ the optimization Problem 1 has an exact analytical solution $\hat{X} = b_d^{-1} J_i^T Q_m J_i b_d^{-T}$ leading to $f(X) = 0$. In this case the controller matrices B_c and Q_c can be chosen as:*

$$B_c = J_i, \quad Q_c = Q_m = \tilde{Q}_1 - Q_1. \quad (\text{IV.38})$$

Proof. The matrix A is full rank, therefore, (IV.36) admits a minimum in 0 when

$$\hat{X} = A^{-1} Q_m A^{-T} = b_d^{-1} J_i^T Q_m J_i b_d^{-T} = J_i^T Q_m J_i. \quad (\text{IV.39})$$

As $\hat{X} = B_c^T Q_c B_c$, one can choose B_c and Q_c as in (IV.38) to satisfy (IV.39). \square

Remark 12. *The choice $B_c = J_i$ can be regarded as the finite dimensional approximation of the spatial derivation $\frac{\partial}{\partial \zeta}$. This choice has also been used in the late lumping control design approach in [Trenchant 17].*

IV.2.2 Under-actuated case

We consider now the more realistic case depicted in Fig. IV.4, where the control is delivered by the use of patches for instance, i.e. the same control is applied to a set of elements. Let k be the number of elements under the same actuator. $m = \frac{n}{k}$

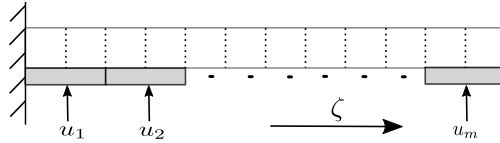


Figure IV.4 – Under-actuated case with $k = 2$.

is then the number of independent inputs distributed all over the spatial domain. This is the case when the string is discretized in n elements and actuated by m uniform actuator patches, each of which acting homogeneously over k elements. The plant system can still be formulated in the form (IV.13) with b_d formulated explicitly as:

$$b_d = I_m \otimes \begin{pmatrix} 1 \\ \vdots \\ 1 \end{pmatrix}_{k \times 1} \in \mathbb{R}^{n \times m}, \quad (\text{IV.40})$$

where $I_m \in \mathbb{R}^{m \times m}$ is the identity matrix, and \otimes denotes the Kronecker product. The input vector $\mathbf{u}_d(t) \in \mathbb{R}^m$ contains m independent (and distributed) forces that can be used for control design. The conjugated output are given by:

$$\mathbf{y}_d = \begin{pmatrix} \sum_{i=1}^{i=k} \dot{\omega}_i \\ \sum_{i=k+1}^{i=2k} \dot{\omega}_i \\ \vdots \\ \sum_{i=n-k+1}^{i=n} \dot{\omega}_i \end{pmatrix}.$$

To solve the optimization Problem 1, the following lemma 1 helps to find the optimal minimizer of $f^2(X)$, thus $f(x)$.

Lemma 1. $f^2(X)$ is convex for $X \in SR_0^{m \times m}$.

Proof.

$$\begin{aligned} f^2(X) &= \|AXA^T - Q_m\|_F^2 \\ &= \text{tr} \left(Q_m Q_m + AXA^T AXA^T - 2AXA^T Q_m \right), \end{aligned} \quad (\text{IV.41})$$

where $\text{tr}(\cdot)$ gives the trace of a matrix, defined as the sum of its diagonal entries [Golub 13]. The gradient of $f^2(X)$ is given by

$$\nabla_X f^2(X) = 2v \left(A^T AXA^T A \right) - 2v \left(A^T Q_m A \right), \quad (\text{IV.42})$$

where $v(\cdot)$ is the entry vector of a matrix, and has the property that [Woodgate 87]:

$$v(A)^T v(B) = \text{tr}(AB^T). \quad (\text{IV.43})$$

It is proposed in [Woodgate 87] that, for a continuously differentiable function $f^i : \mathbb{R}^n \rightarrow \mathbb{R}^1$, it is convex if and only if

$$f^i(X) + \nabla_X f^i(X)^T v(Y - X) \leq f^i(Y), \forall X, Y \in \mathbb{R}^{n \times n}. \quad (\text{IV.44})$$

From above calculations in (IV.41) and (IV.42), $f^2(X)$ is continuously differentiable. Substituting (IV.41)-(IV.43) into (IV.44), one gets:

$$\begin{aligned} & f^2(X) + \nabla_X f^2(X)^T v(Y - X) \\ &= \text{tr} \left(Q_m Q_m + AXA^T AXA^T - 2AXA^T Q_m \right) \\ &\quad + 2v \left(A^T AXA^T A - A^T Q_m A \right)^T v(Y - X), \\ &= \text{tr} \left(Q_m Q_m \right) + \text{tr} \left(AXA^T AXA^T \right) - 2\text{tr} \left(AXA^T Q_m \right) \\ &\quad + 2\text{tr} \left(\left(A^T AXA^T A - A^T Q_m A \right) (Y - X)^T \right) \\ &= \text{tr} \left(Q_m Q_m \right) + \text{tr} \left(AY A^T AY A^T \right) - \text{tr} \left(AY A^T AY A^T \right) + 2\text{tr} \left(A^T AXA^T AY^T \right) \\ &\quad - 2\text{tr} \left(A^T Q_m AY^T \right) - 2\text{tr} \left(A^T AXA^T AX^T \right) \\ &= f^2(Y) - \text{tr} \left(A(Y - X) A^T A(Y - X) A^T \right). \end{aligned}$$

According to the trace property,

$$\text{tr} \left(A(Y - X) A^T A(Y - X) A^T \right) \geq 0, \forall X, Y \in SR_0^{m \times m}.$$

Therefore, condition (IV.44) is satisfied. \square

Unlike the fully-actuated case, the under-actuated case contains less degrees of freedom and the optimization Problem 1 is ill-conditioned. This sort of optimization problem has been studied in [Hua 96], [Zheng 09] under the symmetric/Hermitian matrix or positive semi-definite matrix constraint. The solution of our optimization problem is given in Proposition 6.

Proposition 6. $f^2(X)$ has a unique minimum given for $\hat{X} = V\Sigma_0^{-1}U_1^T Q_m U_1 \Sigma_0^{-1}V^T$, with V , Σ_0 and U_1 the matrices of the singular value decomposition (SVD) of A i.e.

$$A = U\Sigma V^T = \begin{pmatrix} U_1 & U_2 \end{pmatrix} \begin{pmatrix} \Sigma_0 \\ 0 \end{pmatrix} V^T, \quad (\text{IV.45})$$

where $U \in \mathbb{R}^{n \times n}$ and $V \in \mathbb{R}^{m \times m}$ are unitary matrices, satisfying $UU^T = U^T U = I$, and $VV^T = V^T V = I$. $U_1 \in \mathbb{R}^{n \times m}$, $U_2 \in \mathbb{R}^{n \times p}$, $p = n - m$, and $\Sigma_0 \in D_0^{m \times m}$ is the matrix of singular values of the matrix A .

Proof. Substituting the SVD of A (IV.45) into (IV.41), because U is unitary, one gets:

$$\begin{aligned} \min_{X \in SR_0^{m \times m}} f^2(X) &= \min_{X \in SR_0^{m \times m}} \|U\Sigma V^T X V \Sigma^T U^T - Q_m\|_F^2 \\ &= \min_{X \in SR_0^{m \times m}} \|\Sigma V^T X V \Sigma^T U^T - U^T Q_m\|_F^2 \\ &= \min_{X \in SR_0^{m \times m}} \|\Sigma V^T X \Sigma^T - U^T Q_m U\|_F^2 \\ &= \min_{X \in SR_0^{m \times m}} \left\| \begin{pmatrix} \Sigma_0 \\ 0 \end{pmatrix} V^T X \begin{pmatrix} \Sigma_0^T & 0 \end{pmatrix} - \begin{pmatrix} U_1^T \\ U_2^T \end{pmatrix} Q_m \begin{pmatrix} U_1 & U_2 \end{pmatrix} \right\|_F^2 \\ &= \min_{X \in SR_0^{m \times m}} \left\| \begin{pmatrix} \Sigma_0 V^T X V \Sigma_0^T - U_1^T Q_m U_1 & U_1^T Q_m U_2 \\ U_2^T Q_m U_1 & U_2^T Q_m U_2 \end{pmatrix} \right\|_F^2 \\ &= \min_{X \in SR_0^{m \times m}} \left\| \begin{pmatrix} \Sigma_0 V^T X V \Sigma_0^T - T_1 & T_2 \\ T_2^T & T_3 \end{pmatrix} \right\|_F^2 \\ &= \min_{X \in SR_0^{m \times m}} \left(\|\Sigma_0 V^T X V \Sigma_0^T - T_1\|_F^2 + 2\|T_2\|_F^2 + \|T_3\|_F^2 \right), \end{aligned} \quad (\text{IV.46})$$

where $T_1 = U_1^T Q_m U_1$, $T_2 = U_1^T Q_m U_2$, and $T_3 = U_2^T Q_m U_2$. Since $\|T_2\|_F^2$ and $\|T_3\|_F^2$ are given once the matrices A and Q_m are defined, the minimization problem (IV.46) becomes:

$$\min_{\bar{X} \in SR_0^{m \times m}} \|\bar{X} - T_1\|_F^2, \quad \text{with } \bar{X} = \Sigma_0 V^T X V \Sigma_0^T. \quad (\text{IV.47})$$

The solution of (IV.47) is obtained according to the Theorem 2.1 of [Higham 88] that: the nearest positive semi-definite matrix to an arbitrary matrix \mathcal{A} is unique and is given by $(\mathcal{B} + \mathcal{H})/2$ with $\mathcal{B} = (\mathcal{A} + \mathcal{A}^T)/2$ and \mathcal{H} the symmetric polar factor of \mathcal{B} [Higham 88].

In our case, $T_1 \in SR_0^{m \times m}$ hence (IV.47) admits a unique solution $\hat{X} = T_1$. Finally we get the solution of (IV.46):

$$\hat{X} = V\Sigma_0^{-1}\hat{X}\Sigma_0^{-1}V^T = V\Sigma_0^{-1}U_1^T Q_m U_1 \Sigma_0^{-1}V^T, \quad (\text{IV.48})$$

that concludes the proof. \square

Remark 13. *It is shown in Proposition 6, there exists a bound for the product $B_c^T Q_c B_c$ for the optimization Problem 1. However, the choice of controller matrices B_c and Q_c is not unique, as long as they satisfy the condition (IV.48). Several suggestions are listed below:*

$$B_c = \Sigma_0^{-1} V^T, Q_c = U_1^T Q_m U_1; \quad (\text{IV.49a})$$

$$B_c = J_m, Q_c = J_m^{-T} V \Sigma_0^{-1} U_1^T Q_m U_1 \Sigma_0^{-1} V^T J_m^{-1}. \quad (\text{IV.49b})$$

where $J_m \in \mathbb{R}^{m \times m}$ in (IV.49b) stems from the spatial discretization of $\frac{\partial}{\partial c}$.

The in-domain distributed control design procedure for the dissipative vibrating string is summarized in the following procedure as listed in Algorithm 1:

Algorithm 1 In-domain distributed control design procedure

- 1: Structure preserving discretization of the infinite dimensional port-Hamiltonian system.
 - 2: Power preserving interconnection of the discretized plant system and the controller of port-Hamiltonian formulation.
 - 3: Interconnect the state of the plant system and that of the controller with Casimir function.
 - 4: **if** the controller is fully-actuated **then**
 - 5: use (IV.38) to design the controller matrices B_c and Q_c .
 - 6: **else**
 - 7: use (IV.48) and Remark 13 to design the controller matrices B_c and Q_c .
 - 8: **end if**
-

IV.2.3 Closed loop stability

In the early lumping approach the controller is finite dimensional. In this subsection, we study the closed loop stability of the infinite dimensional system (IV.1) controlled by the finite dimensional controller (IV.32). The closed loop is formulated as:

$$\dot{\mathcal{X}} = \mathcal{J}_{cl} \mathcal{X}(t), \quad (\text{IV.50})$$

with $\mathcal{X}(0) \in L_2([0, L], \mathbb{R}^2) \times \mathbb{R}^m$ and $\mathcal{X} = \begin{pmatrix} x \\ x_{cd} \end{pmatrix} \in L_2([0, L], \mathbb{R}^2) \times \mathbb{R}^m$ and the linear operator \mathcal{J}_{cl} given by:

$$\mathcal{J}_{cl} \mathcal{X} = \begin{pmatrix} (\mathcal{J} - \mathcal{R}) \mathcal{Q} & -B B_c^T Q_c \\ B_c B^* \mathcal{Q} & 0 \end{pmatrix} \mathcal{X}. \quad (\text{IV.51})$$

We consider the following assumptions:

Assumption 4.a. *The operator \mathcal{A}_c defined by $\mathcal{A}_c \mathcal{X} = \mathcal{J}_{cl} \mathcal{X}$ generates a contraction semigroup on $L_2([0, L], \mathbb{R}^2) \times \mathbb{R}^m$.*

Assumption 4.b. *We also consider the compactness of the closed loop resolvent set.*

The closed loop asymptotic stability relies on Lyapunov arguments and LaSalle's invariance principle (Theorem 3.64 of [Luo 12]) and is expressed in Theorem 1.

Theorem 1. *For any $\mathcal{X}(0) \in L_2([0, L], \mathbb{R}^2) \times \mathbb{R}^m$, the unique solution of (IV.50) tends to zero asymptotically, and the closed loop system (IV.50) is globally asymptotically stable.*

Proof. Choosing the energy of the closed loop system as Lyapunov function, with (IV.11), (IV.16), (IV.17) and (IV.32), we have

$$\begin{aligned}
\frac{dH_{cl}}{dt}(t) &= \frac{dH}{dt}(t) + \frac{dH_{cl}}{dt}(t) \\
&= \mathbf{y}_d^T(t) \mathbf{u}_d(t) - \int_{\zeta} e_2(\zeta, t)^T R e_2(\zeta, t) d\zeta + \mathbf{u}_c^T(t) B_c^T Q_c x_{cd}(t) \\
&= \mathbf{y}_d^T(t) \mathbf{u}_d(t) - \int_{\zeta} e_2(\zeta, t)^T R e_2(\zeta, t) d\zeta + \mathbf{u}_c^T(t) (\mathbf{y}_c(t) - D_c \mathbf{u}_c(t)) \quad (\text{IV.52}) \\
&= - \int_{\zeta} e_2(\zeta, t)^T R e_2(\zeta, t) d\zeta - \mathbf{u}_c^T(t) D_c \mathbf{u}_c(t) \\
&\leq - \int_{\zeta} e_2(\zeta, t)^T R e_2(\zeta, t) d\zeta \\
&\leq 0.
\end{aligned}$$

Using LaSalle's invariance principle it remains to show that the only solutions associated with $\frac{dH_{cl}}{dt}$ is 0 i.e the only solutions associated with $e_2 = 0$ is zero. e_2 denotes the velocity. Due to the internal dissipation and zero boundary input, the only solution associated with this problem is 0. The controller being a simple integrator, if well initialized it also converges to 0 as the state of the system converges to 0. \square

IV.3 NUMERICAL SIMULATIONS

We consider here the vibrating string example with length $L = 2$ m, stiffness $T = 1.4 \times 10^6$ N and density $\rho = 1.225$ kg/m in a clamped-free scenario $x_1(L, t) = x_2(0, t) = 0$. The dissipation term $R = 10^{-3}$. The initial conditions are set to a spatial distribution $x_1(\zeta, 0) \sim \mathcal{N}(1.5, 0.113)$ for the strain distribution and to zero for the velocity distribution *i.e.*, $x_2(\zeta, 0) = 0$. The string is discretized into 50 elements. To be more precise, we consider a time step of 5×10^{-5} s and mid-point time discretization method (see details about this time integration in Appendix C) for simulations. The open loop evolution of the strain $x_{1d}(t)$ and of the Hamiltonian are given in Fig. IV.5a and IV.5b.

Next we investigate the numerical simulations of the closed-loop system considering both fully-actuated and under-actuated cases.

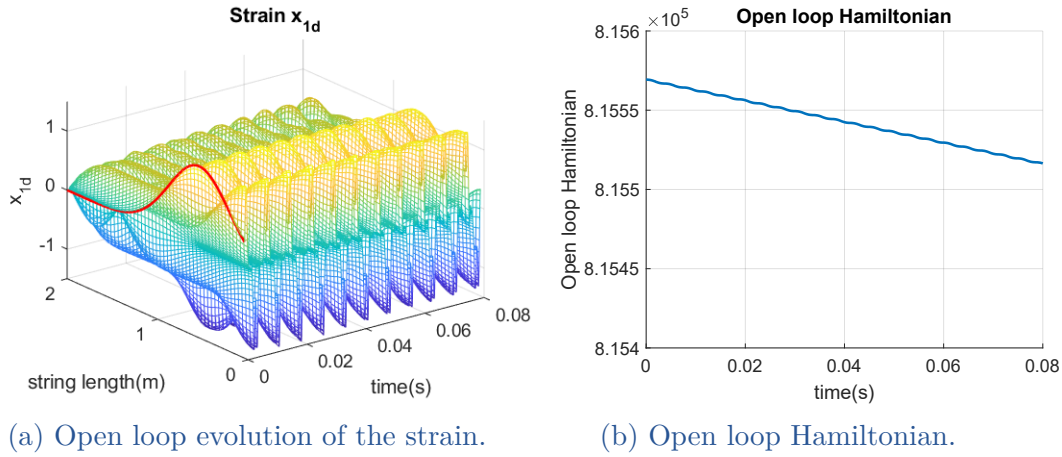


Figure IV.5 – Open loop simulation.

IV.3.1 Fully-actuated case

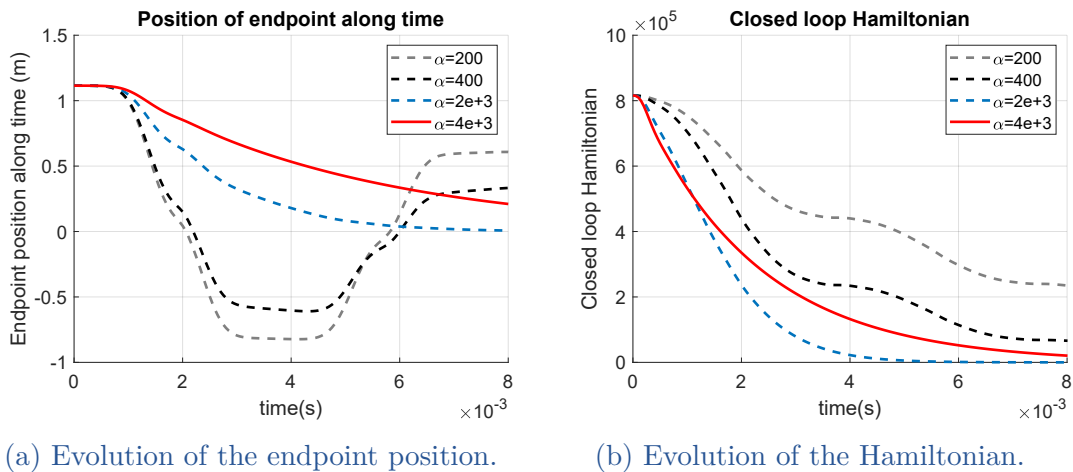
The matrix b_d is formulated in (IV.37). Following Proposition 5 we choose $B_c = J_i$. From Proposition 4, the initial conditions of the controller are chosen such that $C = 0$. In this case (IV.21) becomes:

$$x_{cd} = x_{1d},$$

and the closed loop system (IV.23) reads:

$$\begin{pmatrix} \dot{x}_{1d} \\ \dot{x}_{2d} \end{pmatrix} = \begin{pmatrix} 0 & J_i \\ -J_i^T & -(R_d + D_c) \end{pmatrix} \begin{pmatrix} \tilde{Q}_1 x_{1d} \\ Q_2 x_{2d} \end{pmatrix}.$$

One can see that *the equivalent* closed loop stiffness \tilde{Q}_1 can be shaped through


 Figure IV.6 – Closed loop simulation in the fully-actuated case with pure damping injection and different damping coefficients α .

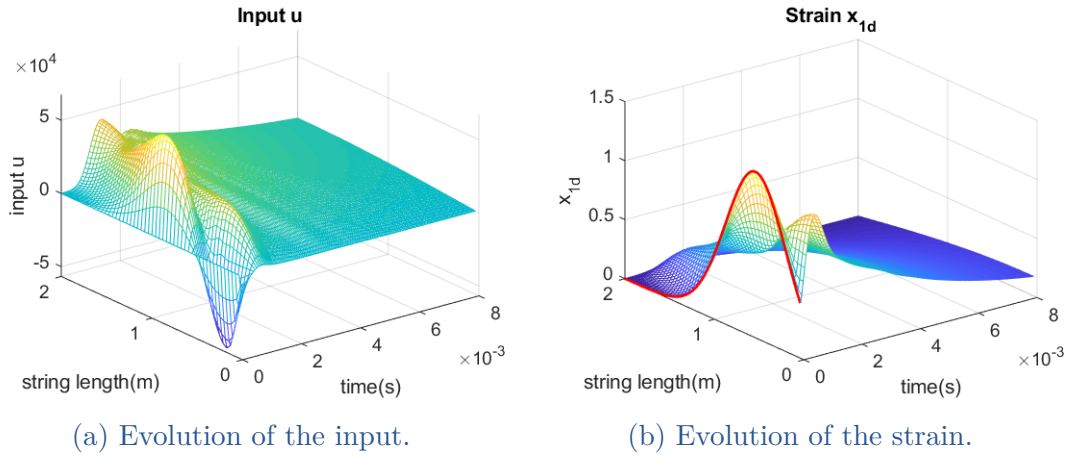


Figure IV.7 – Closed loop simulation in the fully-actuated case with pure damping injection and with $\alpha = 4 \times 10^3$.

the choice of Q_c . The control law is given by:

$$\begin{aligned}
 \mathbf{u}_d &= -\mathbf{y}_c \\
 &= -B_c^T Q_c x_{cd} - D_c \mathbf{y}_d \\
 &= -B_c^T Q_c x_{1d} - D_c b_d^T Q_2 x_{2d}.
 \end{aligned} \tag{IV.53}$$

Fully-actuated case with only the damping injection In a first instance we consider the pure damping injection case, *i.e.* varying D_c with $Q_c = 0$. Given:

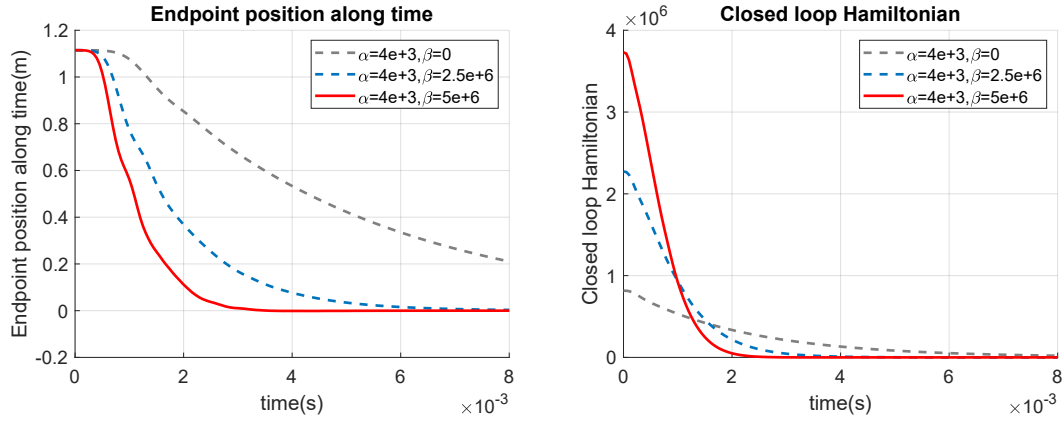
$$D_c = \text{diag}(\alpha L_{ab}) \in \mathbb{R}^{n \times n}, \tag{IV.54}$$

with α denoting the damping coefficient. In Fig. IV.6a and IV.6b one can notice that, in a certain interval, the bigger α is, the faster the closed-loop system converges to zero. But once α continues to augment for example $\alpha = 4 \times 10^3$, the system becomes over-damped and slow. Figure IV.7a and IV.7b illustrate the evolution of the distributed input and that of the strain along time and space with the over-damped phenomenon. We can conclude that this degree of freedom allows to damp the vibrations of the string to the detriment of the time response.

Fully-actuated case with the damping injection and the energy shaping Next we fix $\alpha = 4 \times 10^3$ corresponding to the aforementioned slightly over-damped case in order to illustrate the effect of the energy shaping on the achievable performances. The energy matrix of the controller Q_c is formulated by :

$$Q_c = \text{diag}\left(\frac{\beta}{L_{ab}}\right), \tag{IV.55}$$

where β is the energy shaping parameter. We can see in Fig. IV.8a that we can speed up the closed-loop system by augmenting β and therefore increasing the closed loop stiffness via the energy shaping, without introducing any overshoot. A



(a) Evolution of the endpoint position.

(b) Evolution of the Hamiltonian.

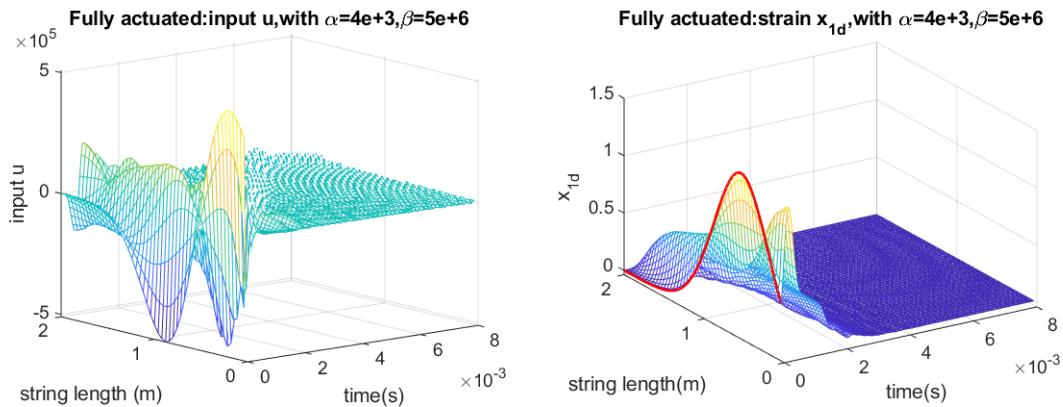
Figure IV.8 – Close loop simulation in the fully-actuated case with energy shaping and damping injection and with different energy shaping parameters β .

good dynamic performance is achieved when $\beta = 5 \times 10^6$. According to (IV.38), this tuning value makes the energy matrix with respect to x_1 in the closed loop be:

$$\tilde{Q}_1 = Q_1 + Q_c = \frac{T + \beta}{L_{ab}} = \frac{6.4 \times 10^6}{L_{ab}}, \quad (\text{IV.56})$$

which is relates to an equivalent string stiffness of $\tilde{T} = 6.4 \times 10^6 \text{N}$.

The evolution of the distributed input and of the strain along time with both the damping injection and the energy shaping for $\alpha = 4 \times 10^3$ and $\beta = 5 \times 10^6$ are given in Fig. IV.9a and IV.9b, respectively. We can see in Fig. IV.9a that the control remains smooth. Fig. IV.9b shows that the closed-loop stabilization time is about $3 \times 10^{-3} \text{s}$ which is much faster than $8 \times 10^{-3} \text{s}$ resulting from the pure damping injection case as depicted in Fig. IV.7b.



(a) Evolution of the input.

(b) Evolution of the strain.

Figure IV.9 – Close loop simulation in the fully-actuated case with energy shaping and damping injection and with $\alpha = 4 \times 10^3$, $\beta = 5 \times 10^6$.

IV.3.2 Under-actuated case

We now consider that the control is achieved using m patches as depicted in Fig. IV.4 with $k = n/m$. The aim of the controller design is to modify as far as possible the internal elasticity \tilde{T} of the string. The controller matrices B_c and Q_c are chosen as formulated in (IV.49b). D_c is chosen such that the time derivative of the Hamiltonian formulated in (IV.34) behaves similarly as in the fully-actuated case, *i.e.* in order to satisfy

$$\min_{D_c \in \mathbb{R}^{m \times m}} \|b_d D_c b_d^T + R_d - \text{diag}(\alpha L_{ab}) - R_d\|_F,$$

where b_d is given in (IV.40). This optimization problem is similar to Problem 1, and the optimal D_c is given by

$$\hat{D}_c = \text{diag}\left(\frac{\alpha L_{ab}}{k}\right).$$

The control law now becomes:

$$\begin{aligned} \mathbf{u}_d &= -\mathbf{y}_c \\ &= -B_c^T Q_c x_{cd} - \hat{D}_c \mathbf{y}_d \\ &= -B_c^T Q_c B_c b_d^T J_i^{-1} x_{1d}(t) - \hat{D}_c b_d^T Q_2 x_{2d}. \end{aligned} \quad (\text{IV.57})$$

We first consider the case with 10 patches, *i.e.* $n = 50$ and $k = 5$. In this case the input and strain evolution is quite similar to the one obtained in the fully-actuated case as depicted in Fig. IV.10a and IV.10b. This indicates that if the controller matrices B_c , Q_c and D_c are adequately selected, the achievable performances in the under-actuated case can be optimized in order to be close to the ones obtained in the fully-actuated case as depicted in Fig. IV.9.

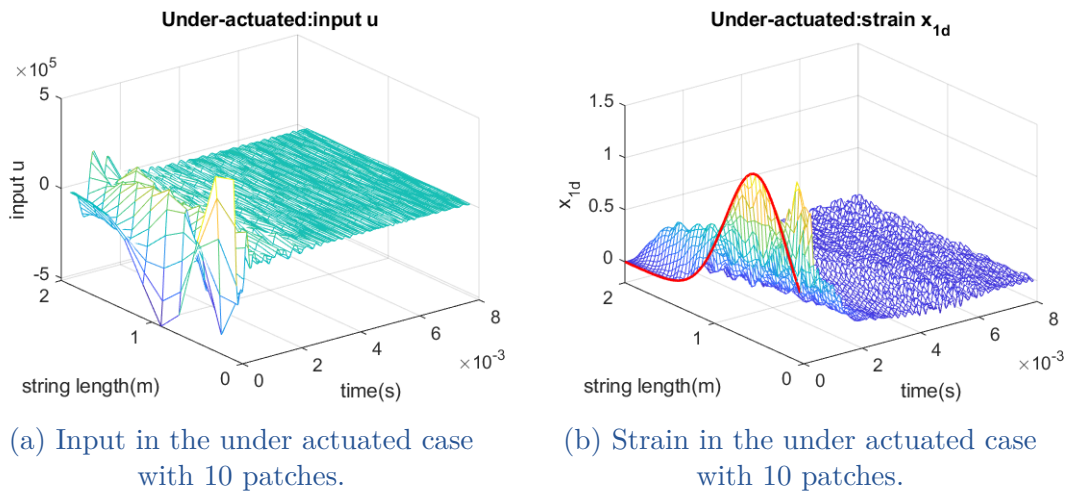
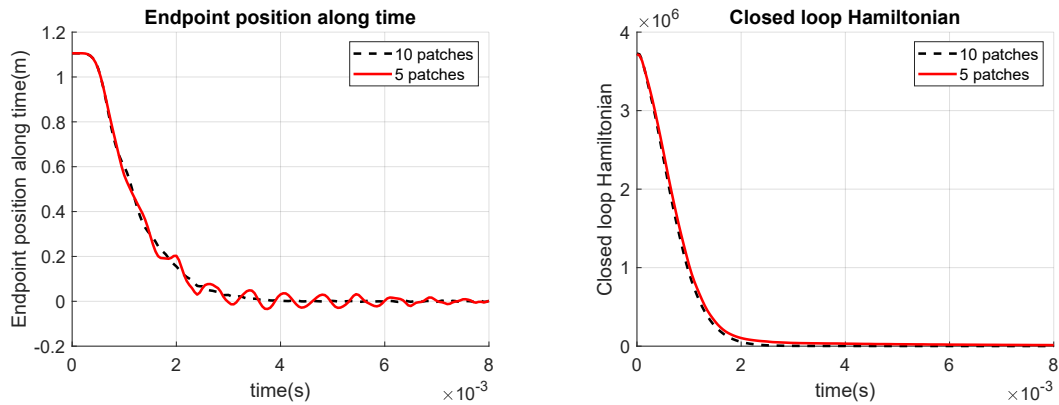


Figure IV.10 – Evolution of the closed loop in the energy shaping and damping injection case with under actuation with 10 patches.

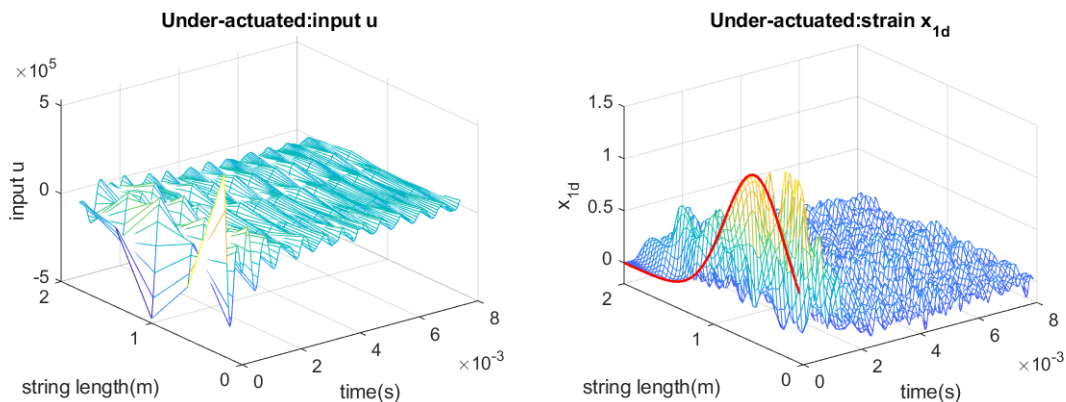
When the number of patches is reduced to 5, *i.e.* $n = 50$ and $k = 10$ these performances are slightly deteriorated in the high frequencies as shown in Fig. IV.11a, where a more significant oscillation for the endpoint displacement is observed with only 5 patches. The closed loop Hamiltonian converges also slightly lower with 5 patches than that with 10 patches. These oscillations are also evident



(a) Comparison of endpoint positions. (b) Comparison of closed loop Hamiltonian.

Figure IV.11 – Comparisons in the under-actuated case with 10 patches and 5 patches, respectively.

by comparing the control input and strain evolution in Fig. IV.12a and IV.12b with Fig. IV.10a and IV.10b.



(a) Input in the under actuated case with 5 patches.

(b) Strain in the under actuated case with 5 patches.

Figure IV.12 – Evolution of the closed loop in the energy shaping and damping injection case with under actuation with 5 patches.

In order to illustrate the effect of the neglected dynamics on the achievable performances we implement the controller designed considering 10 patches on the discretized system where $n = 50$ to a more precise model of the string derived using the discretization number $n = 200$. In Fig. IV.13 we can see that, due to

the damping injection and the associated closed loop bandwidth, the neglected dynamics do not impact significantly the closed loop response of the system to the considered initial condition.

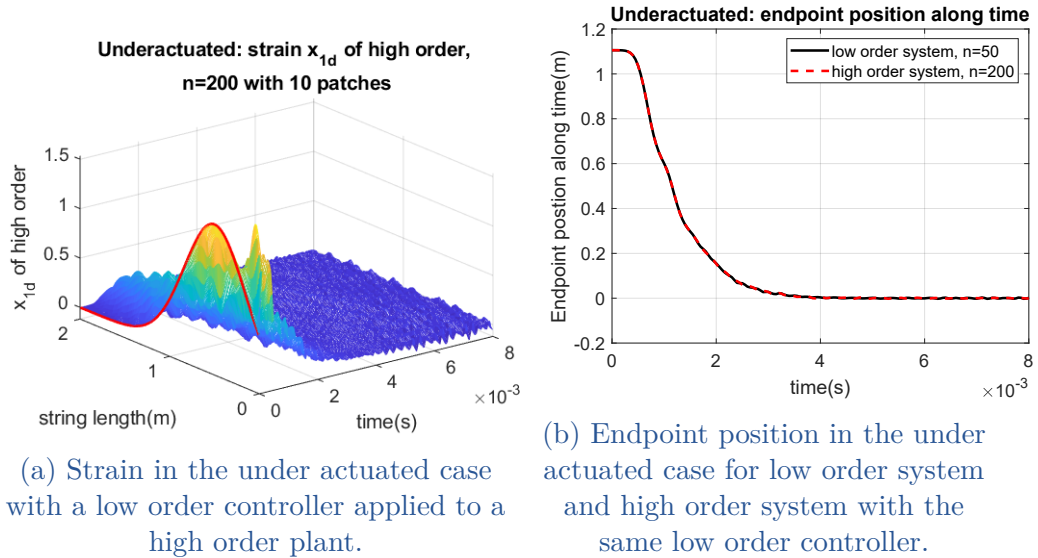


Figure IV.13 – Closed loop evolution of the strain of the high order system, and comparison of the endpoint position of the low order and high order systems using the same controller.

IV.4 SUMMARY

In this chapter we consider the in-domain distributed control of the infinite dimensional PHS using an early lumping approach. For the sake of clarity and compactness, the plant system is formulated with the example of a dissipative vibrating string. For control design purposes, we extend the CbI method to the use of controllers distributed in space. The distributed structural invariants, *i.e.* the Casimir functions, are used to interconnect the state variables of the discretized plant system and the state variables of the controller and herein to modify the closed loop potential energy of the system, *e.g.* the stiffness of the vibrating string example.

Two different cases of the controller design are investigated due to the independent number of inputs: the ideal case where the system is fully-actuated and the under-actuated case where the control action is achieved using piecewise homogeneous inputs. In this latter case the controller is derived by optimization.

As for the early lumping approach, the stability of the closed loop between the infinite dimensional system and the finite dimensional controller is studied. With our controller a PHS and the CbI to keep the passivity, the closed loop system is asymptotically stable.

Simulations of both fully-actuated and under-actuated cases show that the damping injection renders the system asymptotically stable, while the energy shaping improves the dynamic performances of the closed loop system. Comparisons of the two cases also indicate that with an appropriate choice of the controller parameters, one can achieve similar performances for the under and fully-actuated cases over a given range of frequencies.

Conclusions and perspectives

CONCLUSIONS

This thesis is concerned with the modeling and control of micro-endoscopes actuated by electro-active polymer actuators. The low driven voltage, large deformation, wide bandwidth and good biocompatibility make the ionic polymer metal composite (IPMC) a well suited actuator proposed for smart micro-endoscopes in minimally invasive surgeries. The models are established under the port-Hamiltonian framework in order to tackle the multiphysical coupling and to design the controller using the control by interconnection (CbI) approach.

In Chapter I is provided a literature review on different kinds of endoscopes and actuation approaches, as well as the designing models of micro-endoscopes. A detailed introduction of the structure, working principles, applications as well as the existing models of the IPMC actuator is given. The multiphysical and multiscale model of the IPMC actuated endoscopes make the port-Hamiltonian framework necessary to deal with the interconnections. The technical background of both finite dimensional PHS and infinite dimensional PHS is given. To modify the dynamic performance and to carry out shape control of micro-endoscopes, the passivity based control is introduced under the port-Hamiltonian framework, especially the CbI approach.

Chapter II is devoted to the modeling of the IPMC actuator and of the endoscope. The IPMC model is derived using the infinite dimensional port-Hamiltonian formulation, including the electrical, the electro-stress diffusion and the mechanical components of the system. This modeling is based on the work already done by Nishida [Nishida 08, Nishida 11]. The originality of the proposed model with respect to [Nishida 08, Nishida 11] is the different assumptions it considers and the use of Lagrange multipliers to deal with the mechanical constraints between the electro-stress diffusion system and the mechanical system resulting from the local homogeneous deformation assumption for the gel in the IPMC actuator. The Stokes-Dirac structure of the overall IPMC actuator is pointed out in Proposition 1. Different from [Nishida 08, Nishida 11], we consider the bending moments generated in the electro-stress diffusion system as an external input for the mechanical system in order to avoid the potential singularity that may happen in [Nishida 08, Nishida 11] when the deformation is homogeneous. We also model the mechanical structure of the actuated endoscope with three kinds of models: the Timoshenko beam model for the small deformation case, the infinite dimensional inertial frame reference model for the large deformation case and the Soedel's model under the cylindrical coordinates for the 2D elastic thin shell case.

In Chapter III, we extend the existing structure preserving discretization methods: the mixed finite element method and the finite difference method on staggered grids to the dissipative PHS with distributed input. Comparisons of these two discretization approaches show that the finite difference method on staggered grids has the benefit of simplicity and the mixed finite element method can get more precise approximated solution with less discretization numbers compared to its counterpart. We herein use the finite difference method on staggered grids to approximate the established IPMC actuator model and validate the model with the experimental data.

The objective of Chapter IV is the design of an in-domain distributed control law in order to modify the dynamic performances of the closed loop and to guarantee its stability. For the sake of simplicity and clarity we consider in this chapter the simplified control problem of an elastic string actuated by actuator patches. We apply the early lumping approach to design a finite dimensional controller on the basis of the discretized plant system, which is related to our studied problem. Two cases are investigated, the ideal fully-actuated case and the under-actuated case, depending on the independent number of inputs. The CbI approach is used to keep the passivity of the closed loop system. The Casimir function based structural invariants are used to relate the states of the controller with that of the plant. The originality lies in the fact that the controller is distributed in space, bringing new degrees of freedom as soon as the control design is concerned. Two methodologies of the passivity based control are applied: the energy shaping to modify the potential energy of the closed loop system and therefore modify the dynamic performances, and the damping injection to render the system asymptotically stable. We then study the stability of the closed loop system when the finite dimensional controller is applied to the infinite dimensional plant system in Theorem 1. For the ideal fully-actuated case, we can obtain the analytic solution of controller matrices for a given desired potential energy in Proposition 5, but we can only get an optimal solution for the under-actuated case using the singular value decomposition in Remark 13. It is shown in the simulations that with appropriate choice of the controller matrices, we can get similar dynamic performance in the under-actuated case than in the fully-actuated case. The passivity of the closed loop system is preserved due to the power preserving interconnection. We can guarantee the asymptotic stability when we apply the finite dimensional controller to the infinite dimensional plant.

FUTURE WORK AND PERSPECTIVES

There are several interesting perspectives for this work.

From the application point of view, the proposed models and control strategies still have to be adjusted and applied to a real flexible micro endoscope. The practical design and the instrumentation of such complex micro-system is quite demanding and the fabrication of multi actuated structures is still under progress.

From the methodological point of view, many research lines remain open. About the modeling, the structure preserving finite difference method on staggered grids has been used to discretize the proposed IPMC model due to its simplicity. However, a large number of discretization elements are needed to match the experimental data in a precise way. It would be important to reduce the order of the discretized model such that the model becomes more suitable for simulation of complex structures and for the control design. To this end, we propose possible solutions for future work. Based on the simulation comparison in Chapter III, the mixed finite element method can approximate the infinite dimensional plant with much fewer discretized elements than the finite difference method on staggered grids. Hence, the use of the mixed finite element method to the proposed infinite dimensional IPMC actuator model could be interesting to obtain a lower order discretized model. Second, in the literature, different structure preserving model reduction methods for large scale finite dimensional port-Hamiltonian system are presented [Polyuga 10, Polyuga 12]. One can adopt these methods to reduce the high order discretized model for control design purpose. It would also be interesting to push forward this model order reduction to its limit in order to get an equivalent first order/second order dynamic system, even if non-linear.

In this work, only the 1D IPMC model has been simulated and compared with the experimental data. Since we proposed the 2D shell model for such systems, it would be very interesting to validate this 2D model on an experimental setup. To do so, the 2D structure preserving discretization methods [Liu 20] can be employed to discretize the 2D infinite dimensional model and to validate the 2D model with the experimental data. At the same time, the control methodology for the proposed 2D model remains challenging and worth to investigate in the future.

For the control design aspect, this thesis first considered the in-domain control of vibrating string. Interesting work is to apply the proposed control methodology to a larger class of systems such as beam equations. The adaptation of the proposed control law to the endoscope model is also worth investigating in the future. The proposed in-domain CbI method focuses on the performances assignment in the closed loop system using the early lumping approach. The robustness of this control method has not been considered and necessitates further investigations. Furthermore the controller that is designed using state feedback or dynamic extension and needs appropriate initialization. In order to overcome this limitation one has to design a state observer. Many works on observer design using port-Hamiltonian formulations have been recently investigated. An interesting perspective is the combination of these approaches with the in-domain control techniques we consider in this thesis. A long term perspective to this control design technique is the use of similar strategy for multidimensional systems.

Appendix A

Bond Graph

A.1	Nodes with one port	122
A.2	Nodes with two ports	124
A.3	Nodes with multiple ports	124

The concept of the Bond Graph was firstly raised out in [Paynter 61], and was later developed to illustrate the dynamics of the system and the signal flow geometrically. Because of its modeling based on flow and effort variables, which are derived from the energy of the system, this Bond Graph is very powerful in terms of the multiphysical system interconnections. It is mainly composed of nine node types sorted in five categories [Duindam 09]:

- Boundary conditions: ‘Se’ (source of effort) and ‘Sf’ (source of flow).
- Interconnections: ‘0’ junction and ‘1’ junction.
- Storage elements: ‘I’ element and ‘C’ element.
- Dissipation element: ‘R’ element.
- Reversible transformation: ‘TF’ (transformer) and ‘GY’ (gyrator).

Additionally, for distributed parameter systems, we add the node ‘DTF’ (differential transformer) to illustrate the Stokes-Dirac structure. Moreover, for the multiscale system, we add another node ‘BMS’ (boundary multiscale coupling) for the interconnections of two different domains. These aforementioned elements are connected with each other via their *ports* through the *bonds* (the half arrow in the Bond Graph).

As power is the common language in terms of different physical domains, the power conjugated flow f and effort variables e are added in the Bond Graph. Conventionally, effort variables are positioned above or on the left of the bond, while flow variables are below or on the right [Duindam 09], as shown in Fig. ???. The direction of the half arrow indicates the direction of the power flow. Besides, to make sure that the established model causal, the causality should also be pointed out, which is the causal stroke in the Bond Graph (e.g. labeled red stroke in Fig. A.4a). The causal stroke is placed at the end of the bond where the effort variables goes out [Duindam 09].

In what follows, we will make a detailed explanation of the constitutive relations about these node types.

A.1 NODES WITH ONE PORT

The ‘Se’ and ‘Sf’ elements are depicted in Fig. A.1. They can model the exerted force for mechanical system, or the applied voltage for electrical system, etc. As the former describes the source of effort and the later is related to the source of flow, their causalities are fixed.



Figure A.1 – Bond Graph representations of Se and Sf.

The ‘R’ element models the dissipation term in the system, e.g. the damper in mechanical system or the resistor in electrical circuit. The relation between flow and effort variables for a linear ‘R’ element is:

$$e = Rf,$$

which is depicted in Fig. A.2. For nonlinear representation, one is referred to [Borutzky 10]. The causality for ‘R’ element is free to choose, as long as it fits the causality of the entire system.

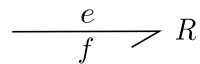


Figure A.2 – Bond Graph of linear R element.

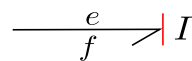
The ‘I’ and ‘C’ element are related to the power storage. The two differ in terms of either the time integration is related to effort variables e or to flow variables f . The ‘I’ element can model for example the inertial in mechanical system or the inductor in electrical circuit, representing the storage of kinetic energy or of magnetic energy, respectively [Borutzky 10]. Its constitutive relation is formulated as:

$$f = \frac{1}{I} \int e \, dt,$$

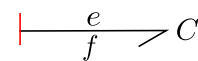
which is represented in Fig. A.3a. The ‘C’ element can model the spring in mechanical system or the capacitor in electrical circuit, with the constitutive equations written as:

$$e = \frac{1}{C} \int f \, dt,$$

which is illustrated in Fig. A.3b. The causalities for storage elements are divided into integral causality and differential causality, depending on whether the causes is integrated or differentiated [Borutzky 10]. In conventional modeling, an **integral** causality is preferred to a differential causality. One can find in Fig. A.3 of the ‘I’ element and ‘C’ element with integral causality.



(a) I element.



(b) C element.

Figure A.3 – Bond Graph representations of ‘I’ and ‘C’ with integral causality.

A.2 NODES WITH TWO PORTS

The ‘TF’ and ‘GY’ are two port elements, modeling the power transducer of two pairs of power conjugated variables f_1, e_1 and f_2, e_2 , e.g. gear transmission for ‘TF’ and DC motor for ‘GY’. The constitutive relations of ‘TF’ and ‘GY’ read:

$$\begin{aligned} \text{TF: } f_1 &= k f_2, & e_1 &= \frac{1}{k} e_2, \\ \text{GY: } f_1 &= \frac{1}{r} e_2, & e_1 &= r f_2. \end{aligned}$$

Their causality are also free, under the constrains that the ‘TF’ has only **one** causal stroke close to it while the ‘GY’ has either **two** causal strokes close to it or away from it [Duindam 09], which is illustrated in Fig. A.4.

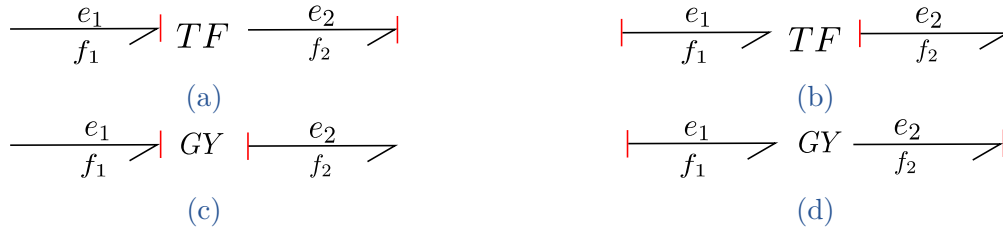


Figure A.4 – Bond Graph representations of ‘TF’ and ‘Se’.

A.3 NODES WITH MULTIPLE PORTS

In terms of the causality, the multi-ports ‘0’ junction and ‘1’ junction describe the power distribution. The former has common effort variables, and their flow variables sum to zero. While the latter share common flow variables with effort variables summing to zero. Herein, their constitutive relations are:

$$\begin{aligned} \text{‘0’ junction: } f_1 + f_2 + \dots + f_n &= 0, & e_1 &= e_2 = \dots = e_n, \\ \text{‘1’ junction: } e_1 + e_2 + \dots + e_n &= 0, & f_1 &= f_2 = \dots = f_n. \end{aligned}$$

The ‘0’ junction can only have one causal stroke close to it, while the ‘1’ junction can only have one away from it. One can find the representation of these two junctions in Fig. A.5a and A.5b with a causal example.

Apart from the aforementioned nine node types, we have also largely used the node ‘DTF’ during the modeling of distributed parameter systems in Chapter II. The element ‘DTF’ refers to the Stokes-Dirac structure [Baaiu 07]. It has two main ports in the domain and two boundary ports. Taking an example of a 1D distributed parameter system formulated under the port-Hamiltonian framework:

$$\begin{pmatrix} f_1 \\ f_2 \end{pmatrix} = \begin{pmatrix} \frac{\partial x_1}{\partial t} \\ \frac{\partial x_2}{\partial t} \end{pmatrix} \begin{pmatrix} 0 & \frac{\partial}{\partial \zeta} \\ \frac{\partial}{\partial \zeta} & 0 \end{pmatrix} \begin{pmatrix} e_1 \\ e_2 \end{pmatrix},$$



(a) Bond Graph of ‘0’ junction.

(b) Bond Graph of ‘1’ junction.

Figure A.5 – Bond Graph representation of node types with multi-ports.

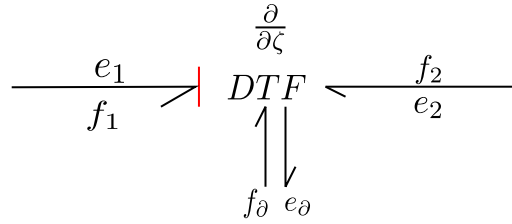
with its boundary port variables f_∂ and e_∂ defined according to (I.25). The system defines a Stokes-Dirac structure that is written as:

$$\mathcal{D} = \left\{ \left(\begin{pmatrix} f \\ f_\partial \end{pmatrix}, \begin{pmatrix} e \\ e_\partial \end{pmatrix} \right) \in \mathcal{F} \times \mathcal{E} \mid f_1 = \frac{\partial e_2}{\partial \zeta}, f_2 = \frac{\partial e_1}{\partial \zeta}, \begin{pmatrix} f_\partial \\ e_\partial \end{pmatrix} \text{ calculated by (I.25)} \right\},$$

with the flow space \mathcal{F} and effort space \mathcal{E} given by:

$$\mathcal{F} = \left\{ \begin{pmatrix} f \\ f_\partial \end{pmatrix} \in L_2([a, b], \mathbb{R}^n) \times \mathbb{R}^2 \right\}, \quad \mathcal{E} = \left\{ \begin{pmatrix} e \\ e_\partial \end{pmatrix} \in H^1([a, b], \mathbb{R}^n) \times \mathbb{R}^2 \right\}.$$

This Stokes-Dirac structure can be represented with the element ‘DTF’ as follows:


Figure A.6 – Bond Graph representation of *DTF*.

The introduction of the last multi-ports node ‘BMS’ has been detailed in Section II.2.4 at page 43.

Appendix B

Differential forms

In this part we give several definitions related to the differential forms, which serves in the mixed finite element discretization of infinite dimensional PHS in Subsection III.1.1.

To start this part, we will give a brief introduction of manifolds. The manifold is an abstract space, that can locally be described by an Euclidean space [Duindam 09]. A direct example of the manifold is the surface of the earth, which is globally a sphere, but can be presented locally with the coordinates in \mathbb{R}^2 .

Definition 3 (Differential forms [Flanders 63]). *A k -form at point K is expressed as:*

$$\sum a_H dx^{h_1} \dots dx^{h_k},$$

with a_H constants.

A k -form on the manifold \mathcal{M} is a smooth assignment of a k -form to each point K of \mathcal{M} .

Here are some examples of common used k -forms [Golo 02, Flanders 63]. Functions $f(x)$ which can be evaluated at any point of the spatial domain x define a 0-form.

A line integral

$$\int A dx + B dy + C dz$$

defines a 1-form

$$w = A dx + B dy + C dz.$$

A surface integral

$$\iint P dy dz + Q dz dx + R dx dy$$

defines a 2-form

$$w = P dy dz + Q dz dx + R dx dy.$$

Similarly, a volume integration defines a 3-form.

Concerning to the differential forms, several calculus operator are defined hereafter.

Definition 4 (Wedge product). *A wedge product (represented by \wedge) of two differential forms, a k -form $\alpha \in \Omega^k(M)$ and an l -form $\beta \in \Omega^l(M)$ is a $(k+l)$ -form $\alpha \wedge \beta$ [Ivancevic 07].*

The wedge product is associative, i.e.

$$(\alpha \wedge \beta) \wedge \gamma = \alpha \wedge (\beta \wedge \gamma),$$

and skew-symmetric, i.e.

$$\alpha \wedge \beta = (-1)^{kl} \beta \wedge \alpha.$$

To relate the differential forms of different degrees, the Hodge star is introduced, which is defined as follows:

Definition 5 (Hodge star). *For an n -dimensional Riemannian manifold Ω^n , the Hodge star, denoted by $*$, renders the k -form into $(n - k)$ -form.*

Besides the product operations, an operator which unifies the gradient, curl and divergence [Flanders 63] of differential forms is also proposed:

Definition 6 (Exterior derivative). *The exterior derivative, noted by d , is a derivation that transforms k -forms into $(k + 1)$ -forms [Ivancevic 07].*

Appendix C

Time integration

After the spatial discretization of PDEs, the system turns to be certain ordinary differential equations (ODEs) $\dot{x} = f(x)$. The numerical time integration is necessary to simulated the evolution of the states. Based on the literature, a variety of numerical integration approaches are available, such as the simple approaches: explicit (or implicit) Euler method, the implicit midpoint rule, the symplectic Euler method, the leap-frog method, and sophisticated the Runge-Kutta methods etc [Hairer 06]. It has been shown that either the explicit or implicit Euler method introduces significant numerical errors (either spirals outwards or inwards in contrast to the exact solution trajectory [Hairer 06]) when it comes to long time integration. While the symmetric methods like implicit midpoint, symplectic Euler and leap-frog have little numerical discrepancy. Moreover, the implicit midpoint rule could be considered as a special case of the Gauss collocation (a subclass of the Runge-Kutta method) with 1 stage and a collocation parameter equal to $\frac{1}{2}$ [Hairer 06]. When applied to the port-Hamiltonian systems, the numerical integration is required to be structure preserving and conservative of the invariant, i.e. the Hamiltonian for a non-autonomous system.

It has been proven in [Aoues 13] that the implicit midpoint rule satisfies both the structure-preservation and the energy conservation. Hence, it is well suited for the numerical integration of the PHS. The algorithm is formulated by:

$$x_{n+1} = x_n + \Delta t f\left(\frac{x_{n+1} + x_n}{2}\right), \quad (\text{C.1})$$

where Δt denotes the time step. The implicit lies in the fact that the approximation x_{n+1} is calculated implicitly by the known value of x_n [Hairer 06].

For a linear spatial discretized finite dimensional PHS, the dynamic equation is given by:

$$\begin{aligned} \dot{x} &= (J - R)Qx + Bu, \\ y &= B^T Qx. \end{aligned} \quad (\text{C.2})$$

Substituting the integration scheme (C.1) into (C.2), one obtains the discrete linear PHS [Aoues 13]:

$$\frac{x_{n+1} - x_n}{\Delta t} = (J - R)Q\frac{x_{n+1} + x_n}{2} + Bu_n, \quad (\text{C.3})$$

$$y_n = B^T Q\frac{x_{n+1} + x_n}{2}. \quad (\text{C.4})$$

After simple computations, (C.4) gives the explicit algorithm of calculating x_{n+1} and y_{n+1} :

$$x_{n+1} = f_{mid}^{-1}\left(\left(I + \frac{\Delta t}{2}(J - R)Q\right)x_n + \Delta t Bu_n\right), \quad (\text{C.5})$$

$$y_{n+1} = \frac{1}{2}B^T Q\left(f_{mid}^{-1}\left(I + \frac{\Delta t}{2}(J - R)Q\right) + I\right)x_n + \frac{\Delta t}{2}B^T Qf_{mid}^{-1}Bu_n, \quad (\text{C.6})$$

with

$$f_{mid} = I - \frac{\Delta t}{2}(J - R)Q,$$

and I the identity matrix of appropriate size.

Remark 14. *As it is noted before, the implicit midpoint rule is a special case of the Runge-Kutta method. The latter has also been applied to the time integration of PHS, see [Kotyczka 18a].*

Bibliography

- [Abd-El-Barr 13] M. M. Abd-El-Barr & A. R. Cohen. *The origin and evolution of neuroendoscopy*. Child's Nervous System, vol. 29, no. 5, pages 727–737, may 2013.
- [Aoues 13] S. Aoues, D. Eberard & W. Marquis-Favre. *Canonical interconnection of discrete linear port-Hamiltonian systems*. In 52nd IEEE Conference on Decision and Control, pages 3166–3171. IEEE, dec 2013.
- [Asaka 14] K. Asaka & H. Okuzaki. Soft actuators: Materials, modeling, applications, and future perspectives, volume 9784431547679. Springer Japan, jul 2014.
- [Aureli 10] M. Aureli, C. Prince, M. Porfiri & S. D. Peterson. *Energy harvesting from base excitation of ionic polymer metal composites in fluid environments*. Smart Materials and Structures, vol. 19, no. 1, page 015003, jan 2010.
- [Baaiu 07] A. Baaiu. *Approche hamiltonienne pour la modélisation, l'estimation et la commande d'un procédé de séparation*. PhD thesis, Université de Lyon 1, 2007.
- [Baaiu 09] A. Baaiu, F. Couenne, L. Lefevre, Y. Le Gorrec & M. Tayakout. *Structure-preserving infinite dimensional model reduction: Application to adsorption processes*. Journal of Process Control, vol. 19, no. 3, pages 394–404, mar 2009.
- [Balas 78] M. J. Balas. *Active control of flexible systems*. Journal of Optimization Theory and Applications, vol. 25, no. 3, pages 415–436, jul 1978.
- [Bao 02] X. Bao, Y. Bar-Cohen & S.-S. Lih. *Measurements and macro models of ionomeric polymer-metal composites (IPMC)*. In Y. Bar-Cohen, editeur, Smart Structures and Materials 2002: Electroactive Polymer Actuators and Devices (EAPAD), pages 220 – 227. SPIE, 2002.
- [Bar-Cohen 04] Y. Bar-Cohen. *Electroactive Polymer (EAP) Actuators as Artificial Muscles: Reality, Potential, and Challenges*, Second Edition. SPIE, 1000 20th Street, Bellingham, WA 98227-0010 USA, mar 2004.
- [Berzeri 00] M. Berzeri & A. Shabana. *Development of simple models for the elastic forces in the absolute nodal co-ordinate formulation*. Journal of Sound and Vibration, vol. 235, no. 4, pages 539–565, 2000.

- [Bhandari 12] B. Bhandari, G.-Y. Lee & S.-H. Ahn. *A review on IPMC material as actuators and sensors: Fabrications, characteristics and applications*. International Journal of Precision Engineering and Manufacturing, vol. 13, no. 1, pages 141–163, jan 2012.
- [Bontsema 88] J. Bontsema & R. Curtain. *A note on spillover and robustness for flexible systems*. IEEE Transactions on Automatic Control, vol. 33, no. 6, pages 567–569, jun 1988.
- [Borutzky 10] W. Borutzky. *Bond Graph Methodology*. Springer London, London, 2010.
- [Boushaki 14] M. N. Boushaki, C. Liu & P. Pognet. *Task-space position control of concentric-tube robot with inaccurate kinematics using approximate Jacobian*. In 2014 IEEE International Conference on Robotics and Automation (ICRA), pages 5877–5882. IEEE, may 2014.
- [Branco 06] P. J. C. Branco & J. A. Dente. *Derivation of a continuum model and its electric equivalent-circuit representation for ionic polymer–metal composite (IPMC) electromechanics*. Smart Materials and Structures, vol. 15, no. 2, pages 378–392, apr 2006.
- [Brugnoli 19a] A. Brugnoli, D. Alazard, V. Pommier-Budinger & D. Matignon. *Port-Hamiltonian formulation and symplectic discretization of plate models Part I: Mindlin model for thick plates*. Applied Mathematical Modelling, vol. 75, pages 940–960, nov 2019.
- [Brugnoli 19b] A. Brugnoli, D. Alazard, V. Pommier-Budinger & D. Matignon. *Port-Hamiltonian formulation and symplectic discretization of plate models Part II: Kirchhoff model for thin plates*. Applied Mathematical Modelling, vol. 75, pages 961–981, nov 2019.
- [Cardoso-Ribeiro 17] F. L. Cardoso-Ribeiro, D. Matignon & V. Pommier-Budinger. *A port-Hamiltonian model of liquid sloshing in moving containers and application to a fluid-structure system*. Journal of Fluids and Structures, vol. 69, pages 402–427, feb 2017.
- [Cardoso-Ribeiro 18] F. L. Cardoso-Ribeiro, D. Matignon & L. Lefèvre. *A structure-preserving Partitioned Finite Element Method for the 2D wave equation*. IFAC-PapersOnLine, vol. 51, no. 3, pages 119–124, 2018.
- [Cha 13] Y. Cha, F. Cellini & M. Porfiri. *Electrical impedance controls mechanical sensing in ionic polymer metal composites*. Physical Review E, vol. 88, no. 6, page 062603, dec 2013.

-
- [Chen 12] Z. Chen, T. Um & H. Bart-Smith. *Ionic Polymer-Metal Composite Artificial Muscles in Bio-Inspired Engineering Research: Underwater Propulsion*. In Smart Actuation and Sensing Systems - Recent Advances and Future Challenges. InTech, oct 2012.
- [Chen 14] Y. Chen, J. Liang & I. W. Hunter. *Modular continuum robotic endoscope design and path planning*. In 2014 IEEE International Conference on Robotics and Automation (ICRA), pages 5393–5400. IEEE, may 2014.
- [Chikhaoui 14a] M. T. Chikhaoui, K. Rabenorosoa & N. Andreff. *Kinematic Modeling of an EAP Actuated Continuum Robot for Active Micro-endoscopy*. In Advances in Robot Kinematics, pages 457–465. Springer International Publishing, Cham, 2014.
- [Chikhaoui 14b] M. T. Chikhaoui, K. Rabenorosoa & N. Andreff. *Towards clinical application of continuum active micro-endoscope robot based on EAP actuation*. In SURGETICA 2014 “Gestes médico-chirurgicaux assistés par ordinateur: problèmes scientifiques, outils et applications cliniques”, pages 1–4, Chambéry, France, 2014.
- [Chikhaoui 16] M. T. Chikhaoui. *New concept of concentric tube robots with micro-actuators based on electro-active polymers*. Theses, Université de Franche-Comté, November 2016.
- [Curtain 95] R. F. Curtain & H. Zwart. An Introduction to Infinite-Dimensional Linear Systems Theory, volume 21 of *Texts in Applied Mathematics*. Springer-Verlag New York, New York, NY, 1995.
- [Dalsmo 98] M. Dalsmo & A. van der Schaft. *On Representations and Integrability of Mathematical Structures in Energy-Conserving Physical Systems*. SIAM Journal on Control and Optimization, vol. 37, no. 1, pages 54–91, jan 1998.
- [De Falco 17] I. De Falco, M. Cianchetti & A. Menciassi. *A soft multi-module manipulator with variable stiffness for minimally invasive surgery*. Bioinspiration & Biomimetics, vol. 12, no. 5, page 056008, sep 2017.
- [de Gennes 00] P. G. de Gennes, K. Okumura, M. Shahinpoor & K. J. Kim. *Mechanoelectric effects in ionic gels*. Europhysics Letters (EPL), vol. 50, no. 4, pages 513–518, may 2000.
- [De Greef 09] A. De Greef, P. Lambert & A. Delchambre. *Towards flexible medical instruments: Review of flexible fluidic actuators*. Precision Engineering, vol. 33, no. 4, pages 311–321, oct 2009.
- [Donnell 33] L. H. Donnell. Stability of thin-walled tubes under torsion. US Government Printing Office, 1933.
-

- [Duindam 09] V. Duindam, A. Macchelli, S. Stramigioli & H. Bruyninckx. *Modeling and Control of Complex Physical Systems*. Springer Berlin Heidelberg, Berlin, Heidelberg, 2009.
- [Eickhoff 07] A. Eickhoff, J. Van Dam, R. Jakobs, V. Kudis, D. Hartmann, U. Damian, U. Weickert, D. Schilling & J. F. Riemann. *Computer-Assisted Colonoscopy (The NeoGuide Endoscopy System): Results of the First Human Clinical Trial (“PACE Study”)*. *The American Journal of Gastroenterology*, vol. 102, no. 2, pages 261–266, feb 2007.
- [Flanders 63] H. Flanders. *Differential Forms with Applications to the Physical Sciences*. Academic Press, Inc., New York, 1963.
- [Gifari 19] M. W. Gifari, H. Naghibi, S. Stramigioli & M. Abayazid. *A review on recent advances in soft surgical robots for endoscopic applications*. *The International Journal of Medical Robotics and Computer Assisted Surgery*, vol. 15, no. 5, oct 2019.
- [Girerd 17] C. Girerd, K. Rabenorosoa, P. Rougeot & P. Renaud. *Towards optical biopsy of olfactory cells using concentric tube robots with follow-the-leader deployment*. In *2017 IEEE/RSJ International Conference on Intelligent Robots and Systems (IROS)*, pages 5661–5887. IEEE, sep 2017.
- [Golo 02] G. Golo, V. Talasila & A. van der Schaft. *Approximation of the Telegrapher’s equations*. In *Proceedings of the 41st IEEE Conference on Decision and Control, 2002.*, volume 4, pages 4587–4592. IEEE, 2002.
- [Golo 03] G. Golo, A. van der Schaft & S. Stramigioli. *Hamiltonian Formulation of Planar Beams*. *IFAC Proceedings Volumes*, vol. 36, no. 2, pages 147–152, apr 2003.
- [Golo 04] G. Golo, V. Talasila, A. van der Schaft & B. Maschke. *Hamiltonian discretization of boundary control systems*. *Automatica*, vol. 40, no. 5, pages 757–771, may 2004.
- [Golub 13] G. H. Golub & C. F. V. n. Loan. *Matrix Computations*. The Johns Hopkins University Press, 2013.
- [Haga 04] Y. Haga & M. Esashi. *Biomedical Microsystems for Minimally Invasive Diagnosis and Treatment*. *Proceedings of the IEEE*, vol. 92, no. 1, pages 98–114, jan 2004.
- [Hairer 06] E. Hairer, C. Lubich & G. Wanner. *Geometric Numerical Integration*, volume 31 of *Springer Series in Computational Mathematics*. Springer-Verlag Berlin Heidelberg, Berlin/Heidelberg, 2006.
- [Han 99] S. M. Han, H. Benaroya & T. Wei. *Dynamics of transversely vibrating beams using four engineering theories*. *Journal of Sound and vibration*, vol. 225, no. 5, pages 935–988, 1999.

-
- [Higham 88] N. J. Higham. *Computing a nearest symmetric positive semidefinite matrix*. Linear Algebra and its Applications, vol. 103, pages 103–118, may 1988.
- [Hua 96] D. Hua & P. Lancaster. *Linear matrix equations from an inverse problem of vibration theory*. Linear Algebra and its Applications, vol. 246, no. 1996, pages 31–47, oct 1996.
- [Ikuta 88] K. Ikuta, M. Tsukamoto & S. Hirose. *Shape memory alloy servo actuator system with electric resistance feedback and application for active endoscope*. In Proceedings. 1988 IEEE International Conference on Robotics and Automation, pages 427–430. IEEE Comput. Soc. Press, 1988.
- [Ivancevic 07] V. G. Ivancevic & T. T. Ivancevic. *Applied Differential Geometry*. WORLD SCIENTIFIC, may 2007.
- [Kanno 95] R. Kanno, S. Tadokoro, T. Takamori, M. Hattori & K. Oguro. *Modeling of ICPF (ionic conducting polymer film) actuator-modeling of electrical characteristics*. In Proceedings of IECON '95 - 21st Annual Conference on IEEE Industrial Electronics, volume 2, pages 913–918. IEEE, 1995.
- [Karnopp 97] D. Karnopp. *Understanding multibody dynamics using bond graph representations*. Journal of the Franklin Institute, vol. 334, no. 4, pages 631–642, jul 1997.
- [Kim 05] B. Kim, S. Lee, J. H. Park & J. O. Park. *Design and fabrication of a locomotive mechanism for capsule-type endoscopes using shape memory alloys (SMAs)*. IEEE/ASME Transactions on Mechatronics, vol. 10, no. 1, pages 77–86, 2005.
- [Kotyczka 16] P. Kotyczka. *Finite Volume Structure-Preserving Discretization of 1D Distributed-Parameter Port-Hamiltonian Systems*. IFAC-PapersOnLine, vol. 49, no. 8, pages 298–303, 2016.
- [Kotyczka 18a] P. Kotyczka & L. Lefèvre. *Discrete-time port-Hamiltonian systems based on Gauss-Legendre collocation*. IFAC-PapersOnLine, vol. 51, no. 3, pages 125–130, 2018.
- [Kotyczka 18b] P. Kotyczka, B. Maschke & L. Lefèvre. *Weak form of Stokes-Dirac structures and geometric discretization of port-Hamiltonian systems*. Journal of Computational Physics, vol. 361, pages 442–476, may 2018.
- [Kraus 67] H. Kraus. *Thin elastic shells : an introduction to the theoretical foundations and the analysis of their static and dynamic behavior* / Harry Kraus. New York (N.Y.) : Wiley, 1967.
- [Le Gorrec 05] Y. Le Gorrec, H. Zwart & B. Maschke. *Dirac structures and Boundary Control Systems associated with Skew-Symmetric Differential Operators*. SIAM Journal on Control and Optimization, vol. 44, no. 5, pages 1864–1892, jan 2005.
-

- [Lee 20] Y. N. Lee, J. H. Moon, T. H. Lee, H. J. Choi, T. Itoi, T. Beyna & H. Neuhaus. *Prospective randomized trial of a new multibending versus conventional ultra-slim endoscope for peroral cholangioscopy without device or endoscope assistance (with video)*. *Gastrointestinal Endoscopy*, vol. 91, no. 1, pages 92–101, jan 2020.
- [Lehman 09] A. C. Lehman, J. Dumpert, N. A. Wood, L. Redden, A. Q. Visty, S. Farritor, B. Varnell & D. Oleynikov. *Natural orifice cholecystectomy using a miniature robot*. *Surgical Endoscopy*, vol. 23, no. 2, pages 260–266, feb 2009.
- [Leissa 73] A. W. Leissa. *Vibration of shells*. NASA, Washington, United States, 1973.
- [Li 16] Z. Li, M. Zin Oo, V. Nalam, V. Duc Thang, H. Ren, T. Kofidis & H. Yu. *Design of a Novel Flexible Endoscope—Cardioscope*. *Journal of Mechanisms and Robotics*, vol. 8, no. 5, page 051014, may 2016.
- [Liu 20] N. Liu, Y. Wu, Y. Le Gorrec, H. Ramirez & L. Lefèvre. *Structure-preserving discretization and control of a 2D vibro-acoustic tube*. *IMA Journal of Mathematical Control and Information*, page 22, 2020.
- [Loeve 10] A. Loeve, P. Breedveld & J. Dankelman. *Scopes Too Flexible...and Too Stiff*. *IEEE Pulse*, vol. 1, no. 3, pages 26–41, nov 2010.
- [Love 88] A. E. H. Love & G. H. Darwin. *XVI. The small free vibrations and deformation of a thin elastic shell*. *Philosophical Transactions of the Royal Society of London. (A.)*, vol. 179, pages 491–546, dec 1888.
- [Lucarini 15] G. Lucarini, G. Ciuti, M. Mura, R. Rizzo & A. Mencias. *A New Concept for Magnetic Capsule Colonoscopy Based on an Electromagnetic System*. *International Journal of Advanced Robotic Systems*, vol. 12, no. 3, page 25, mar 2015.
- [Luo 12] Z.-H. Luo, B.-Z. Guo & Ö. Morgül. *Stability and stabilization of infinite dimensional systems with applications*. Springer Science & Business Media, 2012.
- [Luqman 11] M. Luqman, J.-W. Lee, K.-K. Moon & Y.-T. Yoo. *Sulfonated polystyrene-based ionic polymer–metal composite (IPMC) actuator*. *Journal of Industrial and Engineering Chemistry*, vol. 17, no. 1, pages 49–55, jan 2011.
- [Macchelli 04] A. Macchelli & C. Melchiorri. *Modeling and Control of the Timoshenko Beam. The Distributed Port Hamiltonian Approach*. *SIAM Journal on Control and Optimization*, vol. 43, no. 2, pages 743–767, jan 2004.

-
- [Macchelli 05] A. Macchelli, C. Melchiorri & L. Bassi. *Port-based Modelling and Control of the Mindlin Plate*. In Proceedings of the 44th IEEE Conference on Decision and Control, pages 5989–5994. IEEE, 2005.
- [Macchelli 17] A. Macchelli, Y. Le Gorrec, H. Ramirez & H. Zwart. *On the Synthesis of Boundary Control Laws for Distributed Port-Hamiltonian Systems*. IEEE Transactions on Automatic Control, vol. 62, no. 4, pages 1700–1713, apr 2017.
- [Masashi Ikeuchi 08] Masashi Ikeuchi & Koji Ikuta. *"Membrane micro emboss following excimer laser ablation (MeME-X) process" for pressure-driven micro active catheter*. In 2008 IEEE 21st International Conference on Micro Electro Mechanical Systems, pages 62–65. IEEE, jan 2008.
- [Maschke 92] B. Maschke, A. van der Schaft & P. Breedveld. *An intrinsic Hamiltonian formulation of network dynamics: non-standard poisson structures and gyrators*. Journal of the Franklin Institute, vol. 329, no. 5, pages 923–966, sep 1992.
- [Maschke 00] B. Maschke & A. van der Schaft. *Port Controlled Hamiltonian Representation of Distributed Parameter Systems*. IFAC Proceedings Volumes, vol. 33, no. 2, pages 27–37, mar 2000.
- [Meurer 13] T. Meurer. *Control of Higher-Dimensional PDEs*. Communications and Control Engineering. Springer Berlin Heidelberg, Berlin, Heidelberg, 2013.
- [Mindlin 89] R. D. Mindlin. *Influence of Rotatory Inertia and Shear on Flexural Motions of Isotropic, Elastic Plates*. In The Collected Papers of Raymond D. Mindlin Volume I, pages 225–232. Springer New York, New York, NY, 1989.
- [Morris 10] K. Morris. *Control of Systems Governed by Partial Differential Equations*. In IEEE Control Handbook, pages 67–167–37. dec 2010.
- [Moulla 12] R. Moulla, L. Lefèvre & B. Maschke. *Pseudo-spectral methods for the spatial symplectic reduction of open systems of conservation laws*. Journal of Computational Physics, vol. 231, no. 4, pages 1272–1292, feb 2012.
- [Nada 10] A. A. Nada, B. A. Hussein, S. M. Megahed & A. A. Shabana. *Use of the floating frame of reference formulation in large deformation analysis: Experimental and numerical validation*. Proceedings of the Institution of Mechanical Engineers, Part K: Journal of Multi-body Dynamics, vol. 224, no. 1, pages 45–58, mar 2010.
- [Naghdi 64] P. Naghdi & J. Berry. *On the equations of motion of cylindrical shells*. Journal of Applied Mechanics, vol. 21, pages 160—166, 1964.
-

- [Nemat-Nasser 02] S. Nemat-Nasser. *Micromechanics of actuation of ionic polymer-metal composites*. Journal of Applied Physics, vol. 92, no. 5, pages 2899–2915, sep 2002.
- [Newbury 02] K. M. Newbury & D. J. Leo. *Electromechanical Modeling and Characterization of Ionic Polymer Benders*. Journal of Intelligent Material Systems and Structures, vol. 13, no. 1, pages 51–60, jan 2002.
- [Nishida 05] G. Nishida & M. Yamakita. *Distributed port Hamiltonian formulation of flexible beams under large deformations*. In Proceedings of 2005 IEEE Conference on Control Applications, 2005. CCA 2005., pages 589–594. IEEE, 2005.
- [Nishida 08] G. Nishida, K. Takagi, B. Maschke & Z.-w. Luo. *Multi-Scale Distributed Port-Hamiltonian Representation of Ionic Polymer-Metal Composite*. IFAC Proceedings Volumes, vol. 41, no. 2, pages 2300–2305, 2008.
- [Nishida 11] G. Nishida, K. Takagi, B. Maschke & T. Osada. *Multi-scale distributed parameter modeling of ionic polymer-metal composite soft actuator*. Control Engineering Practice, vol. 19, no. 4, pages 321–334, apr 2011.
- [OGURO 92] OGURO & K. *Bending of an Ion-Conducting polymer Film-Electrode Composite by an Electric Stimulus at Low Voltage*. J. Micromachine Society, vol. 5, pages 27–30, 1992.
- [Ortega 88] R. Ortega & M. W. Spong. *Adaptive motion control of rigid robots: A tutorial*. In Proceedings of the IEEE Conference on Decision and Control, pages 1575–1584. Publ by IEEE, 1988.
- [Ortega 98] R. Ortega, A. Loría, P. J. Nicklasson & H. Sira-Ramírez. *Passivity-based Control of Euler-Lagrange Systems*. Communications and Control Engineering. Springer London, London, 1998.
- [Ortega 99a] R. Ortega, A. van der Schaft, B. Maschke & G. Escobar. *Energy-shaping of port-controlled Hamiltonian systems by interconnection*. In Proceedings of the IEEE Conference on Decision and Control, volume 2, pages 1646–1651. IEEE, 1999.
- [Ortega 99b] R. Ortega, A. J. van der Schaft & B. M. Maschke. *Stabilization of port-controlled Hamiltonian systems via energy balancing*. In D. Aeyels, F. Lamnabhi-Lagarrigue & A. van der Schaft, editors, *Stability and Stabilization of Nonlinear Systems*, pages 239–260, London, 1999. Springer London.
- [Ortega 00] R. Ortega & M. W. Spong. *Stabilization of Underactuated Mechanical Systems Via Interconnection and Damping Assignment*. IFAC Proceedings Volumes, vol. 33, no. 2, pages 69–74, mar 2000.

- [Ortega 01] R. Ortega, A. J. van der Schaft, I. Mareels & B. Maschke. *Putting energy back in control*. IEEE Control Systems, vol. 21, no. 2, pages 18–33, apr 2001.
- [Ortega 02] R. Ortega, A. van der Schaft, B. Maschke & G. Escobar. *Interconnection and damping assignment passivity-based control of port-controlled Hamiltonian systems*. Automatica, vol. 38, no. 4, pages 585–596, apr 2002.
- [Ortega 08] R. Ortega, A. van der Schaft, F. Castanos & A. Astolfi. *Control by Interconnection and Standard Passivity-Based Control of Port-Hamiltonian Systems*. IEEE Transactions on Automatic Control, vol. 53, no. 11, pages 2527–2542, dec 2008.
- [Panwar 12] V. Panwar, C. Lee, S. Y. Ko, J.-O. Park & S. Park. *Dynamic mechanical, electrical, and actuation properties of ionic polymer metal composites using PVDF/PVP/PSSA blend membranes*. Materials Chemistry and Physics, vol. 135, no. 2-3, pages 928–937, aug 2012.
- [Paquette 03] J. W. Paquette, K. J. Kim, J.-D. Nam & Y. S. Tak. *An Equivalent Circuit Model for Ionic Polymer-Metal Composites and their Performance Improvement by a Clay-Based Polymer Nano-Composite Technique*. Journal of Intelligent Material Systems and Structures, vol. 14, no. 10, pages 633–642, oct 2003.
- [Paynter 61] H. M. Paynter, P. Briggs & M. I. of Technology. *Analysis and design of engineering systems: class notes for M.I.T. course 2.751*, 1961.
- [Phee 10] S. J. Phee, A. P. Kencana, V. A. Huynh, Z. L. Sun, S. C. Low, K. Yang, D. Lomanto & K. Y. Ho. *Design of a master and slave transluminal endoscopic robot for natural orifice transluminal endoscopic surgery*. Proceedings of the Institution of Mechanical Engineers, Part C: Journal of Mechanical Engineering Science, vol. 224, no. 7, pages 1495–1503, jul 2010.
- [Polyuga 10] R. Polyuga & A. Schaft, van der. *Structure preserving model reduction of port-Hamiltonian systems by moment matching at infinity*. Automatica, vol. 46, no. 4, pages 665–672, 2010.
- [Polyuga 12] R. V. Polyuga & A. J. van der Schaft. *Effort-and flow-constraint reduction methods for structure preserving model reduction of port-Hamiltonian systems*. Systems & Control Letters, vol. 61, no. 3, pages 412–421, 2012.
- [Ponsky 12] T. A. Ponsky, A. Khosla & J. L. Ponsky. *Minimally Invasive Surgery*. In Textbook of Clinical Gastroenterology and Hepatology, pages 1182–1189. Wiley-Blackwell, Oxford, UK, apr 2012.

- [Porfiri 17] M. Porfiri, A. Leronni & L. Bardella. *An alternative explanation of back-relaxation in ionic polymer metal composites*. Extreme Mechanics Letters, vol. 13, pages 78–83, may 2017.
- [Qatu 02a] M. S. Qatu. *Recent research advances in the dynamic behavior of shells: 1989-2000, Part 1: Laminated composite shells*. Applied Mechanics Reviews, vol. 55, no. 4, pages 325–350, jul 2002.
- [Qatu 02b] M. S. Qatu. *Recent research advances in the dynamic behavior of shells: 1989–2000, Part 2: Homogeneous shells*. Applied Mechanics Reviews, vol. 55, no. 5, pages 415–434, sep 2002.
- [Ramirez 13] H. Ramirez, B. Maschke & D. Sbarbaro. *Irreversible port-Hamiltonian systems: A general formulation of irreversible processes with application to the CSTR*. Chemical Engineering Science, vol. 89, pages 223–234, feb 2013.
- [Reissner 41] E. Reissner. *A New Derivation of the Equations for the Deformation of Elastic Shells*. American Journal of Mathematics, vol. 63, no. 1, page 177, jan 1941.
- [Rodriguez 01] H. Rodriguez, A. van der Schaft & R. Ortega. *On stabilization of nonlinear distributed parameter port-controlled Hamiltonian systems via energy shaping*. In Proceedings of the 40th IEEE Conference on Decision and Control (Cat. No.01CH37228), volume 1, pages 131–136. IEEE, 2001.
- [Sanders 60] J. L. Sanders. *An improved first-approximation theory for thin shells*, volume 24. US Government Printing Office, 1960.
- [Sandhu 90] J. Sandhu, K. Stevens & G. Davies. *A 3-D, co-rotational, curved and twisted beam element*. Computers & Structures, vol. 35, no. 1, pages 69–79, jan 1990.
- [Selig 01] J. Selig & X. Ding. *A screw theory of static beams*. In Proceedings 2001 IEEE/RSJ International Conference on Intelligent Robots and Systems. Expanding the Societal Role of Robotics in the the Next Millennium (Cat. No.01CH37180), volume 1, pages 312–317. IEEE, 2001.
- [Shahinpoor 92] M. Shahinpoor. *Conceptual design, kinematics and dynamics of swimming robotic structures using ionic polymeric gel muscles*. Smart Materials and Structures, vol. 1, no. 1, pages 91–94, mar 1992.
- [Shahinpoor 99] M. Shahinpoor. *Electromechanics of ionoelastic beams as electrically controllable artificial muscles*. In Y. Bar-Cohen, editeur, Smart Structures and Materials 1999: Electroactive Polymer Actuators and Devices, volume 3669, pages 109 – 121. International Society for Optics and Photonics, SPIE, 1999.

-
- [Shahinpoor 01] M. Shahinpoor & K. J. Kim. *Ionic polymer-metal composites: I. Fundamentals*. Smart Materials and Structures, vol. 10, no. 4, pages 819–833, aug 2001.
- [Shahinpoor 05] M. Shahinpoor & K. J. Kim. *Ionic polymer-metal composites: IV. Industrial and medical applications*. Smart Materials and Structures, vol. 14, no. 1, pages 197–214, feb 2005.
- [Shahinpoor 16] M. Shahinpoor, editeur. Ionic polymer metal composites (ipmcs), volume 1 of *Smart Materials Series*. The Royal Society of Chemistry, 2016.
- [Shahmoon 11] A. Shahmoon, H. Slovin & Z. Zalevsky. *Biomedical Super-resolved Imaging Using Special Micro-probe*. Bio-NanoScience, vol. 1, no. 3, pages 103–109, sep 2011.
- [Shoa 09a] T. Shoa, J. D. Madden, N. R. Munce & V. X. D. Yang. *Steerable Catheters*. In Biomedical Applications of Electroactive Polymer Actuators, pages 229–248. John Wiley & Sons, Ltd, Chichester, UK, 2009.
- [Shoa 09b] T. Shoa, N. R. Munce, V. Yang & J. D. Madden. *Conducting polymer actuator driven catheter: overview and applications*. In Electroactive Polymer Actuators and Devices (EAPAD) 2009, volume 7287, page 72871J. SPIE, mar 2009.
- [Shores 07] T. S. Shores. Applied Linear Algebra and Matrix Analysis. Undergraduate Texts in Mathematics. Springer New York, New York, NY, 2007.
- [Simo 86] J. C. Simo & L. Vu-Quoc. *On the Dynamics of Flexible Beams Under Large Overall Motions—The Plane Case: Part I*. Journal of Applied Mechanics, vol. 53, no. 4, pages 849–854, dec 1986.
- [Soedel 82] W. Soedel. *On the vibration of shells with timoshenko-mindlin type shear deflections and rotatory inertia*. Journal of Sound and Vibration, vol. 83, no. 1, pages 67–79, jul 1982.
- [Sokolnikoff 56] I. S. Sokolnikoff & R. D. Specht. Mathematical theory of elasticity. McGraw-Hill New York, 1956.
- [Spaner 97] S. J. Spaner & G. L. Warnock. *A Brief History of Endoscopy, Laparoscopy, and Laparoscopic Surgery*. Journal of Laparoendoscopic & Advanced Surgical Techniques, vol. 7, no. 6, pages 369–373, dec 1997.
- [Subramanian 05] S. Subramanian, M. M. Amonkar & T. L. Hunt. *Use of colonoscopy for colorectal cancer screening: Evidence from the 2000 National Health Interview Survey*. Cancer Epidemiology Biomarkers and Prevention, vol. 14, no. 2, pages 409–416, feb 2005.
-

- [Takagi 14] K. Takagi, N. Tomita & K. Asaka. *A simple method for obtaining large deformation of IPMC actuators utilizing copper tape*. *Advanced Robotics*, vol. 28, no. 7, pages 513–521, apr 2014.
- [Timoshenko 21] S. Timoshenko. *LXVI. On the correction for shear of the differential equation for transverse vibrations of prismatic bars*. *The London, Edinburgh, and Dublin Philosophical Magazine and Journal of Science*, vol. 41, no. 245, pages 744–746, may 1921.
- [Timoshenko 59] S. P. Timoshenko & S. Woinowsky-Krieger. *Theory of plates and shells*. McGraw-Hill New York, 1959.
- [Timoshenko 09] S. P. Timoshenko & J. M. Gere. *Theory of elastic stability*. Courier Corporation, 2009.
- [Trenchant 17] V. Trenchant, T. Vu, H. Ramirez, L. Lefèvre & Y. Le Gorrec. *On the use of structural invariants for the distributed control of infinite dimensional port-Hamiltonian systems*. In *2017 IEEE 56th Annual Conference on Decision and Control (CDC)*, pages 47–52, 2017.
- [Trenchant 18a] V. Trenchant, W. Hu, H. Ramirez & Y. L. Gorrec. *Structure Preserving Finite Differences in Polar Coordinates for Heat and Wave Equations*. *IFAC-PapersOnLine*, vol. 51, no. 2, pages 571–576, 2018.
- [Trenchant 18b] V. Trenchant, H. Ramirez, Y. Le Gorrec & P. Kotyczka. *Finite differences on staggered grids preserving the port-Hamiltonian structure with application to an acoustic duct*. *Journal of Computational Physics*, vol. 373, pages 673–697, nov 2018.
- [van der Schaft 94] A. van der Schaft & B. Maschke. *On the Hamiltonian formulation of nonholonomic mechanical systems*. *Reports on Mathematical Physics*, vol. 34, no. 2, pages 225–233, aug 1994.
- [van der Schaft 02] A. van der Schaft & B. Maschke. *Hamiltonian formulation of distributed-parameter systems with boundary energy flow*. *Journal of Geometry and Physics*, vol. 42, no. 1-2, pages 166–194, may 2002.
- [van der Schaft 14] A. van der Schaft & D. Jeltsema. *Port-Hamiltonian Systems Theory: An Introductory Overview*. *Foundations and Trends® in Systems and Control*, vol. 1, no. 2, pages 173–378, 2014.
- [van der Schaft 17] A. van der Schaft. *L2-Gain and Passivity Techniques in Nonlinear Control*. *Communications and Control Engineering*. Springer International Publishing, Cham, 2017.

-
- [Villadsen 78] J. Villadsen & M. L. Michelsen. Solution of differential equation models by polynomial approximation. Englewood Cliffs, N.J. : Prentice-Hall, ©1978., 1978.
- [Villegas 07] J. Villegas. *A Port-Hamiltonian Approach to Distributed Parameter Systems*. PhD thesis, University of Twente, 2007.
- [Vlasov 51] V. S. Vlasov. *Basic differential equations in general theory of elastic shells. NACA-TM-1241*. National Advisory Committee for Aeronautics, no. February, 1951.
- [Voss 10] T. Voss. *Port-Hamiltonian modeling and control of piezoelectric beams and plates : application to inflatable space structures*. PhD thesis, University of Groningen, 2010.
- [Wang 15] J. Wang, A. McDaid, R. Sharma & K. Aw. *A Compact Ionic Polymer Metal Composite (IPMC) System with Inductive Sensor for Closed Loop Feedback*. *Actuators*, vol. 4, no. 2, pages 114–126, may 2015.
- [Webster 10] R. J. Webster & B. A. Jones. *Design and Kinematic Modeling of Constant Curvature Continuum Robots: A Review*. *The International Journal of Robotics Research*, vol. 29, no. 13, pages 1661–1683, nov 2010.
- [Woodgate 87] K. G. Woodgate. *Optimization over positive semi-definite symmetric matrices with application to Quasi-Newton algorithms*. PhD thesis, Imperial College London, 1987.
- [Wu 14] Y. Wu, B. Hamroun, Y. L. Gorrec & B. Maschke. *Port Hamiltonian System in Descriptor Form for Balanced Reduction: Application to a Nanotweezer*. *IFAC Proceedings Volumes*, vol. 47, no. 3, pages 11404–11409, 2014.
- [Wu 20] Y. Wu, B. Hamroun, Y. Le Gorrec & B. Maschke. *Reduced Order LQG Control Design for Infinite Dimensional Port Hamiltonian Systems*. *IEEE Transactions on Automatic Control*, pages 1–1, 2020.
- [Yamaue 05] T. Yamaue, H. Mukai, K. Asaka & M. Doi. *Electrostress Diffusion Coupling Model for Polyelectrolyte Gels*. *Macromolecules*, vol. 38, no. 4, pages 1349–1356, feb 2005.
- [Yoon 07] W. J. Yoon, P. G. Reinhall & E. J. Seibel. *Analysis of electroactive polymer bending: A component in a low cost ultra-thin scanning endoscope*. *Sensors and Actuators A: Physical*, vol. 133, no. 2, pages 506–517, feb 2007.
- [Yosida 95] K. Yosida. *Functional Analysis*, volume 123 of *Classics in Mathematics*. Springer-Verlag Berlin Heidelberg, Berlin, Heidelberg, 1995.
-

- [Zheng 09] B. Zheng, L. Ye & D. S. Cvetkovic-Ilic. *The *congruence class of the solutions of some matrix equations*. Computers and Mathematics with Applications, vol. 57, no. 4, pages 540–549, 2009.
- [Zhu 12] Z. Zhu, H. Chen, Y. Wang & B. Li. *Multi-physical modeling for electro-transport and deformation of ionic polymer metal composites*. In Y. Bar-Cohen, editeur, Electroactive Polymer Actuators and Devices (EAPAD) 2012, pages 191 – 202. SPIE, apr 2012.
- [Zhu 13] Z. Zhu, K. Asaka, L. Chang, K. Takagi & H. Chen. *Multi-physics of ionic polymer–metal composite actuator*. Journal of Applied Physics, vol. 114, no. 8, page 084902, aug 2013.

Titre : Modélisation Hamiltonienne à ports et commande distribuée de structures flexibles: application aux endoscopes biomédicaux à actionneurs à base de polymère électro-actif.

Mots clefs: systèmes Hamiltoniens à ports, actionneurs à base de polymère électro-actif, méthodes de discrétisation préservant la structure, commande par interconnection, commande distribuée

Résumé : Les travaux exposés dans cette thèse traitent de la modélisation multiphysique et de la commande distribuée de structures flexibles actionnées à l'aide de polymères électro-actifs de type Ionic Polymer Metal Composite (IPMC). Dans un premier temps, nous proposons une formulation Hamiltonienne à ports de l'actionneur IPMC afin de tenir compte des couplages multiphysiques et multiéchelles. Des multiplicateurs de Lagrange sont utilisés pour gérer les contraintes mécaniques apparaissant au sein de l'actionneur. La structure mécanique de la structure flexible est quant à elle modélisée en 1D à l'aide de modèles de poutres et

en 2D à l'aide d'un modèle de coques fines. Dans un second temps, deux méthodes de discrétisation préservant la structure sont présentées et étendues aux systèmes Hamiltoniens à ports de dimension infinie avec dissipation et entrée distribuée. Le modèle de l'actionneur est validé expérimentalement à l'aide d'une discrétisation de type différences finies sur grilles en quinconces. Dans un troisième temps, nous développons sur un modèle simplifié de type corde vibrante, une loi de commande distribuée dans le domaine à l'aide de patches, permettant de modéliser la fonction d'énergie globale du système et d'injecter de la dissipation.

Title : Port-Hamiltonian modeling and distributed control of flexible structures: application to bio-medical endoscopes with electro-active polymer actuators

Keywords : port-Hamiltonian systems, electro-active polymer actuators, structure-preserving discretization methods, control by interconnection, distributed control

Abstract : This thesis deals with the multiphysical modeling and the distributed control of flexible structures actuated by Ionic Polymer Metal Composite (IPMC) actuators. We firstly propose a model for the IPMC actuator using infinite dimensional port-Hamiltonian formulations in order to tackle the multiphysical and multiscale couplings. Lagrange multipliers are used to handle the mechanical constraints appearing in the actuator. The mechanical structure of the flexible structure is then modeled in 1D with beam models and in 2D with a thin shell model. Secondly, two struc-

ture preserving discretization methods are presented and extended to infinite dimensional dissipative port-Hamiltonian system with distributed input. The proposed IPMC actuator model is then discretized using the structure preserving finite differences method on staggered grids and validated on experimental data. Thirdly, we propose an in-domain distributed control law on a simplified model i.e. the vibrating string actuated with patches, that allows to shape the total energy of the system and to inject damping in order to stabilize the overall system with predefined performances.